DOE/MC/23075 -- 5031
(DE9600 2215)
Vol. I, Part 2

Measurement and Modeling of Advanced Coal Conversion Processes Volume I, Part 2

Final Report September 1986 - September 1993

Peter R. Solomon
Michael A. Serio
David G. Hamblen
L. Douglas Smoot
B. Scott Brewster
Predrag T. Radulovic

September 1995

Work Performed Under Contract No.: DE-AC21-86MC23075

For
U.S. Department of Energy
Office of Fossil Energy
Morgantown Energy Technology Center
Morgantown, West Virginia

By
Advanced Fuel Research, Inc.
East Hartford, Connecticut
and
Brigham Young University
Provo, Utah

DISCLAIMER

DOE/MC/23075 -- 5031

MEASUREMENT AND MODELING OF ADVANCED COAL CONVERSION PROCESSES
Volume I, Part 2

DOE

DOE/MC/23075 -- 5031
(DE96002915)
Vol. I, Part 2
Distribution Category UC-109

Measurement and Modeling of Advanced Coal Conversion Processes Volume I, Part 2

Final Report
September 1986 - September 1993

Peter R. Solomon
Michael A. Serio
David G. Hamblen
L. Douglas Smoot
B. Scott Brewster
Predrag T. Radulovic

Work Performed Under Contract No.: DE-AC21-86MC23075

For
U.S. Department of Energy
Office of Fossil Energy
Morgantown Energy Technology Center
P.O. Box 880
Morgantown, West Virginia 26507-0880

By
Advanced Fuel Research, Inc.
87 Church Street
East Hartford, Connecticut 06108
and
Brigham Young University
Provo, Utah 84602

September 1995

II.E. SUBTASK 2.e. - LARGE PARTICLE/THICK BED SUBMODELS

Senior Investigator - Michael A. Serio
Advanced Fuel Research, Inc.
87 Church Street
East Hartford, CT 06108
(203) 528-9806

Objective

The objectives of this task were to develop or adapt advanced physics and chemistry submodels for the reactions of "large" coal particles (i.e., particles with significant heat and/or mass transport limitations) as well as thick beds (multiple particle layers) and to validate the submodels by comparison with laboratory scale experiments. The results were coal chemistry and physics submodels which were integrated into the fixed-bed (or moving-bed) gasifier code developed by BYU in Subtask 3.b. Consequently, this task was closely coordinated with Subtask 3.b.

Summary of Accomplishments

A literature review of heat and mass transport effects in coal pyrolysis was completed. In addition, calculations were done to define regimes of internal and external heat and mass transport control for conditions of interest. This was done to define the boundary regions where such considerations become important.

A single particle FG-DVC model was developed for use in the fixed bed reactor code. This version of the model is based on an ordinary differential equation (ODE) version of the 2-σ percolation FG-DVC model. The code was delivered to BYU for integration into the FBED-1 Model.

A model for the destruction of tar in fixed bed gasifiers was developed in order to account for the relatively low yield of tar from these systems. According to the predictions of the FBED-1 model, the tar evolution occurs in a relatively small region near the top of the reactor where the gas and particle temperatures are changing rapidly. While the coal particles are entering at room temperature, the exit gas temperature is close to 1000 K and is 1300 K in the region where tar evolves. Some experiments were done to assess the relative importance of tar gasification and tar cracking reactions. It was found that, while the thermal cracking effects were significant, the addition of CO_2 did not have much effect on the yield or composition of tar. Consequently, it was concluded based on the laboratory data and literature review that the tar destruction in the top part of a fixed-bed gasifier can probably be attributed primarily to thermal cracking rather than gasification reactions.

II.E.1. Literature Review

A literature review of heat and mass transport effects in coal pyrolysis was completed as part of this subtask. A critical evaluation was made of models that have been used to describe intraparticle heat transfer during pyrolysis. Since mass transfer effects are well covered in the review by Eric Suuberg (see Appendix A in the Second Quarterly Report), this review was focused primarily on heat transport processes. In addition, calculations were done to define regimes of internal and external heat and mass transport control for conditions of interest. This was to determine the boundary regions where such considerations become important. Finally, a review was made of previous work on fixed-bed pyrolysis experiments in preparation for our own experimental effort.

Heat and Mass Transport Effects in Coal Pyrolysis

Introduction - Given the large particles used in fixed-bed gasifiers, it is likely that transport effects

nearly always play a role. However, it is also true that at the very high heat fluxes encountered in some gasification and combustion processes, gradients may be important for particles in the pulverized fuel range. Consequently, the review was not strictly limited to large (> 0.5 mm) particles since what constitutes a "large" particle will depend on the experimental conditions.

The first objective was to examine previous experimental and modeling studies of heat transport. A close examination of this work indicated widely different assumptions about the values of coal physical properties and how these change with temperature and the extent of pyrolysis. Consequently, it was decided that a review of the literature on coal physical properties would also be necessary. Most of this literature review was included in the paper of Solomon et. al. (1992), which also includes a detailed review of chemical kinetic rates from the literature.

Review of Modeling Studies - Since much of the work on devolatilization in the last several years has included rapid pyrolysis of fine (pulverized) particles or slow pyrolysis of large particles, most pyrolysis studies and models have not been concerned with internal transport effects. However, with the relatively recent interest in pyrolysis under fluidized-bed or moving-bed conditions, where large (> 1mm) particles are pyrolyzed at relatively high heating rates (10 to 1000 K/s), the interest in internal transport has increased.

Models for simultaneous heat and mass transport for devolatilization have been developed by Mills et al. (1976) and James and Mills (1976) for plastic coals and by Devanathan and Saxena (1985, 1987) and Bliek et al. (1985) for non-plastic coals. Freihaut et al. (1977) and Agarwal et al. (1984a, 1984b) have developed coupled reaction and heat transport models for non-plastic coals.

Heat Transfer/Reaction Models - A model by Freihaut et al. (1977) considered the combined influence of heat transfer, heats of reaction and chemical kinetics on intraparticle temperature gradients during pyrolysis. Not many details of the model have been published in the open literature. Mass transfer effects were neglected.

Agarwal et al. (1984a) have developed a general devolatilization model for large non-plastic particles under fluidized-bed conditions which includes coupled reaction and heat transfer. Good agreement was obtained for devolatilization times measured for Mississippi lignite. A simpler version was developed for the pure heat transfer control regime (Agarwal et al., 1984b). Neither version includes a treatment of mass transfer of secondary cracking effects.

Heat Transfer/Mass Transfer Reaction and Models - Workers at UCLA (Mills et al., 1976) developed a model for particles undergoing rapid pyrolysis which included a fundamental description of heat transport starting with the conservation equations. A consecutive reaction scheme, similar to that of Chermin and van Krevelen (1957) was used. The porosity of the particle was assumed to be governed by a foaming law and the particle was allowed to swell and shrink, accordingly.

The thermal conductivity was assumed to decrease linearly with the decrease in particle density. The model was primarily concerned with the variation in thermal response of a particle with the variation in parameters such as particle diameter, ambient temperature, heating rate, heats of reaction and activation energies. The equations were solved numerically by a finite-difference method. The model was successful in qualitatively describing many important features of coal pyrolysis. Mills et al. (1976) also evaluated the work of Peters and Berlting (1965), who injected 1000 - 1500 μm particles into a fluidized bed at temperatures ranging from 600 to 1100°C. They noted that the relatively weak diameter dependence observed by Peters and Berlting ($d_o^{-0.26}$) is evidence that the experiments were primarily controlled by chemical reactions and not dominated by heat transfer, as was suggested by Peters and Berlting.

The model of Mills et al. was improved in a later paper by James et al. (1976). In order to account

for pressure and particle size effects, models were included to describe (1) the porous structure of a coal particle; (2) the flow of gases through voids and pores, and the resultant pressure distribution, (3) evaporation of tar species and (4) cracking of gaseous species as they percolate through the pores. Again, the qualitative predictions of the model were in good agreement with expectations, but this version of the model was never rigorously validated against experimental data.

The original model of Devanathan and Saxena (1985) was developed for the devolatilization of large non-plastic coal particles. Their objective was to develop a comprehensive pyrolysis model considering heat and mass transport resistances. Since the primary focus of their work was the effects of the transport parameters, the initial (Devanathan and Saxena, 1985) paper used a simple single-reaction model with a global activation energy for primary pyrolysis. They also ignored the temperature variation of the physical properties (heat capacity, thermal conductivity). The latter simplification is a major weakness of their approach, but can be easily remedied. In addition, they assumed pyrolysis is thermally neutral, which is probably not a bad assumption.

This model was developed to describe non-plastic coals which largely retain their pore structure during pyrolysis. The volatile species were lumped into a single component. An effective diffusion coefficient was assumed to account for volatile transport by diffusion and convective flow under small pressure gradients.

The pyrolysis reaction in this model is represented by:

C (Coal) ----------> A (Volatiles) + S (Char) (II.E.I-1)

The nonlinear partial differential equations obtained for the material and energy balances were solved using the DPDES routine of IMSL. This routine uses the method of lines which reduces the system of partial differential equations into a system of ordinary differential equations, which are subsequently solved with a Gear Integration method. The equations were solved for various values of the Thiele modulus, corresponding to high, medium and low reaction rates.

Using and assumed set of kinetics, thermal properties and diffusion coefficients, they identified regimes of chemical reaction control (at low reaction rates), and heat and mass transfer control (at high reaction rates). By doing parametric studies they identified the Thiele modulus (chemical reaction rate/diffusion rate), the Lewis number (thermal diffusivity/mass diffusivity) and the heat transfer Biot number (ratio of external to internal heat transfer rate) as important dimensionless groups. The analogous mass transfer Biot number was found to be unimportant since the external film resistance was assumed to be negligible.

A second paper (Devanathan and Saxena, 1987) extended the model to include secondary reactions. The description of the volatiles was also extended to three components (tar, gas, hydrogen). The global primary and secondary pyrolysis reactions were:

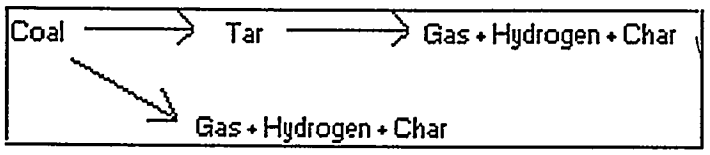

(II.E.I-2)

In this paper, Devanathan and Saxena used the primary pyrolysis kinetic parameters of Suuberg et al. (1978) instead of the parameters of Kobayashi et al. (1977) used in the previous paper. This change was presumably to accommodate a multi-component pyrolysis model. However, it is surprising that the

authors do not comment of the significantly higher kinetic rates implied by the former set of parameters. Again, the physical properties were assumed to be constant, the heat of reaction assumed to be zero, and the mass transfer model utilized an effective diffusion coefficient to account for volatile transport both by molecular diffusion and convection flow under a small pressure gradient. It was also assumed that tar was only present in the vapor phase. The kinetics for the tar decomposition reactions were based on the values assumed by Suuberg et al. (1979). The numerical scheme used to solve the set of 7 partial differential equations for a 3-component system was a similar technique as discussed above.

The authors used the expanded model to examine the effects of bulk temperature, pressure, and particle size on the extent of secondary reactions and volatile yields. Qualitative comparisons were made to the data of Suuberg et al. (1978) for Montana Lignite for the effects of pressure, temeprature and particle size. Comparisons were made to the data of Stubington and Sumaryono (1984) for product evolution profiles from large particles. The simulations indicated two peaks in the H_2 evolution curve in agreement with Stubington and Sumaryono (1984). The first peak in the model was due to primary pyrolysis reactions while the second was due to tar decomposition.

One weakness of their approach is that the secondary reactions of tar outside the particle are ignored so that the predictions which show tar yield leveling off at relatively high temperatures do not make sense. They also predict a temperature of 750°C for the maximum tar yield, which is 150 - 200°C higher than most experimental observations. By assuming an inverse relation of the diffusion coefficient with pressure, they can predict the type of pressure dependence indicated by the data of Suuberg et al. (1978). One interesting prediction of their model is the fact that the pressure dependence is more prominent in the later stages of devolatilization since the volatiles have to travel a further distance to get to the surface.

The total volatile yield was found to depend weakly on particle size while the total devolatilization time was found to depend strongly on particle size. These particle size trends, as well as the trends with pressure and temperature discussed above, are in qualitative agreement with literature results. However, when quantitative comparisons are made, such as the temperature for maximum tar yield, the predictions are often far off, as noted above. This is a result of the fact that the physical and chemical parameters which go into the model were selected somewhat arbitrarily. The authors did note that some of these parameters could not be estimated accurately and did a sensitivity analysis on the external heat transfer coefficient, thermal diffusivity, external mass-transfer coefficient, effective diffusion coefficient and porosity. Of this set, the choice of the effective internal diffusion coefficient was found to be crucial. This parameter is also one of the most difficult to specify. Unfortunately, the authors did not examine the sensitivity to the kinetic parameters.

A comprehensive model for large particle pyrolysis was also developed by Bliek et al. (1985). They used essentially the same global pyrolysis scheme (including tar secondary reactions) as Devanathan and Saxena (1987). One difference in the kinetic models was to assume that each of the three volatile components evolves by a reaction which is second-order in the amount of volatiles yet to be released. This is a simpler alternative to the distributed activation energies model to describe the "tailing" of volatile evolution curves at higher temperatures. This model also treats coals which essentially retain their pore structure.

One of the major differences of this model when compared to that of Devanathan and Saxena (1987) is in the treatment of internal mass transfer. Bliek et al. chose to use the continuum limit of the Dusty Gas model (Mason et al., 1967; Mason and Malinauskas, 1983). This model can account for the combined transport of volatiles by viscous flow and diffusion. Viscous flow becomes more important as the particle size increases, so this approach should be applicable over a wider range of particle sizes. The model requires an estimate of the viscous permeability, the effective Knudsen diffusivity, and the effect binary diffusivity. The latter quantity also appeared in the diffusive mass transport model of Devanathan and Saxena (1987). Bliek et al. (1985) used literature values of permeability parameters obtained from stationary mass flux experiments.

The transport of volatiles from the particle outer boundary to the ambient gas was assumed to be infinitely fast. This assumption is probably reasonable for light gases but not for heavy tars. The heat of devolatilization was assumed to be zero as in the Devanathan and Saxena (D-S) model. Unlike the D-S model, Bliek et al. did not concern themselves with the details of external heat transfer and specified the particle surface temperature. However, they did account for the temperature variation of the particle thermal conductivity and heat capacity, which the D-S model does not include. Bliek et al. also did pyrolysis experiments in a TGA with particles 50-1000 microns in size in order to extract primary pyrolysis kinetic information and generate data for model validation. The equations were solved numerically using an implicit backward descretization scheme. This transformed the partial differential equations to non-linear algebraic equations, which were subsequently linearized. A combination of iteration and the algebra of diagonal matrices was used to produce the numerical results.

The qualitative results of the simulations largely agree with those of the D-S model since both were developed to agree with the experimental observations of Suuberg et al. (1978), among others. The more detailed description of mass transfer allowed Bliek et al. to establish regimes of particle size and heating rate where mass transfer was controlled by either diffusion or viscous flow. The most interesting prediction was that the tar yield went through a maximum with heating rate. This was explained by the fact that, at high heating rates, the volatiles would have to diffuse through a hot outer layer of char. However, this trend has not been observed experimentally. The model also did not agree well with the effects of ambient pressure observed for bituminous coal by Anthony and Howard (1976). However, this could be due to the fact that it was developed for a non-plastic coal.

While both the Bliek model and the D-S model are important contributions to understanding large particle pyrolysis, the published versions are lacking in several respects. The major problem is the relative lack of care which has gone into the choice of the physical and kinetic parameters when compared to the effort expended to develop the numerical solution schemes. A corresponding defect is the lack of a complete sensitivity analysis. If one compares the choices of physical and chemical parameters made for the two models, which are shown in Table II.E.1-1 and II.E.1-2, respectively, the magnitude of the problem is apparent. For example, there are several orders of magnitude variation in the species diffusivities. As discusses above, this was identified as a crucial parameter in the partial sensitivity analysis done by Devanathan and Saxena (1987).

Additional problems with these two models include an oversimplified description of tar secondary reactions, and the inability to describe plastic coals. The models of Devanathan and Saxena (1985, 1987) and Bliek et al. (1985) appear to be the best starting point for developing a model for use in the current program since they include all of the relevant phenomena (heat transfer, mass transfer, kinetics). However, the advantages of using such a model must be balanced against the added computational burden in a fixed-bed comprehensive code.

Physical Properties - It was expected that there would be variations in the pyrolysis kinetic parameters chosen in different modeling studies. However, significant variations in assumed physical properties were also observed and variations in these properties with temperature and extent of pyrolysis are often neglected. A detailed evaluation of literature on the key physical parameters important in a heat transfer analysis was done. This included consideration of data on specific heat, thermal conductivity, emissivity, density, and transpiration cooling. The results of this review of physical properties are summarized by Solomon et. al., (1992). A wide variety of values was found, as shown in Table II.E.1-1.

Heat Transfer Calculations - Calculations of the characteristic times for internal and external heat transfer were made for a 60 micron particle. A simplified case is considered where the particle is assumed to be dropped into a stagnant gas at an elevated temperature where radiation and convective heat transfer can be neglected. The characteristic time for internal conduction heat transfer is given as follows:
where ρ_p is the density, C_p the heat capacity, d_p the diameter, and k_p the thermal conductivity of the particle. The characteristic time for external gas phase conduction is:

Table II.E.1-1. Comparison of Physical Parameters for Two Pyrolysis Reaction / Transport Models.

Property	Units	Devanathan and Saxena (1987) 25°C	500°C	Bliek et al. (1985) 25°C	500°C
Thermal Conductivity	cal/(cm s K)	5.497×10^{-4}		4.45×10^{-4}	
Heat Capacity	cal/(g K)	0.916		0.27	0.51
Density	g/cm^3	1.5		0.9	
Thermal Diffusivity	cm^2/s	4×10^{-4}		1.8×10^{-3}	9.7×10^{-3}
Gas Molecular Weight	g/g-mol	30		20	
Tar Molecular Weight	g/g-mol	216		325	
H_2 Diffusivity	cm^2/s	4×10^{-3}		---	
Gas Diffusivity	cm^2/s	4×10^{-4}		4.2×10^{-1}	3.2×10^{-1}
Tar Diffusivity	cm^2/s	4×10^{-5}		4.2×10^{-1}	3.2×10^{-1}
Coal Porosity	---	0.4		0.10	
Char Porosity	---			0.25	

Table II.E.1-2. Comparison of Kinetic Parameters for Two Pyrolysis Reaction / Transport Models.

			Devanathan and Saxena (1987)	Bliek et al. (1985)
V_1	(ultimate yield of H_2)	g/g	0.005	0.000
V_2	(ultimate yield of gas)	g/g	0.381	0.358
V_3	(ultimate yield of tar)	g/g	0.054	0.160
f_4	fraction of tar which can react		1.0	1.0
k_{01}	preexponential	s^{-1}	10^{18}	---
k_{02}	preexponential	s^{-1}	10^{12}	8.0×10^{4}
k_{03}	preexponential	s^{-1}	10^{17}	7.6×10^{11}
k_{04}	preexponential	s^{-1}	10^{13}	2.7×10^{4}
E_1		kcal/mole	80	---
E_2		kcal/mole	50	22
E_3		kcal/mole	75	37
E_4		kcal/mole	65	14

$$t_{c,i}=\frac{\rho_p C_p d^2{}_p}{20 k_p} \qquad \text{(II.E.1-3)}$$

$$t_{c,e}=\frac{\rho_p C_p d_p^2}{6 Nu\ k_g} \qquad \text{(II.E.1-4)}$$

The definitions are the same as for Eq. II.E.1-3 except that k_g is the gas thermal conductivity and Nu is the Nusselt number for heat transfer, which equals 2 for a spherical particle in an infinite stagnant medium.

The reciprocal of the characteristic time is, by definition, the rate constant for a first order process. This can be compared to the first order rate constant for pyrolysis mass loss which we have determined based on data for a number of coals. The results of these calculations are shown in Fig. II.E.1-1. This plot indicates three distinct regions of behavior. At low temperatures (< 600°C), $k_{chem} << k_{next}$, k_{hint} and pyrolysis of the particle occurs isothermally at the maximum temperature of the gas without any internal temperature gradient. As the gas temperature increases above 600°C, but is lower than 1000°C, the particle pyrolyzes while heating to the final temperature but has a relatively small internal temperature gradient. At temperatures near 1000°C, there is not adequate time to collapse the internal temperature gradients before significant pyrolysis can occur.

The variation with temperature of the particle and gas thermal properties was included in these calculations. Of course, these calculations can be done for many different conditions to include variations in particle size, external pressure, and the addition of other modes of heat transfer, such as radiation.

Mass Transfer Calculations - The analogous calculations have been done for mass transfer (in the case of a bituminous coal), as shown in Fig. II.E.1-2. The situation is more complex because the molecular weight dependence of the transport rates and the fact that the values of the species liquid phase and gas phase diffusivities are not well known. The calculation of the characteristic time requires the assumption of a model for internal and external mass transport. Generally, it is assumed that there are no mass transport limitations for light gas species (< 100 mw) for particles in the pulverized fuel size range (< 200 mesh). Consequently, the problem becomes one of defining the transport of the tar species.

As discussed in Solomon et al. (1988), success was achieved in describing the tar transport with a simple model which assumes that tars are carried out of a particle at their equilibrium vapor pressure in the light devolatilization products.

Because the assumed internal mass transport model depends to a large extent on heating rate, the calculations were done for high (20,000 K/s) and low (0.5 K/s) heating rates. In the former case, the pyrolysis chemical rate would reach a maximum at 948 K, while in the latter case it would maximize at 748 K. The internal and external mass transport rates were calculated for two molecular weights (314 and 1042) at these temperatures and plotted in Fig. II.E.1-2.

The calculations indicate that species close to 1000 in molecular weight are subject to significant internal and external transport limitations at all conditions of practical interest. Species which are close to 300 in molecular weight are limited by internal mass transport at low temperature (low heating rate) due to the low generation rate of the light species. At high temperature (high heating rates) the transport of 300 mw species is limited by the relatively slow vaporization rate from the surface.

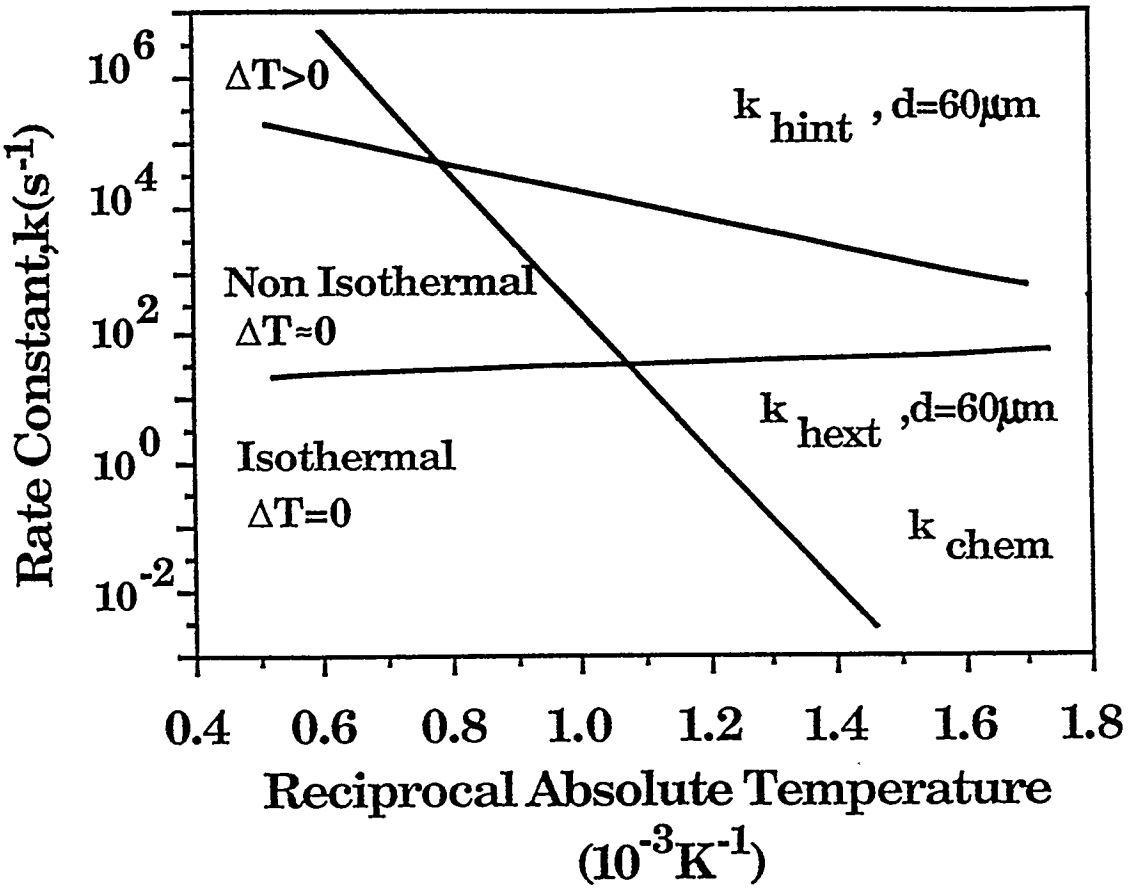

Figure II.E.1-1. Comparison of Chemical Kinetic Rate for Pyrolysis Mass Loss with Reciprocal Characteristic Times for External (k_{hext}) and Internal (k_{hint}) Heat Transfer.

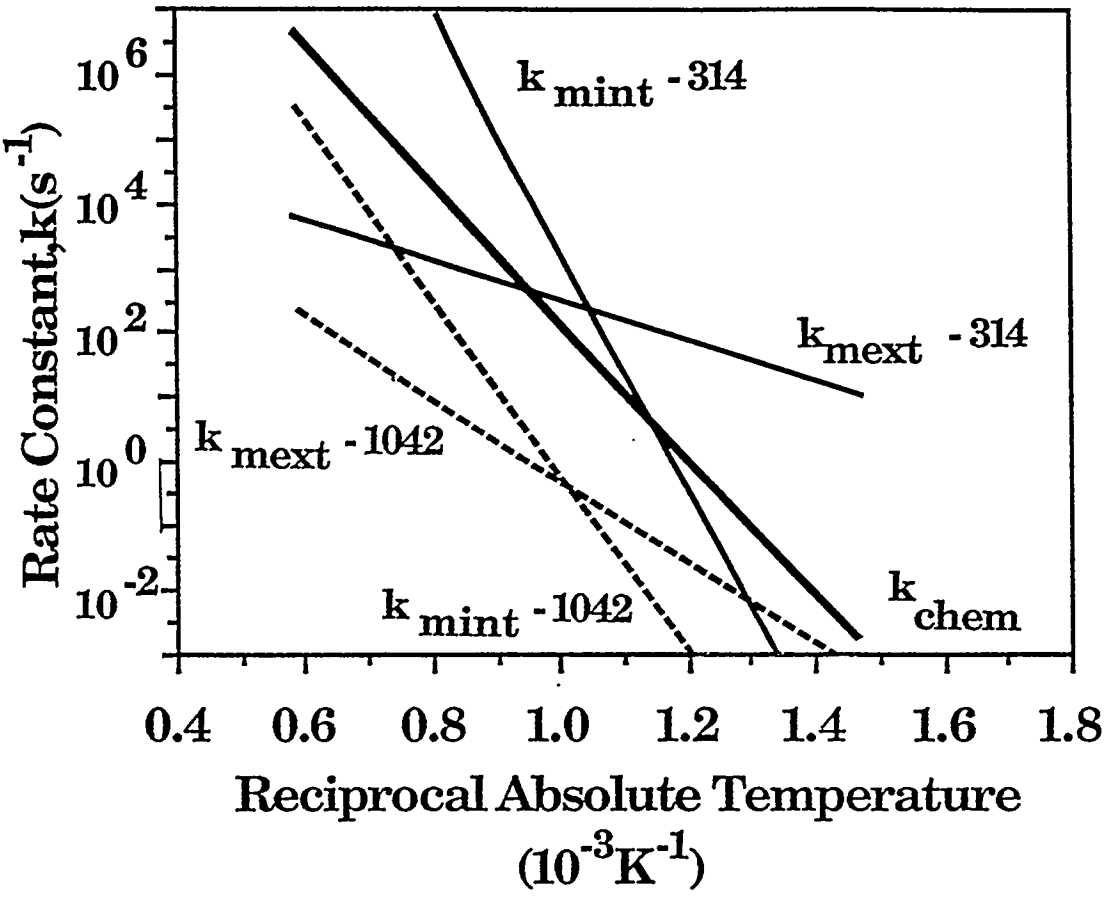

Figure II.E.1-2. Comparison of Chemical Kinetic Rate for Pyrolysis Mass Loss with Reciprocal Characteristic Times for External (k_{mext}) and Internal (k_{mint}) Mass Transfer. The Calculations were done for a 60 micron Bituminous Coal Particle.

II.E.2. Comparison of Tars Produced by Fixed-Bed and Entrained Flow Reactor Experiments

The motivation behind mild gasification of coal is to produce a high quality liquid product which can be used with little or no upgrading, while still maintaining a high enough yield to make the process economical. The approach that has been taken is to allow the tars to undergo some secondary cracking and repolymerization reactions while percolating through a packed bed. The tars produced are similar to those which are formed in moving-bed gasifiers. However, few studies have addressed in a systematic way how pyrolysis in thick beds affects the composition and quality of tar produced, and only a few previous studies (Peters and Bertling, 1965; Khan, 1987a,b) where a comparison has been made to rapid rate tars produced from the same coal.

In this work, tars were compared which were produced at the U.S. D.O.E. in a slow heating, fixed bed system with those produced at Advanced Fuel Research, Inc. (AFR) in rapid heating, entrained flow reactor system. Tars produced from these coals by slow heating in vacuum in the inlet of the SRI International Field Ionization Mass Spectrometer (FIMS) provided an additional point for comparing the effect of reaction severity on the nature of the evolved tars. The tars were subsequently analyzed by a variety of techniques. The study was done on tar samples produced from coals selected from the Argonne Premium Coal Sample Program. Details are provided in Khan et al. (1989).

Experimental

Bulk samples of the Argonne coals were obtained from Karl Vorres and sieved to produce +200, 200x325 and -325 mesh size fractions. The -325 mesh size fraction was sent to METC and pyrolysis experiments were done in the Slow Heating Rate Organic Devolatilization Reactor (SHRODR) described previously (Khan, 1987a,b). A thick bed (3.8 cm) of coal was heated at 12.5°C/min to a final temperature of 650°C and held for 60 minutes. The tars were taken off overhead using a water cooled condenser. The experiments were done without sweep gas. Samples of the 200 X 325 mesh size fraction of each coal were subjected to pyrolysis in AFR's entrained flow reactor system, described elsewhere (Solomon et al., 1982). The experiments were done with a maximum reactor temperature of 700°C. The heating rate has been estimated to be 5000 - 10000°C/s while the time at final temperature is approximately 0.5 s (Serio et al., 1987). The entire effluent from the reactor system is collected in a polyethylene bag which is secured on a plexiglass manifold covered with aluminum foil. The tars form an aerosol and collect on the walls of the bag and the foil liner. The tars used in the present study were scraped from the foil liner.

The tars were analyzed by FT-IR at AFR using a KBr pellet method. A quantitative analysis technique has been developed at AFR using a Nicolet 7199 FT-IR. The techniques, which are described in previous publications (Solomon et al., 1981, 1982) have been used to determine quantitative concentrations of the hydroxyl, aliphatic and aromatic hydrogen, and aliphatic and aromatic carbon for a wide number of coals, lignins, chars, tars, coal liquefaction products, oil shales, coal extracts and jet fuels. Qualitative information is also obtained concerning the types of ether linkages (oxygen linked to an aliphatic or aromatic carbon), carbonyl contents, the distribution of aromatic hydrogen (whether 1,2 or more adjacent hydrogens on a ring) and the forms of aliphatic hydrogen (methyl or methylene).

The tars were analyzed by Field Ionization Mass Spectrometry (FIMS) at SRI International. FIMS has proven to be an invaluable technique for the analysis of complex mixtures, particularly fossil fuels (St. John et al., 1978). The technique of field ionization consists of passing the vaporized material of interest through a very high electric field, typically about 1 MV/cm. Field ionization is unique in its ability to produce unfragmented molecular ions from almost all classes of compounds. The sample is vaporized by gradually heating while continuously collecting mass spectral data. The pyrolysis tars studied evolved below 200°C and did not undergo any thermal reaction during FIMS analysis. If desired, the samples can be heated to temperatures as high at 500°C and the coals themselves were pyrolyzed in the inlet by heating them at 3°/min to 500°C. Mass analysis was performed by a medium resolution 60° magnetic

sector analyzer, which has a maximum range up to 2000 daltons.

Results and Discussion

FIMS Analysis - A summary of the FIMS results in given Table II.E.2-1. In general, the tars produced from the slow-heating fixed bed reactor have low average molecular weights and narrow molecular weight distributions. A comparison is made of FIMS spectra from the three experiments for three of the coals in Figs. II.E.2-1 TO II.E.2-3. The overall MW profiles of the tars formed by in-situ pyrolysis in FIMS and the entrained-flow reactor are similar to each other. In both cases, the tars represent primary products of pyrolysis with little secondary reactions. Consistent with the lower N content of the SHRODR tars, their FI-mass spectra show a decreased abundance of odd-mass peaks.

In-situ pyrolysis tars appear to have relatively greater amounts of low molecular weight materials than the EFR tars. This difference is most likely due to differences in the sampling efficiency.

A surprising result was that both SHRODR and FIMS tars are richer in simple phenols like cresols and catechols than the EFR tars. In the case of in-situ FIMS of coals, these peaks evolved only at high temperatures (>350°C) and represent thermal fragments from a large matrix. Again, differences in the methods for collecting tars in the various experiments may be partly responsible.

FT-IR Analysis - A comparison of the results from FT-IR analysis of the EFR and SHRODR tars is given in Table II.E.2-2. These analyses were done with the KBr pellet method. Because of the high volatility of the SHRODR tars, these results are not as reliable as for the EFR tars. The FT-IR analysis of the tars from slow heating and rapid heating indicates that the former tars were more aliphatic (less aromatic), lower in oxygen content, lower in heteroatom content, and the aromatic rings are less substituted. These indicators are consistent with the idea behind mild gasification, which is that higher quality liquids can be produced from slow heating, fixed-bed systems, although in lower yields.

Tar Yield Data - A comparison of the tar yields from the SHRODR and the EFR is given in Table II.E.2-3. In all cases, the tar yields are lower in the SHRODR. However, there does not appear to be a direct correlation between a single tar composition parameter; such as percent aromatic carbon, and the ratio of tar yields in the two reactors. Additional tar composition data from H-NMR and elemental analysis will soon be available which may provide an explanation.

Discussion - These results are consistent with those of Peters and Bertling (1965) who compared rapid heating rate tars produced from a fluidized bed reactor with slow heating rate tars produced from a standard Fischer assay. They found close to a factor of two higher yields of tar in the former experiment with a corresponding lower yield gas and coke. They also found that the tar from the Fischer assay contained a higher fraction of light oil (b.p. < 140°C/1mm Hg), while the tar from the fluidized bed contained predominantly pitch (b.p. < 230°C/1mm Hg). The yield of the middle oil fraction (140°C < b.p. < 230°C/1mm Hg) was about the same for either process. They concluded that, in the slow heating process, the longer residence time of the tar leads to condensation and decomposition of the pitch to yield primarily coke, with some formation of light gases and light oils. An important conclusion from the study by Peters and Bertling (1965) is that the differences in the yield and composition of tar between the two experiments are a result of both cracking processes, which remove high molecular weight products as light oils and gas, and repolymerization processes, which remove high molecular weight products as coke and gas. The relative importance of these two processes depends on the coal type, bed geometry, particle size, and heating rate in a way which is currently not well understood.

A nearly similar tradeoff between tar yield and tar quality was found by Khan (1987a,b) when comparing results from SHRODR experiments on Pittsburgh No. 8 coal with fluidized bed experiments by Tyler (1980). A comparison was also made between the SHRODR tars and tars produced in an entrained flow reactor at Brookhaven National Lab (BNL) where differences similar to those found in the present

TABLE II.E.2-1. - RESULTS FROM FIMS ANALYSIS OF TARS FROM THREE REACTORS

	SHRODR		IN-SITU FIMS		EFR	
COAL	Wt. Av. MW	MW Range	Wt. Av. MW	MW Range	Wt. Av. MW	MW Range
Pocahontas	---	---	426	100 - 700	566	200 - 900
Upper Freeport	324	100 - 500	526	100 - 900	536	100 - 900
Pitts. No. 8	326	100 - 500	497	100 - 900	484	150 - 800
Lewiston-Stockton	---	---	546	100 - 900	478	150 - 750
Utah Blind Canyon	331	120 - 600	524	100 - 900	493	130 - 850
Wyodak	---	---	527	100 - 850	504	100 - 800

TABLE II.E.2-2. - SOME RESULTS FROM FT-IR ANALYSIS OF TARS FROM THREE REACTORS

	SHRODR			EFR		
COAL	H_{ar}/H_{tot}	H_{oh}	C=0	H_{ar}/H_{tot}	H_{oh}	C=0
Pocahontas	.41	.27	(32.3)	.43	.13	6.7
Upper Freeport	.25	.18	8.6	.40	.23	9.3
Pitts. No. 8	.24	.18	5.7	.37	.29	9.1
Lewiston-Stockton	.23	.14	9.8	.37	.33	12.7
Utah Blind Canyon	.13	.19	5.7	.28	.32	13.0
Wyodak	.15	.19	14.5	.30	.35	20.3

TABLE II.E.2-3. - COMPARISON OF TAR YIELDS FROM VARIOUS REACTIONS
(Yields on Dry-Ash-Free Basis)

COAL	SHRODR	EFR
Pocahantas	8	10
Upper Freeport	14	22
Pitts. No. 8	19	30
Lewiston-Stockton	13	17
Utah Blind Canyon	20	26
Wyodak	12	13

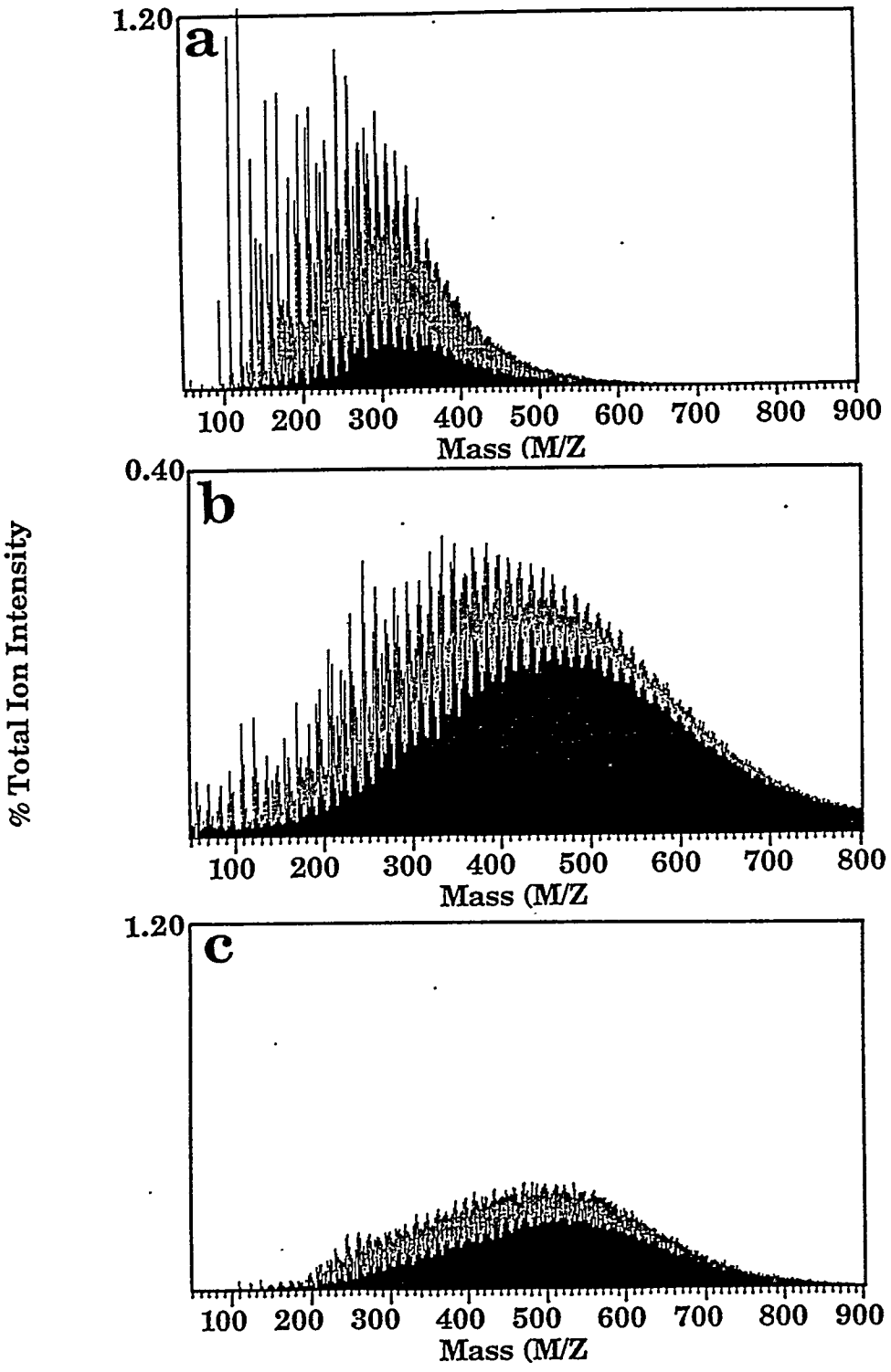

Figure II.E.2-1. FIMS Spectra from Upper Freeport Coal for Three Reactors. a) SHRODR; b) In-Situ FIMS; c) EFR.

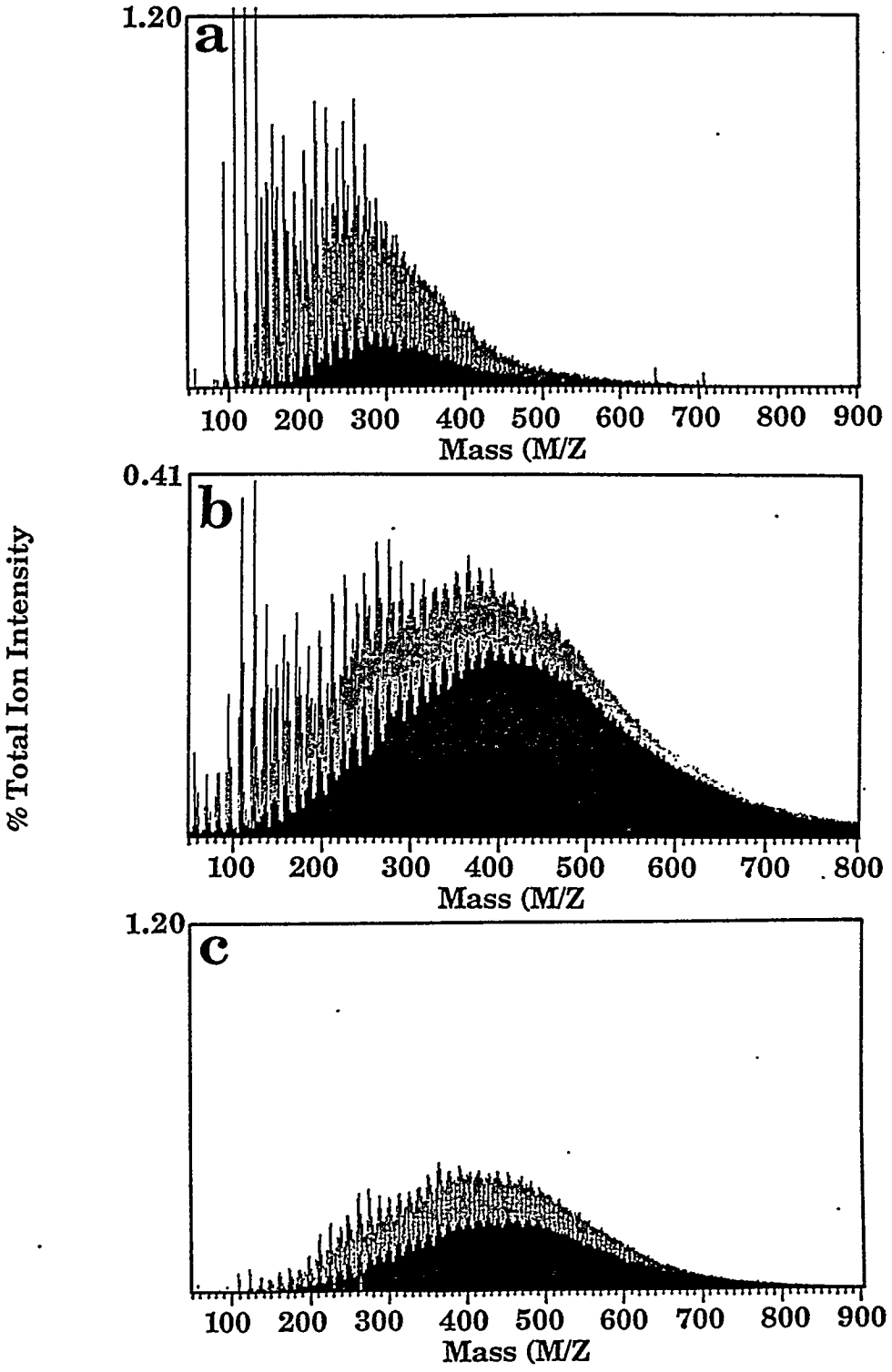

Figure II.E.2-2. FIMS Spectra from Pittsburgh No. 8 Coal for Three Reactors. a) SHRODR; b) In-Situ FIMS; c) EFR.

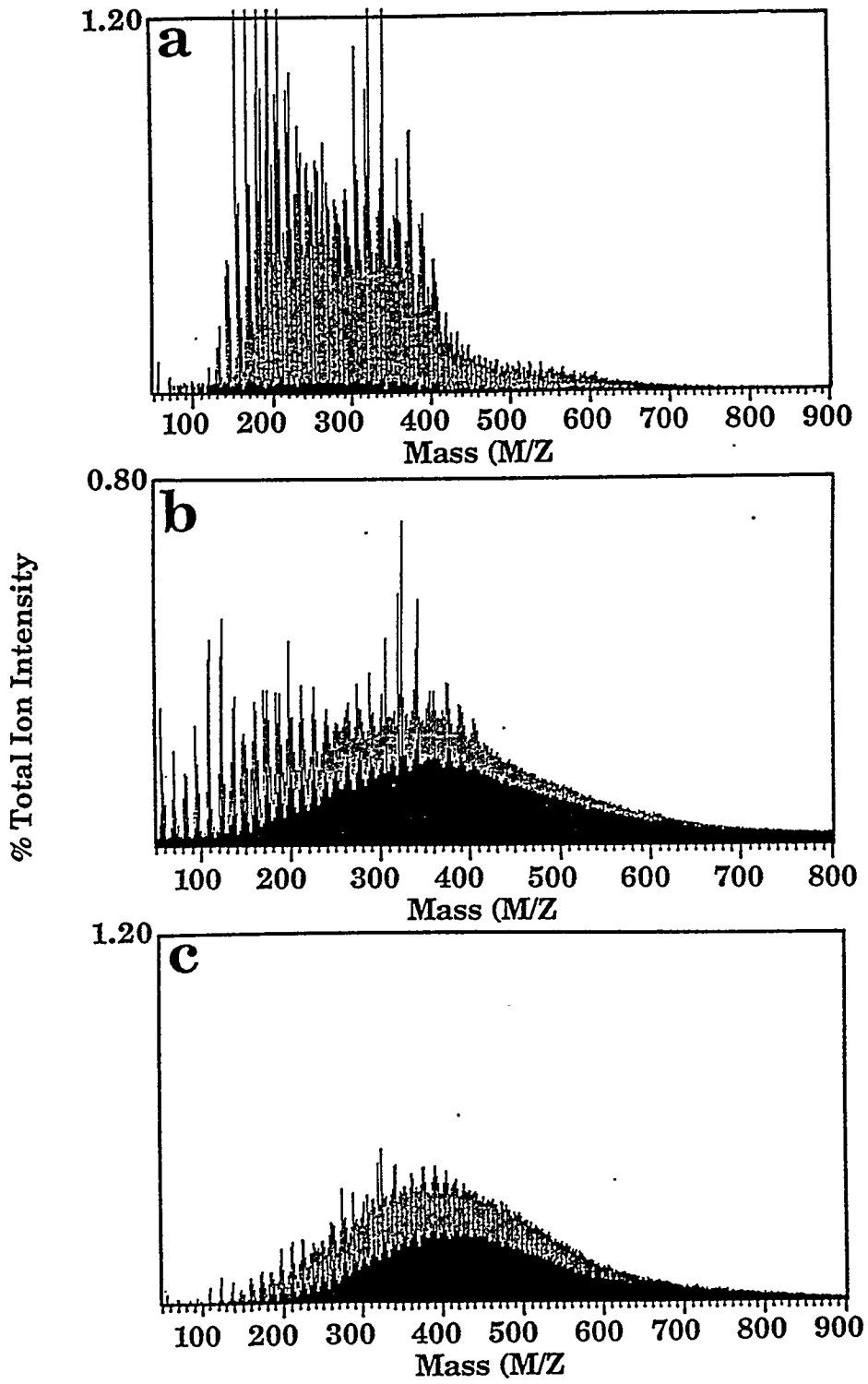

Figure II.E.2-3. FIMS Spectra from Utah Blind Canyon Coal for Three Reactors. a) SHRODR; b) In-Situ FIMS; c) EFR.

study were found.

The changes in the tar molecular weight distribution between the rapidly heated and slowly heated tars are consistent with a thermal cracking process which would produce primarily lower molecular weight material. Similar results were obtained by Serio (1984) from homogenous cracking of tars produced at low temperature and low residence time in gas-swept fixed bed. This would suggest that the difference between the two systems is primarily a residence time effect. However, based on the chemical changes in the tars and the large reductions in tar yield, one cannot rule out a repolymerization process in the bed.

II.E.3 Laboratory Scale Fixed-Bed Reactor Experiments

A laboratory scale fixed-bed reactor (FBR) system was designed, constructed and tested under this subtask. A schematic of the current version is shown in Fig. II.E.3-1. Several experiments were done with Pittsburgh Seam bituminous coal which covered a range of bed depths. There did not appear to be a strong effect of bed depth on tar yield over the range of conditions studied. There was some effect on the tar composition, with the deeper beds giving tars which were more aliphatic (less aromatic).

There did appear to be some very interesting effects on the temperature of the maximum tar evolution rate as bed depth increased. Initially, this value remained fairly constant, then went up dramatically. This increase coincided with the evolution of the tar by a "bursting" phenomenon in the bed rather than from individual particles. One problem with the tar "burst" is that it interferes with the quantitation of the gases during that period. Consequently, a redesign the system was done so that we can separate most of the tar prior to the gas cell. This is the version shown in Fig. II.E.3-1. This system allowed better quantitation of the tar yields and independent control of the temperature of the second bed.

Additional experiments were done with Zap lignite coal. In the case of the Zap, there were no problems in gas quantitation due to a "tar burst" which happened from the Pittsburgh Seam coal due to the significantly larger tar production. The tar amounts from the fixed bed experiments with the Zap lignite coal for small amounts of coal agree fairly well with the TG-FTIR results. As the bed depth increased, the tar yield was the same within the reproducibility of the measurements.

A second series of pyrolysis experiments was done with the fixed-bed reactor using Pittsburgh Seam bituminous coal. The reactor was modified so that the coal could be held in two separate layers on top of each other with a gap in between. The temperatures of the sweep gas and of the top coal layer were continuously monitored during the experiment. The temperature of the lower layer was approximately 100-200°C less than the upper layer depending on the flow rate and the gas temperature. The objective of these experiments was to measure the occurrence of tar recondensation on the lower layer. A glass wool tar filter was used to make quantitative measurements of tar yields. When the tar filter was in place, lower yields of gases were obtained and the T_{max} values came at higher temperatures. This could be attributed to either gas adsorption on the tar filter or on the tar particles.

Since the maximum temperature that could be reached in the top layer (I) was ~ 600°C, the second layer (II) could not reach high enough temperatures for all of the tar to be volatilized. Therefore, a second run was done with the char from layer II placed in layer I. A key to the various reactor configurations is given in Table II.E.3-1. Three different configurations of the reactor system were used. Setup A was used to obtain the baseline tar yield from the first layer. Setup B was the experiment to measure the effect of having a lower temperature coal layer in series. Setup C was used to obtain the baseline tar yield from the second layer.

The experiments were done at two different flow rates. The detailed results are given in Table II.E.3-2. The preliminary conclusions from these data are as follows:

1) The higher flow rate resulted in an increase in tar and a decrease in CH_4 and char

TABLE II.E.3-1.

CONFIGURATION OF FIXED-BED REACTOR

	FIRST RUN		SECOND RUN	
Setup	Layer I	Layer II	Layer I	Layer II
A	coal	empty	-------	-------
B	coal	coal	II char	empty
C	char	coal	II char	empty

TABLE II.E.3-2.

SUMMARY OF EXPERIMENTAL RESULTS FROM EXPERIMENTS WITH TWO BEDS OF PITTSBURGH SEAM COAL IN THE FIXED-BED REACTOR

Setup	He Flowrate ml/min	Tar Filter	FIRST RUN						SECOND RUN					TOTAL		
			T_{max} °C		Yield Weight % I + II		Yield Weight % Char		T_{max} °C		Yield Weight % II		Yield Weight % Char	Σ Yield		
			Tar	CH_4	Tar	CH_4	I	II	Tar	CH_4	Tar	CH_4	II	Tar	CH_4	Char
A (I)	400	Yes	530	530	19.1	2.6	67.0							19.1	2.6	67.4
		No	457	486			67.8									
B (I+II)	400	Yes														
		No	474	497	16.8	3.8	70.0	80.7	527	571	7.6	4.6	86.2	19.9	5.7	68.3
C (II)	400	Yes														
		No			15.1	1.0		81.8	538	570	7.7	2.5	84.4	21.3	3.0	69.1
A (I)	1240	Yes	487	501	26.3	0.8	68.6							26.3	0.8	68.6
		No														
B (I+II)	1240	Yes	560	505	16.6	0.1	66.4	85.1								
		No							471	520	12.3	2.0	79.1	23.0	1.0	66.8
C (II)	1240	Yes			*7.5	0.1		84.5								
		No							492	535	9.8	1.9	81.0	16.0*	1.6	68.4

* May be exp. error

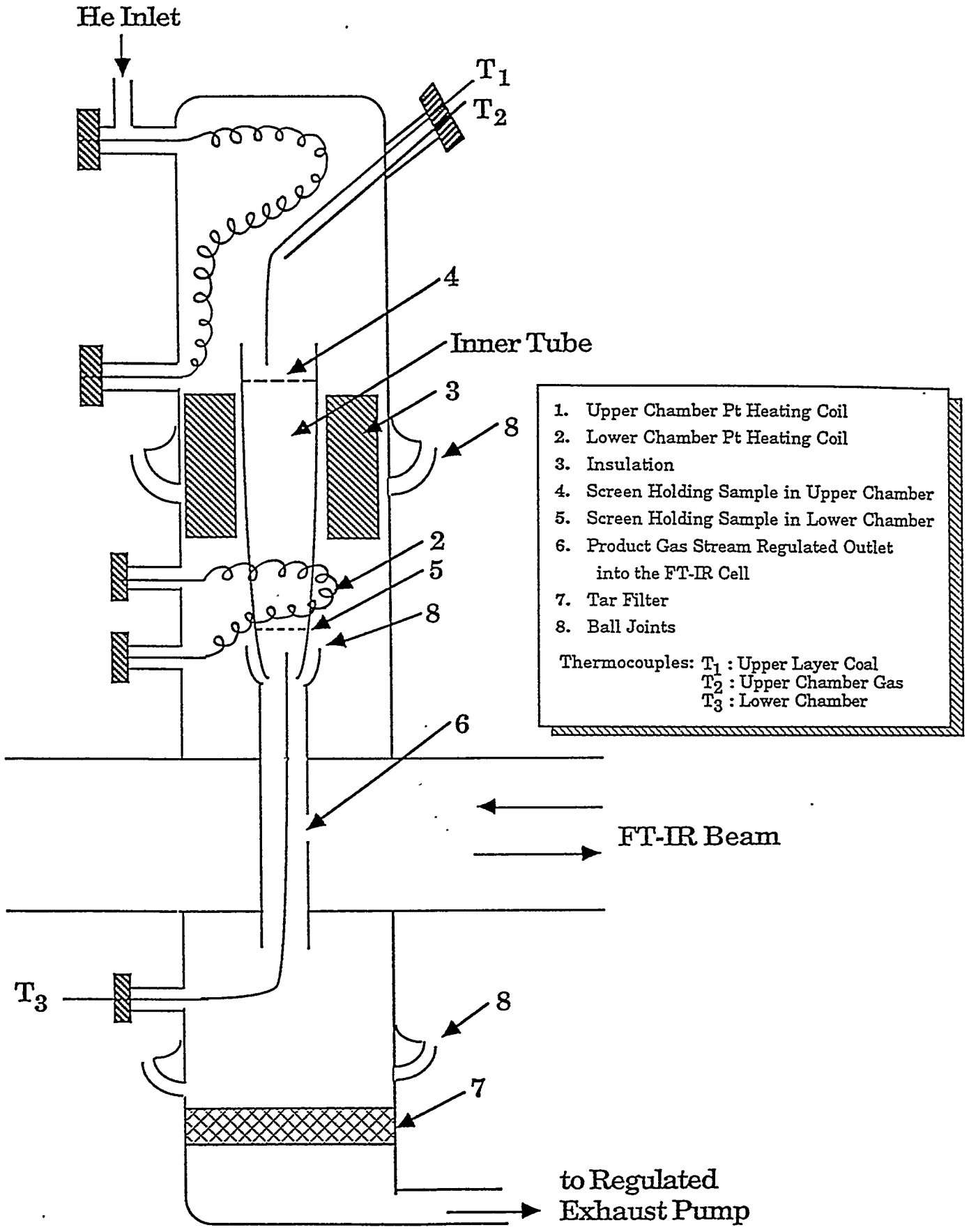

Figure II.E.-3-1. Schematic of New Fixed-Bed Reactor.

yields in both the single and dual bed experiments.

2) The two layer configuration, with about a 150°C temperature difference between them, resulted in a large increase in methane yields at low flow rates and a small decrease in the tar yield at high flow rates.

3) In a separate set of experiments, the pyrolysis was stopped at different temperatures to measure the weight of the first (I) and second (II) layer chars. The results show that a weight gain occurred for the II layer at ~ 300°C (assuming ~ 150°C average temperature difference between the two layers) coincident with the temperature of the maximum tar evolution rate from the first layer.

4) It appears that most of the tar which is condensed onto the cooler layer can be revolatilized under the conditions that have been studied to date. However, the percentage of tar which does revolatilize and the temperature at which this occurs appear to be sensitive to oxidation.

A third series of experiments was done in the FBR with a single layer of Pittsburgh Seam bituminous coal over a range of temperatures from 200 to 600°C to determine extractable yields as a function of pyrolysis temperature. The experimental variables also included the flow rate, bed depth, quenching rate, and exposure level to oxygen during product workup. The amount of extractable material as a function of temperature appeared to be most sensitive to flow rate, quenching rate, and the presence of oxygen during handling.

II.E.4 Interface of FG-DVC Model and Fixed-Bed Reactor Model

Historically, some fixed-bed gasifier models have assumed the devolatilization process to be instantaneous. Others have included finite rates for devolatilization and secondary reactions. A literature review by BYU (see subtask 3.b.) identified three properties the devolatilization model should be able to predict: 1) the individual chemical species that will be evolved; 2) the amount of each that will be evolved; 3) the rate at which each will be evolved as a function of the pertinent variables (particle size, temperature, heating rate, pressure, gas velocity).

The goal was to provide a model for BYU to incorporate into their fixed-bed code as well as one which can treat the tar destruction processes which are important in mild gasification. The decision was for BYU to incorporate the current FG-DVC model in their initial fixed-bed code and to continue work on a new version that can treat the tar secondary reactions. A revised version of the FG-DVC model which does not have a lot of extraneous variables which have accumulated over many years of development. This code is also better documented and better organized in terms of the input and output. In order to accommodate the solution approach being used in the fixed-bed code being under development at BYU (see subtask 3.b.), this version of the FG-DVC model can be solved using a standard solver for ordinary differential equations (ODE). The solver used is the Livermore Solver of Ordinary Differential Equations with Sparse jacobian (LSODES). Previously, the equations were solved with a combination of analytic solutions, where known, and Newton's method. It was assumed that the temperature was constant over a time step so that many of the equations could be solved analytically, and a suitably small time step was used to treat cases where the temperature was changing. For integration with the FBED-1 code development modelling of subtask 3.b., it was necessary to treat variable time-temperature behaviors in a more general manner; so the FG-DVC equations were cast into a form suitable for the LSODES code. The details of the equations are described in Appendix A of the Fifteenth Quarterly Report.

The model is identical in concept to that described in Solomon et al. (1988) and Solomon et al., (1990) except for a change made in the treatment of the distributed activation energy model (DAEM) of

the kinetic rates. In the old versions, the assumption is that the starting distribution of activation energies, E_i, is assumed to be a truncated gaussian, and is simulated using 21 subpools, each of which is evolved over time and temperature. This means that after a short time, these distributions are no longer gaussian. Since the low energy subpools in the distribution evolve much faster (exponentially) than the higher energy pools, we were led in the new version to keep the distribution as a truncated guassian, but to evolve the low energy truncation point with time. The validity of this assumption is supported by Figure II.E.4-1, which shows the evolution of the shape of the distribution in the original version of the model for several pools as a function of time. The improved version would have a vertical line for the leading edge of the pool and is thus a reasonable approximation of the shapes in Fig. II.E.4-1. The benefit is of course that we have replaced 21 ODE's with a single one, for each of 27 functional groups.

The cpu run time in seconds for several cases run on a SUN 3/50 with a 68881 floating point chip is shown below:

Case	Improved ODE	ODE Version (7 subpools)	Standard 2-σ Percolation (21 subpools)	Monte Carlo FG-DVC (high rank coal)	Monte Carlo FG-DVC (low rank coal)
1	105 sec	500 sec	25 sec	180 sec	1600 sec
2	126 sec	619 sec	25 sec	180 sec	1600 sec
3	129 sec	632 sec	25 sec	180 sec	1600 sec
4	112 sec	287 sec	25 sec	180 sec	1600 sec

Case 1 is the slow heating rate (3°C/min) simulation of the TG-Plus (no tar cracking).
Case 2 is the regular heating rate (30°C/min) simulation of the TG-Plus (no tar cracking).
Case 3 is the fast heating rate (100°C/min) simulation of the TG-Plus (no tar cracking).
Case 4 is the slow heating rate (3°C/s) simulation of the viscosity measurement (with tar cracking).

The predicted gas and tar evolutions using the improved ODE version look identical to the original prediction using 21 subpools with a minimum adjustment of the activation energies (3% reduction)

II.E.5. Tar Destruction Submodel

Under this subtask, a model for the destruction of tar in fixed bed gasifiers was developed. A compilation was made of literature data that can be used to help validate the model. The focus has been on data for the Pittsburgh seam coal which shows the change in tar yield and/or composition with variations in heating rate, bed depth, flow rate, particle size, and reactor type.

It has been observed that the tar yields from moving-bed gasifiers are much lower than those reported in laboratory-scale coal pyrolysis under inert conditions. In order to understand the cause of these tar yield differences, these two categories will be separately considered.

Results from Laboratory Studies for Inert Pyrolysis:

Tar yields (DAF) from pyrolysis under inert gas conditions of Pittsburgh Seam (or equivalent) coals under atmospheric pressure and for pulverized-sized coal particles are summarized in Table II.E.5-1.

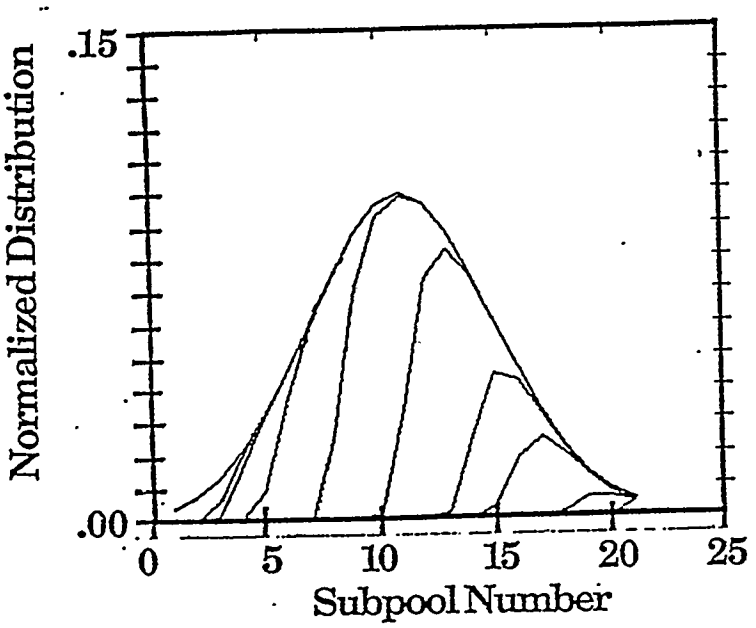

Figure II.E.-4-1. Shape of the Species Source Distribution Function as it is Depleted (CO_2 extra loose at 30°C/min).

Table II.E.5-1 Tar Yields from Pyrolysis in Laboratory Reactors at One Atmosphere

Tar Yield (DAF wt.%)	Coal	Coal Rank	Reactor Type	Particle Size (μm)	Reference
26	Pittsburgh	hvbit	Wire-Grid	74	Suuberg (1977)
24	Pittsburgh	hvbit	Fixed-Bed	250	Serio (1984)
30	Pittsburgh	hvbit	Entrained Flow	60	Solomon et al. (1988)
31	Pittsburgh	hvbit	Fluidized-Bed	75-105	Tyler (1980)
31-28	Linby	hvbit	Fluidized Bed	100-150	Katheklakis et al. (1990)
19	Pittsburgh	hvbit	Fixed-Bed	---	Khan (1989)
9.1-13.3	Pittsburgh	hvbit	Fixed-Bed	2.5 cm	Kalson and Briggs (1985)

The above data reveal that coal pyrolysis performed under these conditions results in a tar yield around 20-30%, even when pyrolysis is done in a fixed-bed configuration (in the presence of a gas flow). The results of Kalson and Briggs (1985) with large coal particles show a significant reduction in the tar yield. The low tar yields of large coal particles may be attributed to the increased residence time of tar in the coal particles, which could result in cracking or repolymerization of the tars inside the particles to form low molecular weight gases and char, respectively. However, since the tar yields in Kalson's experiment were very sensitive to the external gas flow rate, it is possible that the yields were not fully optimized in this system. Consequently, the results, as far as particle size effects are concerned, must be considered inconclusive.

There have been few systematic studies of particle size effects on pyrolysis yields in the literature. Suuberg (1977) studied particles of size ranges 74 μm, 297-833 μm, and 833-991 μm in his wire grid apparatus. The observed tar (plus hydrocarbon liquids) yields were 24, 23, and 21 wt.% (as received-basis) from pyrolysis of Pittsburgh Seam coal. If only the tar yields are considered, the differences were somewhat larger between the two extreme size cuts (23 vs. 18 wt.%), which largely disappeared when the large particles were reground (in order to test for maceral enrichment effects). It is not clear whether possible heat transfer effects were completely eliminated by holding the larger particles for a longer time at higher temperature. Assuming that these effects were not present, the work of Suuberg would suggest a reduction in tar yield of 10 to 20% from increasing the particle diameter from < 100 μm to ~ 1000 μm (1 mm). Studies on particle size effects on tar yields from pyrolysis in fluidized beds were done in the 3 to 11 mm size range by Stubington and Sumaryono (1984). Three different Australian coals were tested at three different reactor temperatures (750, 850, 950 °C). At the lowest temperature studied (750 °C), only one coal indicated a significant particle size effect on the tar yield in this size range. At the highest pyrolysis temperature (950 °C), the tar yields were reduced by about 1/3 over this size range for two of the coals and were unchanged for the third coal. A possible conclusion is that the intraparticle secondary

reactions are more important at higher temperatures, when the primary volatiles must diffuse through a hotter char layer to escape the particle.

Pressure has also been reported to affect tar yields from coal pyrolysis. A higher pressure external to the coal particles decreases the pressure gradient produced by the creation of volatiles within the coal particle. Hence, the residence time of these reactive gases within the particle is increased, leading to a greater extent of secondary tar reactions, and a reduction in tar yields.

Suuberg (1977) has studied the pressure effects on tar yields from coal pyrolysis under inert conditions. His data obtained with a Pittsburgh No. 8 bituminous coal shows clearly that, as gas pressure external to a particle is increased, the yield of tar obtained during pyrolysis is decreased. The tar yield was 32 wt. % under vacuum, 23 wt. % at 1 atm and 12 wt. % at 69 atm (as-received basis). At the same time, the yield of light gases increases with increasing pressure.

There is general qualitative agreement on the role of mass transfer limitations in coal pyrolysis. If the rate of escape of the tar decreases with increasing pressure, this implies a longer residence time for tar precursors in the particle, thus allowing a large fraction of them to be repolymerized into the char structure. Once reincorporated into the solid matrix by more stable bonds, the tar precursors can yield volatiles only by reactions which involve cracking off of small side groups (hence the increased yields of gas with decreasing tar yield).

The concept of repolymerization of tar precursors into the char structure is supported by Suuberg's results, which show that the char yield was 48 wt.%, at vacuum, 53 wt.% at 1 atm and 62 wt.% at 69 atm (as-received basis). However, the above pressure effect results were obtained for coal pyrolysis carried out in static systems, in which the coal is heated in a captive sample reactor and the volatiles are evolved from the coal, through a hot screen and into a cold gas. It is possible that the observed pressure effect is primarily due to inhibition of diffusion of tar away from the hot screen.

The papers that have been published on pyrolysis of coals under pressure in flow systems are primarily in the German and Russian literature. Several of these papers have been summarized in the review of Dryden and Sparham (1963). Even though this review is fairly old, it is not dated since little else has been done since that time. This review also covered work on high pressures of reactive atmospheres (H_2, H_2O).

The authors have distinguished between two different cases: a) increasing pressure at constant volatile residence time and b) volatile residence time increasing in direct proportion to pressure. The essential conclusion of their work was that increases in pressure at constant volatile residence time were not that important. There was slight effect of polymerization and condensation reactions and to retard decomposition reactions among the primary products; an increase in pressure also promoted reactions between gases in the primary products and the semicoke (e.g., auto-hydrogenation). Volatile (tar and gas) residence time, the value of which was proportional to pressure, was a more important factor in influencing the yield and composition of products. The major effect of increasing volatile residence time was to increase the decomposition reactions of the primary volatiles.

Thus, although pressure has some direct effects on the secondary reactions of volatiles, its major effects appear to be due to corresponding changes in volatile residence time.

The effects of volatile residence time in a fixed or moving bed reactor can be explained as follows: 1) increased residence time allows increased time for gas phase secondary reactions which remove tar; 2) the corresponding reduced carrier gas flow rate would reduce the mass transfer rate of tar from the particle surface, thus increasing the opportunity for tar repolymerization reactions. The secondary gas phase reactions could either be the cracking or gasification (reaction with oxygenated volatiles) type. The latter would be more important for low rank coals.

The only criticism that can be made of the Dryden and Sparham (1963) review is that the volatile residence times (20-100 sec.) were longer than those in a real moving bed gasifier (~ 1 sec.), the particle sizes (powdered to 1 cm) were somewhat smaller, and the heating rates (1-10 °C/min) much lower. If their conclusions are correct about the lack of a significant true pressure effect, a corollary conclusion would be the lack of a significant particle size effect.

Results From Gasifier Systems

Some examples of tar yields of bituminous coal from coal gasifiers are shown in Tables II.E.5-2 and II.E.5-3. All of the results in this section were taken from the compilation by Thimsen and Maurer (1990).

Table II.E.5-2. Tar Yields from Atmospheric Pressure (Wellman Galusha) Gasifier (AR wt.%)

Coal		Tar Yield
Jetson		12.9±5.4
Ill 6		14.4±4.2

Table II.E.5-3. Tar Yields from Pressurized Gasifiers (AR wt.%)

Gasifier	Coal	Ox/Coal Ratio	Steam/Coal Ratio	Tar Yield	Pressure (psig)
British Gas	Pitt 8	0.5	0.3	6.4±3.1	335
METC	Pitt 8	2.8	0.5	4.4±4.6	~150
GE	Ill 6	2.4	0.9	3.4±1	~300

Table II.E.5-2 presents the results from atmospheric pressure gasifiers, and Table II.E.5-3 presents results from pressurized gasifiers. It can be seen that the tar yield of a pressurized gasifier is much lower than that of an atmospheric gasifier. It has been concluded in the inert-pyrolysis discussion that increasing residence time in the reactor should decrease the yield of tar. In a gasifier at identical oxygen-steam rates, increasing operating pressure will increase residence time. Therefore, the low tar yield in the pressurized reactor may be due to the increase in residence time which causes more tar secondary reactions. On the other hand, if the pressure in the reactor is kept constant, increasing the gas flow rate will decrease the residence time and, therefore, the tar yield should increase with the gas flow rate. Although the data are scattered, the compilation of Thimsen and Maurer (1990) supports the conculsion that changes in residence time due to changes in total flow rate or pressure affect tar yeilds from these gasifiers.

It is likely that tar gasification reactions resulting from the reactions of tar with CO_2 and /or H_2O cannot be neglected by comparison, since the gas phase temperature is 200 - 300 °C higher than the solid phase temperature in the volatilization zone of a gasifier, and gasification or cracking of tar can occur once the tar is released from the solid to the gas phase. Laboratory experiments were done at AFR (reported in the 22nd Quarterly) which support this conclusion.

The particle size effect on tar yields in atmospheric pressure gasification is revealed in Table II.E.5-4.

Table II.E.5-4. Particle Size Effect on Tar Evolution in an Atmospheric Pressure Gasifier

Test #	Coal	Coal Flow	Dry Gas Flow	Particle Size	Tar Yield
007-02	Ill #6	2025	6471	+3/4	13.4
007-11	Ill #6	1983	6511	+1/4	8.6
007-04	Ill #6	2042	6357	+3/4	14.1
007-10	Ill #6	2067	6361	+1/4	14.7
007-06	Ill #6	3861	12314	+3/4	15.6
007-13	Ill #6	4142	12258	+1/4	13.7
008-03	Elkhorn (hvAb)	2355	7893	+3/4	15.6
008-09	Elkhorn	2315	7501	+1/4	15.6
008-04	Elkhorn	2574	8718	+3/4	14.3
008-10	Elkhorn	2554	8505	+1/4	14.6
008-05	Elkhorn	2990	9828	+3/4	15.6
008-11	Elkhorn	2900	9596	+1/4	14.5

* The above results were all obtained at 1 atm (Data from Thimsen and Maurer, 1990).

According to the results in Table II.E.5-4, particle size has little effect on the tar yield, which implies that intra-particle and boundary layer mass transfer does not control the tar yield in these gasifiers. This result is consistent with Dryden and Sparham's (1963) conclusion that pressure has little effect on tar yield in a flowing system under inert gas pressure, implying no intra-particle and boundary layer mass transfer limitation. It is also consistent with results discussed previously for inert gas pyrolysis which show little effect of particle size under conditions where the particles devolatilize (isothermally) at low temperatures.

Summary and Conclusions

The overall conclusions are as follows: 1) The effects of particle size on devolatilization time are

very important- the effects on tar yield are not; 2) The residence time of tar in the gasifier is inversely correlated with tar yield because of cracking and gasification reactions; 3) The reduced yields for pressurized gasifiers are due to increased residence time, increased gasification rate and/or a related temperature effect; 4) Both increased particle size and pressure would tend to move the tar evolution zone toward the hotter part of the gasifier.

The recommendations are as follows: The effect of particle size on shifting and broadening the devolatilization zone should be included. This is more realistic and may help solve the numerical problems introduced by the occurrence of the tar spike using the current model. One possibility is to use the simplified version of the model developed by Agarwal and coworkers (1984, 1986) for devolatilization in fluidized beds. These calculations could then be compared to the same calculations using a kinetic model in order to develop a correction factor for the values of A and/or E in the FG-DVC model.

The second recommendation is to allow the tar gasification to occur at the same rate as for the char and to allow the tar cracking to occur at the same rate as for coal pyrolysis, but at the gas temperature. These two assumptions will probably underestimate the gasification and cracking rates which could be compensated for by a single adjustable parameter (or two if necessary) in order to allow the predicted tar yields to match the measured tar yields. These recommendations are short term solutions which were incorporated under the current contract (see subtask 3.b.).

II.E.6 Modeling of Tar Evolution in PyGas™ Riser

Introduction

Based on the information obtained from METC, Figure II.E.6-1 displays a schematic of the PyGas™ reactor that will be used in the Gasification Product Improvement Facility (GPIF). In the center of this system, there is a vertical riser stand pipe from which the coal particles are fed and transported into the surrounding fixed bed section. The geometry and the flow conditions inside the riser should be designed such that there is a sufficient particle residence time so that the coal particles will be completely or almost completely pyrolyzed in the riser. Depending on the length of the required particle residence time, either a transport reactor or a fluidized bed reactor will be designed for the center pyrolysis riser. It is, therefore, crucial to determine the particle pyrolysis time.

The objective of this task is to calculate the coal particle pyrolysis time inside the GPIF center riser and to identify the key process parameters that would affect the pyrolysis time.

PyGas™ Reactor

The PyGas™ schematic reactor given in Figure II.E.6-1 is based on the information supplied by METC. Although it represents the basic concept of the GPIF system, the dimensions and the flow conditions given do not necessarily reflect the final design but are our current knowledge of the GPIF based on which the calculations were performed in this task.

The height of the center riser is 20 ft (6.1 m). The coal and the transport air are fed from the bottom of the riser. The coal and air feed rates are given as 12,000 lb/hr (1.5 kg/s) and 10,800 lb/hr (1.35 kg/s). The diameter of the riser is 24". The riser section will run at 1600°F (1144 K) and 600 psi (40.8 atm). The coal particle diameter is 1/4" (6.35 mm). The coal that is expected to be used in the GPIF system is a Fort Mountain low sulfur coal. The chemical composition of this coal is given in Table II.E.6-1. In terms of its chemical composition, this coal is very similar to the Lewston-Stockton West Virginia coal of the Argonne Premium Coal Sample Program, whose composition is also displayed in Table II.E.6-1 for comparison. The pyrolysis kinetics for the Lewston-Stockton coal were used in modeling the pyrolysis of the Fort Mountain coal in this task.

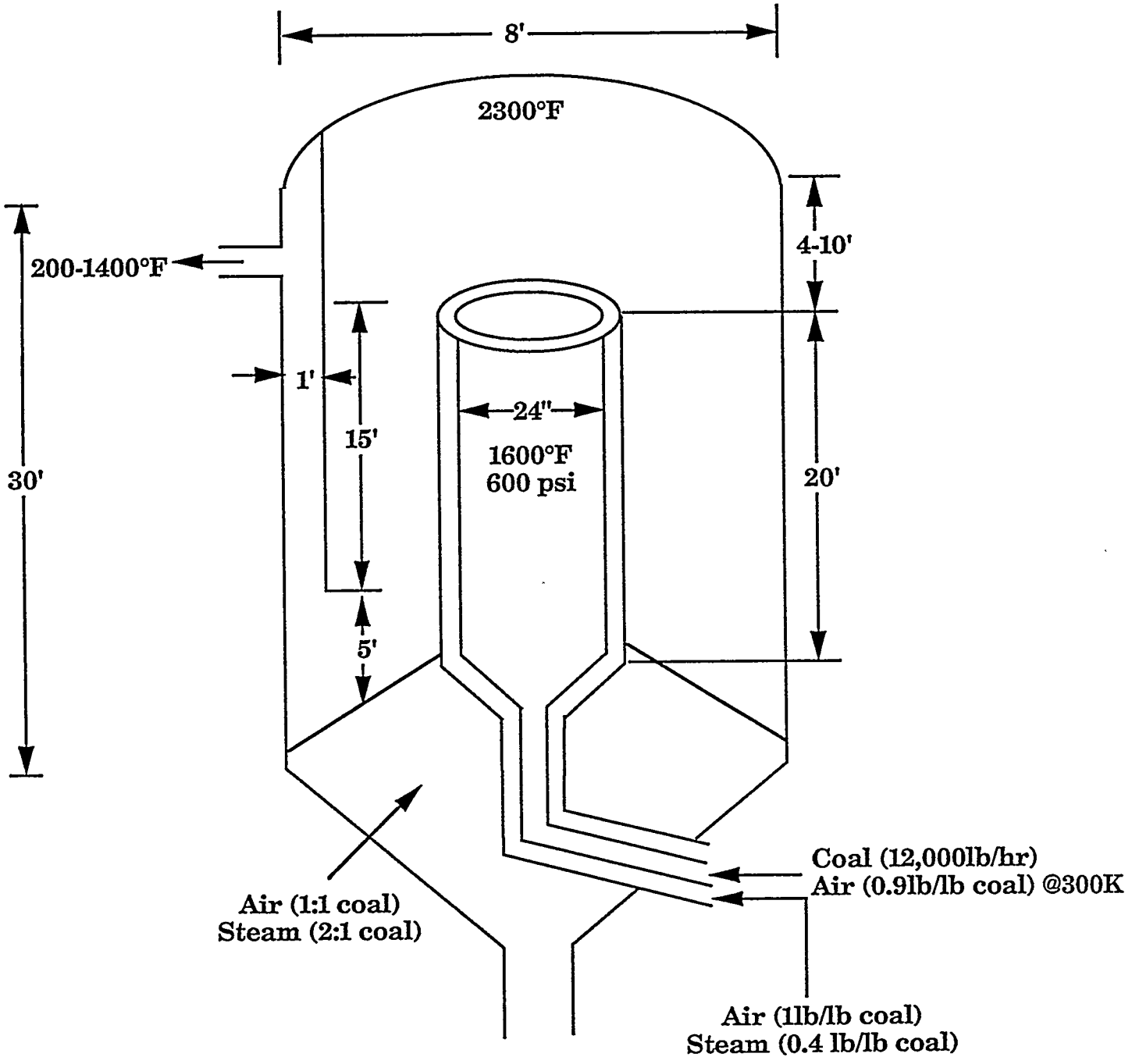

Figure II.E.6-1. Schematic of the GPIF System.

Table II.E.6-1 Chemical compositions of the Fort Mountain coal and the Lewston-Stockton coal.

	Chemical Compositions, wt% DAF	
	Fort Mountain	Lewis-Stockton
Carbon	82.41	82.53
Hydrogen	5.33	5.25
Oxygen	9.62	9.82
Nitrogen	1.5	1.56
Sulfur	1.14	0.84

Results of Modeling Studies

As stated above, the particle residence time inside the riser needs to be long enough for the completion of coal devolatilization in the riser. Determination of coal particle pyrolysis time is the focus of this task.

The Limiting Processes - Three processes can affect the progress of pyrolysis devolatilization of a coal particle in the particle laden flow, i.e., the heat transfer from gas phase to the coal particle, the heat transfer from the surface to the interior of the particle, and the pyrolysis kinetics. For a 1/4" coal particle, the pyrolysis kinetics appear to be much faster than the heat transfer processes. This is shown in Figure II.E.6-2, in which the extent of pyrolysis is represented by the weight loss. The devolatilization occurs almost instantly upon the coal particle is heated to a high enough temperature. The pyrolysis is limited by the heat-up of the particle.

There is no further information that would determine whether the gas to particle heat transfer or the heat conduction inside the particle is the limiting process. The gas to surface heat transfer correlates closely with the processes of heat radiation and convection, and collisions between particles and the reactor wall. Although without enough supporting evidence, we believe that it is reasonable for a 1/4" coal particle that the particle surface can be assumed to be heated up instantly compared to the temperature change of the interior portion. The limiting process is, therefore assumed to be the heat conduction from the particle surface to the interior.

Particle Temperature History - As discussed by Solomon et al. (1992), the heat-up of a coal particle involves many complex and simultaneous processes, especially the pyrolysis and the accompanying changes in solid density, specific heat, and conductivity. Modeling this phenomenon is beyond the scope of this contract. This type of modeling was performed by Wanzl, et al. (1987) for a 4 mm particle. In their work, the temperature distribution inside the particle was calculated as a function of time by assuming instant surface heat-up and the particle temperature became homogeneous in 6 seconds. Since our particle size is 6.3 mm and is quite close to 4 mm calculated in Wanzl et al. (1987), we believe that the temperature profile given by Wanzl et al. is applicable to the coal particles in GPIF except that the time variation needs to be scaled up for the size difference. It is well understood that the heat-up time is proportional to the square of the particle size. To be conservative, we assume that the total particle heat-up time inside the GPIF riser is 20 seconds. If we divide the 1/4" particle into four layers as given in Figure II.E.6-3, the temperature histories of each of the layers are estimated from the results of Wanzl et al. (1987) and are displayed in Figure II.E.6-3.

Pyrolysis Modeling - Given the particle model (Fig. II.E.6-3a) and the temperature histories (Fig. II.E.6-3b), the pyrolysis of the particle was modeled with the FG-DVC pyrolysis model. Four individual FG-

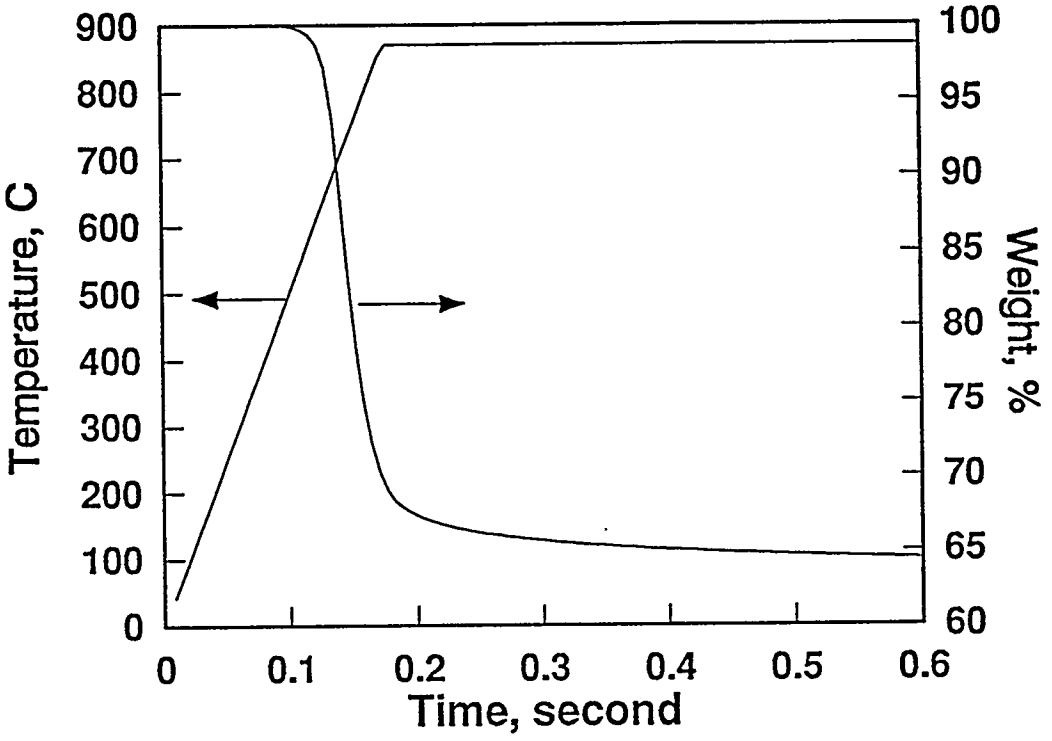

Figure II.E.6-2. Pyrolysis Weight Loss at 5000°C/s of a Lewiston-Stockton Coal Showing Fast Pyrolysis Kinetics Calculated by FG-DVC.

a

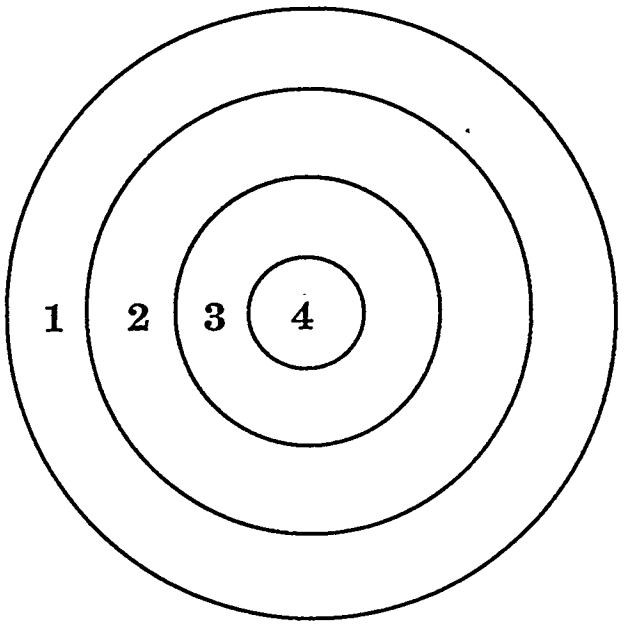

b

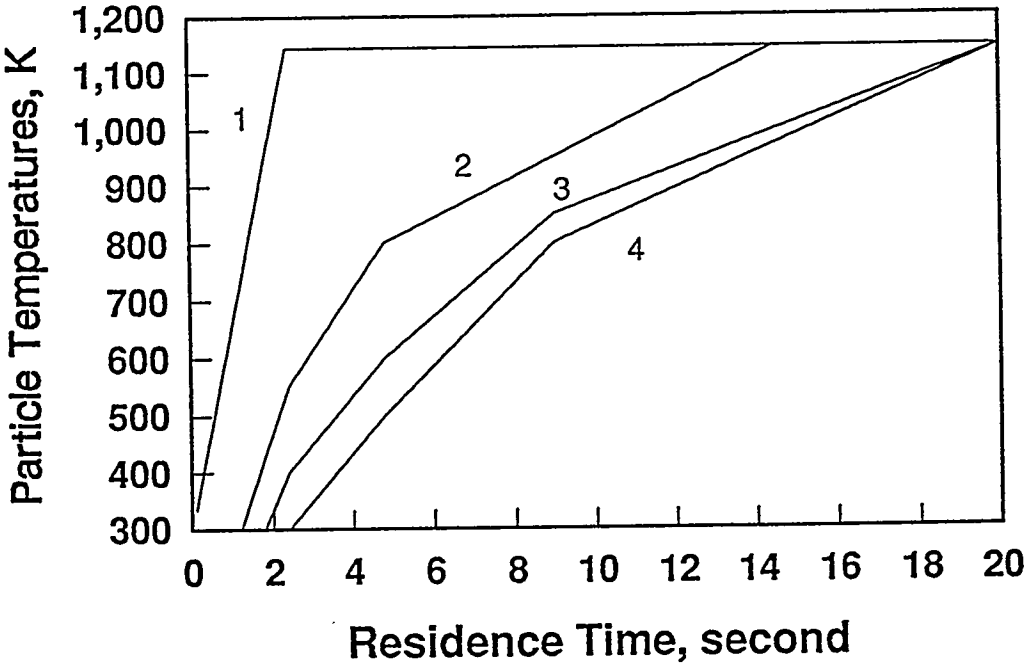

Figure II.E.6-3. a) The Coal Particle Model; b) The Particle Temperatures as a Function of Time.

DVC runs were performed for four layers of this 1/4" particle. The final result of the particle pyrolysis was the volume average of these four runs and the total weight loss curve is plotted in Fig. II.E.6-4. The pyrolysis devolatilization was almost completed in 20 seconds. However, about 50% of the total devolatilization was finished within 2.5 seconds and 85% was completed within 10 seconds. This is due to the fact that 58% of the weight of the particle is in the layer 1 and 88% is in layers 1 and 2 which are heated up much faster than the core of the particle (Fig. II.E.6-3b).

The major gas yields from the coal pyrolysis are given in Table II.E.6-2 and the chemical composition of the char is presented in Table II.E.6-3.

Based on the results presented above, the minimum particle residence time is required to be 10 seconds, in order to complete the pyrolysis inside the riser. However, it is recognized that the pyrolysis time of a particle is roughly proportional to the square of its diameter. If the particle size is reduced from 1/4" to 1/8", the minimum residence time becomes 2.5 seconds.

Conclusions

It was identified that the pyrolysis time of the coal particles inside the GPIF riser is not determined by the pyrolysis kinetics, but by the heat conduction inside the particles. Calculations have shown that the minimum residence time for a 1/4" coal particle is about 10 second, in order to complete the pyrolysis inside the riser, but this minimum residence time can be largely reduced if smaller coal particles are used. For example, the minimum residence time is 2.5 seconds for a 1/8" particle. Hence, the key parameter that dictates the process design is the particle size. Depending on the size of the coal particles, either a transport reactor or fluidized bed needs to be used as the center pyrolyzer of the GPIF system to satisfy the particle residence time requirement.

Table II.E.6-2. Major gas pyrolysis yields in GPIF riser predicted for a 20 second particle residence time.

	Gas yields, wt% DAF
H_2O	7.48
CO	2.40
CO_2	0.88
CH_4	4.62
tar	11.1

Table II.E.6-3. Chemical composition of the Char

	Composition, wt%
Carbon	94.24
Hydrogen	2.14
Oxygen	1.47
Nitrogen	1.59
Sulfur	0.56

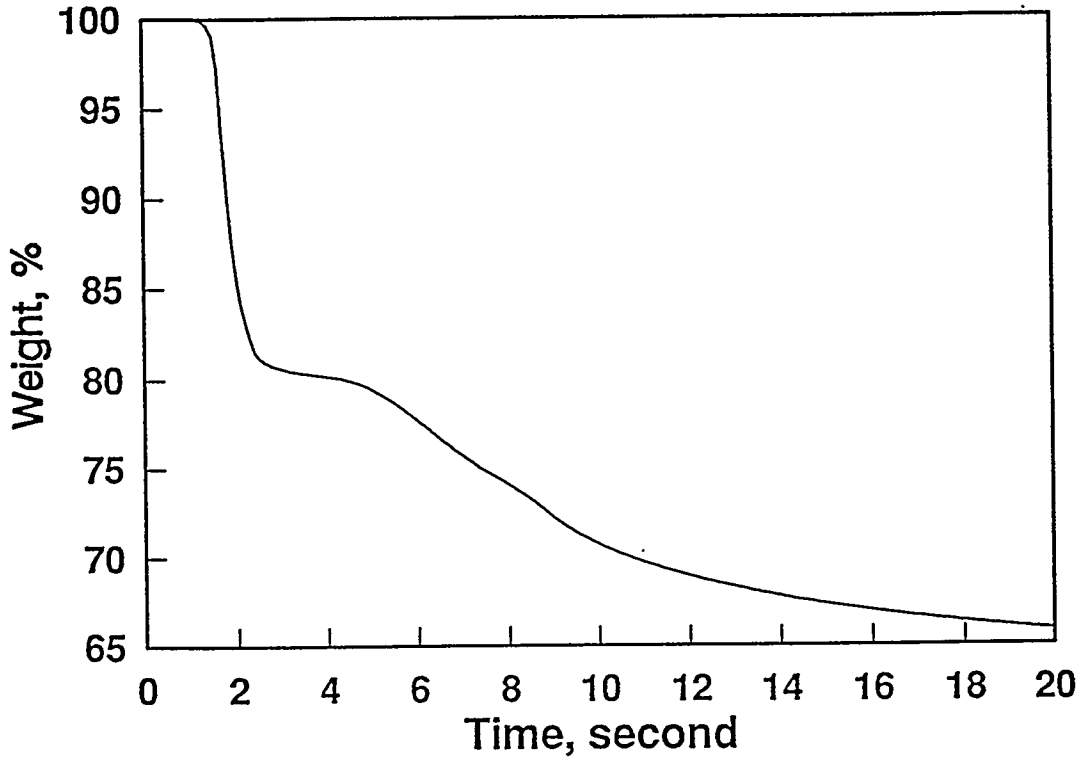

Figure II.E.6-4. Pyrolysis Weight Loss of a 1/4" Coal Particle in GPIF, Predicted by FG-DVC. Particle Profiles are Given in Figure II.E.6-3.

References for Subtask 2.e.

Agarwal, P.K., Fuel, 65, 803 (1986).

Agarwal, P.K., Genetti, W.E., and Lee, Y.Y., Fuel, **63**, 1157, (1984).

Agarwal, P.K., Genetti, W.E., and Lee, Y.Y., Fuel, **63**, 1157, (1984a).

Agarwal, P.K., Genetti, W.E., and Lee, Y.Y., Fuel, **63**. 1748, (1984b).

Bliek, A., van Poelje, W.M., van Swaaij, W.P.M., and van Beckum, F.P.H., AIChE J., **31**, (10),1666, (1985).

Chermin, H.A.G., and van Krevelen, D.W., Fuel, **35**, 85, (1957).

Devanathan, N. and Saxena, S.C., Proceedings of the 2nd Annual Pittsburgh Coal Conference, Pittsburgh, PA, p. 605, (1985).

Devanathan, N. and Saxens, S.C., Ind. Eng. Chem. Res., **26**, 548, (1987).

Dryden, I.G.C., and Sparham, G.A., Carbonization of Coals Under Gas Pressure, B.C.U.R.A. Monthly Bull., 27, 1 (1963).

Freihaut, J.D., Leff, A., and Vastola, F.J., ACS Div. of Fuel Chem. Preprints, **22**, (1), 149, (1977).

James, R.K., and Mills, A.F., Lett. Heat and Mass Transfer, **3**, 1, (1976).

Kalson, P.A., and Briggs, D.E., AIChE J., 31, 1047 (1985).

Kathelakis, I.E., Shi-Lin, L., Bertle, K.D., and Kandiyoti, R., Fuel, 69, 172 (1990).

Khan, M.R., Proc. of the Seventh Annual Gasification and Gas Stream Cleanup Systems Contractors Review Meeting, DOE/MET-87/6079, Vol. 1, p. 170 (1987a).

Khan, M.R., Proc. 1987 Int. Conf. on Coal Science, Elsevier, (J.A. Moulijn et al., Eds), Amsterdam, pp. 647-651 (1987b).

Khan M.R., Serio, M.A., Malhotra, R., and Solomon, P.R., ACS Div. of Fuel Chem. Prepr., 34, (4), 1054 (1989).

Kobayashi, H., Howard, J.B., Sarofim, A.F., 16th Symposium (International) on Combustion, The Combustion Institute, Pittsburgh, PA, p. 411, (1977).

Mason, E.A. and Malinauskas, A.P., Gas Transport in Porous Media: The Dusty Gas Model, Chem. Eng. Monograph, 17, Elsevier, Amsterdam, (1983).

Mason, E.A., Malinauskas, A.P., and Evans, III, R.B., J. Chem. Phys. 46, 3, 199 (1967).

Mills, A.F., James, R.K., and Antoniuk, D., Analysis of Coal Particles Undergoing Rapid Pyrolysis, in *Future Energy Production Systems*, (J.C. Denton and N. Afgan, Eds.), Hemisphere Publishing, Co., (1976).

Peters, W. and Berlting, H., Fuel, 44, 317 (1965).

Serio, M.A., Ph.D Thesis. Deptartment of Chemical Engineering, Massachusetts Institute of Technology, Cambridge, MA (1984).

Serio, M.A., Hamblen, D.G., Markham, J.R., Solomon, P.R., Energy & Fuels, 1, 138,(1987).

Solomon, P.R., *Coal Structure*, Advances in Chemistry Series, 192, 95 (1981).

Solomon, P.R., Hamblen, D.G., and Carangelo, R.M., Coal and Coal Products: Analytical Characterization Techniques, American Chemical Society, Washington, D.C., ACS Symposium Series, 205, p. 77 (1982).

Solomon, P.R., Hamblen, D.G., Carangelo, R.M., Serio, M.A., and Deshpande, G.V., A General Model of Coal Devolatilization, ACS Div. of Fuel Chem. Preprints, 32, (3), 83 (1988).

Solomon, P.R., Hamblen, D.G., Deshpande, G.V., and Serio, M.A., A General Model of Coal Devolatilization, in *Coal Science & Technology* 11, (J.A. Moulijn, K.a. Nater, and H.A.G. Chermin, Eds.) 597, Elsevier Science Publishers, Amsterdam, (1987).

Solomon, P.R., Hamblen, D.G., Yu, Z.Z., and Serio, M.A., Network Models of Coal Thermal Decomposition, Fuel, 69, 754, (1990).

Solomon, P.R., Serio, M.A., and Suuberg, E.M., Coal Pyrolysis: Experiments, Kinetic Rates and Mechanisms, Prog. Energy Combust. Sci. 18, p. 133, (1992).

St. John, G.A., Butrill, S.E., Jr., and Anbar, M., Field Ionization and Field Desorption Mass Spectroscopy Applied to Coal Research, in *Organic Chemistry of Coal*, (Ed. J. Larsen), ACS Symposium Series, 71, p.223 (1978).

Stubington, J.F. and Sumaryono, R., Fuel, 63, 1013 (1984).

Suuberg, E.M., Rapid Pyrolysis and Hydropyrolysis of Coal, Sc.D. Thesis, Dept. of Chemical Engineering, Mass. Inst. of Tech., Cambridge, MA (1977).

Suuberg, E.M., Peters, W.A., and Howard, J.B., Ind. Eng. Chem. Process Des. Dev., **17**, 37, (1978).

Suuberg, E.M., Peters, W.A., and Howard, J.B., Seventeenth Symposium (Int) on Combustion, The Combustion Institute, Pittsburgh, PA, 117, (1979).

Thimsen, D.P., and Maurer, R.E., Coal Devolatilization in a Moving Bed Gasifier, Research Project 2225-14 Final Report (October, 1990).

Tyler, R.J., Fuel 50 (4), 218 (1980).

Wanzl, W., Kabler, van Heek, K.H., Juntgen, H., Modeling of Coal Pyrolysis under the Conditions of an Entrained Phase Reactor, ACS Div. Fuel Chem. Prepr., 32, p. 125, (1987).

II.F. SUBTASK 2.F. - LARGE PARTICLE OXIDATION AT HIGH PRESSURES

Senior Investigators: Angus U. Blackham , Geoffrey J. Germane and L. Douglas Smoot
Brigham Young University
Provo, Utah 84602
(801) 378-2355 and 6536
Student Research Assistants: Kenneth Bateman, Gary Pehrson, Layne Pincock, Wade Riser and Parvin Yousefi

Introduction

Consumption or conversion of coals and coal chars as large particles has been practiced for centuries, and remains a viable technology. High pressure, fixed-bed gasifiers are used commercially for liquid fuels production and for power generation. In the U.S. Clean Coal Technology program, advanced fixed bed gasifiers are currently being demonstrated for air-blown, integrated gasification combined cycle (IGCC) power generation using Lurgi technology and for mild gasification of lump coal in air at atmospheric pressure for liquid and solid product production (LFC process). Demonstration plants are nearing completion in Florida and Wyoming, respectively. Yet, very little rate data are available for oxidation of large coal particles. At high temperatures in air, diffusional processes are thought to control the oxidation rate, but the role of ash layers for various coals has not been addressed. At lower temperatures, kinetic rate processes will be important. Nor has there been any data reported at elevated pressures.

The overall objective for this subtask is to provide data for the reaction rates of large char particles of interest to fixed-bed coal gasification and combustion systems operating at a range of pressures.

The specific projects have included:

1. Atmospheric Char Oxidation in Simple Devices.

2. Oxidation at Elevated Pressures in the HPCP Reactor.

Accomplishments

Char oxidation tests of cm-sized particles have been made at atmospheric pressure in simple devices. A high pressure facility has been designed, constructed and tested for char oxidation tests at elevated pressures. This facility includes a cantilever balance assembly which can be attached to the HPCP reactor of Subtask 2b. The key design feature of the high pressure reactor is has been a ceramic tube attached to a force transducer, the other end of which is attached to a platinum balance pan for supporting a large char particle. A three axis slide was designed for moving this cantilever beam balance unit so that the char particle is properly positioned in the flow path of the reactor gases. The construction and testing of this assembly was completed. A test program involving tests at 5 and 7.5 atm. has been completed for two coals in this facility. A correlative method has been developed to correlate the observed data at both atmospheric and elevated pressures.

Atmospheric Char Oxidation Rates in Simple Devices

Introduction and Previous Work - While the sophisticated high pressure facility (HPCP) was being modified for large particles, large char particle oxidation experiments were conducted in either one of two simple laboratory devices: (a) a crucible of either platinum or ceramic heated in the flame of a Meker burner or in a muffle furnace; (b) a platinum mesh basket placed in the open end of a heated ceramic tube

with air flowing at a controlled rate of flow. Results provided useful insights into the behavior of large particles.

Essenhigh (1981) summarized early work in oxidation of somewhat smaller lignite[4] and bituminous coal[5] chars with particle sizes in the range of 0.1-0.4 cm. For these data, burning times of 3-200 s varied as the square of particle diameter, suggesting diffusional control at the reported temperature of 1500 K. Wang and Wen (1972) investigated the role of mineral matter in the combustion of large carbonaceous particles (d_p ~2.4 cm) by preparing particles with different mineral matter percentages. They combined finely divided charcoal with finely divided clay and then fabricated spherical particles. Burn times were from 80 minutes to 2 hours for these large particles at lower temperatures. Combustion in air at 800 K showed that ash-layer diffusion controlled the combustion process. Effective ash layer diffusivities were 10-40% of the molecular diffusivity. More recently Park and Edgar (1987) investigated the effects of the ash layer on burning of lignite coal cylinders (2.5 cm dia. x 8 cm long) in air. Devolatilization preceded char oxidation. Burning rates were in the range of 1-2 cm/hr and varied inversely with increasing ash layer thickness.

Froberg and Essenhigh (1978) investigated the burning rate behavior of 1.26 cm dia. carbon spheres of high purity for solid temperatures up to 1370 K in air and oxygen. They noted that boundary layer diffusion (Zone III) controls above about 1270 K. At lower temperatures, they were able to deduce kinetic rates for the large carbon spheres. Presence of an ash layer will increase diffusional resistance and lower the transition temperature to diffusional control, as will more reactive carbonaceous fuels. Ragland and Yang (1982) oxidized four coals of different rank in air at atmospheric pressure in a convective TGA furnace with temperatures of 800-1100 K, gas velocities of about 2-8 m/s, and particle diameters from 0.4-1.2 cm. The initial phase of reaction over 25-90 s was coal devolatilization. This was followed by char oxidation for 2-6 minutes. Sometimes the ash broke away and sometimes it remained intact. CO and CO_2 concentrations in the effluent gas varied during the char oxidation. Burnout times were reduced by half when temperature was increased from 800 to 1100 K, indicating some kinetic control. At 1100 K, doubling gas velocity from 1.7-3.4 m/s decreased burning time, suggesting some diffusion control. Their Fig. 12 (at 1.7 m/s, 1100 K) showed that lignite char, with the highest ash level of 16.6% (dry basis) oxidized most slowly when compared with the other three chars (bituminous, non-swell bituminous, sub-bituminous coals with ash levels 8.5-9.2%) Reactivities of these chars at comparable sizes and temperatures, are higher than most of the data of this study, possibly due to convective air effects.

Essenhigh (1981) and Smith (1983) provided reviews of coal char modeling processes for several reactants but neither explicitly considered large particles and neither discussed the role of the ash layer in any detail. Amundson and Arri (1978) reported a comprehensive model of large char particle reaction, applicable to a fixed-bed gasifier. Their work treats ash layer effects where kinetic and diffusional resistances were considered in a comprehensive model with numerical solution. The focus was on the fixed bed behavior and no data were provided or correlated for burning of individual particles. Several other publications, mostly one to two decades ago (e.g., Wen and Wang (1970); Srinivas and Amundson (1980)) have modeled single particle char oxidation processes. However, this body of work has not provided demonstrated rate data for ash layer-forming, large, cm-sized char particle oxidation.

The specific objectives of this work have been to: (1) establish a simple experimental method for determining rate data for large char particles, applicable to fixed bed reactors; (2) measure and report rate data for several common coals in air at ambient pressure and high temperatures, typical of fixed beds; (3) develop and apply a simple correlative method, based on rate-controlling processes, for incorporating rate data into fixed bed models.

Experimental Method - A simple experimental method has been demonstrated to provide quantitative rate data for oxidation of large coal char particles. The method makes use of a muffle furnace or a Meker burner and a single crucible containing the char particle. Air flow to the particle in the crucible is by natural convection. In this study, single particles were investigated with equivalent spherical diameters in the range of 0.5-1 cm. The particle and crucible were weighed and placed into the furnace. After a fixed

reaction period (5-15 min), the crucible was removed, cooled, weighed, and mass loss of the char was determined. This process was repeated until the carbon of the char was consumed. The method makes use of the assumptions that heating and cooling times are very fast compared to reaction times.

These transient heating and cooling times will be maximum for the largest particles toward the end of burnout when the ash layer is thickest. Ambient temperatures are in the range of 300 K while reaction temperatures are in the range of 690-1420 K. Burning rate data are linear to at least 80% consumption of the char mass, which for spheres, is 40% decrease in char radius ($d_p/d_{po} \sim 0.6$). Thermal diffusivities of ash layers are in the range of 0.02-0.05 cm^2/s for either loose ash deposits or solid slag materials, based on data of Singer (1981). This is so because, while thermal conductivities of loose ash layers are much lower than for fused ash, densities are also lower by about the same factors. With these data, unsteady spherical heat transfer analysis (Bird, Stewart, Lightfoot, 1960) shows that maximum heating and cooling times are of the order of 2 seconds, compared to at least 300 s between weighings. Ash layer sluffing and convective or radiative heat transfer will lower these heating and cooling times.

Test Program - Table II.F-1 shows the test program. Variables were coal type, particle mass, temperature, a flow rate and numbers of particles. One hundred fifty tests were performed.

TABLE II.F-1

THE TEST PROGRAM OF CHAR OXIDATION IN SIMPLE EXPERIMENTAL DEVICES AT ATMOSPHERIC PRESSURE

Main Objective of Char Oxidation	Range of Variables	Coals Used	Number of Tests
Effect of Coal Type and Particle Mass	Six Coals - 1150-1470 K	Utah	28
		Colorado	3
		Ill. #6	1
		North Dakota	1
		Wyoming	1
		Pitt. #8	1
Effect of Temperature	Five Coals - 690-1280 K	Illinois	24
		Utah	27
		North Dakota	13
		Colorado	4
		Wyoming	2
Effect of Air Flow Rate	Two Coals - Reynold's No. 1.5 to 77	Illinois	8
		Utah	6
Effect of Surface Area	Three Coals - One, Two, and Four Particles Compared	Illinois	18
		Utah	6
		North Dakota	7

[1]This test program includes those conducted in a crucible and those conducted in the ceramic tube with forced air flow. The air flow facility and test results are discussed following crucible results.

Effects of Coal Type and Particle Mass - Five different sets of coal particles were oxidized. Procedures for each set follow.

Set I - Utah Bituminous Coal-Meker Burner - For Set I, a lump of coal was fractured into several pieces by striking the lump with a hammer. From these pieces, six particles were selected, each in the 0.5 to 1.0 gram range. One particle was placed in each of six platinum crucibles. The rationale in this replicate set of six tests was that if the results for one or two of the particles varied widely from the others, the remaining four or five would give a satisfactory average response.

In Set I, a Meker burner was used to examine the impact of heat source. Also, the coal was used directly rather than preparing char first. The mass of each crucible and the mass of each particle plus the crucible were recorded. Each crucible was placed in a slanted position on a clay triangle over the Meker burner. The flame of the burner was located at the mouth of the slanted crucible. The crucible wall carried the heat of the flame to the coal particle at the bottom of the crucible. As devolatilization started, the combustible volatiles burned at the mouth of the crucible. The visual burning of combustible gases continued for two to three minutes, depending on the size of the particle. As the flame from these gases gradually decreased the tar that was deposited on the top wall of the slanted crucible gradually disappeared, particularly as the Meker burner was shifted so that the flame enveloped the crucible and the brightest glow of the crucible was at the bottom where the resulting char particle was located. The crucible and char particle cooled as the burner flame was removed. When the six crucibles had cooled to room temperature, the weighings were made. A Mettler-P163, top-loading balance was used. The masses of the particles at this point were taken to be the initial char masses including the ash. The six crucibles were then heated again with the Meker burner, this time for a period of five minutes. They were cooled to room temperature and by weighing, the mass loss for each was determined. This sequence was repeated several times with the periods of heating being five, ten or fifteen minutes until only the ash was left.

For this set, a temperature of approximately 1150 K was determined by placing a Pt/Pt(Rd) thermocouple junction between the char particle and the bottom of a crucible while the burner was operating with the natural gas valve on the laboratory bench fully opened. It was assumed that conditions for this set and also Sets IV and V gave approximately the same temperature.

Set II - Utah Bituminous Coal - Muffle Furnace - A second set of six particles of the Utah coal was oxidized under similar conditions except that the heating source after the devolatilization was a muffle furnace. The temperature of approximately 1230 K for this set was taken directly from the reading of the muffle furnace pyrometer without calibration.

A significant difference in the results from this set was that the measured ash percentages in the Utah coal were larger. The reason for this difference has been shown to be due to random variation in the initial mineral matter levels of the large coal particles.

Set III - Utah Bituminous Coal - Temperature Variation - The influence of temperature on the oxidation was next determined. In Set III, four subsets each with four coal particles each were separately oxidized in the muffle furnace over a specific temperature range. Set IIIa had a temperature range of 1270-1320 K. The reason for the range was that the temperature reading decreased as the furnace door was opened. The four crucibles were placed in the furnace and the door was almost closed leaving a slight opening for a small current of air to circulate through the furnace box. The temperature reading increased and could be maintained within the indicated temperature range with slight adjustments of the manual heat controller. Other temperature ranges were: Set IIIb - 1320-1370 K; Set IIIc - 1370-1420 K; Set IIId - 1420-1470 K.

Set IV - Colorado Bituminous Coal - Coal Type - Some lump coal from a mine near Delta, Colorado was available. In Set IV, three coal particles from a shattered lump were separately oxidized in platinum crucibles in a Meker flame as in Set I.

Set V - Various Coal Types - Samples of Illinois #6, North Dakota Lignite, Wyoming subbituminous, and Pittsburgh #8 coals were oxidized in air with Meker burners as in Set I. The particle of Pittsburgh #8 coal was formed by pressing pulverized coal particles into a larger agglomerated mass. A sample of the pulverized coal was pressed in a die and press used for preparing potassium bromide windows for infrared spectral determination of organic compounds. Some difficulty resulted in removing the disk from the die and it cracked. However, a piece of sufficient size was obtained to devolatilize it to a swollen char particle for the oxidation test run.

Test Results - Table II.F-2 provides a summary of the properties of the six test coals. Table II.F-3, reports the properties of the test chars for 35 of the experiments. Data include initial mass, initial ash percentage, and coal type for each of the five sets of tests. Char density data were not available for these tests. Char densities differed from coal density through loss of volatiles, swelling, and loss of mass through oxidation. An example of data obtained from one of the tests in Set I is shown in Fig. II.F-1 with char mass remaining as a function of time. While the curve appears to follow an exponential decay, a more satisfactory curve fit was obtained with a graph of the cube root of char mass remaining as a function of time. The time-dependent burning rate data are reported in Figs. II.F-2 through II.F-6 for the five sets of tests respectively. In all but Fig. II.F-2b, the data are plotted as $m^{1/3}$ vs. time. In Fig. II.F-2b, the data are plotted as $m^{1/3}$ vs. $t^{1/2}$. This alternative plotting method did not lead to a linear representation of the data. These observations will be discussed in a following section.

Effect of Temperature - From an examination of Fig. II.F-4, no strong effect of temperature on the burning times of the char particles was observed because of the dominant effect of the initial particle mass. However, the temperature range was only 200 degrees, from 1270 K to 1470 K. Therefore a series of tests with initial particle mass close to 0.2 grams was made over a much wider temperature range of 690 K to 1280 K.

Results of seventy tests with five coals are presented in Table II.F-4. A test series was conducted for the Utah coal and for the Illinois coal with the initial particle mass close to 0.2 gram so that the dependence of initial particle mass or the rate of reaction would not be the main observation and the effect of temperature could more clearly be observed. Under these conditions it was observed that the burning time decreased with increasing temperature for the Utah and Illinois coals over a 600 K degree range. The data for the Illinois coal are presented as an example in Fig. II.F-7.

Effect of Air Flow

In order to increase the rate of natural convective air flow around the oxidizing char particle, some tests were made with the particle in a larger, more shallow crucible instead of the crucible used for the previous tests. The observed burning times decreased somewhat as shown subsequently in Fig. II.F-10 where the effect of ash layer is also shown. While this method suggests some impact of air flow rate, a more definitive experimental method was sought to clarify effects of air flow rate.

In order to know more precisely the rates of convective air flow past the oxidizing char particle, a second simple experimental device was set up. In this arrangement, air passing through a flow meter entered one end of a ceramic tube with an inside diameter of 25 mm. The tube about 30 cm in length, was heated with two Meker burners. The coal or char particle in a platinum wire mesh basket was placed about 3 cm into the open end of the ceramic tube. The air flow rates varied up to 2000 ml/min. The data obtained are presented in Table II.F-5 for samples of the Utah and Illinois coals with burning times shown as a function of Reynold's number. Initial char mass was held close to 0.12 grams. The burning time decreased with increasing Reynold's number as shown for the Illinois coal in Fig. II.F-8. Burning times changed from 20 to 8 minutes as Reynold's number changed from 2 to 77 with oxidation temperature approximately 1070 K.

TABLE II.F-2

TEST COAL PROPERTIES

Coal	Prox. Analysis % Volatile Content	Fixed Carbon	Ash	Moisture	Elemental Analysis % Carbon	Hydrogen	Nitrogen	Sulfur	Oxygen	Mine	Rank	Density g/cm^3
Utah bituminous	**34.9**[1]	**54.8**	**6.3**	**4.0**	**71.2**	**5.9**	**1.3**	**0.7**	**10.6**	Near Price, Utah	HVBB	1.30
Illinois #6	**39.4** 40.1	**43.5** 42.7	**10.4** 10.2	**6.7** 7.0	**62.4**	**4.4**	**1.3**	**4.0**	**10.7**	St. Clair Co., Ill.	HVCB	1.23
North Dakota Lignite	**39.8** 45.1	**35.1** 30.5	**6.1** 2.6	**19.0** 21.8	**46.7**	**3.4**	**0.8**	**1.0**	**23.6**	Mercer, Co., ND	LIGA	1.34
Wyoming Subbituminous	**47.3** 43.2	**40.3** 31.3	**6.4** 3.9	**6.0** 21.6	**63.5**	**5.5**	**1.2**	**0.3**	**18.6**	Campbell, Co., WY	SUBC	1.33
Colorado bituminous	**41.0** 39.8	**50.7** 51.8	**4.3** 3.0	**6.5** 7.0	not available					Near Delta, Colorado	BIT	1.31
Pittsburgh #8	**36.6**	**55.4**	**6.0**	**2.0**	**76.0**	**5.2**	**1.5**	**1.2**	**8.3**	Green Co., PA	HVAB	NA[2]

[1]Values in bold type were taken from Smith and Smoot (1985).
[2]Density for pressed coal pellet not measured.

TABLE II.F-3

RESULTS FOR COAL TYPE AND PARTICLE MASS

Char Sample	Initial Mass ash free (g)	Ash/g.	Burning Time (min)	Ave. Mass Reactivity (g/g-min)
	Utah Bituminous Coal ~1150 K			
I-1	0.189	0.011	50	0.069
I-2	0.287	0.020	66	0.047
I-3	0.345	0.023	64	0.045
I-4	0.349	0.022	62	0.047
I-5	0.244	0.013	52	0.057
I-6	0.166	0.012	42	0.060
	Utah Bituminous Coal ~1230 K			
II-1	0.565	0.083	73	0.044
II-2	0.438	0.051	62	0.053
II-3	0.661	0.063	88	0.038
II-4	0.435	0.049	65	0.047
II-5	0.425	0.068	53	0.059
II-6	0.468	0.051	73	0.044
Utah Bituminous Coal	a-1270-1230 K b-1320-1370 K c-1370-1420 K d-1420-1470 K			
III-1a	0.571	0.061	72	0.043
III-2a	0.262	0.018	50	0.063
III-3a	0.237	0.032	52	0.061
III-4a	0.596	0.087	73	0.038
III-1b	0.316	0.030	43	0.061
III-2b	0.445	0.040	63	0.050
III-3b	0.555	0.068	68	0.044
III-4b	0.556	0.065	74	0.042
III-1c	0.614	0.116	76	0.041
III-2c	0.505	0.073	68	0.045
III-3c	0.253	0.028	38	0.073
III-4c	0.644	0.055	74	0.042
III-1d	0.248	0.061	57	0.056
III-2d	0.371	0.034	74	0.041
III-3d	0.155	0.015	31	0.089
III-4d	0.154	0.011	33	0.076
	Colorado Bituminous Coal ~1150 K			
IV-1	0.577	0.026	88	0.040
IV-2	0.689	0.021	100	0.033
IV-3	0.437	0.008	66	0.050
	Various Coals ~1150 K			
V-1 Illinois #6	1.040	0.248	200	0.020
V-2 North Dakota	0.905	0.076	110	0.034
V-3 Wyoming	0.561	0.070	62	0.045
V-4 Pitts. #8	0.106	0.006	38	0.080

TABLE II.F-4

EFFECT OF PARTICLE TEMPERATURE ON CHAR OXIDATION TIMES
(Performed in the Muffle Furnace; 70 Tests)

Sample ID	Initial Char Mass (g)	Ash (g)	Approx. Burning Time (min)	Approx. Temp. (K)
Illinois Coal				
A-1	0.243	0.041	85	693
A-2	0.215	0.037	85	
A-3	0.241	0.050	60	813
A-4	0.218	0.102	50	
A-5	0.241	0.023	50	
A-6	0.241	0.044	43	893
A-7	0.411	0.023	80	
A-8	0.223	0.053	45	
A-9	0.216	0.058	45	
A-10	0.497	0.030	110	
A-11	0.251	0.017	43	923
A-12	0.603	0.016	145	
A-13	0.221	0.026	45	963
A-14	0.237	0.021	46	
A-15	0.235	0.011	45	1093
A-16	0.336	0.013	60	1113
A-17	0.230	0.030	45	1173
A-18	0.154	0.013	38	
A-19	0.182	0.018	40	
A-20	0.171	0.023	40	
A-21	0.113	0.006	25	
A-22	0.220	0.058	38	1283
A-23	0.259	0.034	40	
A-24	0.254	0.033	40	
Utah Bituminous Coal				
B-1	0.200	0.015	70	693
B-2	0.210	0.012	58	813
B-3	0.235	0.033	62	
B-4	0.174	0.050	60	
B-5	0.195	0.012	38	893
B-6	0.405	0.041	90	
B-7	0.569	0.068	90	
B-8	0.158	0.015	35	
B-9	0.178	0.018	35	
B-10	0.254	0.015	43	923
B-11	0.561	0.060	105	
B-12	0.219	0.011	40	963
B-13	0.217	0.011	35	
B-14	0.206	0.010	35	1093

TABLE II.F-4 (CONTINUED)

B-15	0.214	0.010	40	1093
B-16	0.206	0.011	40	
B-17	0.367	0.027	60	
B-18	0.184	0.010	40	
B-19	0.322	0.027	50	1113
B-20	0.215	0.011	41	1173
B-21	0.167	0.047	30	
B-22	0.173	0.018	30	
B-23	0.163	0.024	30	
B-24	0.190	0.014	40	
B-25	0.206	0.013	40	
B-26	0.189	0.010	30	1283
B-27	0.189	0.014	30	

North Dakota Coal

C-1	0.270	0.078	45	893
C-2	0.327	0.026	95	
C-3	0.142	0.014	40	923
C-4	0.593	0.025	125	
C-5	0.144	0.011	36	963
C-6	0.107	0.024	25	
C-7	0.191	0.020	35	1093
C-8	0.746	0.035	105	
C-9	0.164	0.021	50	1113
C-10	0.151	0.018	27	1173
C-11	0.246	0.016	32	1283
C-12	0.142	0.012	60	1333
C-13	0.514	0.054	60	1333

Colorado Coal

D-1	0.513	0.020	100	893
D-2	0.596	0.021	110	923
D-3	0.260	0.010	40	
D-4	0.340	0.013	60	1113

Wyoming Coal

E-1	0.184	0.052	52	893
E-2	0.189	0.025	34	1113

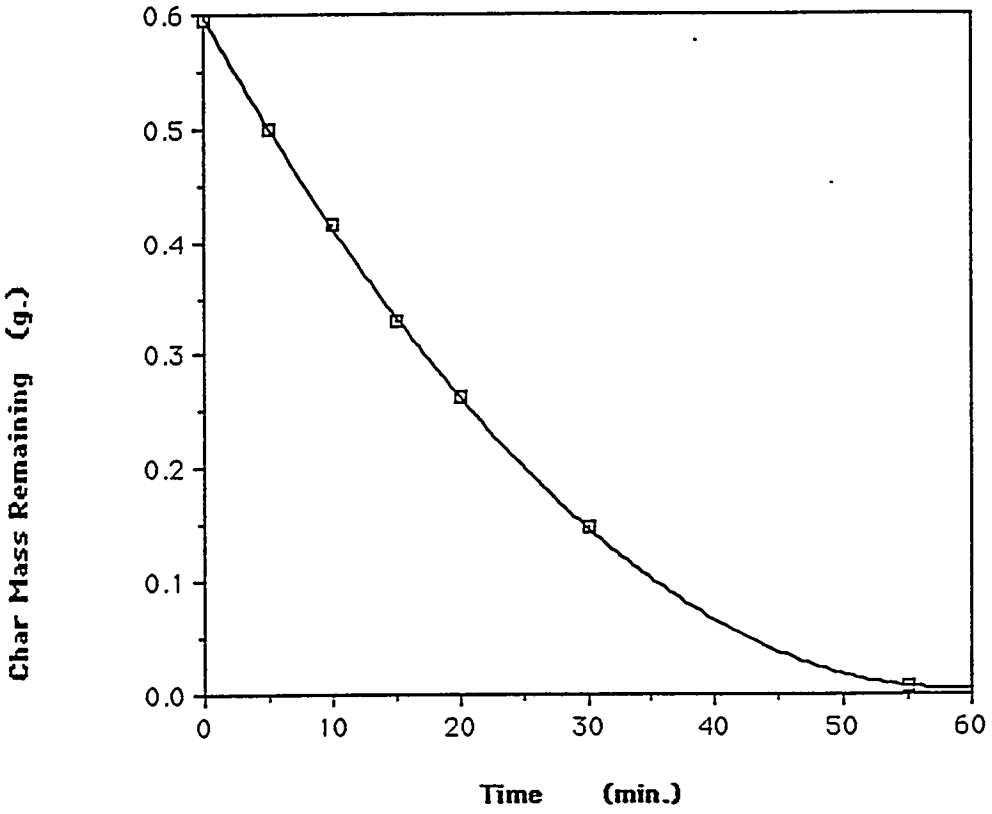

Figure II.F-1. Oxidation of a large Utah bituminous coal char particle in air in a Meker burner at about 1250 K - Char sample III-4a.

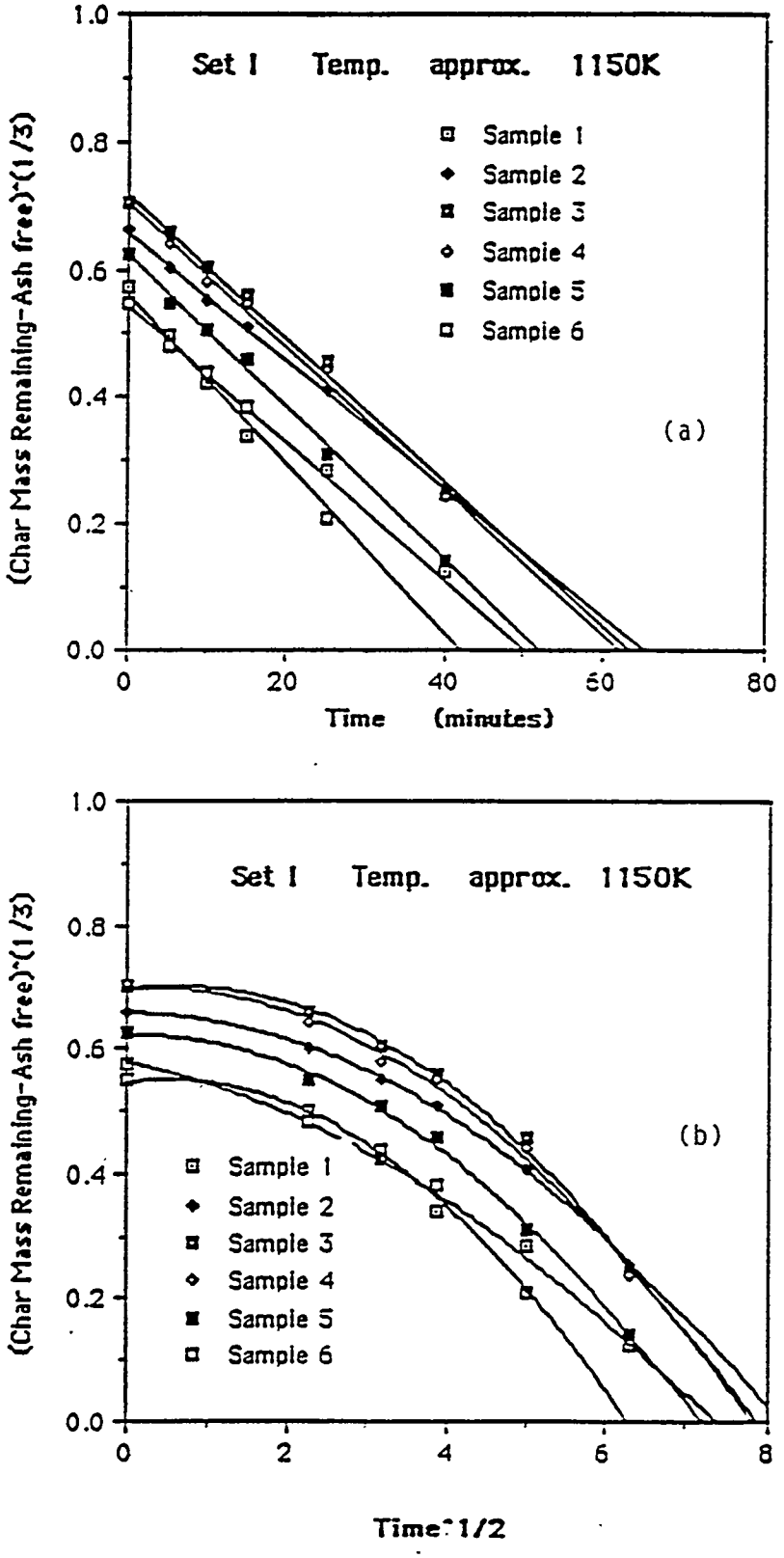

Figure II.F-2. Oxidation of large Utah bituminous coal char particles in air in a Meker burner at about 1150K. a) $m_p^{1/3}$ vs. time, b) $m_p^{1/3}$ vs. $(time)^{1/2}$.

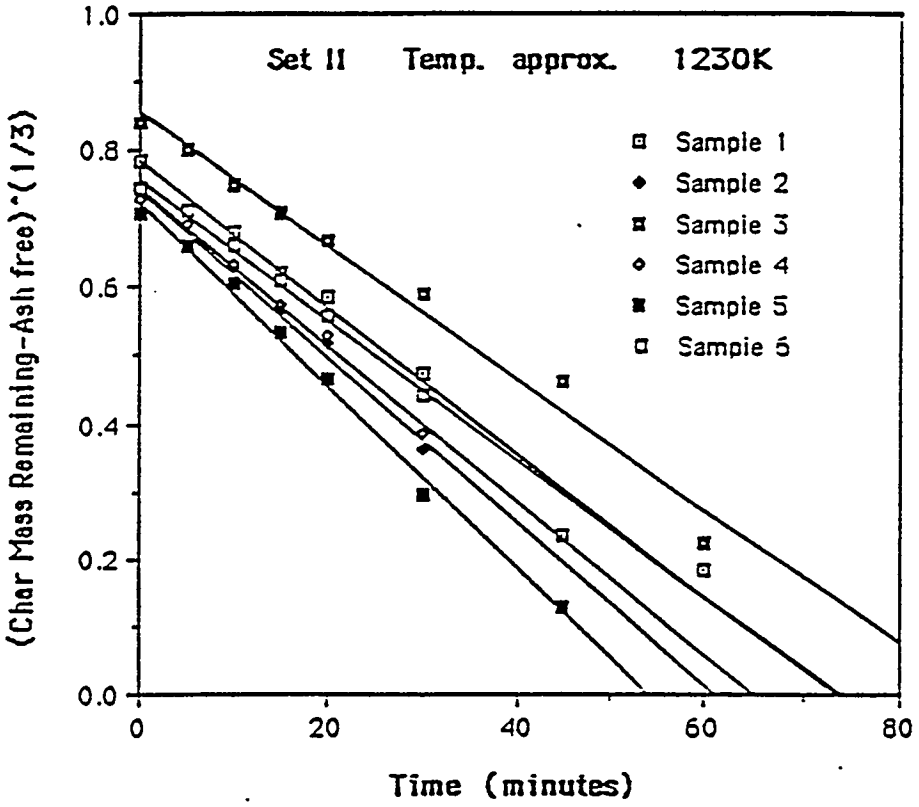

Figure II.F-3. Oxidation of a set of six large Utah bituminous coal char particles in a muffle furnace at about 1230K.

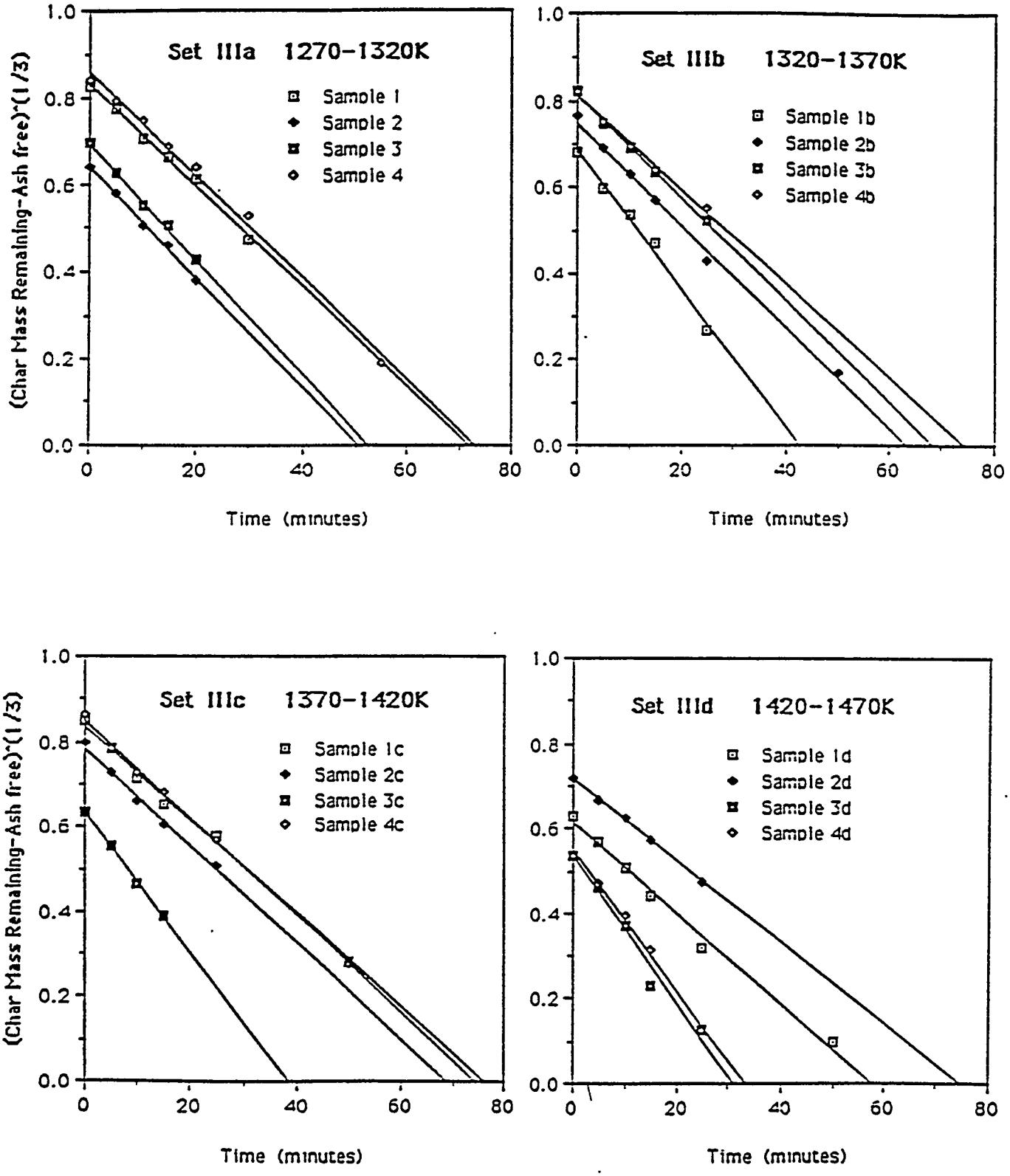

Figure II.F-4. Oxidation of four sets of large char particles from a Utah biuminous coal. Each set at a different temperature range with four particles in each set.

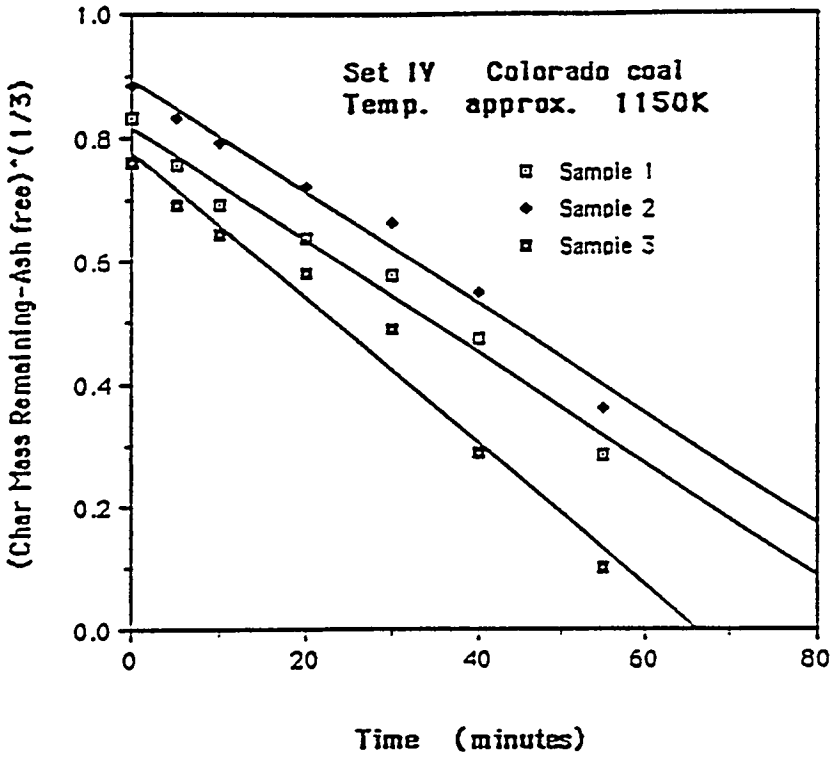

Figure II.F-5. Oxidation of a set of large char particles prepared from a Colorado bituminous coal in a Meker burner at about 1150K.

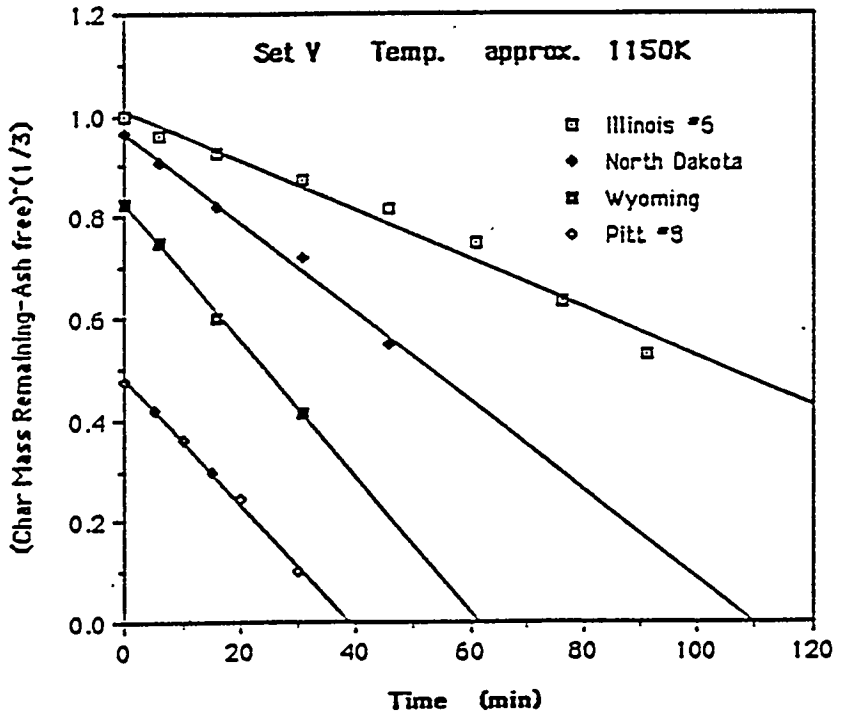

Figure II.F-6. Oxidation of large char particles prepared from four different coals in a Meker burner at about 1150K.

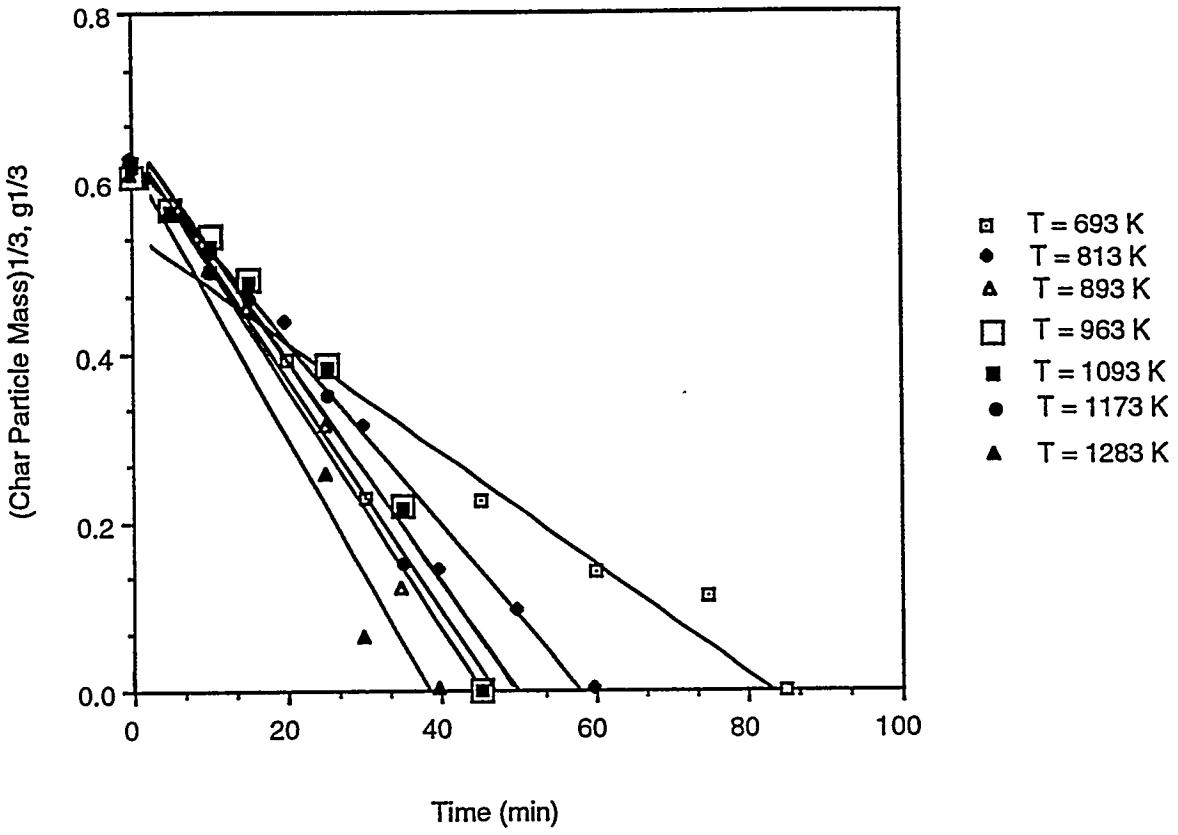

Figure II.F-7. Effect of particle temperature on time of oxidationof Illinois coal char particles of about 0.2 gram initial mass in a muffle furnace.

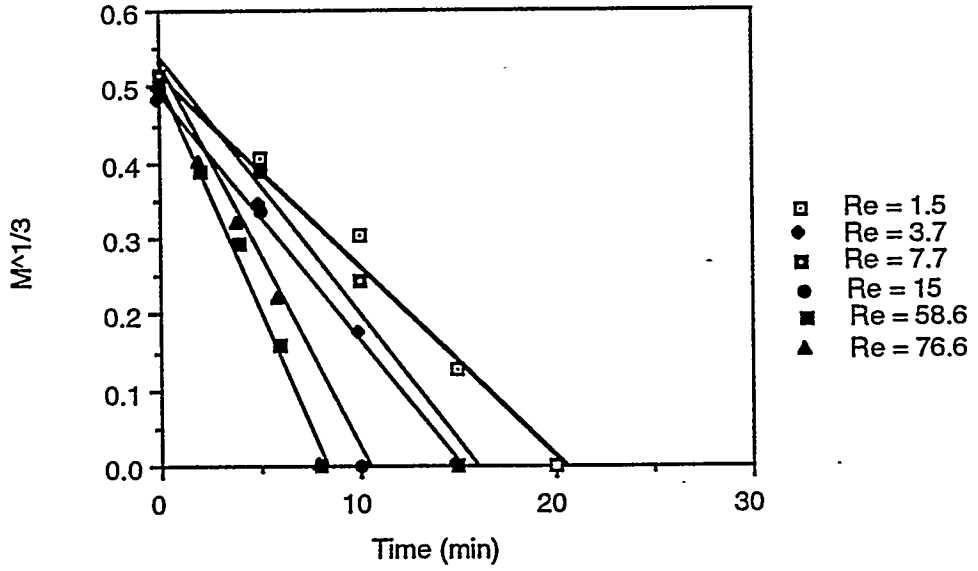

Figure II.F-8. Effect of air flow Reynold's Number on burning times of Illinois char in the ceramic tube at about 1070 K.

TABLE II.F-5

EFFECT OF AIR FLOW RATE ON CHAR BURNING TIMES
(Performed in the Ceramic Tube; 14 Tests)

Sample ID	Initial Char Mass (g)	Ash (g)	Burning Time (min)	Re
Illinois Coal	Approx. Temp. 1070 K			
F-1	0.123	0.035	20	1.5
F-2	0.108	0.017	15	3.7
F-3	0.119	0.040	15	5.4
F-4	0.134	0.034	15	7.7
F-5	0.116	0.023	10	11.3
F-6	0.125	0.025	10	15
F-7	0.118	0.020	8	58.6
F-8	0.123	0.031	8	76.6
Utah Bituminous Coal	Approx. Temp. 1070 K			
F-9	0.131	0.008	15	1.5
F-10	0.105	0.026	10	3.7
F-11	0.107	0.017	10	5.4
F-12	0.108	0.019	10	7.7
F-13	0.115	0.011	10	11.3
F-14	0.119	0.014	10	15

Effect of Multiple Particles

It might be expected that the burning rate of a char particle would increase with an increase in the surface area of the char particle. Accordingly 31 tests were made in which the burning rate of a single particle of a specific mass was compared to the overall burning rate of multiple particles of the same total mass. Some tests were with four particles; a few were with two particles. Tests were conducted both in the crucible and inthe ceramic tube. Three coals were used and the data are presented in Table II.F-6. Selected data for the Illinois coal char are presented in Fig. II.F-9. Further multiple-particle data are compared subsequently in Figs. II.F-10 and II.F-11. The striking observation is that the burning times for four small particles was always about the same as for one large particle with the same overall mass in both facilities. A qualitative indication of a decrease in burning time with an increase in air flow into the crucible is noted in Table II.F-6 for the Illinois coal where a comparison is made between tests with char particles in crucibles with and without additional flow of air from a small glass tube directed into the crucible. This effect is shown quantitatively in the next entry for tests in the ceramic tube where the flow is controlled and burning time is compared to Reynolds's number and initial mass.

Effect of Ash Layer - One of the variables considered as influencing the burning time of a char particle was the ash layer surrounding the decreasing carbon core. An effort was made in a few tests to remove the ash layer each time the char particle was cooled for weighing during the course of burnout, with char samples from the Illinois coal of about the same mass. Figure II.F-10 shows a burning time of 75 minutes in (a) where the ash layer was not removed, a burning time of 56 minutes in (b) where the ash layer was removed and a burning time of 30 minutes in (c) where a larger more shallow crucible was used instead of the standard size platinum crucible used in earlier tests. With char samples from the Utah coal, Figure II.F-11 shows a burning

TABLE II.F-6

EFFECT OF SURFACE AREA ON BURNING TIME
(31 Tests)

Furnace	Number Particles	Initial Mass	Ash (g)	Burning Time(min)	Approx. Temp. (K)
Illinois Coal					
Muffle	One Small	0.113	0.006	25	1173
	Two	0.214	0.020	35	
	Four	0.482	0.036	75	
	One Large	0.537	0.057	75	
Meker					
with flow	Four	0.530	0.061	50	1070
(see text)	One Large	0.491	0.081	45	
	Four	0.477	0.059	40	
	One Large	0.511	0.042	40	
Meker					
no flow	Four	0.485	0.063	150	1070
	One Large	0.468	0.033	130	
Ceramic Tube					
Re 15.6	Four	0.484	0.051	20	1070
	One Large	0.470	0.055	20	
3.7	One Small	0.108	0.017	15	
	Four	0.481	0.077	25	
	One Large	0.472	0.079	25	
5.4	One Small	0.119	0.040	15	
	Four	0.480	0.100	30	
	One Large	0.500	0.086	30	
Utah Bituminous Coal					
Muffle	One Small	0.259	0.021	45	1093
	Two	0.899	0.061	125	
	One Small	0.312	0.027	54	
	Two	0.687	0.056	90	
	One Small	0.190	0.014	38	1173
	Four	0.745	0.062	105	
North Dakota Coal					
Muffle	One Small	0.151	0.018	27	1173
	Two	0.496	0.041	50	
	Four	1.371	0.078	90	
	One Small	0.142	0.012	40	1333
	Two	0.282	0.026	60	
	Four	0.571	0.041	80	
	One Large	0.514	0.054	60	

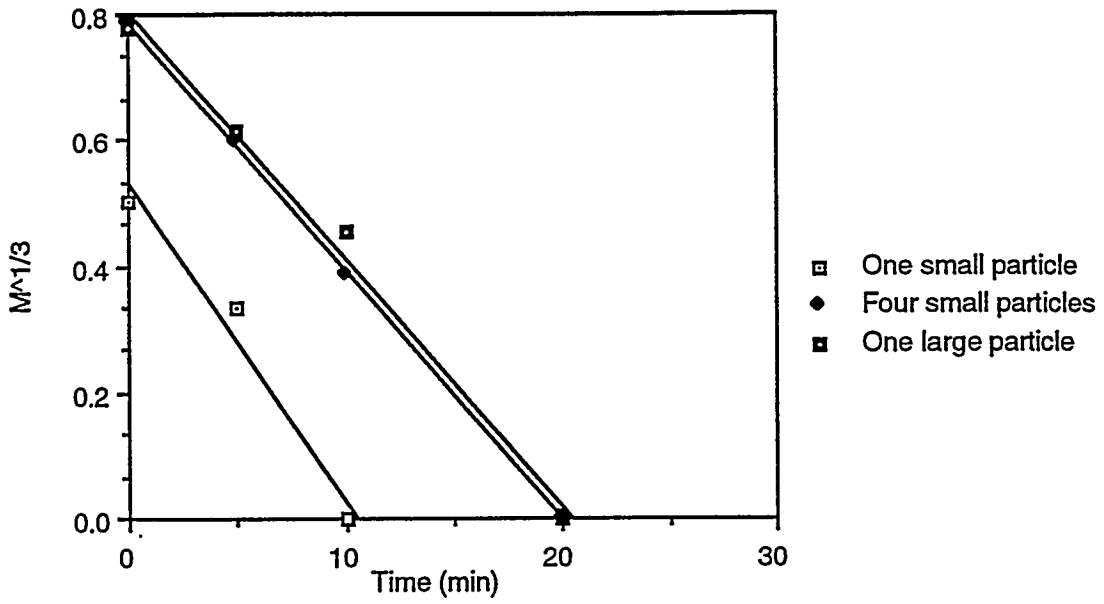

Figure II.F-9. Effect of char surface area (number of particles) on oxidation rate of Illinois char in a ceramic tube at a particle temperature of about 1070 K. Re = 15.6

time of 85 minutes in (a) where the ash layer was not removed, a burning time of 30 minutes in (b) where the ash layer was not removed but the larger more shallow crucible was used and a burning time of 35-40 minutes in (c) where ash was removed and the larger more shallow crucible was used.

Though ash layer seemes to be a factor, these observations suggest that the effect of ash removal is not as significant as is the availability of oxygen near the particle surface. These data indicate that removal of ash may result in a slightly decreased burning time if there is limited access of air to the char particle. When there is more air available the burning time sharply decreases and almost no effect of the ash layer is observed.

Summary of Observations - From the simple test experiments, several observations were made relating to large char particle oxidation.

(1) The first simple experimental method consisted of a single char particle heated in a crucible in either a muffle furnace or a Meker burner flame. These tests provided burning rate data of large (0.5 - 1 g) individual char particles from five coals of varying rank in air at ambient pressure over a range of high temperatures from 1150 - 1475 K. Test variables included initial char mass, oxidation temperature and coal type. For all coals and all conditions, linear decrease in cube root of char mass vs. time was observed until sometimes, toward the very end of burnout, faster decay occurred. Initial mass is the major factor that influences burning time and is consistent in all tests.

(2) Data in two different-types of reactors (Meker, muffle) gave similar results for burning rates of a given coal of comparable mass.

(3) Burning times of 0.5 - 2 hours with natural convective air flow observed here are longer than those of other investigators for comparable char masses in air.

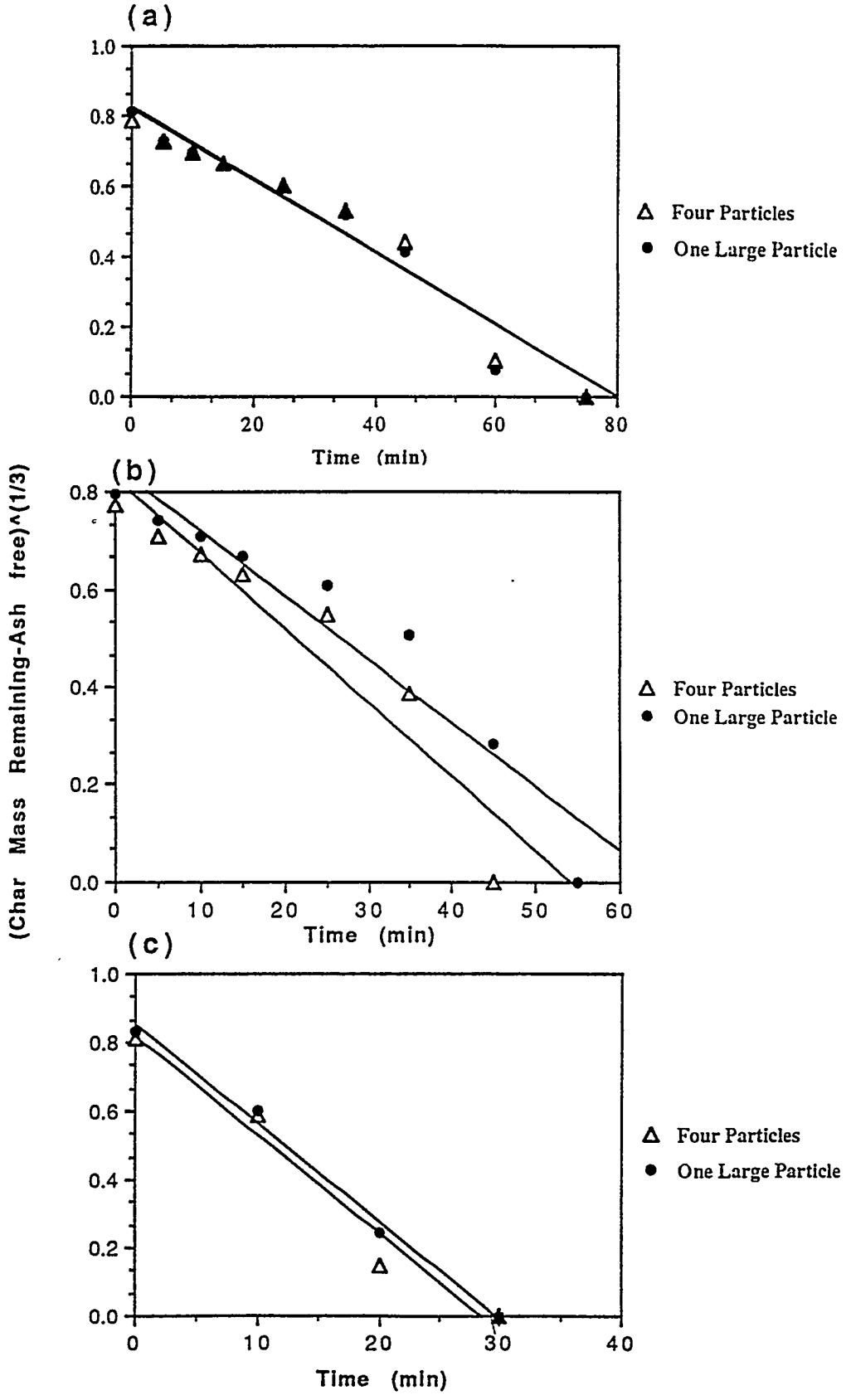

Figure II.F-10. Effect of number of particles and ash layer on the burning times of char particles from the Illinois coal at 1170K with ash intact in (a),removed in (b) and burning in a larger crucible in (c).

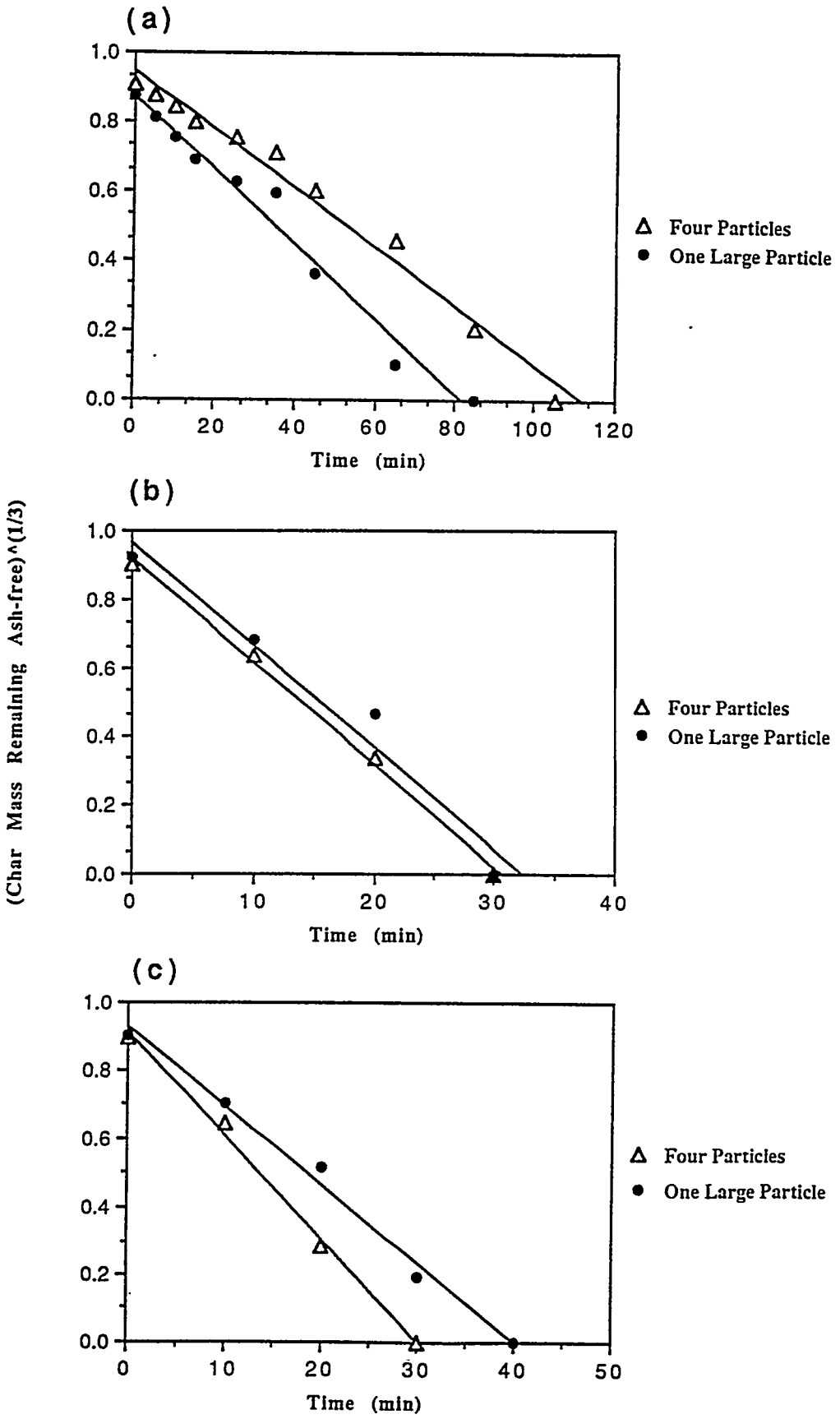

Figure II.F-11. Effect of number of particles and ash layer on the burning times of char particles from the Utah coal at 1170K with ash layer intact in (a), removed in (c) in larger more shallow crucibles.

(4) The rate of reaction, dm_p/dt for a given coal char of fixed initial mass initially varies linearly with temperature and at lower temperatures then at higher temperatures, becomes largely independent of T.

(5) In a standard crucible for two different coals of the same initial mass, the burning times for one large particle and four smaller particles of the same mass were about the same. This indicates little dependence of surface area on burning time for these closely spaced particles.

(6) When a char particle of fixed mass is burned in a more shallow, larger base crucible, the burning time is reduced by over half but is still independent of the number of particles (or surface area).

(7) When ash is removed (manually), periodically during the burning process, the Utah coal burning time was not reduced (large crucible). The burning time of Illinois #6 coal was reduced from 80 min. to 60 min. for a small crucible or by 30 min. to 20 min. for a large crucible by removal of the ash layer.

Correlative Methods

Bulk Diffusion or Kinetic Control - Available large-particle data (Wen and Wang, 1970; Essenhigh, 1981; Ragland and Yang, 1985) suggest that oxidation of large coal char particles in air at ambient pressures and high temperature is controlled by diffusional processes. Ragland and Yang (1985), among others, show the simple diffusion-controlled equation for oxidation of a spherical char particle in laminar flow:

$$dm_p/dt = k_c\, A_p\, (C_{ob} - C_{os})\, M_p S \qquad \text{(II.F-1)}$$

where $A_p = (\pi)d_p^2$, and the rate of burning is proportional to the square of the particle diameter. Assuming k_c is not time-dependent and C_{os}~0, integration of this equations gives:

$$m_p^{1/3} = m_{p_o}^{1/3} - C_d\, t \qquad \text{(II.F-2)}$$

where $$C_d = \left(M_p S k_c\, \pi/3\right)\left(6/\rho_p \pi\right)^{2/3}$$

Thus, a plot of $m_p^{1/3}$ vs. t should yield a straight line with slope C_d. The data in the previous section consistently reveal this linear relationship. However, this observation does not prove the mechanism, as will be evident.

If, on the other hand, the char particle oxidation is controlled by first order surface reaction with oxygen, then commonly:

$$dm_p/dt = k_r A_p C_{os} M_p S \qquad \text{(II.F-3)}$$

For constant temperature oxidation, and C_{os}~C_{ob}, integration yields:

$$m_p^{1/3} = m_{p_o}^{1/3} - C_r\, t \qquad \text{(II.F-4)}$$

Thus, either kinetic or diffusion control could yield the observed linear dependence between $m_p^{1/3}$ and t.

Further, accumulation of an ash layer may alter the burning mechanism. Wang and Wen (1972) demonstrated the controlling role of ash layer diffusion for 2.4 cm charcoal/clay particles under certain conditions. Ragland and Yang (1985) note the increasing role of the ash layer toward the end of burnout.

Ash Layer Control - Simple theories of the ash layer effects were also explored. The following assumptions were made:

(1) Diffusion of oxygen through the ash layer controls the oxidation rate.

(2) The large coal char particles can be approximated as spherical in shape.

(3) The ash remains around the char and does not expand or contract, leaving the particle diameter unchanged.

(4) Blowing effects are neglected based on low oxidation rates.

Two alternatives were explored, a particle with thin ash layer and one with thick ash layer.

Thin Ash Layer Theory - The mass rate of oxidation of char can then be approximated as:

$$dm_p/dt = -D_{oa}\,(C_{ob} - C_{os})\,A_p\,M_p\,S/0.5(d_{po} - d_p) \qquad \text{(II.F-5)}$$

Eqn. II.F-5 is referred to as the "thin ash layer" theory, since the concentration gradient across the ash layer is taken to be linear. Taking $C_{os} = 0$ (assumption 1), $A_p = \pi\ d_p^2$ and $m_p = (\pi/6)\rho_p\, d_p^3$ (assumption 2), then:

$$(d_{po} - d_p)\frac{d(d_p)}{dt} = -4\ D_{oa}\ C_{ob}\ M_p\ S/\rho_p \equiv C_1(\text{near constant}) \qquad \text{(II.F-6)}$$

Integrating:

$$C_1\ t/d_{po}^2 = 1/2\left[\left(\frac{d_p}{d_{po}}\right)^2 - 1\right] \qquad \text{(II.F-7a)}$$

and

$$t_b(\text{at } d_p = 0) = d_{po}^2/2\ C_1 \qquad \text{(II.F-8)}$$

For ash layer-dominated oxidation, the dependence of burnout time (t_b) on diameter varies inversely as the d_{po}^2, which is also the case for droplet or solid burning controlled by external bulk diffusion.

Rearranging Eqn. II.F-7:

$$(d_p - d_{po})^2 = (8\ D_{oa}\ C_{ob}\ M_p\ S/\rho_p)\ t \qquad \text{(II.F-7b)}$$

or

$$d_p = d_{po} - (8\ D_{oa}\ C_{ob}\ M_p\ S/\rho_p)^{1/2}\ t^{1/2} \qquad \text{(II.F-7c)}$$

Or, in terms of mass:

$$m_p^{1/3} = m_{po}^{1/3} - C_2\ t^{1/2},\ \text{where } C_2 = (\pi\ \rho_p/6)^{1/3}(2C_1)^{1/2} \qquad \text{(II.F-7d)}$$

Thus, Eqn. II.F-7 suggests that a plot of d_p or $m_p^{1/3}$ vs. $t^{1/2}$ should be linear, with the slope varying somewhat among coal types. The slope of this line is independent of initial coal size for a given coal. This result differs from Eqns. II.F-2 and II.F-4, and from the data (see Figs. II.F-2 to II.F-11).

Thick Ash Layer Theory - The above correlative method depends on the "thin ash layer" assumption, which is not likely valid during the entire period of burning of large char particles. Since formal treatment of the whole burning process, by solution of the equations of change, in spherical coordinates, adds unwanted complexity, a simple revised correlative method has been sought. If one extreme is the "thin ash layer," the other extreme is the "thick ash layer." In the limit, the maximum ash layer thickness is the initial particle radius, when the particle is entirely consumed. Thus, an alternative correlative method is derived by simply assuming that the ash layer is constant, $0.5d_{po}$, or more generally kd_{po}. This generalization allows the ash layer to be proportional to the initial diameter, and may apply better to partially consumed particles. Eqn. II.F-5, revised, then becomes:

$$\frac{dm_p}{dt} \cong -D_{oa}(C_{ob} - C_{os})\, A_p\, M_p\, S/(k\, d_{po}) \qquad \text{(II.F-8)}$$

Integrating Eqn. II.F-8:

$$(d_p/d_{po}) = 1 - (C_b/d_{po}^2)t \qquad \text{(II.F-9a)}$$

where C_b = burning rate coefficient, $[(2/k)D_{oa}\, C_{ob}\, M_p\, S/\rho_p]$.

Converting Eqn. II.F-9a in terms of m_p,

$$\left(\frac{m_p}{m_{po}}\right)^{1/3} = 1 - \left[(2/k)\, D_{oa}\, C_{ob}\, S\, M_p/\rho_p\, d_{po}^2\right]t = 1 - (C_b/d_{po}^2)t \qquad \text{(II.F-9b)}$$

From Eqn. II.F-9b, the slope of the plot of $m_p^{1/3}$ vs. t should decrease with increasing initial particle diameter. This equation shows that d_p (or $m_p^{1/3}$) decreases linearly with time, the same as Eqns. II.F-2 and II.F-4, while Eqn. II.F-7 (thin ash layer) showed that $m_p^{1/3}$ decreases as $t^{1/2}$. When $d_p = 0$, $t = t_b$, and Eqn. II.F-9b becomes,

$$t_b = k\, d_{po}^2\, \rho_p/2\, D_{oa}\, C_{ob}\, M_p S \text{ (thick layer)} \qquad \text{(II.F-10)}$$

while for the thin layer, from Eqn. II.F-6:

$$t_b = d_{po}^2\, \rho_p/8\, D_{oa}\, C_{ob}\, M_p S \quad \text{(thin layer)} \qquad \text{(II.F-11)}$$

Interestingly, both the thin and thick ash layer limits show that burning time is proportional to the square of the initial particle diameter (or $m_{po}^{2/3}$), with the burning time for the thick layer twice that of the thin layer (when $k = k_{max} = 0.5$).

<u>Average Mass Reactivity</u> - For the various simple model equations, average mass reactivity can be determined through integration.

To obtain the mass reactivity, R, Eqn. II.F-1 can be re-expressed:

$$R = -\frac{1}{m_p}\frac{dm_p}{dt} = k_c\, A_p\, C_{ob}\, M_p\, S/m_p = \dot{C}_d/d_p \qquad \text{(II.F-12)}$$

Average reactivity, $\overline{R}$, can then be determined:

$$\overline{R} = -\overline{(1/m_p)(dm_p/dt)} = C_d'/\overline{d_p} \qquad \text{(II.F-13)}$$

The mean particle diameter can be analytically determined:

$$\overline{d_p} = \int_o^{t_b} d_p \, dt/t_b \qquad \text{(II.F-14)}$$

Since d_p varies linearly with time (Eqn. II.F-2), the average reactivity is inversely proportional to $d_{p_o}^2$, as in the ash layer theory below.

The average mass reactivity for the ash layer theories can be similarly derived. For the thin ash layer theory:

$$R = -\frac{1}{m_p}\frac{dm_p}{dt} = 12\, D_{oa}\, C_{ob}\, M_p\, S/\rho_p\, d_p\,(d_{po} - d_p) \qquad \text{(II.F-15)}$$

For near complete burnout, $d_p << d_{po}$ and $12\, D_{oa}\, C_{ob}\, M_p\, S/p_p$ is near constant ($3\, C_1$); then, the mass reactivity is:

$$R \cong 3\, C_1/d_p\, d_{po} \qquad \text{(II.F-16)}$$

Then, the average reactivity, $\overline{R}$, is:

$$\overline{R} \cong \overline{(1/m_p)(dm_p/dt)} = \overline{3\, C_1/d_{po}\, d_p}\,(3\, C_1/d_{po})(1/\overline{d_p}) \qquad \text{(II.F-17)}$$

The mean particle diameter can be analytically determined:

$$\overline{d_p} = \int_o^{t_b} d_p \, dt/t_b \qquad \text{(II.F-18)}$$

Substituting for d_p from Eqn. II.F-7, and integrating,

$$\overline{d_p} = d_{po}/3 \qquad \text{(II.F-19)}$$

therefore:

$$\overline{R} = 9\, C_1/d_{po}^2 = 36\, D_{oa}\, C_{ob}\, M_p\, S/\rho_p\, d_{po}^2 \qquad \text{(II.F-20)}$$

This suggests that average reactivity varies inversely as d_{po}^2 or with initial char particle mass, $m_{po}^{-2/3}$.

It has been suggested that (Wang and Wen, 1972):

$$D_{oa} \cong (1 - F_a) D_{om} \qquad \text{(II.F-21)}$$

where D_{om} is the diffusion coefficient of oxygen in the gaseous mixture.

Further (Bird, et al, 1960):

$$C_{ob}\, D_{om} \propto T^{0.6} \qquad \text{(II.F-22)}$$

Thus:

$$\overline{R} \cong 36\,(1\text{-}F_a)(D_{om}\, C_{ob})^o \left(\frac{T}{T^o}\right)^{0.6} M_p S/\rho_p\, d_{po}^2 \qquad \text{(II.F-23)}$$

The superscript, o, refers to a reference temperature. Thus, it is expected that the average reactivity will be related to gas temperature, char ash fraction, char density and initial mass as follows:

$$\overline{R} \propto T^{0.6}(1-F_a)/\rho_p\, m_{po}^{2/3} \qquad \text{(II.F-24)}$$

Average reactivity is not very sensitive to temperature. For a gas temperature range of 1100-1500 K, the average mass reactivity of the particles would vary by about ± 10%, which is generally consistent with experimental measurements.

The value of S comes into question. Amundson and Arri (1978) investigated the details of large char particle gasification including gaseous reactions in the ash layer and in the bulk gas phase. For this study, if indeed, the oxidation rate is controlled by diffusion, then the temperature is not a major variable. Thus, gaseous reaction of fuel and oxygen serves principally to deplete the oxygen concentration. At the lower limit for no gaseous reaction, then at the particle surface:

$$C + 1/2\,O_2 \rightarrow CO, \qquad S = 2 \qquad \text{(II.F-25)}$$

At the other limit, with full oxidation either at the surface or in the ash layer:

$$C + O_2 \rightarrow CO_2, \qquad S = 1 \qquad \text{(II.F-26)}$$

Gaseous oxidation of $CO \rightarrow CO_2$ in the ash layer serves principally to reduce the oxygen supply at the unreacted char surface. While the data measured in this study do not lend themselves to identification of ash layer reactions, the burn time-char mass data can be used to evaluate the burning coefficient.

Ragland and Yang (1985) measured effluent CO and CO_2 concentrations from their convective TGA reactor while chars from four coals of different rank were being consumed in air at about 1000 K. They observed significant quantities of CO and CO_2, with CO_2 generally higher and decreasing and CO lower and increasing with time. While these concentrations can't be taken as those near the char surface, it seems clear that not all of the CO is converted to CO_2 near the char surface.

Thick Ash Layer - For the thick ash layer, the average mass reactivity, is:

$$\overline{R_t} \equiv \overline{(1/m_p)(dm_p/dt)} = \left(\frac{6\, D_{oa}\, C_{ob}\, M_p S}{k\, d_{po}}\right)\left(1/\overline{d_p}\right) \qquad \text{(II.F-27)}$$

Formal integration of Eqn. II.F-9 after the manner of Eqn. II.F-18 shows that $\overline{d_p} = 0.5\, d_{po}$ Thus:

$$\overline{R_t} \equiv 12\,(1\text{-}F_a)\, D_{om}\, C_{ob}\, S/k\, d_{po}^2 \qquad \text{(II.F-28a)}$$

$$\equiv 12\,(1-F_a)(D_{om}\, C_{ob})^0 \left(\frac{T}{T^o}\right)^{0.6} S/k\, d_{po}^2 \qquad \text{(II.F-28b)}$$

Comparing Eqn. II.F-28b with the thin ash layer result shows the same functional dependence, but an average reactivity of 1.5 times less for the thick ash layer, compared to the thin ash layer, when $k = k_{max} = 0.5$.

Thus, in either limit, a plot of:

$$\overline{R} \text{ vs. } (1\text{-}F_a)\, T^{0.6}/\rho_p\, m_p^{2/3} \qquad \text{(II.F-29)}$$

should produce a linear result.

It is readily acknowledged that these correlative methods are, at best, approximations to a very complex burning process. Several processes have been neglected in one treatment or another, such as bulk gas diffusion, surface reaction, char pore diffusion, ash crumbling, ash layer gaseous reaction ($CO + O_2 \rightarrow CO_2$), non-sphericity of particles, particle fragmentation and non-linear concentration gradients within the ash layer.

Data Correlation and Discussion

Comparisons of Burning Times - From the measurements, estimated burning times for these 0.5-1 cm diameter particles of various coals are in the range of 8 minutes to 2.5 hours. Corresponding burning times for liquid droplets of initial comparable size are in the range of 0.5-1 minute, or up to two orders of magnitude faster. The data for 0.3 cm diameter bituminous coal chars correlated by Essenhigh (1981) have burning times in the range of 3-5 minutes. Extrapolation of these data suggest that 1 cm diameter char particles would burn out in about 0.5 hour. Burning times for this study are comparable to, though possibly somewhat longer than for this bituminous char. Differences in ash percentages, ash layer behavior and reaction temperature could explain the differences in burning times. Burning times observed by Ragland and Yang (1982) for 0.4-1.2 cm diameter for single particles of four coal types varied from 2-6 minutes, including devolatilization times in their convective TGA. Shorter times here, are likely due, principally to convective air flows, and are comparable to the shortest burning times of this study.

Time-mass dependence - Figs. II.F-2a and b compare the time dependence of mass loss for Set I of the data. The thin-layer theory suggests that a plot d_p (or $m_p^{1/3}$) vs. $t^{1/2}$ should be linear (Eqn. II.F-7d). This is clearly not the case, as shown in Fig. II.F-2b. The thick layer theory suggests that a plot of $m_p^{1/3}$ vs. t should be linear (Eqn. II.F-9b) as do the oxygen diffusion (Eqn. II.F-2) and surface reaction (Eqn. II.F-4) options. The data for set I shown in Fig. II.F-2a are clearly linear. Data for the balance of the tests were shown in Figs. II.F-3 to 11, all plotted in linear form as $m_p^{1/3}$ vs. t. The linear lines in Figs. II.F-2a, 3 to 5 are least squares plots. Statistical correlation coefficients were 0.97 or higher in every case, and above 0.99 in most of the cases.

For many of the initial experiments, towards the end of burning, when values of $m_p^{1/3}$ were below about 0.4 (over 90% consumed), the measured char mass values fell somewhat below the linear correlation line, suggesting more rapid consumption. Particle fragmentation may be a factor in this region. It should also be noted that ordinate values of $m_p^{1/3}$ as small as 0.1 imply m_p values as small as 1 mg, which is in the range of weight measurementsensitivity, where weight loss is taken as the difference in weights of thesample plus the crucible at two different times. Possibly for this reason,some of the data points at low ordinate values of $m_p^{1/3}$ vary from the straight line correlations. About five such data points were not included in the correlative lines of Figs. II.F-2 to 6.

Table II.F-7 provides a summary of the decay slopes for the initial 35 sets of experiments, together with test conditions and coal and char properties. Slopes for all experiments vary from -0.0044 g/m to -0.0172 g/min. This variation is caused principally by initial char size. Variation in reaction temperature between 1270 K and 1470 K had only a small effect on reactivity as illustrated in Fig. II.F-12 and summarized in Table II.F-7, though it does appear that increasing temperature increases the slope somewhat and consequently, the reactivity.

For the thick ash layer theory, the slope of Figs. II.F-2a, 3 to 5 is, from Eqn. II.F-9b:

$$1-\left[(2/k)D_{om}(1-F_a)\,C_{ob}\,S\,M_p/\rho_p d_{po}^2\right]t = 1-\left(C_b/d_{po}^2\right)t \qquad \text{(II.F-9b)}$$

TABLE II.F-7

SUMMARY OF LARGE COAL CHAR PARTICLE BURNING RATE PARAMETERS

Sample ID	Furnace	Coal Type	Initial Char Mass (g)	Char Ash $(1-F_a)$	Burning Rate Slope x 10^2 (g/min)	Burning Rate Coefficient, C_h (cm^2/min)	Approx. Temp. (K)
I - 1	Meker	Utah bit.	0.189	0.945	-1.19	0.014	1150
2			0.287	0.935	-0.99	0.014	
3			0.345	0.938	-1.12	0.015	
4			0.349	0.941	-1.13	0.016	
5			0.244	0.949	-1.20	0.015	
6			0.166	0.933	-1.33	0.014	
II - 1	Muffle	Utah bit.	0.565	0.872	-1.07	0.018	1230
2			0.438	0.896	-1.21	0.018	
3			0.661	0.913	-0.98	0.016	
4			0.435	0.899	-1.14	0.016	
5			0.425	0.862	-1.34	0.018	
6			0.468	0.902	-1.03	0.015	
III - 1a	Muffle	Utah bit.	0.571	0.903	-1.16	0.019	1270-1320
2a			0.262	0.936	-1.27	0.016	
3a			0.237	0.913	-1.32	0.023	
4a			0.596	0.873	-1.18	0.020	
1b	Muffle	Utah bit.	0.316	0.913	-1.62	0.021	1320-1370
2b			0.445	0.918	-1.18	0.018	
3b			0.555	0.891	-1.19	0.020	
4b			0.556	0.895	-1.09	0.019	
1c	Muffle	Utah bit.	0.614	0.841	-1.10	0.019	1370-1420
2c			0.505	0.874	-1.15	0.019	
3c			0.253	0.900	-1.64	0.022	
4c			0.644	0.921	-1.15	0.019	
1d	Muffle	Utah bit.	0.248	0.803	-1.06	0.014	1420-1470
2d			0.371	0.916	-0.96	0.014	
3d			0.155	0.912	-1.72	0.020	
4d			0.154	0.933	-1.65	0.017	
IV - 1a	Meker	Colo. bit.	0.577	0.886	-0.90	0.016	1150
2a			0.689	0.881	-0.92	0.016	
3a			0.437	0.817	-1.17	0.018	
1b	Meker	Ill bit.	1.040	0.807	-0.44	0.012	1150
2b		ND Lig.	0.905	0.923	-1.07	0.024	
3b		Wyo. subb.	0.561	0.889	-1.34	0.030	
4b		Pitt. #8	0.106	0.946	-1.23	0.017	

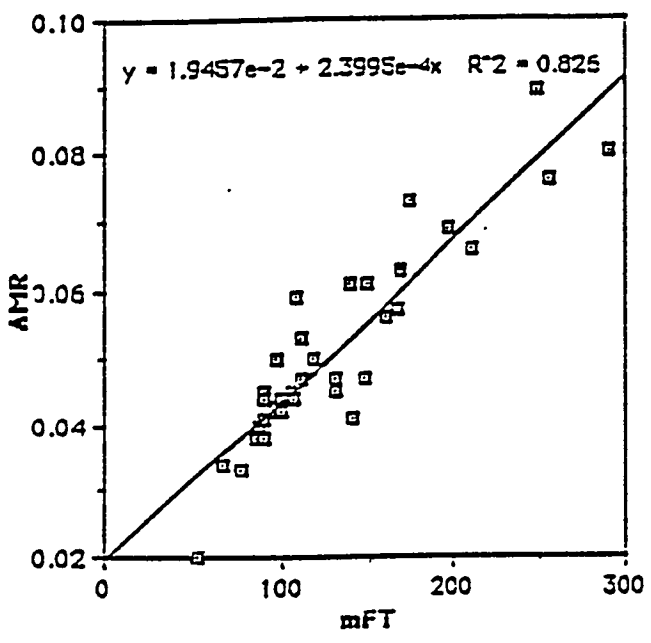

c. Average Mass Reactivity vs. $(1-F_a)T^{0.6}/m_p^{2/3}$

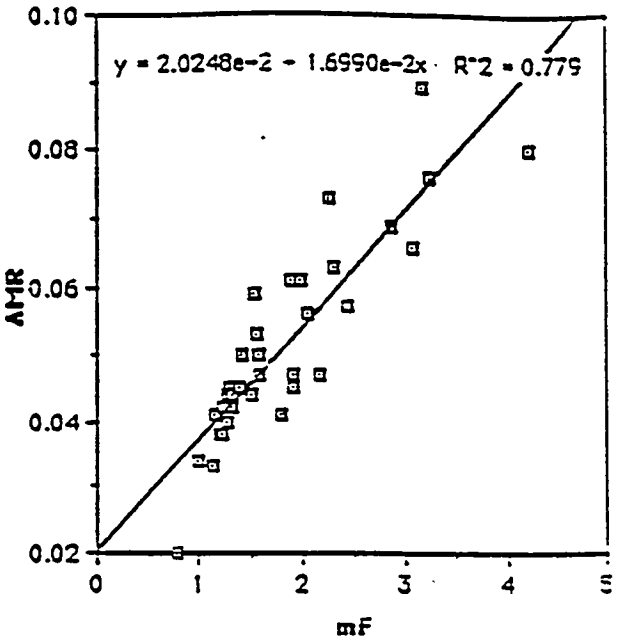

d. Average Mass Reactivity vs. $(1-F_a)/m_p^{2/3}$

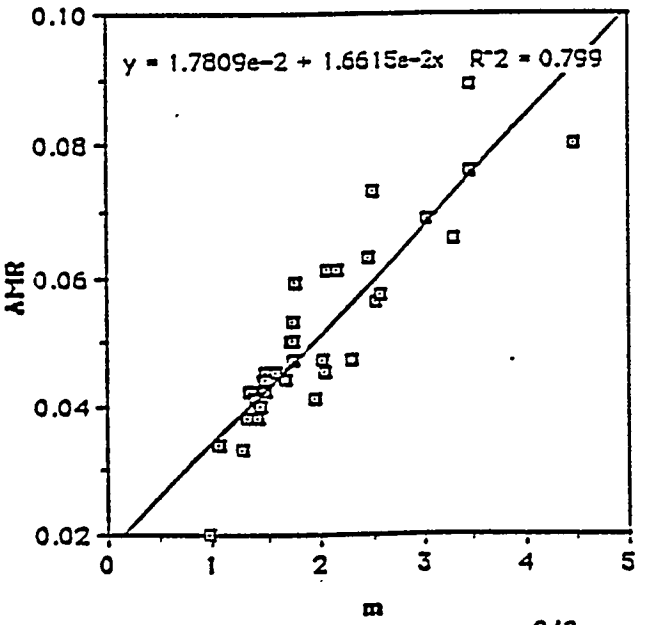

a. Average Mass Reactivity vs. $m_p^{-2/3}$

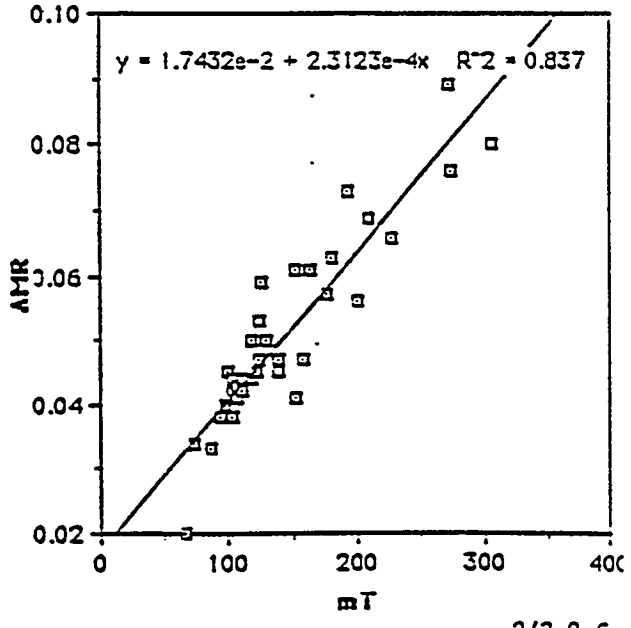

b. Average Mass Reactivity vs. $m_p^{-2/3}T^{0.6}$

Figure II.F-12. Various options in correlating average mass reactivity with reaction variables of initial char mass, fraction of ash and temeprature, from thick ash layer theory. $m = m_p^{-2/3}$; $F = (1-F_a)$; $T = T^{0.6}$.

C_b is termed the burning rate coefficient and is thought to be near constant for a given coal, since its various factors, k D_{om}, $(1-F_a)$, S, M_p, ρ_p can be considered near constant. The values of C_b are reported for each of the 35 sets of experiments in Table II.F-7. Average values of C_b for each coal char from Table II.F-4 are:

Coal Type	% Coal Ash	No. of Test Sets	C_b (cm^2/hr)
1. Utah bituminous	6.3	28	0.017
2. Colorado bituminous	4.3	3	0.016
3. Illinois 6 bituminous	10.4	1	0.012
4. North Dakota Lignite	2.6	1	0.024
5. Wyoming subbituminous	6.4	1	0.030
6. Pittsburgh bituminous	6.0	1	0.017

C_b values may vary somewhat with temperature as shown in Table II.F-4. While this correlative method provides a consistent summary of the data, it does not verify the mechanism, since it was based on oxygen diffusion through the ash layer, which was shown to be a secondary factor. However, the form the correlative equation (Fig. II.F-9b) is the same when the controlling process is bulk diffusion of oxygen (See Fig. II.F-12b).

The measured C_b value can, in principle, be compared with the computed value from Eqn. II.F-9b. However, there is uncertainty in the ash fraction of the char, F_a, the stoichiometric coefficient S (between 1 and 2), the char molecular weight (near 12 when char is mostly carbon), the char density (less than for the coal, through loss of volatiles and by swelling). The constant k, which can theoretically vary from 0 - 0.5, is least known. In the limit, when the ash layer thickness can be the entire initial char particle diameter, k = 0.5. For a particular coal, with 10% ash in char, 40% (ash free) volatiles lost during devolatilization, a coal density of 1.3 g/cm^3, a reaction temperature of 1200 K, and S = 2 (CO product), a realistic computed value of k of 0.12 results from Eqn. II.F-9b. This smaller value of k is indicative of the fact that ash layer diffusion does not dominate the oxidation rate process. Indeed, the data very clearly show that, while the ash layer has some impact on oxidation rate, supplying oxygen to the particle surface is the most important resistance except at the lowest temperatures.

Average reactivity - Another way to interpret the data is through time-averaged reactivity, which was computed experimentally as:

$$\overline{R} = \sum_{1}^{n}\left[\left(1/m_p\right)\left(\Delta m_p/\Delta t\right)\right]/n \qquad \text{(II.F-30)}$$

n is the number of time increments and m_p is the particle mass during the burning increment (taken as the starting mass in each time increment). Theoretically, $\overline{R}$ for either the thick or thin ash layer theory should vary linearly with the quantity:

$$\overline{R}\alpha(1-F_a)T^{0.6}/\rho_p m_p^{2/3} \qquad \text{(II.F-29)}$$

Thus, average reactivity does not distinguish between the two simple theories. Further, for sample diffusion (Eqn. II.F-2) or surface reaction (Eqn. II.F-4), $\overline{R}$ is still expected to vary inversely with $m_p^{2/3}T^{0.6}$ (See Fig. II.F-12B).

For the first 35 data cases, Fig. II.F-12 provides a plot of average reactivity vs. $m_p^{-2/3}$. Various options are shown in Figs. II.F-12a-d. In Fig. II.F-12a, $\overline{R}$ vs. $m_p^{2/3}$ is plotted, neglecting variations in ash percentage, temperature and char density. Initial particle mass is clearly the most important variable in these tests, since there is a general linear trend in the Fig. II.F-7a. The straight line is a least squares fit of the data, with a correlation coefficient of 0.8. However, neither coal ash percentage (6-15%) nor temperature (1150 - 1475 K) varied greatly in these tests. Other alternatives from Eq. 22 are shown in Figs. II.12b-d and do show some improvement in correlation quality. The scatter can be due to uncertainties in parameters F_a, ρ_p, T, and to the model assumptions in the simple theory.

Effects of Multiple Particles - The burning time of an ash-free char particle of 0.60 g. in the absence of forced air convection was ~ 50 minutes. The burning time for a smaller particle ~ 0.15 g. was ~ 10 minutes. From such data it would be expected that four such small particles placed together in a crucible would have a burning time of ~ 10 minutes if there were no particle interactions. Several experimental tests reported above have been made to provide insight into this effect, as shown in Figs. II.F-9 to II.F-11. Results consistently show that total mass principally affects burn time and not significantly numbers of particles or surface area. This could only be so if oxygen delivery to the vicinity of the particles was governing the oxidation rate. These data clearly show that neither ash layer, nor O_2 diffusion to the particle surface, nor surface reaction all of which are surface area-dependent, are controlling the oxidation rate. Closely placed particles do interact substantially in these experiments. Similar behavior might be expected in commercial fixed beds in regions of low bulk oxygen concentration.

Effect of Temperature - In the correlation of temperature effects from the data in Table II.F-7, temperatures in the range of 1170-1430 K did not appear to have significant influence on the average mass reactivity as shown in Fig. II.F-12c. To further clarify effects of particle temperature, several experimental tests over a wider temperature range were made as reported above. At lower temperatures, it was expected that there may have been some dependence of the reactivity on chemical kinetics. Levenspiel (1972) has discussed an approach for determining the reaction rate dependence on diffusion and/or chemical kinetics for gas/solid reactions. This is accomplished with a graph of the rate of mass loss vs temperature. In order to make a graph of $-dm_p/dt$ as a function of temperature, the rate of mass loss was evaluated when the char particle was about half the mass of the original particle. The slope of the $m^{1/3}$ vs t graph was determined from the middle data points (ignoring the first and the last data points). This is taken from the approximate burning time of Table II.F-4. In this range, m_p vs t was plotted and $-dm_p/dt$ evaluated at m_p equal to half the original mass. Then these slopes were graphed as a function of temperature in Figure II.F-13. Particle temperature has a substantial effect on char burning rate for temperatures below about 1200 K (900° C).

Effect of Air Flow - The sharp decrease in burning time as a large particle was placed in a shallow flat crucible instead of a standard crucible (Figs. II.F-10 and 11) indicated that natural convective was providing only limited oxygen for the high temperature combustion of the char particle. The use of an alternative simple reactor in which the flow of oxygen was controlled and measured provided a quantitative indication of the oxygen availability. A calculation shows that 0.21 moles of oxygen are available if the air flow rate is 1.0 liter/min. for 30 minutes. A 0.2 gram char particle requires 0.017 moles of oxygen if all of the mass is assumed to be carbon and is burning to CO_2. The flow pattern of air passed the char particle will not permit all of the oxygen to be used in the chemical reaction and it is helpful to consider the ratio of oxygen required to that available - 0.017/0.21 = 0.08. A similar calculation for the first five minutes of oxidation with a mass loss of 0.1 gram and more oxygen is consumed gives a ratio of 0.24. A flow of 10 liters/min. was required to give a burning time of 8 minutes for a 0.2 gram char particle. The calculated ratio was approximately 0.03. These may represent the approximate limits for reduction of burning time for the reactor configuration of this simple experimental set-up for utilization of available oxygen subject to the experimental conditions.

Conclusions

Two simple experimental methods involving single or multiple char particles inside a crucible or a basket in either a muffle furnace or Meker burner flame or placed in a ceramic tube with convective air flow, have been used to provide burning rate data of large (0.2 - 1 g) char particles from five coals of varying rank in air at ambient pressure over a range of temperatures from 700-1475 K. Test variables included initial char mass, oxidation temperature, coal type, ash layer accumulation and air flow rate. One hundred fifty experiments were conducted. The cube root of char mass (or effective diameter) was shown to decline linearly with time for all experiments except toward the end of burnout, while total burning time was proportional to the square of the initial effective diameter. Burning times varied substantially with initial sample size, air flow rate, somewhat with coal type, and linearly with oxidation temperature for temperatures below about 1200 K. As the char particles were consumed over burn times of 8 minutes to 2.5 hours, an ash layer often accumulated around the remaining char.

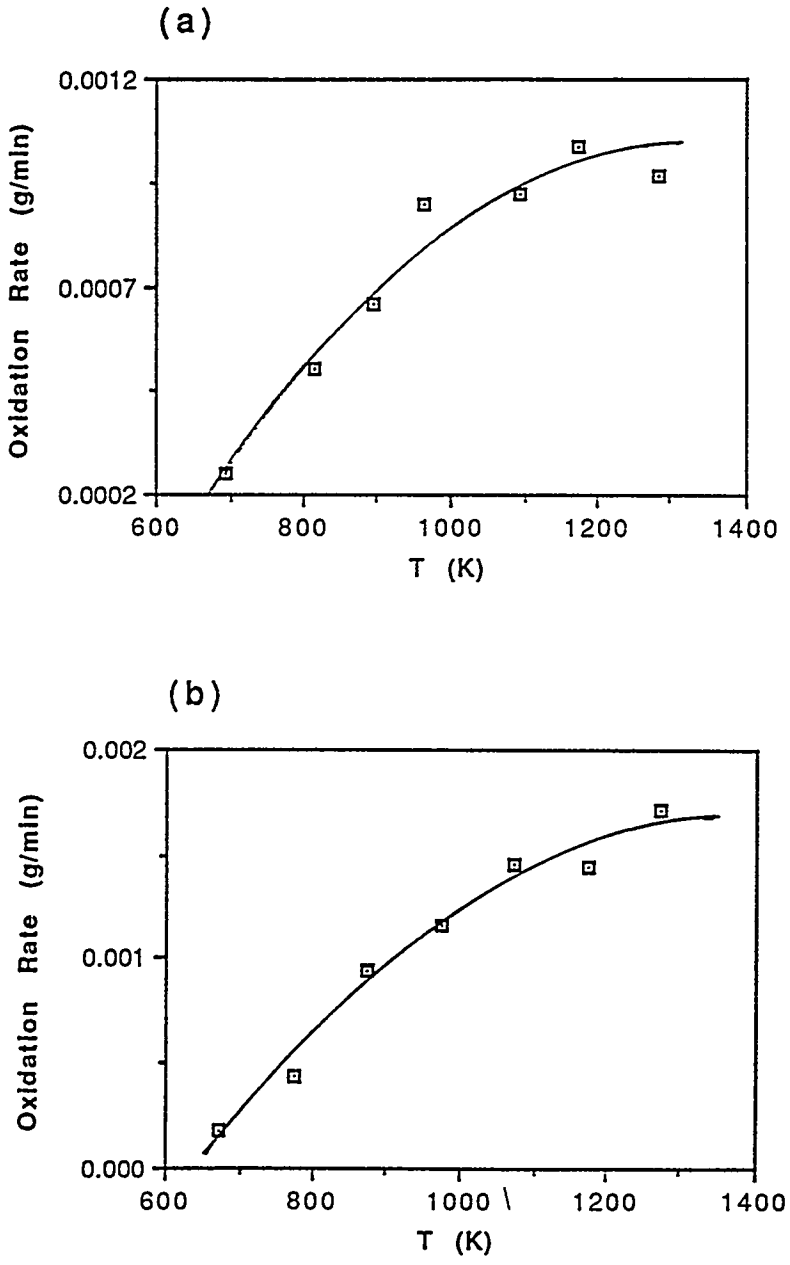

Figure II.F-13. Effect of particle temperature on average reactivity for (a) Illinois char and (b) Utah char.

The linear variation of diameter with time observed for all of the coal types agrees with more than one simple model formulation.All alternatives show that total burning time should vary as the square of the initial diameter, and also that average reactivities should vary as $\overline{R} \propto m_o^{-2/3}$. Average reactivity data, when plotted in this manner do show a general linear dependence, though the data scatter sufficiently to obscure the dependence of average reactivity on char ash fraction (F_a) or char density (ρ_p). Results clearly show the importance of convective oxygen flow and of temperature at lower temperatures.

Oxidation at Elevated Pressures in HPCP Reactor

Review of Facilities - In the original proposal for this subtask a test facility consisting of a TGA unit encased in a high pressure shell was suggested. This suggestion followed the essential features of an experimental unit constructed by Sears, Maxfield and Tamhankar (1982). This facility is a pressurized thermobalance designed to operate to 1000 psig at intermediate temperatures or to almost 2000 K at one atmosphere pressure. The maximum conditions attainable simultaneously were reported to be 1570 K at 450 psig. Results were given for a lignite coal reacting with CO_2. The main objective for this equipment was to study coal pyrolysis and gasification reactions continuously at high temperatures and pressures. A significant observation was that "data of this nature are practically nonexistent for gasification reactions."

In subsequent papers (Tamhankar, Sears and Wen, 1984 and Sears, Tamhankar, Radman and Wen, 1985), this facility has been used to study char oxidation at up to 16 atmospheres at 1170 K reacting in CO_2 and H_2O. No data on reaction in oxygen were reported. Parik and Mahalingan (1987) report the use of a fixed-bed reactor to simulate conditions in the devolatilization zone of a Lurgi-type gasifier. The entering reactive gas contained 2% O_2 and 30% steam. The operating conditions were 600-800 K at a pressure of 30 psig.

Kalson and Briggs (1985) studied the devolatilization of a single lump of coal (15 grams) at 100 kPa (14.7 psia) in the temperature range 700-850 K. The devolatilizer consisted of a 5.25 cm I.D. stainless steel pipe with the sample held in a 4.l cm O.D. stainless steel screen basket. The basket was suspended on a chain that was raised or lowered within the devolatilizer pipe by means of an electrically controlled winch. It was indicated that the design of the unit could operate at a pressure of 1.7 MPa. Also noted is the comment "little systematic information is available for tar production from fixed-bed gasifiers." Nuttall, Stoddart, and Chen (1979) reported on a bench scale single-particle reactor whose internal conditions could be both controlled and monitored by a minicomputer. Coal samples (2.5 cm diameter) were used in devolatilization tests. "The coal particle was place in a wire mesh basket attached to the force transducer by a stainless steel rod." Temperatures were measured by microthermocouples attached to the coal particle.

The references briefly reported above are concerned with thermobalances operating at high pressures for use in coal combustion and gasification. Extension of this literature survey to the use of thermobalances in other types of chemical reactions has given additional information for the design of the experimental unit for this subtask.

Feldkirchner and Johnson (1968) described the construction of a high pressure thermobalance for study of iron ore in cycles of oxidation and reduction. They built this thermobalance to operate "at elevated pressures and temperatures because none were available commercially." The high pressure system consisted of two tubes joined together with the lower tube placed vertically in an electric furnace. The upper tube contained a microforce transducer of 10 g. capacity for weight measurement. A gold suspension chain is attached on one end to a windlass and on the other end to a nickel wire which supports the sample in a nickel mesh basket. The reactor tube was rated for heating to 1200 K. The complete system could be taken to a pressure of 100 atm.

Bae (1972) describes a simple thermogravimetric apparatus which was used at pressures up to 70 atm. The device was dumbbell shaped with the furnace at one end and the balance unit at the other. A microforce transducer was used as the weighing device with an accompanying transducer amplifier-indicator to report and record the output. The maximum sensitivity of the transducer was approximately ± 1 mg. The system reported stability in the thermograms at all pressures tested. The system tested the oxidation (with air) and evaporation of crude oil at temperatures up to 900K (600° C) and at pressures up to 70 atm.

Williams and Wendlandt (1973) reported the use of a high pressure thermobalance to study thermogravimetric curves of $BaBr_2 \cdot 2H_2O$, $CuSO_4 \cdot 5H_2O$ and $NaHCO_3$ at different pressures of nitrogen and/or carbon dioxide. The thermobalance was constructed by placing a DuPont Model 950 balance into a stainless steel enclosure. Maximum operating conditions were 500 atm (N_2) and 800K (500°C). A change in sample mass due to a gas buoyancy effect as the pressure increased was easily corrected.

Dobner et al (1976) discussed a high pressure thermobalance with maximum operating capabilities of 30 atm, 1400K (1100°C), with corrosive atmospheres and steam partial pressures up to 20 atm. A modified DuPont 950 TG was encased in a stainless steel pressure vessel. This modification of the TG was necessary to avoid damage by corrosive gases or steam. The reactions studied were the cyclic CO_2-acceptor reaction for half-calcinated dolomite and the cyclic H_2S absorption and regeneration reaction for half-calcinated dolomite. Two problems were associated with this system. First, at I atm the baseline weight continuously increased with temperature at a rate of ~ 0.07 mg/100K. Second, the baseline weight increased with total gas flow rate at a rate of ~0.08 mg/100 ml at 300K and ~ 0.19 mg/ 100 ml at 1200K. These effects were caused by aerodynamic drag forces exerted by reacting gases flowing over the sample pan.

Li and Rogan (1978) reported the construction of a thermogravimetric system for corrosive environments at high pressures and temperatures. The reactor had a DuPont 951 Thermogravimetric Analyzer encased in a stainless steel high-pressure vessel. The maximum operating conditions were 60 atm and 1100^{0}C with corrosive gases. Thermogravimetric studies were performed on the calcination of dolomite in CO_2/N_2 atm and the sulfidation of dolomite in H_2S/N_2 gas mixtures. A serious problem with this system concerns the initial transient readings of either sample temperature or gas composition.

Ghodsi et al (1979) describe a pressurized thermobalance featuring two symmetrical pans. The use of two symmetrical pans avoids thermogravimetric errors under pressure such as Archimedes' forces, viscosity forces and thermal gradient forces. A Sartorius 4406 thermobalance was modified for use at pressures up to 50 atm of H_2 ant temperatures reaching 1300K. The balance was tested using the hydrogenation of a lignite char as a preliminary application.

Forgac and Angus (1979) constructed a pressure chamber which held a Perkin-Elmer AM-1 autobalance within the walls. The sample is suspended in the hot zone with a wire (15cm length) made from nichrome, platinum and iridium. Sample holders were cylindrical crucibles made from 0.025 mm platinum foil. The thermobalance was run as a static system but is capable of dynamic flow. Experiments were done at temperatures of 1633K and 70 atm. Although the design calculations allow for 2000 K and 136 atm.

Treptau and Miller (1987) describe a novel thermobalance. The reactor is internally heated and the entire reactor is weighed on a Mettler PE-360 top-loading electronic balance with a capacity of 60 ± 0.001 g. The solid sample can be a fixed or fluidized bed through which reactant gas can flow. Gasification tests with CO_2 and O_2 were performed on coconut charcoal samples. Experimental samples were 1250K and 41 atm with a balance sensitivity of ± 10 mg for a 2 g sample. The purpose of weighing the entire reactor was to provide direct measurement of sample temperature and elimination of external mass-transfer resistances via gas flowing through the sample bed. Nevertheless, a large scale drift on the balance of 0.1-0.5 g/hr was noticed when the gas flow rate was changed or pressure was increased during heating of the sample.

Gardner, et al (1974) describes the use of a mass transducer attached to a balance arm with a full scale range of 6 grams. The transducer was used to study the kinetics of catalyzed and non-catalyzed coal char hydrogasification. This systems shows stability at temperatures up to 1300K and pressures up to 68 atm.

Gaissmaier and Agarwal (1990) studied the drying and devolatilization (under combustion conditions) of several low-rank coals in large particle sizes in fluidized bed combustion. The particle sizes ranged from 0.9 - 5.0 mm. They found that drying and devolatilization can be modeled but more experimental work needs to be done to improve their model. Factors that need to be analyzed include a more rigorous determination of the wet-dry interface temperature and the effects of heterogeneous

ignition and combustion of volatiles trapped in the solid matrix of the large particles prior to the formation of the volatiles flame.

These references served as the basis for the discussions upon which the design of the experimental system for the fixed-bed oxidation studies of this subtask was based. The objectives of the design were: (a) to follow the mass loss of the sample to an accuracy of 1-2 mg; (b) to easily manipulate pressures and sample access for quick change of samples; and (c) to support the sample rigidly in the path of the hot gas flow.

Facility Modification

Two design features were considered for the oxidation of large particles at elevated pressures. One design would have given a facility in which the sample basket would have been lowered by a winch into the reaction zone from a micro-balance through a connecting pipe. The micro-balance assembly would have been enclosed in a large steel bell for applying pressure. The other design was a unit in which the sample would come in horizontally through one of the optical access ports of the existingHPCP reactor of Subtask 2b. This design would make use of the technology already developed for the reactor and preheater features. Also the use of the rigid long small-bore ceramic tube for connecting the sample basket to the force transducer would permit a more accurate and more stable positioning of the sample in the reactor. The opening in the horizontal pressure shell provided easier access to the cantilever beam for changing samples. Accordingly the cantilever balance approach was selected. The design and construction followed.

The Cantilever Balance Attachment (CBA) shown in Fig. II.F-14 has been designed to give mass loss readings and sample placement during oxidation experiments using 2.5 -7.5 mm coal particles. The three components of the unit are: a) a balance; b) a three-axis slide; and c) a heat shielding water-cooled valve. The entire assembly will be bolted directly to the HPCP reactor of Subtask 2b.

The balance unit measures the mass loss of the particles as they burn in the HPCP reactor. It consists of a 30 gram force transducer, an 1/8 inch ceramic cantilever rod, and a platinum wire mesh sample basket. The basket is secured to the ceramic rod and inserted through an access port on the HPCP reactor by the stepper motor. The force transducer is mounted on a mobile platform. This platform can move in all three axis directions. The platform moves in and out of the HPCP reactor with the stepper motor and moves horizontally and vertically with manual, external positioners. This motion is accurate to ±0.001 in.

The CBA has been designed to test successive samples without altering the conditions of the HPCP reactor. This is accomplished by closing an aluminum gate valve that separates the CBA from the HPCP when changing coal samples. The valve is mounted between the HPCP and the CBA housing. Cool water is circulated through the valve to maintain constant temperature in the CBA. With the valve in the open position, the cantilever rod and platinum mesh basket can extend through the opening. A temperature probe has been inserted through the top of the HPCP reactor to obtain gas temperature readings during each run. A pressure gauge has been installed on the CBA because the CBA can be pressurized and depressurized independently of the HPCP.

Early in this study a few tests were made with the load cell (force transducer) to study its properties. Measurements of maximum load, stability, and sensitivity were made as function of lever arm length. Lever arms of 10, 15 and 20 cm were studied. The maximum loads measured were 25, 22 and 19 g. respectively. The drift of the transducer was a maximum at 10 mg/hr showing good stability at maximum loads. The sensitivity was approx. 3 mg per division at each length.

Mass-loss tests were then performed on the force transducer by hanging a small pipet on the end of the cantilever beam. One end of the cantilever beam was inserted into a stainless steel block fixed in the side of the force transducer. The block was necessary to eliminate problems that arose due to twisting the strain gauges in the transducer. The twist caused the transducer to give incorrect mass readings. To perform the tests, a quantity of dense alumina was placed in the pipet. A reading on the transducer was recorded and the alumina was then allowed to fall from the pipet. The alumina was then measured and another reading was taken on the transducer. Thus, the total mass of alumina that

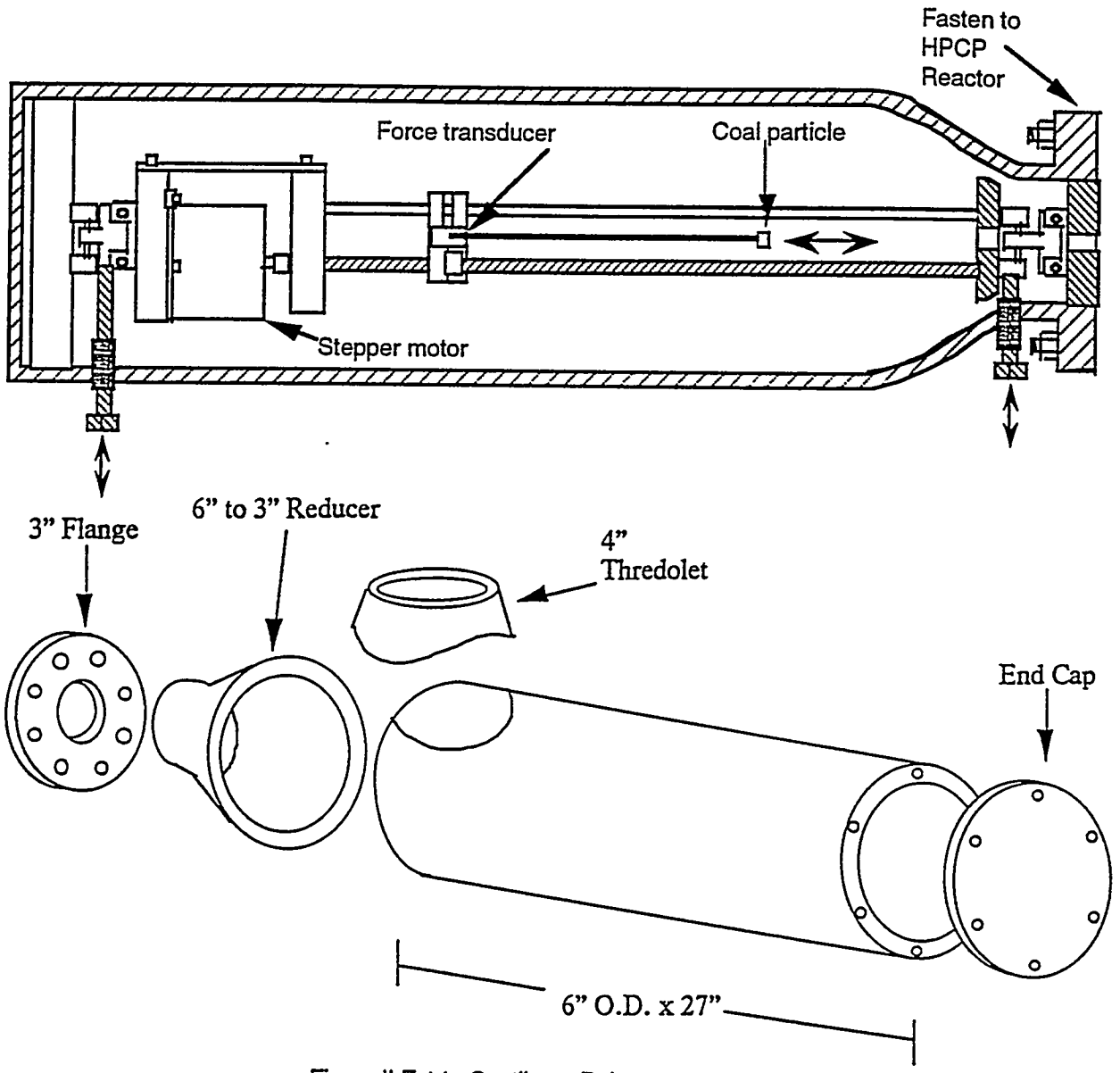

Figure II.F-14. Cantilever Balance Attachment

escaped the pipette was known and the total number of counts read by the transducer was determined from the before and after readings. The results of tests perfomed at 10 cm from the transducer are recorded in Table II. F-8. These results show that the transducer gives good mass-loss measurements at the desired sensitivity and accuracy.

Test Program and Data - In all, 56 tests were completed using two coals, 40 with the Utah Blind Canyon coal, a high volatile bituminous B (HVBB) coal, and 16 with a North Dakota lignite (L). A 2^4 statistical design, consisting of sixteen tests, was duplicated for the Utah coal, while eight additional tests were performed at two of the conditions to check repeatability. The four parameters examined were (1) pressure, (2) temperature, (3) flow rate, and (4) particle size. Table II.F-9 shows the experimental program and the value of each parameter. These parameters were selected in order to simulate atmospheric tests found in the literature. An additional 16 tests (2^4 statistical design) were performed using North Dakota

TABLE II.F-8.

EXPERIMENTAL RESULTS FROM TRANSDUCER MASS-LOSS TESTS

Scale Factor	Total Mass of Alumina (grams)	Total Counts on Transducer	Counts/gram
1	3.333	395	118.5
1	1.670	202	120.9
1	1.270	154	121.2
2	3.318	818	246.5
2	4.111	1000	243.2
2	2.525	614	243.1

TABLE II.F-9

EXPERIMENTAL 2^4 TEST PROGRAM AND DATA FOR UTAH BITUMINOUS (HVBB) COAL AND NORTH DAKOTA LIGNITE (L) COAL

Test Case	Pressure (kPa)	Gas Temp (°K)	Reynolds Number	Particle Mass (g)	Burning Time (s)		Oxidation Time (s)	
					(HVBB)†	(L)	(HVBB)	(L)
1	101	900	63	0.1	255	327	244	313
2	507	900	63	0.1	185	143	162	139
3	101	1200	63	0.1	271	-	251	-
4	507	1200	63	0.1	167	130	149	119
5	101	900	126	0.1	257	180	246	167
6	507	900	126	0.1	175	168	163	156
7	101	1200	126	0.1	264	232	247	205
8	507	1200	126	0.1	195	137	178	123
9	101	900	63	0.2	369	470	341	446
10	507	900	63	0.2	-	195	248	185
11	101	1200	63	0.2	-	-	319	-
12	507	1200	63	0.2	258	207	239	189
13*	101	900	126	0.2	453	421	427	406
14*	507	900	126	0.2	299	229	276	208
15	101	1200	126	0.2	323	346	290	312
16	507	1200	126	0.2	273	207	252	188

* Indicates four additional HVBB runs at that condition.

†Average value of 2 to 6 runs per test case.

lignite (L) coal but where not duplicated. Oxidation times and burning times were occasionally discounted due to excessive particle fragmentation prior to burnout (possibly due to particle preparation). Results for these cases are not reported in Table II.F-9.

Effects of particle size - The two particle sizes were prepared by fracturing a lump coal into several pieces. These pieces were then formed, using pliers, to approximate spheres. Because the simple device tests determined mass to be a major factor, the weight of each particle was either 0.20 grams (approximately 8 mm diameter) or 0.10 grams (approximately 5.5 mm diameter). The trends obtained were similar to the trends obtained with the simple device, as shown in Fig. II.F-15. Figure II.F-15a shows the entire combustion process including heat up, devolatilization, oxidation, and decay. The decay zone typically starts at $m_p^{1/3}$ of about 0.2, which is at the point of about 99% particle burnout. Figure II.F-15b shows just the oxidation portion prior to final burnout. On Fig. II.F-15a the last few points of the curve deviate from the linear trend, consistent with observations from the simple device. These points appear on virtually all of the tests, but because they lie within the error of the force transducer they were omitted on several of the following graphs. These points will be further examined in the Effects of coal type section.

Normalizing the mass axis by dividing by the initial coal mass to the one-third power and normalizing the time axis by dividing by the total burn time results in straight lines for both particle sizes that have the same slope, as shown in Fig. II.F-16.

Effects of pressure - Several tests were performed at two pressures of 101 kPa and 507 kPa (1 atm and 5 atm), while a limited number were performed at 760 kPa (7.5 atm). Figure II.F-17 shows the typical trends found at these pressures. The 507 kPa and 760 kPa tests differed little in burning rate, while they both were different from 101 kPa tests. One of the most notable differences was the burning time, the time between particle ignition and particle burnout. The burning time was obtained using video tape of the tests. The camcorder recorded 30 frames per second and, therefore, 1/30 s was the accuracy of the time. For the 507 kPa and the 760 kPa tests, coals burned in a shorter amount of time (300 s) than for the 101 kPa tests (450 s). Closer examination of all of the tests with variable pressure (Fig. II.F-18) shows that the oxidation time was significantly reduced by increasing pressure. Particle surface temperature was recorded using a pyrometer and strip chart recorder for the higher gas temperature cases. Due to the sensitivity of the pyrometer, surface temperature measurements were only obtainable at the higher gas temperature (1200 K). Fig. II.F-19, a representation of the strip chart recorder, shows that the particle surface temperature during oxidation was approximately 100 K hotter at 507 kPa than at 101 kPa. Figure II.F-20 shows that the plot of $m_p^{1/3}$ vs time remains linear during oxidation at 507 kPa.

Effects of Flow - Two air flow rates, equivalent to particle Reynolds Numbers of Re=63 and Re=126, were tested. Figure II.F-21 shows that there was little effect of Reynolds Number on the burning time of the Utah coal at 507 kPa. Figure II.F-22 shows the effect of air flow rate on the oxidation time and burning time for several Utah coal particles. The effects of flow are uncertain, due to the low number of runs.

Effects of Coal Type - Utah Blind Canyon bituminous coal (HVBB) and North Dakota lignite coal (L) were the two coals tested. Figure II.F-23 illustrates typical differences between the two coals. The burn-out time is somewhat longer for the Utah coal. More mass loss occurs during the devolatilization stage for the lignite coal, resulting in less char to be oxidized.

Smoother burn-out was noticeable during the testing process for the North Dakota coal and was also evident on a video tape of the tests. The completion of burning of the Utah coal was more abrupt, while the North Dakota coals grew dimmer more slowly toward completion of burnout. This observation was also observed from particle surface temperature, represented in Fig. II.F-24. Particle surface temperatures during oxidation at higher pressure were about 200 K hotter than the gas temperatures and remained steady during oxidation until the later stages. The bituminous coal char temperature was hotter than the lignite coal char temperature by about 50 K, presumably due to the higher heat of combustion.

Effects of Temperature - The two gas temperatures used for testing were 900 K and 1200 K. The temperature had little or no effect on the burning time or oxidation time of the coal as shown in Fig. II.F-25, suggesting little kinetic effect on oxidation rate. A similar effect of temperature was also observed

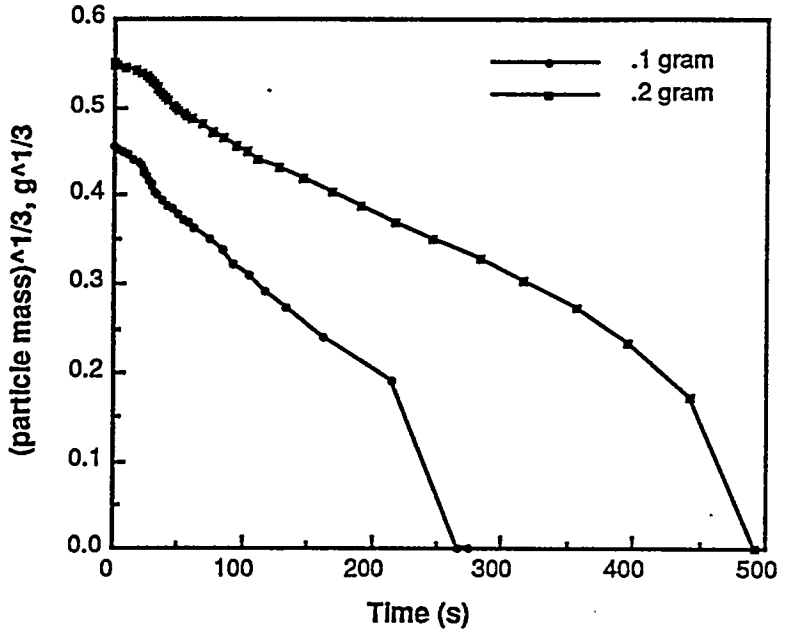

Figure II.F-15a. Combustion of Utah coal, sizes 0.1 gram and 0.2 gram, in HPCP for gas temperature of 900 K and an air flow Reynolds number of 126 at atmospheric pressure.

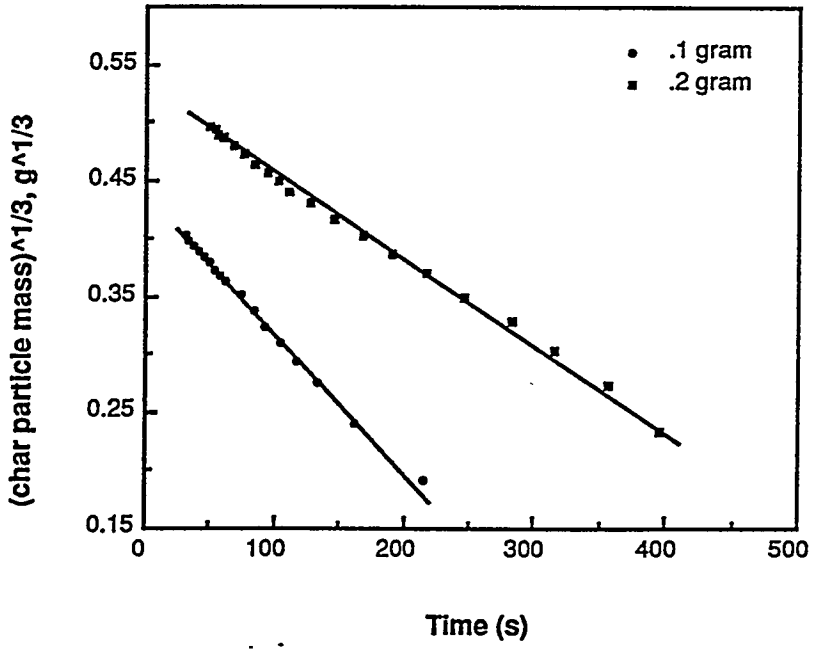

Figure II.F-15b. Oxidation of Utah coal, sizes 0.1 gram and 0.2 gram, in HPCP for gas temperature of 900K and an air flow Reynolds number of 126 at atmospheric pressure.

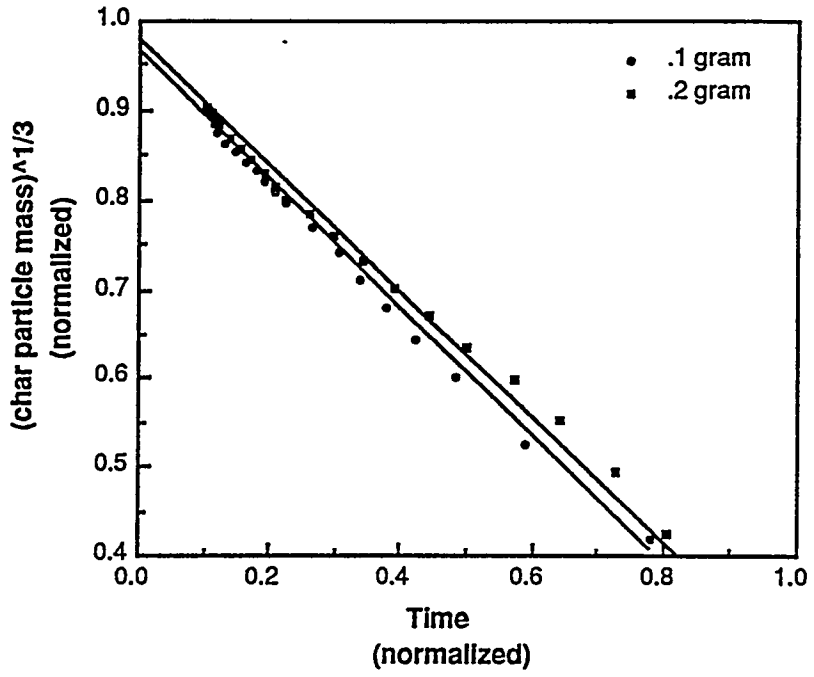

Figure II.F-16. Normalization of the oxidation curve for Utah coal, sizes 0.1 and 0.2 gram, in HPCP for gas temperature of 900 K, and an air flow Reynolds number of 126 at atmospheric pressure.

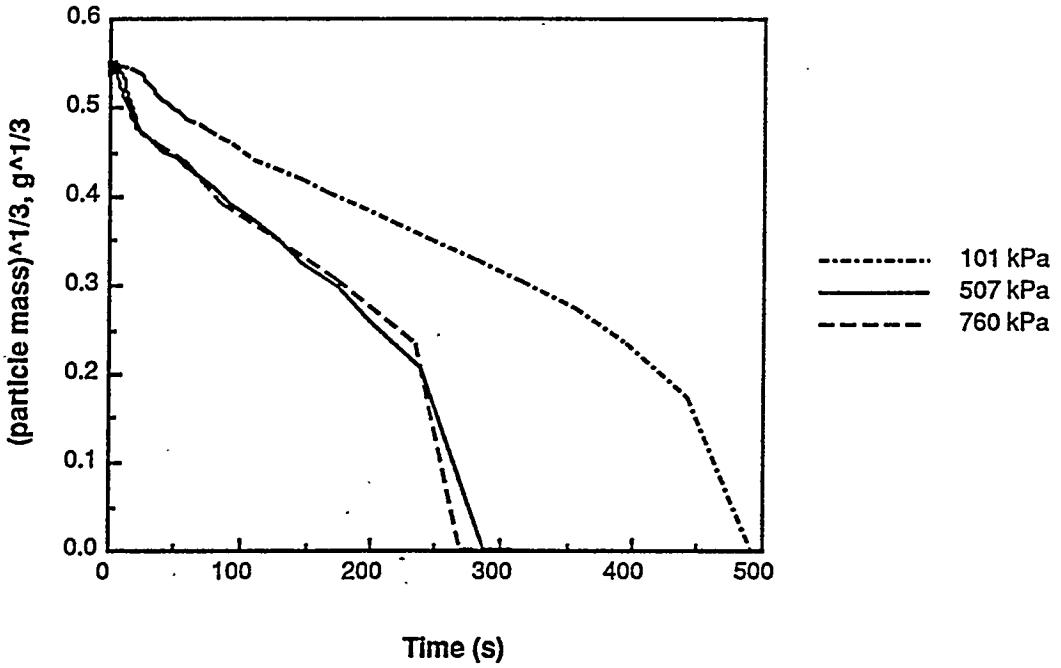

Figure II.F-17. Comparison of trends of 101 kPa, 507 kPa, and & 760 kPa tests for Utah coal, size 0.2 gram, in HPCP for gas temperature of 900 K, and an air flow Reynolds number of 126.

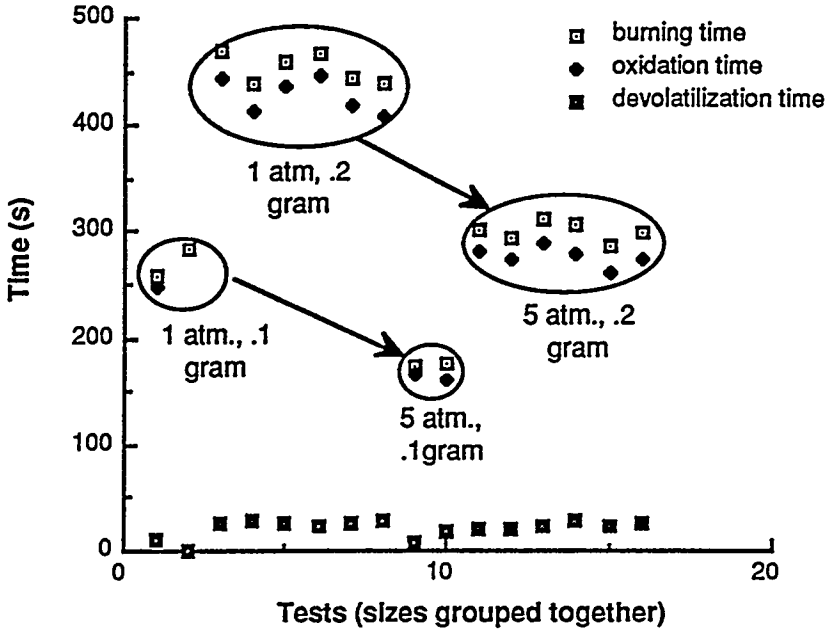

Figure II.F-18. Comparison of burning times of 101 kPa, 507 kPa, and & 760 kPa tests for Utah coal, size 0.2 gram, in HPCP for gas temperature of 900 K, and an air flow Re = 126.

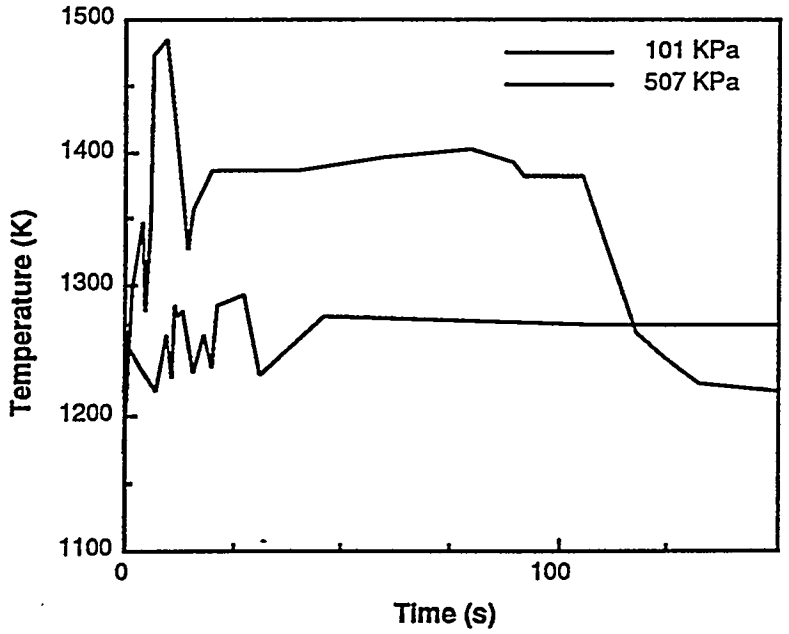

Figure II.F-19. Comparison of 101 kPa and 507 kPa surface temperature, Utah coal, size 0.2 gram, in HPCP, gas temperature of 1200 K and an air flow Reynolds number of 63.

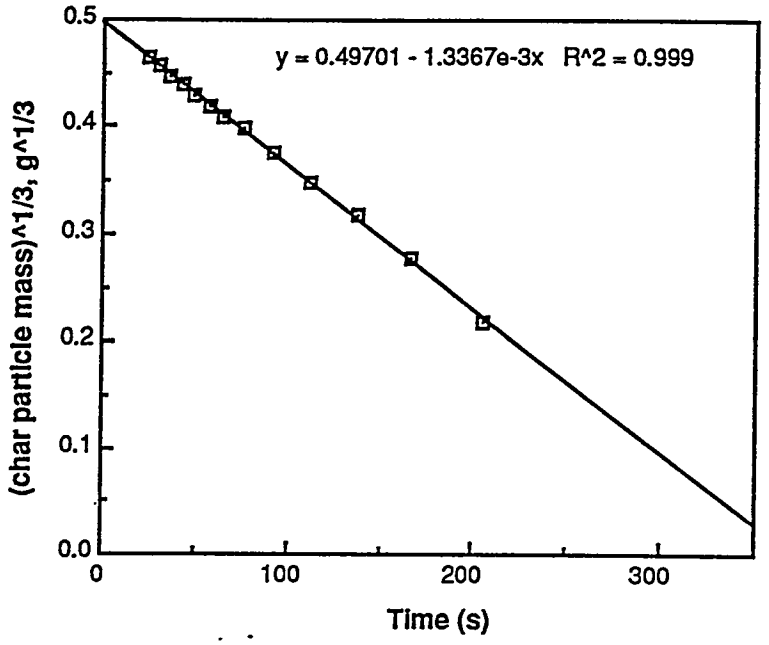

Figure II.F-20. Oxidation at 507 kPa of Utah coal, size 0.2 gram, in HPCP for gas temperature of 900 K and an air flow Reynolds number of 126.

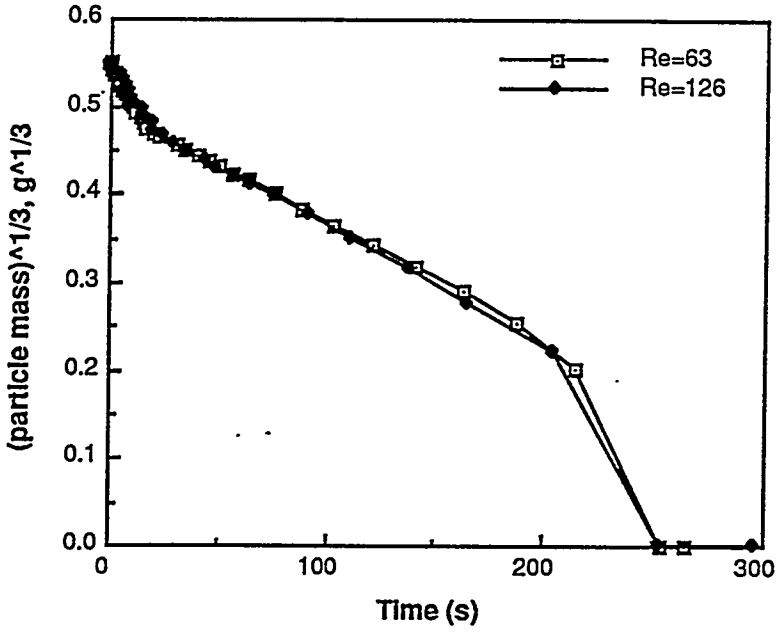

Figure II.F-21. Effect of Reynolds Number on Utah coal burn time, for Utah coal particles of mass 0.2 g, at 900 K gas temperature, and 507 kPa pressure.

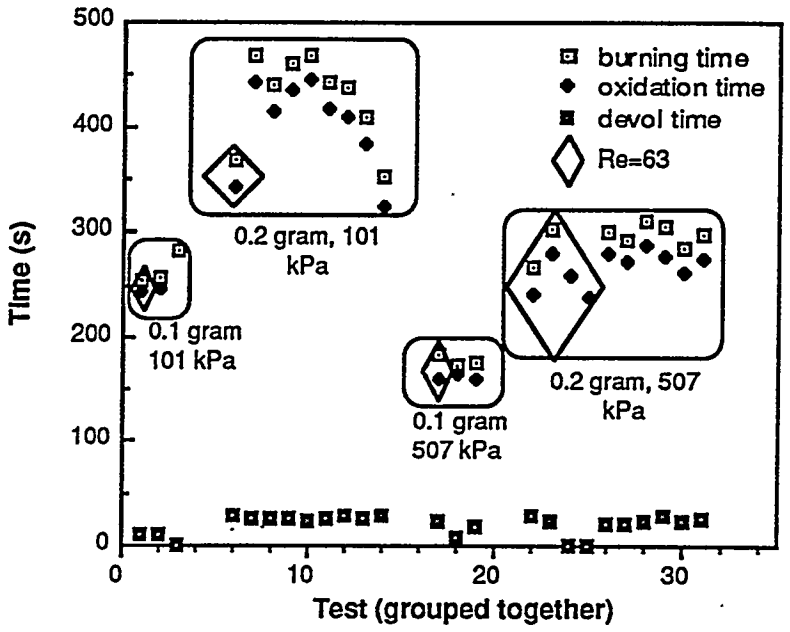

Figure II.F-22. Effects of Reynolds number on Utah coal, with a 900 K gas temperature. Re=63 surrounded with a large diamond, all others are Re=126.

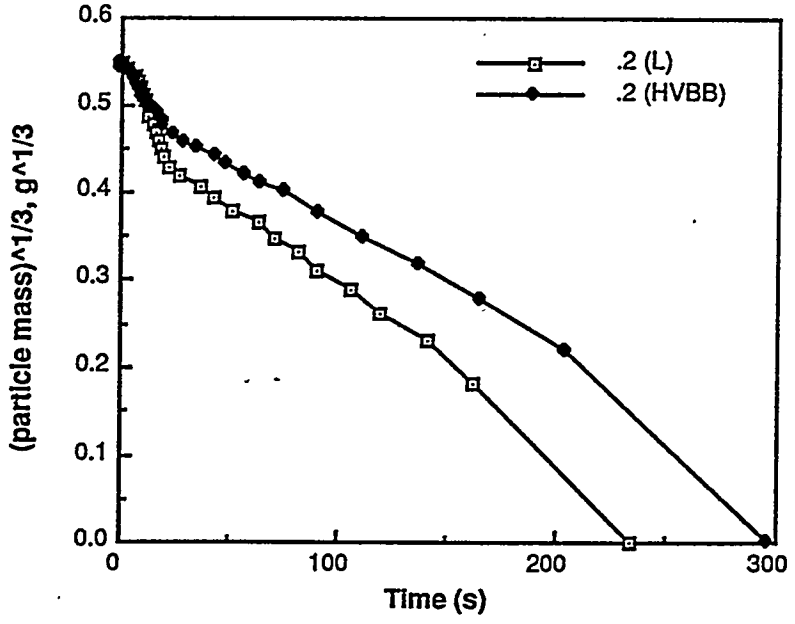

Figure II.F-23. Effects of coal type on burning time for Utah HVBB bituminous coal and North Dakota lignite coal: 0.2 gram particles, 900 K gas temperature, 507kPa, Re=126.

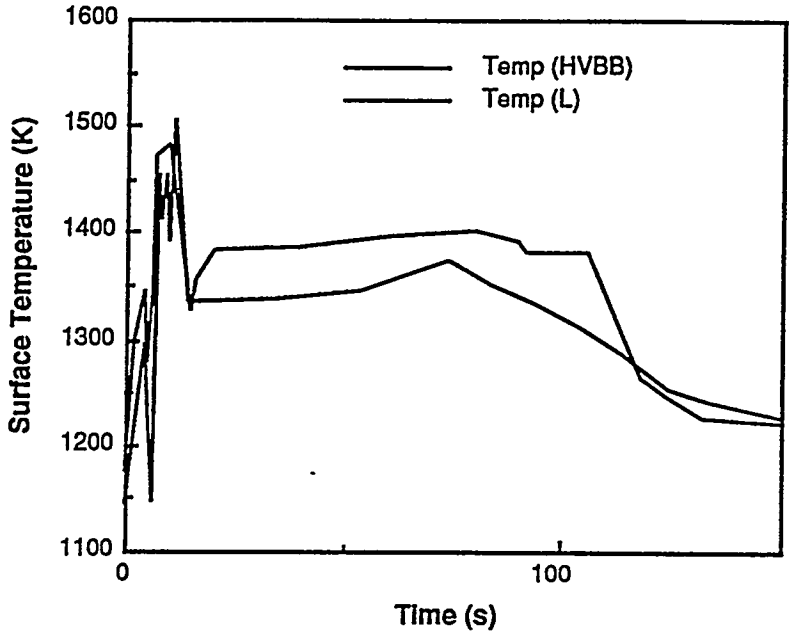

Figure II.F-24. Comparison of surface temperatures of Utah bituminous (HVBB) and North Dakota lignite (L), 0.2 g, Re=63, Gas Temperature = 1200 K, at 507 kPa.

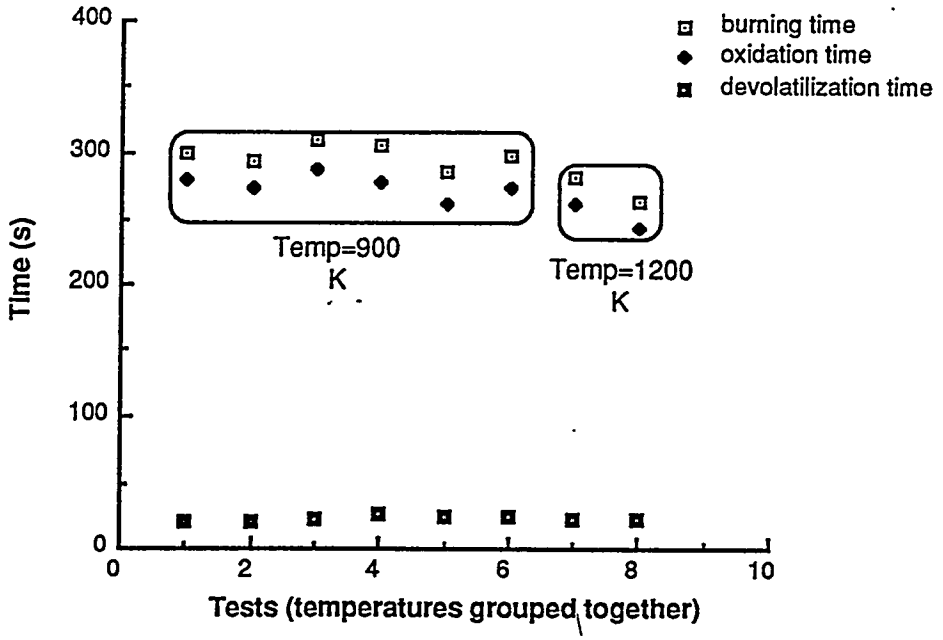

Figure II.F-25. Temperature effects on Utah coal, size 0.2 gram, in HPCP for an air flow Reynolds number of 126, at 507 kPa.

with the simple devices over the range 900 K to 1200 K as is recorded in Table II.F-4, but the effect of temperature was greater at lower temperature.

Effects of Multiple Particles - In addition to the test summarized in Table II.F-9, two 0.1 gram Utah coal samples were set on the same platinum mesh and tested together in such a way that the particles were touching. Results were compared to those for a single particle of the same total mass, 0.2 g. During devolatilization the particles began to swell and fuse together, thus making the combined surface area an estimated 60% greater than for a single particle. Figure II.F-26 shows that the two 0.1 gram particles had an identical burn time to that for the single 0.2 gram particle. Examined more closely, the two 0.1 gram particles indeed had very similar burning times and oxidation times, see Table II.F-10 and Fig. II.F-27. Videos of the tests revealed that the last place for burn-out was between the two particles, and not at the center of each individual particle, as might be expected. Results clearly show, even in the presence of substantial air flow with excess oxygen of about 20 times than needed for oxidation, that closely spaced particles interact and burn at different rates from single particles of the same size. It does seem surprising that burn times would be principally dependent on mass and nearly independent of surface area. Local availability of oxygen must be a vital factor.

Summary of Observations - From the oxidation tests of large coal particles in the HPCP, several observations were made relating to large char particle burning and oxidation. They are as follows:

(1) The tests provided burning rate data of large (0.1 - 0.2 g) individual char particles from two coals of varying rank at ambient pressure and at elevated pressure for temperatures of 900 and 1200K. Test variables included initial coal mass, oxidation temperature, coal type, and pressure.

(2) For all coals and all conditions, a linear decrease in $m_p^{1/3}$ vs. time was observed during oxidation until toward the very end of burnout, where faster decay occurred.

(3) Burnout times were essentially independent of temperature over the range studied.

(4) Burning rates were about 1/3 faster for the 0.1 gram particles than the 0.2 gram particles.

(5) Burning rates were much greater (approaching twice the rate) at elevated pressures of 507 kPa and 760 kPa, as compared to rates at atmospheric pressure. No difference in rates was observed between 507 kPa and 760 kPa.

(6) A pair of similarly sized individual particles of coal had a similar oxidation time to one single particle that had a mass equal to the sum of the pair. This time was much greater than the rate for the individual smaller particle. This was observed at both atmospheric pressure and elevated pressures.

(7) Increasing air flow rate (higher Reynolds number) had little or no effect upon the rate of oxidation of the Utah coal, similar to the tests from the simple devices at high flow rates. This was observed at both atmospheric pressure and elevated pressures.

(8) Normalizing both the $m_p^{1/3}$ axis and the time axis of the same coals, though differing in size, resulted in straight lines with identical slopes.

(9) Extinguishment of the burning Utah coal was more abrupt at the end of burnout than for the North Dakota coal, which more gradually extinguished.

(10) Increasing the pressure to 507 kPa from 101 kPa increased surface temperature during oxidation by approximately 100 K.

(11) Data obtained from the HPCP produced similar results in many respects to the trends observed using the simple devices. This included $(mass)^{1/3}$ vs time dependence, low temperature dependence at higher temperatures, low flow dependence at higher flow rates, and more rapid oxidation rates at the very end of burnout.

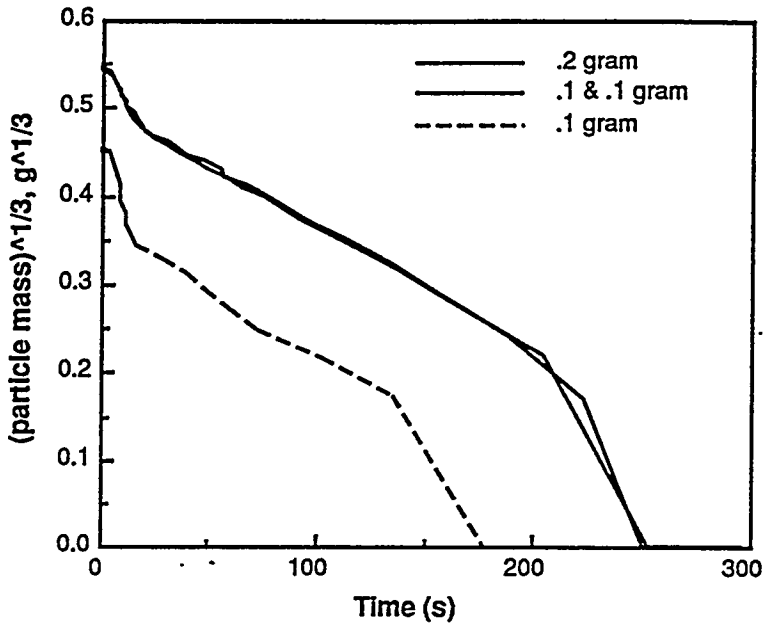

Figure II.F-26. Effects of multiple particles of Utah coal in HPCP for gas temperature of 900 K and an air flow Reynolds number of 126 at 507 kPa.

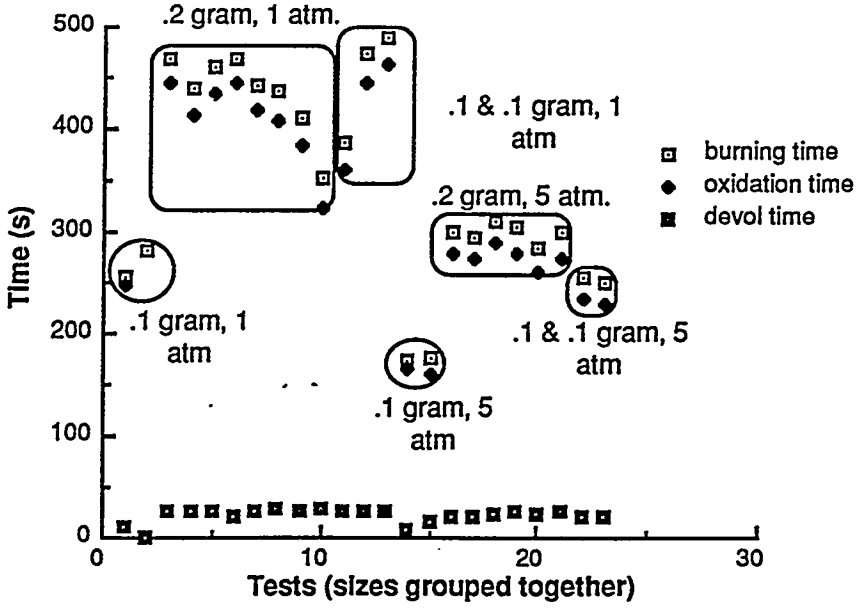

Figure II.F-27. Effects of multiple particles, comparison of burning times, of Utah coal, in HPCP for gas temperature of 900 K and an air flow Reynolds number of 126 at 101 and 507 kPa.

TABLE II.F-10

BURNING TIMES AND OXIDATION TIMES FOR UTAH COAL SINGLE AND DUEL PARTICLES AT 101 AND 507 kPa

Size	101 kPa		507 kPa	
	Burning time (s)	Oxidation time (s)	Burning time (s)	Oxidation time (s)
0.1 gram	257	246	174	166
	283	-	176	159
0.2 gram	469	444	300	280
	440.	413	294	273
	460.	435	311	288
	468	446	306	278
	443	417	286	261
	438	409	299	274
	387	360	-	-
0.1 & 0.1 gram	472	446	256	235
	491	463	249	228

Data Correlation and Discussion

Time-Mass Dependence - Observed burning times of about 2 to 8 minutes were similar to the burning times observed by Ragland and Yang (1985) at atmospheric pressure. Burning times of the 0.1 gram particles were faster than the 0.2 gram samples. This was similar to that for the simple device and was predicted from Eqn. II.F-9b. Particle mass is the dominant factor for oxygen diffusion-controlled oxidation and the cubic root decay of particle mass with time is that expected from this simple burning law. Similar to the results obtained using the simple devices, all of the data obtained at atmospheric conditions plotted in linear form as $m_p^{1/3}$ vs. t. Statistical correlation coefficients were 0.93 or higher in every case and .99 in most cases. Likewise, all of the data obtained at elevated pressures plotted in linear form as $m_p^{1/3}$ vs. t. Statistical correlation coefficients were 0.95 or higher in every case and .99 in most cases.

As in the results obtained using the simple devices, the measured char mass value fell somewhat below the linear correlation line towards the end of burning. This may be due to particle breakup after nearly all of the carbon (about 99%) has been consumed.

Particle Surface Temperature - The energy equation describes the surface temperature. Assuming the particle temperature to be constant during the oxidation process and neglecting the inertial components, the energy equation can be written (Monson, 1992):

$$0 = Nu\,\lambda\,(T_p - T_g)/d_p + \varepsilon\sigma(T_p^4 - T_w^4) - q_a\,\Delta H \qquad \text{(II.F-30)}$$

In combining Eqns. II.F-30 and II.F-1, the two unknowns q_a and T_p can be simultaneously solved using the values shown in Table II.F-11.

The predicted results of Table II.F-12 show that for equal gas and wall temperatures, the burning rate, q_a, and particle temperature, T_p, are not affected by changing pressure, which is contrary to observations. Further examination shows that the particle surface temperature, T_p, increases as wall temperature increases, as shown in Table II.F-12. During the testing process, it was observed that higher wall temperatures were required to sustain the specified gas temperature as pressure was increased, due to the higher heating requirements of larger mass flows of air. Typically, at 507 kPa, measured wall temperatures were 100 K higher than at 101 kPa. This observation, together with the predictions of Table II.F-12 explain the higher particle temperatures observed at higher pressures. These higher particle

TABLE II.F-11

VALUES USED WHEN SOLVING EQUATIONS II.F-1 AND II.F-30

Input	
P_g (atm)	Gas pressure
T_g (K)	Gas temperature
T_w (K)	Wall temperature
d_p (cm)	Particle diameter
Constants	
Nu = 2.0	Nussult number
ε = 0.85	Particle emissivity
σ = 1.354E-12 (cal / cm^2 s K^4)	Stefan-Boltzman
ΔH = -2200 (cal / gK)	CO heat of reaction
Output	
T_p (K)	Particle temperature
q_a (g / cm^2 s)	Burning rate

TABLE II.F-12

PREDICTED RESULTS FROM SOLVING EQUATIONS II.F-1 AND II.F-30 FOR Qa AND T_p

Pressure (kPa)	T_g (K)	T_w (K)	char diameter (mm)	q_a (g/min)	T_p (K)
101	900	900	5.5	0.0198	1055
101	1200	1200	5.5	0.0248	1298
507	900	900	5.5	0.0198	1055
507	1200	1200	5.5	0.0248	1298
101	900	900	8	0.0289	1018
101	1200	1200	8	0.0361	1272
507	900	900	8	0.0289	1018
507	1200	1200	8	0.0361	1272
507	1200	1250	8	0.0360	1312
507	1200	1300	8	0.0359	1353
507	1200	1400	8	0.0358	1440
507	1200	1500	8	0.0357	1530
507	1200	2000	8	0.0361	2005
507	1200	3000	8	0.0387	2995
507	1200	4000	8	0.0420	3994
760	900	900	8	0.0289	1018
760	1200	1200	8	0.0360	1272

temperatures, however, have only a small predicted effect on particle burn time, as predicted and observed.

Gas Temperature - Similar to the results obtained from the simple devices, little gas temperature effect was detected in the range of 900 K to 1200 K. Results from solving Eqns. II.F-1 and II.F-30 and keeping everything constant except gas temperature, T_g, shows a small (20%) decrease in oxidation time with increasing gas temperature. A slight decrease due to temperature was also suggested experimentally, as shown in Fig. II.F-25.

Pressure - Equations II.F-1 and II.F-30 give considerable insight to the reaction process. They however predict reaction rate to be independent of pressure. The diffusion coefficient is inversely proportional to pressure, while the oxygen concentration is directly proportional to pressure, creating no net pressure affect. The observed effect that pressure has upon the reaction rate must lie elsewhere. Since little dependence of oxidation rate on temperature was observed, this pressure dependence is not thought to be due to pressure dependence of surface oxidation rate, nor to the increased particle temperature at higher pressures. Devolatilization times are short compared to oxidation and mass losses were comparable over the pressure range studied. Effects of pressure on the devolatilization process are thought to be secondary. Increasing pressure by a factor of five provides five times the flow rate of oxygen while reaction rate increases by less than twice. Further, the reaction of CO to CO_2 in the boundary layer is pressure dependent and consumes oxygen in that region. It is suspected that these complex interactions near the particle surface are responsible for the changing local oxygen concentration differently at different pressures.

Multiple Particles - Similar to the rates from the simple devices, the rates for two particles were about that for one particle whose mass was the sum of the two individual particles. The boundary layer surrounding the two particles must more closely resemble the larger particle than the smaller individual particle, as shown in Fig. II.F-28. This insight may be valuable in predicting the behavior of closely spaced multiple particles and supports the assumption that a single sphere can approximate two touching particles. This result may well be a function of air flow rate.

Air Flow Rate - The observed effect of increased flow rate, Re=63 to Re=126, was small. There were few tests at the low Reynolds number, and the data were sufficently scattered enough that little or no effect of flow rate was observed. This was consistent with the findings from the simple device, as shown in Fig. II.F-29 (a plot of Table II.F-5). In these tests, higher flow rates reduced burn times for Reynolds Numbers below about 20, but had little impact for higher Re values. Apparently in the HPCP tests, flow rates were sufficiently high to have passed the region of dependence of flow rate.

Conclusions - The main objective was to characterize the mass loss and the burn-out time of large (five and eight millimeters diameter) coal particles at pressures of one and five atmospheres. To this end, a cantilever balance attachment (CBA) was designed, manufactured and implemented, and, in conjunction with the HPCP, coal combustion experiments of large particles were conducted at both atmospheric and elevated pressures.

The CBA was based on the combination of several earlier mass-loss detection devices. The computer-controlled stepper-motor inserted and removed a single coal particle at a precise feed rate. The mass loss of the coal particle was determined by a load cell accurate to 0.01 grams. Manual positioners enabled the coal particle to be centered in the HPCP. A custom valve allowed testing at elevated temperatures without the depressurizing of the HPCP. A portable pyrometer provided particle surface temperature measurements to be plotted on a strip-chart recorder. The use of two camcorders provided valuable video of each test. One of the videos was used to retrieve mass loss data, the other provided magnified footage of the combustion process after the tests were over.

Approximately 90 combustion experiments were performed with two sizes of Utah bituminous (HVBB) coal and North Dakota Lignite (L) coal at 1, 5, and 7.5 atm total pressure. The reactor temperatures varied between 900 and 1200 K and the bulk gas was air. The results obtained using the Utah coal at 1 atm were shown to be consistent with other researchers.

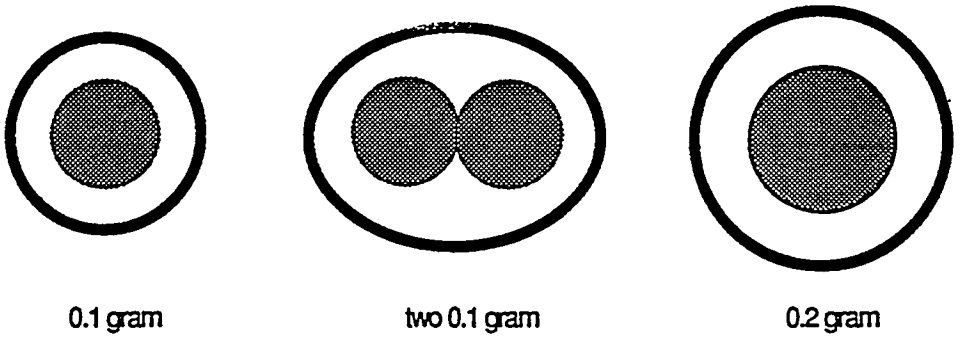

Figure II.F-28. Assumed boundary layer of multiple particles and single particle.

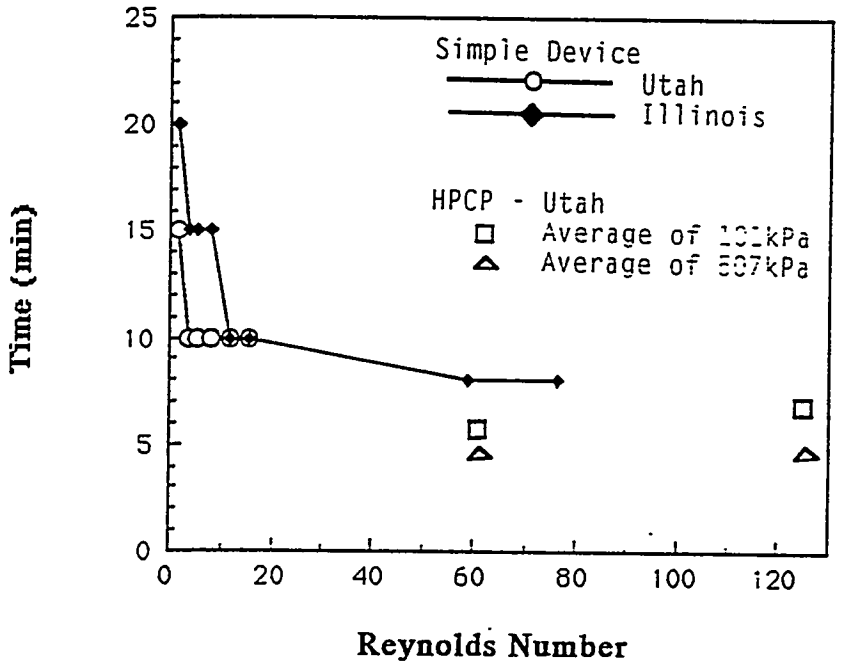

Figure II.F-29. Effect of Reynolds number on Utah and Illinois coals using the simple device and HPCP at gas temperatures of 1070 K and 900 K, respectively. Data from Table II.F-5 and Figure II.F-22.

The following points summarize the results of the study:

(1) In all of the tests, including the elevated pressure tests, a linear decrease in the cube root of char mass verses time was observed until the very end of burnout, which is consistent with a simple oxygen diffusion model.

(2) The global model, combined with the energy equation, reflects the significant effect wall temperature had upon the surface temperature of the coal particle and shows that wall temperature did not significantly affect the oxidation time or the burning time.

(3) As predicted from the global model at constant conditions, the burning rate was inversely proportional to the particle diameter.

(4) The observed pressure effect cannot be explained using the simple global model.

(5) A pair of similarly sized individual particles of coal had a similar oxidation time as one single particle that had a mass equal to the sum of the pair, suggesting substantial interaction among closely placed particles.

With no high pressure large particle combustion data available in the literature, this study has begun to fill a much neglected area of coal combustion. A number of issues, however, still remain unresolved:

(1) Confirmed explanation of the increase in mass loss rate at elevated pressures.

(2) Ability to measure the particle surface temperature when the bulk gas temperature is below 900 K.

(3) The behavior of multiple particles interactions with various extents of separation.

The devolatilization and char oxidation process at elevated pressures is not well understood. Additional work needs to be done to quantify the effects of pressure on the entire combustion process.

NOMENCLATURE

Symbol	Units	Definition
A	cm^2	area
C_1	cm^2/min	constant, $4 D_{oa} C_{ob} M_p S/\rho_p$
C_b	cm^2/min	burning rate coefficient, $[(2/k)D_{oa} C_{ob} M_p S/\rho_p]$
C	$gmol/cm^3$	molar concentration
C_2	$g^{1/3}/s^{1/2}$	constant $(\pi\rho_p/6)^{1/3} (2C_1)^{1/2}$
C_d	$g^{1/3}/s$	coefficient of Eqn. II.F-2
C_r	$g^{1/3}/s$	coefficient in Eqn. II.F-4
d_p	cm	particle diameter
D	cm^2/s	diffusion coefficient
F	—	char ash fraction (dry)
k	—	ash layer thickness coefficient
k_c	cm/s	mass transfer coefficient
k_r	cm/s	reaction rate coefficient
m_p	g	particle mass
M_p	g/gmol	char molecular weight
n	—	number of burning time increments
R	g/g min	char mass reactivity
R	g/g min	time-averaged mass reactivity
S	—	stoichiometric coefficient
t	s, min	time
T	K	temperature
Δ	—	incremental difference
ρ	g/cm^3	density

Subscripts

a	ash
b	bulk
b	burning
m	mixture
max	maximum
o	initial
o	oxidizer
p	particle
s	surface
t	thick

Superscripts

o	reference
–	mean

References for Subtask 2.f.

Amundson, N.R. and Arri, L.E., Char Gasification in a Countercurrent Reactor, AIChE Journal, 24, 87 (1978).

Bae, J.H., A Simple Thermogravimetric Apparatus for Pressures p to 70 Atmospheres, The Review of Scientific Instruments, 43, 983-985 (1972).

Bird, R.B., Stewart, W.E. and Lightfoot, E.N., *Transport Phenomena*, Wiley and Sons, New York, (1960).

Clean Coal Technology Demonstration Program, Program Update, 1990, U.S. Dept. of Energy, DOE/FE-0221P, Washington, DC (June,1991).

Dobner, S., Kan, G., Graff, R.A. and Squires, A.M., A Thermobalance for High Presssure Process Studies, Thermochimica Acta, 16, 251-265 (1976).

Elliott, M.A., editor, *Chemistry of Coal Utilization*, Second Supplementary Volume, Wiley-Interscience, New York (1981).

Essenhigh, R.H., Fundamentals of Coal Combustion, Chapter 19, *Chemistry of Coal Utilization*, Second Supplementary Volume, M.A., Elliott, editor, Wiley-Interscience, New York (1981).

Essenhigh, R.H., and Thring, M.W., The Measurement of Burning Times of Single Coal Particles, Proc. Conf. Science in the Use of Coal, Paper No. 29, Inst. Fuel, D21 (1958).

Feldkirchner, H.L. and Johnson, J.L., High Pressure Thermobalance, Rev. Sci. Instrum, (USA), 39, 1227-9 (1968).

Forgac, J.M. and Angus, J.C., A Pressurized Thermobalance for Use at Extreme Conditions, Ind. Eng. Chem Fund., 18, 416-418 (1979).

Froberg, R.W. and Essenhigh, R., Reaction Order and Activation Energy of Carbon Oxidation During Internal Burning, Seventeenth Symposium (International) on Combustion, The Combustion Institute, 179-187, Pittsburgh, PA (1978).

Gardner, N., Samuels, E., Wilks, K., Catalyzed Hydro Gasification of Coal Chars, Advances Chemical Series, 131, 217 (1974).

Ghodsi, M., Derie, R. and Lempereur, J.P., Construction of an Isothermal Balance with Two Symmetrical Pans for Operation Under Pressure, Thermochimica Acta, 28, 259-264 (1979).

Ivanova, G.P., and Babii, V., A Study of the Burnout Mechanism of Coal Particles, Teploenergetika, 13, 54, 1966; Transl, Thermo. Eng., 13, 70 (1966).

Levenspiel, Octave, *Chemical Reaction Engineering*, Chapter 12, Wiley and Sons, New York (1972).

Li, K. and Rogan, R.H., A Thermogravimetric System for Corrosive Environments at High Pressures and Temperatures, Thermochimica Acta, 26, 185-190 (1978).

Nuttall, H.E., Stoddart, W.G. and Chen, W.J., Pyrolysis of Subbituminous New Mexico Coal, J.Pet. Tech., April, 418-20 (1979).

Parikh, R.S. and Mahalingam, R.,Modeling and Experimental Studies on Devolatilization Yields from a Bituminous Coal, Ind. Eng. Chem, Res., 26, 2378-84 (1987).

Park, K.Y. and Edgar, T.F., Modeling of Early Cavity Growth for Underground Coal Gasification," Ind. Eng. Chem. Res., 26, 237 (1987).

Ragland, K.W. and Yang, J.T., Combustion of Millimeter-sized Particles in Convective Flow, Combustion and Flame, 60, 285-297 (1985).

Ragland, K.W. and Yang, J.T., Convective Thermogravimetric Analysis of Coal Combustion, WSCI 82-19, Western States Section, Combustion Institute (April 5, 1982).

Sears, J.T., Tamhankar, S.S., Radman, A. and Wen, C.Y., Influence of Char Properties on Reaction Rates, Chem. Eng. Commun., 38, 17 (1985).

Sears, J.T., Maxfield, E.A. and Tamhankar, S.S., Pressurized Thermobalance for Use in Oxidizing Atmospheres at High Temperatures, Ind. Eng. Chem. Fund., 21, 474-8 (1982).

Singer, J.G., editor, Combustion, in *Fossil Power Systems*, Combustion Engineering, Inc., Windsor, CN (1981).

Smith, I.W, The Combustion Rates of Coal Chars: A Review, Nineteenth Symposium (International) on Combustion, The Combustion Institute, 1045- 1065, Pittsburgh, PA (1983).

Smith, K.L. and Smoot, L.D., Characteristics of Commonly Used U.S. Coals -- Towards a Set of Standard Research Coals, Progr. Energy Combus. Sci., 16, 1-53 (1990).

Solomon, P.R. and Smoot, L.D., Measurement and Modeling of Advanced Coal Conversion Processes, Fifth Annual Report, METC Contract, DEAC2186MC23075 (December 1991).

Srinivas, B. and Amundson, N.R., Intraparticle Effects in Char Combustion - Steady State Analysis, The Canadian Journal of Chemical Engineering, 58, 476-484 (1980).

Tamhankar, S.S., Sears, J.T. and Wen, C.Y., Coal Pyrolysis at High Temperatures and Pressures, Fuel, 63, 1230 (1984).

Treptau, M.H. and Miller, D.H., An Internally Heated Weighed Reactor Thermobalance for Gas-Solid Reaction Studies, Ind. Eng. Chem. Res., 26, 2007-2011 (1987).

Wang, S.C. and Wen, C.Y., Experimental Evaluation of Nonisothermal Solid-Gas Reaction Model, AIChE Journal, 18, 1231 (1972).

Wen, C.Y. and Wang, S.C., Thermal and Diffusional Effects in Solid-Gas Reactions, Indust. Engineering Chem., 62, 30-51 (1970).

Williams, J.R. and Wendlandt, W.W., A High Pressure Thermobalance, Thermochimica Acta, 7, 253 -260 (1970).

II.G. SUBTASK 2.G. - SO_x/NO_x SUBMODEL DEVELOPMENT

Senior Investigators: L. Douglas Smoot and B. Scott Brewster
Brigham Young University
Provo, Utah 84602
(801) 378-4326 and (801) 378-6240

Research Assistant: Richard D. Boardman

Objectives

The objectives of this subtask are 1) to extend an existing pollutant submodel in PCGC-2 for predicting NO_x formation and destruction to include thermal NO, 2) to extend the submodel to include SO_x reactions and SO_x-sorbent reactions, and 3) to consider the effects of fuel-rich conditions and high pressure on sulfur and nitrogen chemistry in pulverized-fuel systems.

Accomplishments

NO_x Submodel

This work was conducted principally by Dr. Richard Boardman and provided the basis for his doctoral dissertation, entitled "Development and Evaluation of a Combined Thermal and Fuel Nitric Oxide Predictive Model (Brigham Young University, Provo, Utah, Dec. 1990). The dissertation provides an extensive presentation of this work which follows. Several publications have also been published or are in preparation regarding this subtask.

Mechanisms - The original work of Hill et al. (1984) formed the basis for the NO_x submodel. However, this model was developed and evaluated only for fuel-NO_x formation in coal combustion, and did not include thermal NO_x. This original mechanism is represented by the lower part of Fig. II.G-1 with $\alpha = 1.0$.

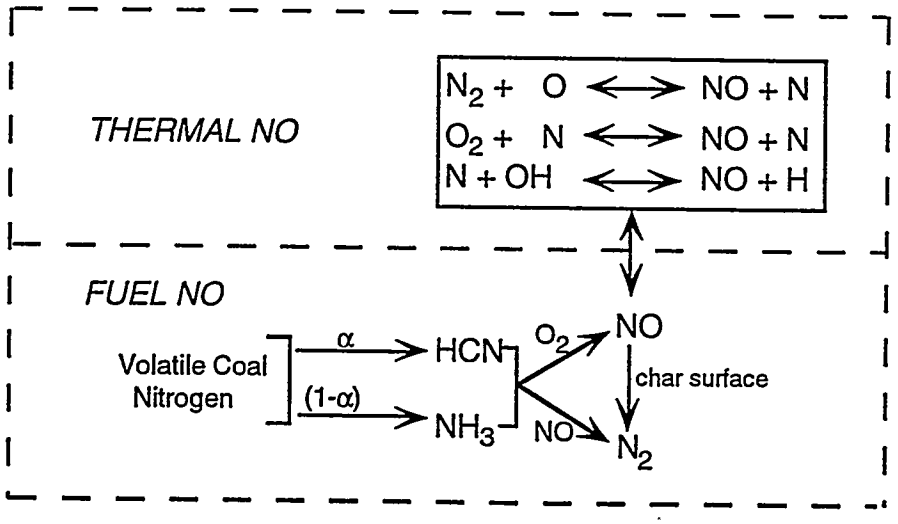

Figure II.G-1. Joint thermal-NO and fuel-NO mechanism of nitricoxide model.

Thermal NO_x Equations - Kinetic rate equations for thermal NO formation in both fuel-lean and fuel-rich systems were developed from the literature (Zeldovich, 1947; Baulch et al., 1973; Sawyer, 1981). In fuel-lean systems, the following rate expression applies:

$$\frac{\partial X_{NO}}{\partial t} = \frac{9.91\times10^{15}K\times sec^{-1}}{T}\exp\left[\frac{-68,500}{T}\right]X_{N_2}X_{O_2}^{0.5}P^{0.5} \qquad \text{(II.G-1)}$$

This equation is based on the well-accepted Zeldovich mechanism and assumes oxygen radicals in equilibrium concentration and the concentration of NO to be small. For fuel-rich conditions, the measured rates are often much greater than predicted by this equation. Allowing for oxygen radicals in excess of equilibrium (Sarofim and Pohl, 1973), the following expression results:

$$\frac{\partial X_{NO}}{\partial t} = \frac{4.09\times10^{11}K\times sec^{-1}}{T}\exp\left[\frac{-34,900}{T}\right]X_{N_2}X_{O_2}X_{CO}X_{CO_2}^{-1} \qquad \text{(II.G-2)}$$

Under highly fuel-rich circumstances (equivalence ratio > 1.15), the additional elementary reaction

$$N + OH \rightarrow NO + H \qquad \text{(II.G-3)}$$

is added to the Zeldovich mechanism. Including both the forward and reverse steps of each elementary step results in the following expression (Westenberg et al., 1971):

$$\frac{\partial Y}{\partial t} = \frac{M}{2}\left[\frac{1-Y^2}{1+CY}\right] \qquad \text{(II.G-4)}$$

where

$$Y = \frac{[NO]}{[NO]_{eq}} \qquad \text{(II.G-5)}$$

$$M = \frac{5.4\times10^{15}K\times sec^{-1}}{T}\exp\left[\frac{-34,900}{T}\right]X_{N_2}^{0.5}P^{0.5} \qquad \text{(II.G-6)}$$

and

$$C = \frac{k_{-2}K_{NO}[N_2]^{0.5}}{k_3[O_2]_{eq}^{0.5}\left[\frac{1+k_4[OH]_{eq}}{k_3[O_2]_{eq}}\right]} \qquad \text{(II.G-7)}$$

The foundational NO_x submodel of PCGC-2 has been revised to allow for any of these three options to be selected. The upper part of Fig. II.G-1 includes the thermal NO_x mechanism.

Oxygen Atom Concentration - Two quasi-equilibrium expressions have been evaluated in the submodel for calculating oxygen atom concentration. Oxygen equilibrium (Eq. II.G-8) has been recommended for fuel-lean zones in the combustor while carbon equilibrium (Eq. II.G-9) has been suggested for fuel-rich regions where primary fuel oxidation occurs.

$$[O] = \left\{K'_{eq}[O_2]\right\}^{1/2} \qquad \text{(II.G-8)}$$

$$[O] = K'_{eq}\frac{[O_2][CO]}{[CO_2]} \qquad \text{(II.G-9)}$$

The sensitivity of the model to these expressions was evaluated and is reported below.

Fuel-Rich Systems - Based on recent work by Peck et al. (1988), who assumed that volatile fuel nitrogen can be partitioned between HCN and NH_3 to improve mechanistic prediction of fuel NO, the existing fuel-NO mechanism of PCGC-2 (Smith et al., 1982) was revised to include a parallel reaction path through HCN or NH_3. Global reaction rates involving oxidation and reduction of NH_3 have been identified in the work by de Soëte (1975) who correlated global rates for the decay of fuel-NO_x species to NO and N_2. The objective was to improve predictions for low-rank coals and fuel-rich combustion, by allowing volatile fuel-nitrogen to form NH_3. The extended fuel-NO mechanism is presented in the lower part of Figure II.G-1. The partition coefficient, α, indicates the relative conversion of volatile fuel nitrogen between HCN and NH_3. The FG-DVC submodel provides devolatilization rates for HCN and NH_3 for low-rank coal.

With global rates for the conversion of NO to N_2 by reaction with NH_3, the model has the further potential of predicting thermal "de-NO_x" strategies in which ammonia is injected into the post combustion environment to reduce NO to N_2.

Use of Elementary Reactions - Although more extensive kinetic models have been developed to predict the gas-phase reactions of nitrogen compounds (eg. Miller and Bowman, 1988; Peck and Glarborg, 1986), these models are based on scores of elementary reactions which require accurate calculation of radical species. Even when the mechanisms can be reduced to a subset of only the intermediates of greatest importance using sensitivity and rate-of-production analysis, it is currently not possible to accurately calculate and track the concentration of the intermediate species in turbulent coal flames. The advantage of global kinetics, based on only key and measurable intermediates, is the ability to compute the governing species and perform the calculations with greater efficiency. Furthermore, even the most sophisticated kinetics schemes require a degree of empiricism and conjecture in obtaining rate parameters for several elementary reactions.

Alternative Global Mechanisms - From the literature, only one alternative global mechanism involving NH_3 was identified that could be adapted to the existing NO_x submodel. This model is the global model presented by Mitchell and Tarbell (1982) involving NH_3, HCN, NO, and N_2 as active species. By assuming the form of the rate equations, which included formation of thermal NO from partial equilibrium of radical oxygen with molecular oxygen, Mitchell and Tarbell calculated the "best-fit" of relevant data to obtain the kinetic parameters for fuel NO formation and destruction. Because the rate expressions are empirical and each rate was not determined independently, the applicability of the mechanism remains questionable. However, since a more complete global mechanism which may be used in coal flames was unavailable, the feasibility of this alternative mechanism was investigated by comparing it to predictions of the existing fuel NO mechanism incorporated by Hill, et al. (1984). Figure II.G-2 shows the global mechanism formulated by Mitchell and Tarbell (1982).

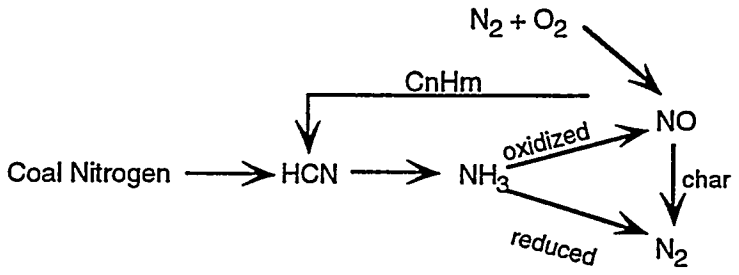

Figure II.G-2. Global fuel NO mechanism correlated by Mitchell and Tarbell (1982) to reactor data of Muzio et al., (1977).

Selected predictions show that the Mitchell and Tarbell mechanism fails to predict the competitive formation and destruction of NO for a subbituminous coal. Figure II.G-3 compares predictions made by the alternate mechanism and the original submodel (including thermal NO rates). However, this alternative global mechanism was included in the revised NO_x submodel.

Options and Equations - The NO_x submodel was refined during this study to include several options for specifying the fuel NO mechanism to be used. Figure II.G-4, which expands on Fig. II.G-1, shows the relationship of the NO_x submodel to PCGC-2 and gives the possible alternatives that have been incorporated into the NO_x submodel. This submodel has been integrated into PCGC-2.

Table II.G-1 lists and defines the equation set and nomenclature for the expanded NO_x submodel, which includes both the thermal and fuel NO mechanisms. The equations do not show the reactions expressions for the Mitchell and Tarbell mechanism.

Code Solution - The solution algorithm involves starting with a guess for the pollutant concentration field and then calculating extents of reaction or deviation from equilibrium. Instantaneous species mole fractions are then calculated and used in the instantaneous rate expressions which are subsequently convolved to obtain mean reaction rates for each control volume of the discretized reaction flow domain., Species continuity, which is cast in finite difference form, is then solved for HCN, NH_3, and NO using the routines available in PCGC-2. The updated mass fraction values are used to re-calculate the mean reaction rates. Thus, the solution is iterative, converging on the predicted concentration fields for HCN, NH_3, and NO.

In order to improve the stability and efficiency of the solution procedure for nitric oxide, the non-linear reaction rate for thermal NO is linearized by expanding the rate in a Taylor series and dropping second order and higher terms:

$$\omega = \omega^{\cdot} + \left(\frac{\partial \omega}{\partial X_{NO}}\right)^{\cdot} \left(X_{NO}^{\cdot} - X_{NO}\right) \qquad \text{(II.G-10)}$$

Model Evaluation - It is generally agreed that the reaction network for thermal NO is correctly described by the modified Zeldovich mechanism based on research carried out by Zeldovich (1947) and the substantial amount of research that has been conducted over the past two decades. The purpose of the model evaluation in this study is not to duplicate this effort for thermal NO mechanism formulation but rather to verify the predictive technique of coupling the kinetics with turbulence in practical combustors. The procedure taken is to begin by verifying the thermal NO and fuel NO mechanisms separately.

TABLE II.G-1.
EQUATION SET FOR EXTENDED NO_X MODEL

$$\overline{W_i} = \overline{\rho u}\left(\frac{\partial Y_i}{\partial x}\right) + \overline{\rho v}\left(\frac{\partial Y_i}{\partial r}\right) - \left(\frac{\partial}{\partial x}\right)\left(\tilde{D}_Y \frac{\partial Y_i}{\partial x}\right) - \frac{1}{r}\left(\frac{\partial}{\partial r}\right)\left(r\tilde{D}_Y \frac{\partial Y_i}{\partial r}\right) \quad i = NO, NH_3, HCN \tag{A}$$

$$\overline{W_{NO}} = [\alpha_n(\overline{\omega_1} - \overline{\omega_2}) + (1 - \alpha_n)(\overline{\omega_3} - \overline{\omega_4}) + \overline{\omega_5} - \overline{\omega_6}]M_{NO} \tag{B}$$

$$\omega_1 = k_{1f} X_{HCN} X_{O_2}^b (\rho/M_{mix}) \qquad b = F(X_{O_2})$$

$$\omega_2 = k_{2f} X_{HCN} X_{NO} (\rho/M_{mix})$$

$$\omega_3 = k_{3f} X_{NH_3} X_{O_2}^b (\rho/M_{mix}) \qquad b = F(X_{O_2})$$

$$\omega_4 = k_{4f} X_{NH_3} X_{NO} (\rho/M_{mix}) \tag{C}$$

$$\omega_5 = 2X_O \left[\frac{k_{1t}X_{N_2} - \left(\frac{k_{-1t}k_{-2t}X_{NO}^2}{k_{2t}X_{O_2}}\right)}{1 + \left(\frac{k_{-1t}X_{NO}}{k_{2t}X_{O_2} + k_{3t}X_{OH}}\right)}\right]\left(\frac{P}{RT}\right) \tag{D}$$

$$\omega_6 = \alpha_p n_p k_{1h} A_E \tilde{\rho}_{NO} \tag{E}$$

$$\overline{\omega_i} = \overline{\rho}\int_t \int_\eta \left(\omega_i(\xi, \eta, h)/\rho(\xi, \eta, h)\right)\tilde{P}(\xi)\tilde{P}(\eta)d\eta d\xi \qquad i = 1 - 5 \tag{F}$$

$$\tilde{\zeta}_{O_2} = \left(\frac{\tilde{X}_{O_2}^{eq} - \tilde{X}_{O_2}}{\tilde{X}_{O_2}^{eq} - \tilde{X}_{O_2}^{min}}\right)$$

$$\tilde{\zeta}_{N_2} = \left(\frac{\tilde{X}_{N_2} - \tilde{X}_{N_2}^{eq}}{\tilde{X}_{N_2}^{max} - \tilde{X}_{N_2}^{eq}}\right) \text{ or } \tilde{\zeta}_{N_2} = \left(\frac{\tilde{X}_{N_2}^{eq} - \tilde{X}_{N_2}}{\tilde{X}_{N_2}^{eq} - \tilde{X}_{N_2}^{min}}\right)$$

$$\tilde{\zeta}_i = \left(\frac{\tilde{X}_i^f - \tilde{X}_i}{\tilde{X}_i^f - \tilde{X}_i^{min}}\right) \qquad i = HCN, NH_3$$

$$\tilde{\zeta}_{NO} = \left(\frac{\tilde{X}_{NO}}{\tilde{X}_{NO}^f + \tilde{X}_{NO}^{eq}}\right) \tag{G}$$

$$\tilde{Y}_i = \tilde{Y}_i^{eq} - \tilde{Y}_{NO}\frac{M_i}{M_{NO}} \qquad i = N_2, O_2 \tag{H}$$

$$\tilde{X}_i = \tilde{Y}_i \frac{M_{max}}{M_i} \qquad i = N_2, O_2, HCN, NH_3, NO \tag{I}$$

$$X_{OH} = \tilde{X}_{OH}^{eq}$$

$$X_{O_2} = X_{O_2}^{eq} - \left(X_{O_2}^{eq} - X_{O_2}^{min}\right)\tilde{\zeta}_{O_2}$$

$$X_{N_2} = X_{N_2}^{eq} - \left(X_{N_2}^{max} - X_{N_2}^{eq}\right)\tilde{\zeta}_{N_2}$$

$$X_i = X_i^f - \left(X_i^f - X_i^{min}\right)\tilde{\zeta}_i \qquad i = HCN, NH_3$$

$$X_{NO} = \left(X_{NO}^{eq} + X_{NO}^f\right)\tilde{\zeta}_{NO}$$

$$X_i^{min} = \max\left(0.0, X_i^{eq} - \left(\frac{X_{HCN}^f}{M_{HCN}} + \frac{X_{NH_3}^f}{M_{NH_3}} + \frac{X_{NO}^{eq}}{M_{NO}}\right)\frac{M_i}{2}\right) \qquad i = O_2, N_2$$

$$X_{N_2}^{max} = X_{N_2}^{eq} + \left(\frac{X_{HCN}^f}{M_{HCN}} + \frac{X_{NH_3}^f}{M_{NH_3}}\right)\frac{M_{N_2}}{2}$$

$$X_i^{min} = \max\left(0.0, X_i^f - \left(X_{O_2}^{eq} 4 M_i / M_{O_2}\right)\right) \qquad i = HCN, NH_3{}^a$$

[a] A factor of 4 is used since every molecule of NO formed byoxidation of HCN or NH_3 can reduce another NH_3 or HCN molecule to N_2

TABLE II.G-1. (Continued)

Equation	Definition
A	Species continuity for HCN, NH_3, and NO
B	Overall mean reaction rate (shown here for NO)
C	Individual instantaneous reactions for homogeneous fuel NO formation and destruction
D	Instantaneous reaction for homogeneous thermal NO formation
E	Mean and instantaneous reaction of NO decay by char surface
F	Individual mean reaction rates by convolving overprobability density functions
G	Species extents of reaction or deviation from equilibrium
H	Species mass fractions
I	Species mole fractions

Symbol	Definition	Units
A_E	char surface area	m^2
D	turbulent viscosity	$m^2 s^{-1}$
h	mixture enthalpy	$J\ kg^{-1}$
k	Ahrrenius rate constant	$m^3\ kmole^{-1}\ s^{-1}$
M	molecular weight	$kg\ kgmole^{-1}$
n	particle number density	m^{-3}
P	pressure	Pa
r	radial coordinate direction	m
R	universal gas constant	$m^3\ Pa\ kmole^{-1}K^{-1}$
T	temperature	K
u	axial velocity	$m\ s^{-1}$
v	radial velocity	$m\ s^{-1}$
W	overall mean reaction rate or source term	$kg_i\ m^{-3}\ s^{-1}$
Y	species mass fraction	$kg_i\ kg^{-1}{}_{mix}$
x	axial coordinate direction	m
X	species mole fraction	$moles_i\ moles^{-1}{}_{mix}$
α_p	particle weight	kg
α_n	fraction of coal nitrogen converted to HCN	-

Symbol	Definition	Units
f	primary mixture fraction	$kg_{primary}\ kg^{-1}{}_{mix}$
η	off-coal-gas mixture fraction	$kg_{coal\text{-}gas}\ kg^{-1}{}_{mix}$
ω	reaction expression	$kgmole_i\ m^{-3}\ s^{-1}$
ρ	density	$kg\ m^3$
ζ	extent of reaction	-

Subscript	Definition
h	heterogeneous reaction constant
f	fuel NO mechanism reaction constant
t	thermal NO mechanism reaction constant
f	primary mixture fraction
η	coal-off-gas mixture fraction

Superscript	Definition
f	full conversion of volatile fuel nitrogen to species
eq	equilibrium species value
max	maximum species value attainable by limiting reactants
min	minimum species value attainable by limiting reactants
~	Favre averaged quantity
—	Reynolds average quantity

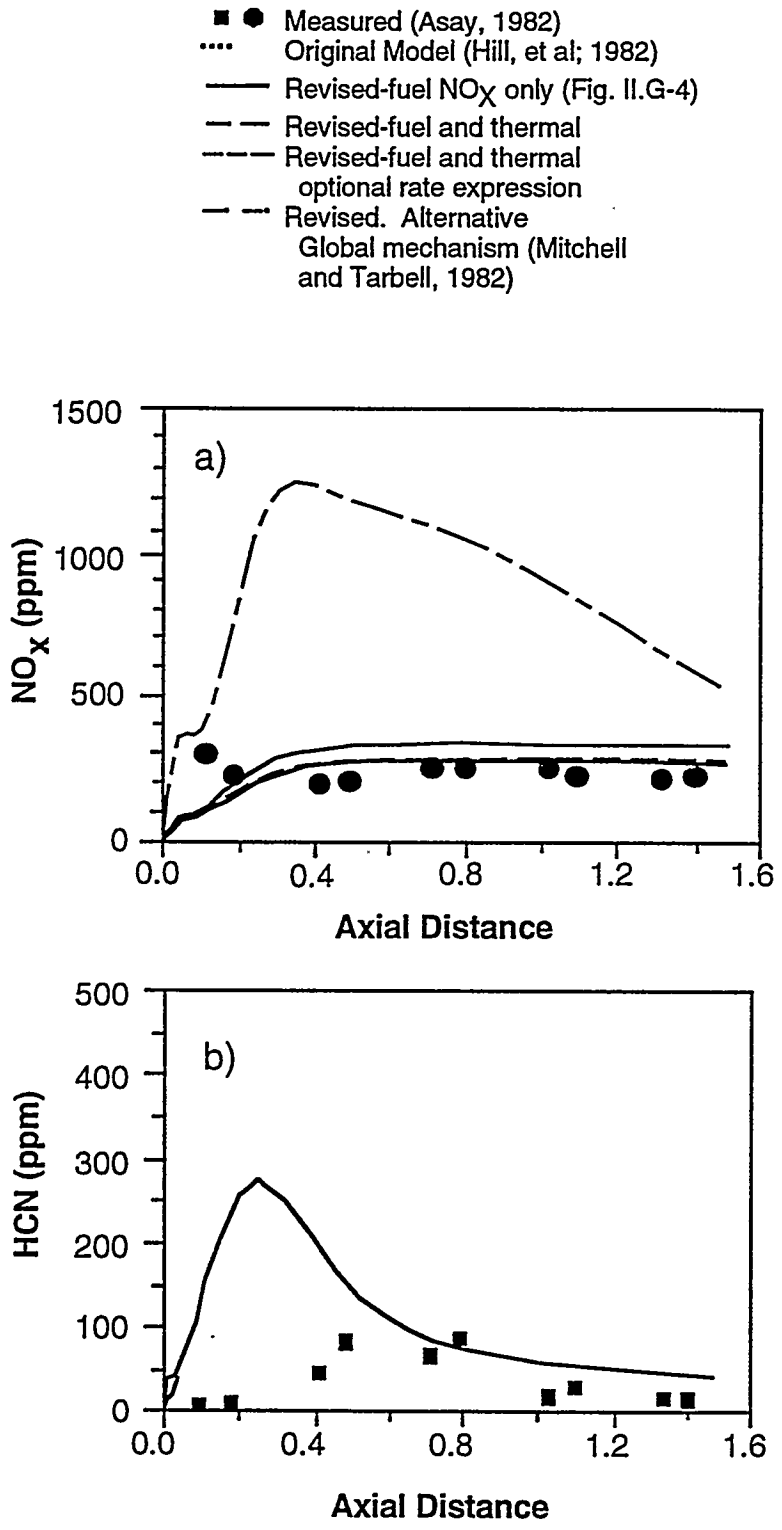

Figure II.G-3. Comparison of measured and predicted a) NO_x andb) HCN concentration using the original submodel and the revised submodel.

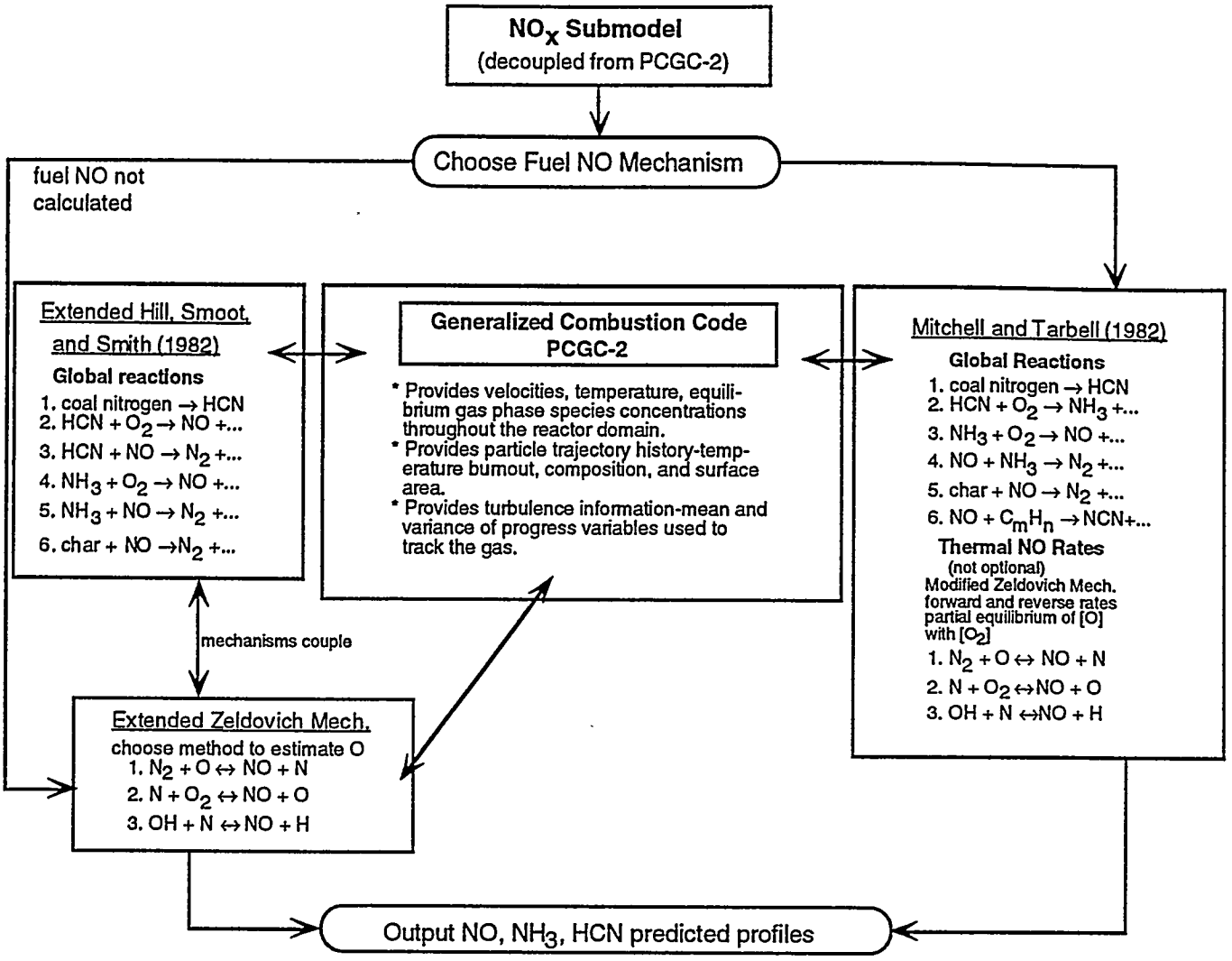

Figure II.G-4. Framework for the expanded fuel and thermal NO model coupled with PCGC-2.

Thermal NO_x Data - At the time this study was initiated, prospective data sources for evaluating the thermal NO mechanism were not available or were inadequate. Although a significant amount of work has been done to study the Zeldovich mechanism, the experimental investigations are limited to small, laboratory-scale burners and reactors. Table II.G-2 lists several investigations and summarizes the major limitations of each study in terms of use for model evaluation. Most studies have been conducted in either well-mixed or laminar flow systems.

New Measurements - Because of the lack of existing data to evaluate the thermal NO contributions of the NO_x model in turbulent combustors, a study was conducted at this laboratory under independent funding to measure thermal NO in a well-Controlled-Profile laboratory Reactor (CPR) constructed recently at Brigham Young University (Eatough, 1989). Tests were conducted by burning approximately 500,000 BTU/hr natural gas/air and propane/air mixtures. Figure II.G-5 shows a schematic of the reactor which has an internal diameter of 0.80 m and a length of 2.7 m. The burner consists of a concentric 2.3-cm-diameter primary tube and 9.8-cm diameter secondary tube equipped with a moveable swirl block generator. The composition of the natural gas (Table II.G-3) remained constant over the period of the test program.

TABLE II.G-2.
PARTIAL LIST OF EXPERIMENTAL THERMAL NO INVESTIGATIONS

Investigator	Reactor System	Fuel	Data Reported	Limitations[1]
Drake, et al. (1984) Drake et al. (1987)	Square duct turbulent jet fuel injector, co-flowing laminar air	$CO/H_2/B_2$ $CO/H_2/NH_3$	Axial and radial NO profiles	Non-axisymmetric Not fully turbulent Insufficient data
Peters & Donnerhach (1981)	110 mm i.d. pyrex tube: jet fuel injector co-flowing laminar air	H_2, CH_4, C_3H_8 natural gas, CO/H_2	NO production rate vs. Re & Fr	Insufficient data Not fully turbulent
Thompson, et al. (1981)	Variable length, 1 in i.d. tube: multiport flame holder	CH_4	H_2, CO, NO axial profiles	Large S/V ratio Oscillatory combustion Inlet geometry
Sadakata, et al. (1981)	80 mm i.d. tube, turbulent jet fuel injector, co-flowing laminar air	CO/H_2 NH_3 seeded	Exit data NO, HCN, NH_3	No source attribution Prompt NO formation possible
Semerjian & Vamos (1981)	Rectangular duct premixed flame	pre-vaporized Jet A fuel	CO, CO_2, NO_x, T axial profiles	Non-axisymmetric Prompt NO formation
Takagi, et al. (1981)	13.3 mm i.d. tube, turbulent jet fuel injector, co-flowing laminar air	H_2 Propane	H_2O, H_2, N_2, CO_2, NO & T axial and radial profiles	Not fully turbulent Prompt NO contributions for propane case
Tang and Churchill (1981)	9.7 mm i.d. tube, premixed laminar flow isothermal reactor	Hexane	CO, NO_x, T exit values for S. R. variation	Non-turbulent Small diameter
Song, et al. (1981)	5.4 cm i.d. tube premixed burner externally heated	Methane NH_3 seeded	NO, HCN, NH_3 radial & radial profiles	No source attribution Prompt NO formation
Singh, et al. (1978)	Jet-stirred	Methanol Methane	Major species, total NO_x, OH, CH radicals	Non-axisymmetric Prompt NO formation
Malte, et al. (1977)	Jet-stirred	CO	NO, T	Non-axisymmetric Insufficient data
Iverach, et al. (1973)	Meker-type burner	CO, H_2, CH_4, C_3H_8, C_2H_4, C_2H_2	O_2, CO, CO_2, O, T, NO rates, axial profile exit NO vs. S.R.	Non-equilibrium chemistry Prompt NO formation
Sarofim & Pohl (1973)	2.5 cm diameter flat-flame, premixed burner	Methane	CO_2, H_2O, CO, T CH_4 axial profiles	Non-turbulent Prompt NO formation possible
Fenimore (1971)	Meker-type burner and porous plate burner	CH_4, C_2H_4, C_3H_8	NO vs. S. R.	Burner geometry Non-turbulent Insufficient data

[1]Limitations with respect to evaluation of the NO_x submodel, combined with the comprehensive combustion model, and applied to practical, turbulent combustors.

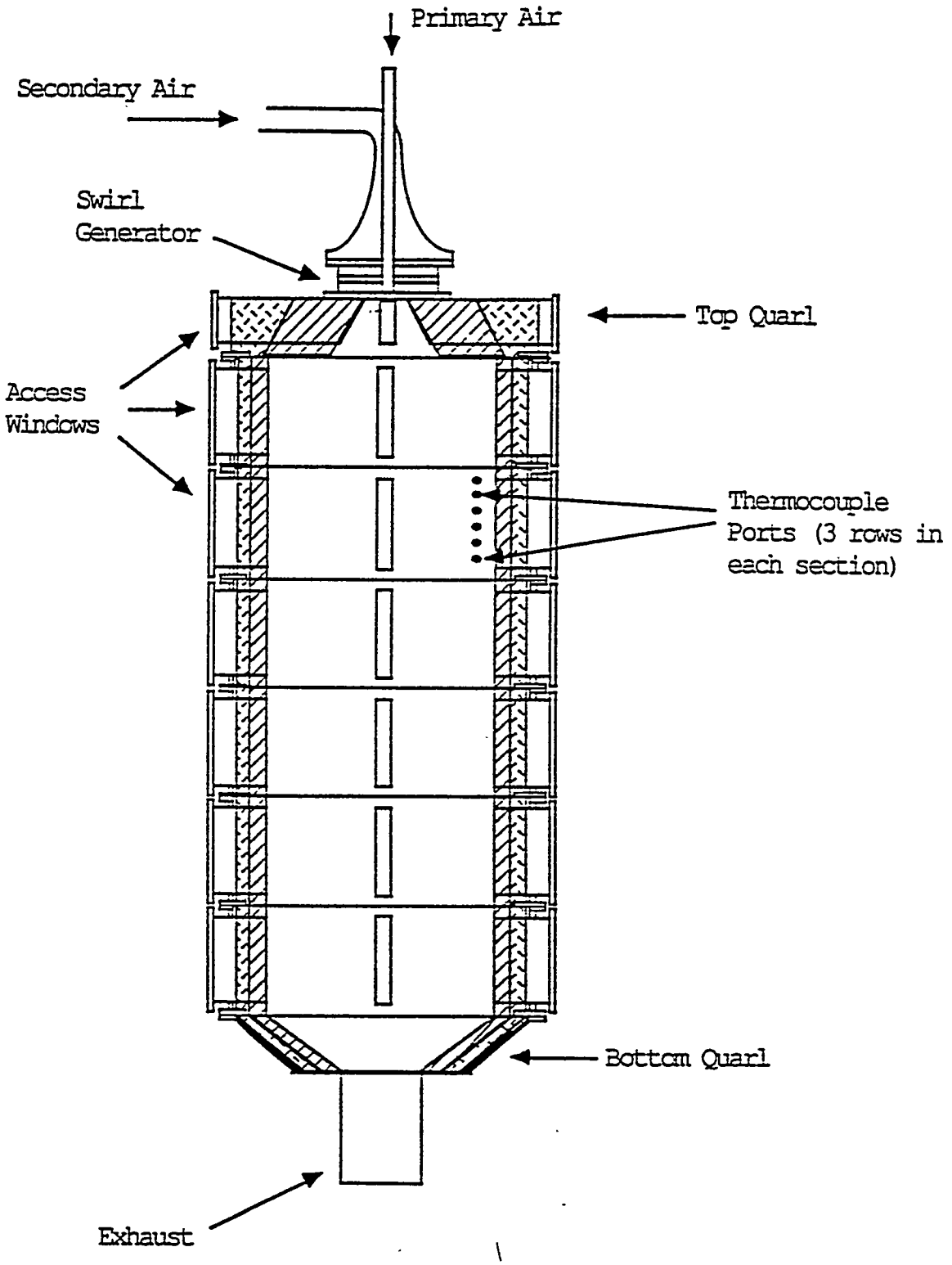

Figure II.G-5. Schematic of BYU-ACERC controlled profile reactor, in which thermal NO_x measurements in natural-gas/air combustion were measured (Eatough, 1989).

TABLE II.G-3

COMPOSITION OF NATURAL GAS AND EXPERIMENTAL OPERATIONAL PARAMETERS

Fuel Composition (by gas chromatograph)

Species	Mole Percent	
N_2	0.6±.1	
CO_2	0.7±.1	
CH_4	88.8±.8	PHT = 0.2 ppm
C_2H_6	6.5±.4	H_20 = 64 ppm
C_3H_8	2.2±.2	TBM = 2.1 ppm
iso-C_4	0.22±.03	
n-C_4	0.2 ±.03	specific gravity = 0.62-0.63
iso-C_5	0.09±.02	Heating Value = 1085-1100 BTU/ft^3
n-C_5	0.08±.02	
C_{6+}	0.06±.02	

Feed Rates for ϕ = 0.98 (by calibrated rotameter and calibrated choked flow nozzle)

Primary (fuel) 0.5430 kgmol hr^{-1}, 298 K

Secondary (air) 5.9230 kg mol hr^{-1}, 298 K

Wall Temperature Control (by electrically-heated and water-cooled walls)

1000-1100K

Effluent and radial-profile gas species compositions were collected with a water-quenched, stainless-steel probe. A NO_x chemiluminescence analyzer was used to monitor NO and NO_2 and a gas-chromatograph was used to measure CO_2, CO, O_2, N_2. Gas temperature profiles were measured using a shielded suction pyrometer. The wall temperature was monitored by multiple thermocouples and controlled with electrical heaters control and to reduce reactor heat loss and to establish an isothermal wall temperature profile at approximately 1050 K throughout the reactor. NO_x concentrations were measured for systematic variation of equivalence ratios with simultaneous variation of secondary-air swirl number.

The range of equivalence ratios was limited to 0.90-1.00 to reduce contributions of N_2O formation to thermal NO_x (at equivalence ratios below 0.90) and from NO_2 formation (at equivalence ratios above 1.0). Below an equivalence ratio of 1.0, prompt NO formation is greatly reduced and will not significantly contribute to total NO concentrations. The conversion of NO back to HCN was not measured in these tests but will be accomplished in future work. Velocity profiles are also being measured to map recirculation zones and to calibrate the swirl block generator.

Tests were conducted to compare differences between propane and natural gas combustion at equivalent heating rates and an equivalence ratio of 1.0 for swirl numbers of 0.0, 1.5 and 3.0. No significant difference between measured effluent NO concentrations was measured for the two gases as demonstrated in Fig. II.G-6. This observation supports the desired goal to avoid prompt NO formation which presumably would be higher for methane flames based on previous experiments (e.g. Song et al., 1981; Fenimore, 1971; and Peters and Donnerhach, 1981). Because little difference in NO concentration was observed between the two fuels, natural gas was used for the remainder of the test program.

Figure II.G-7 plots the variation of measured thermal NO versus secondary-air swirl number for equivalence ratios of 1.00, 0.95, and 0.90. A similar trend is observed for each equivalence ratio with peak NO concentrations being measured at a theoretical swirl number of 1.5. This result shows the

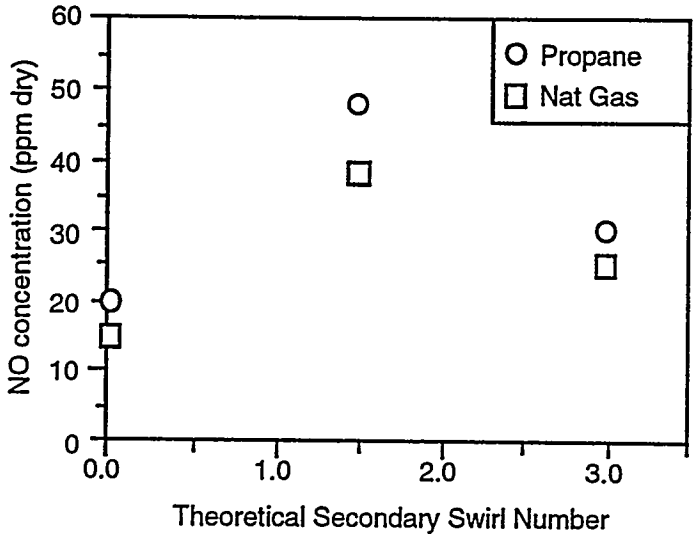

Figure II.G-6 Comparison of effluent NO concentrations for propane and natural gas diffusion flames at equivalent stoichiometries (ϕ=1.0) and similar heating rates.

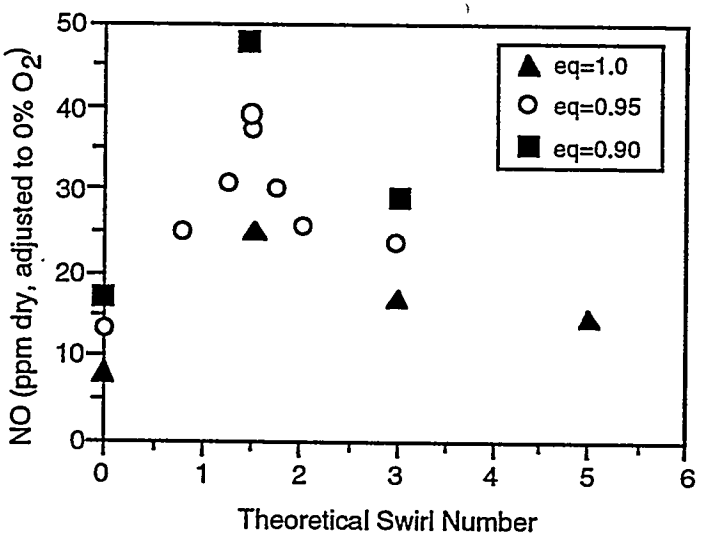

Figure II.G-7. Measured effluent NO concentrations for a 500,000 BTU/hr natural gas diffusion flames (adjusted to 0% oxygen since equivalence ratio, (eq.) varies).

impact of mixing and flame structure on the thermal environment of the furnace. As swirl number was increased up to approximately 1.5, the flame attached to the burner, resulting in a shorter flame length and higher peak temperature in the region of pure inlet air. In the large-diameter reactor in which these tests were conducted, wall effects on the burner aerodynamics are greatly reduced. Strong recirculation patterns along the reactor centerline in proximity of the burner were observed during the experimental study. As swirl number is further increased, the flame becomes aerodynamically unstable and detaches from the quarl. Since these effects are strongly related to the mixing process, the data provide an excellent test of the combined comprehensive model and NO_x submodel theory.

The trend of thermal NO passing through a maximum as swirl number increases is opposite to the trend commonly observed for fuel NO formation. In previous coal combustion tests, NO_x concentrations have been observed to initially decrease with increasing secondary swirl number for a similar burner configuration. Fuel NO then passes through a minimum at a secondary swirl number of 1.5 (Asay, 1982). This trend also is attributed to the mixing process. As swirl number increases, a fuel-rich zone is established in which fuel nitrogen species are destroyed rather than being oxidized to NO. As swirl number increases further, the stable, fuel-rich zone is broken down and intense mixing of the secondary oxidizer increases the formation of NO.

Figure II.G-8 shows the spatial resolution for NO_x concentrations in the reactor for an equivalence ratio of 0.98 and a theoretical swirl number of 1.5. The profiles reveal that thermal NO_x is formed in the early burner region along the flame front where temperature and oxidizer concentrations are high. Shortly following the flame zone, NO_x concentrations mix in the bulk flow but do not decay significantly before exiting the reactor.

Comparisons with Profile Measurements - Figure II.G-9 compares predicted NO profiles with NO data measured in a BYU/ACERC reactor (Boardman, 1990). The predictions follow the general trend of each radial profile, although predicted values are generally lower.

The experimental data suggest that prompt NO formation and possibly other NO_x formation and destruction kinetics not included in the NOx submodel are important in swirling, natural gas diffusion flames. Thus, the mechanism alone is not capable of predicting the complete detail of nitrogen chemistry in swirling-flow, natural gas diffusion flames, even when the overall stoichiometry is fuel-lean. Still, the NO_x model shows that thermal NO is the dominating source of NO_x in Figure II.G-9 for the flame conditions indicated.

In the 14th Quarterly Report (Solomon et al. 1990), experimental data were presented which show that the effects of swirl on effluent NO emissions are varied, and depend on other parameters in addition to secondary swirl number. One important parameter is the ratio of primary-stream (fuel inlet) velocity to secondary-stream (air) inlet velocity. Experimental data were collected in the BYU/ACERC Controlled-Profile Reactor (CPR) for two separate primary tube diameters. A primary tube diameter of 2.6 cm yields a primary stream velocity approximately equal to the secondary-air inlet velocity. A 1.4-cm-diameter primary tube was then used to increase the primary inlet velocity relative to the secondary inlet velocity. Two different trends with increasing swirl were measured for these two burner configurations.

Effect of Equivalence Ratio - Tests at three on the fuel-lean side ($0.9 \leq \phi \leq 1.0$) provided effluent NO concentrations. These data were compared with NO_x model prediction using both options for estimating oxygen atom concentrations (Eqns. II.G-8 and II.G-9). Figure II.G-10 compares the predicted NO concentrations with the experimental values measured (with independent funding) in the ACERC controlled-profile reactor over a narrow range of overall fuel-to-oxidizer equivalence ratios with a secondary air swirl number of 1.5. Thermal NO is substantially overpredicted at lower equivalence ratios (fuel-lean conditions) when carbon equilibrium is assumed. When oxygen equilibrium is assumed, thermal NO is slightly underpredicted. Predictions were not made for higher equivalence ratios where

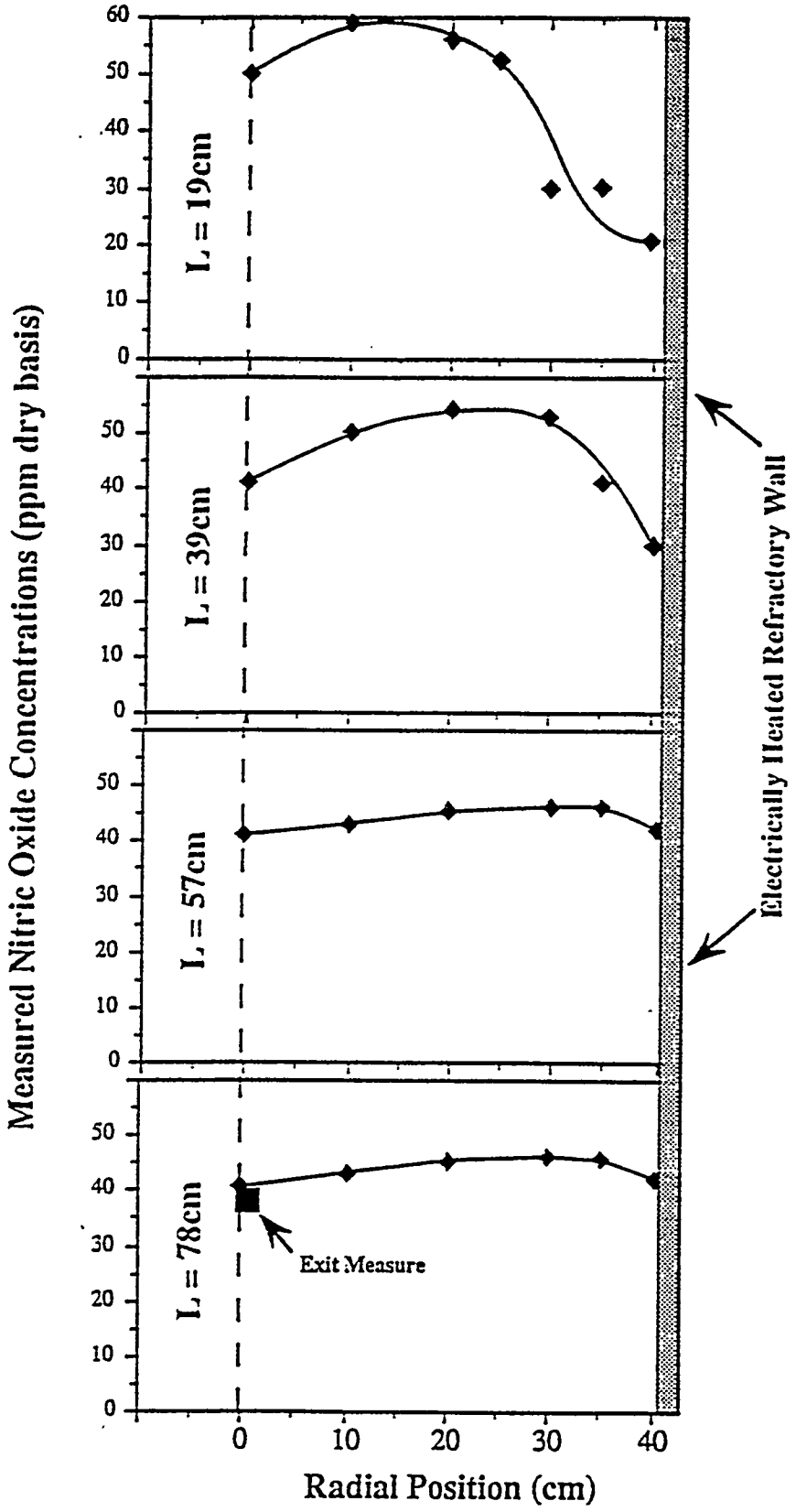

Figure II.G-8. Measured effluent NO concentrations for a 500,000 BTU/hr natural gas/air diffusion flame (ϕ=0.98), theoretical secondary swirl number = 1.5.

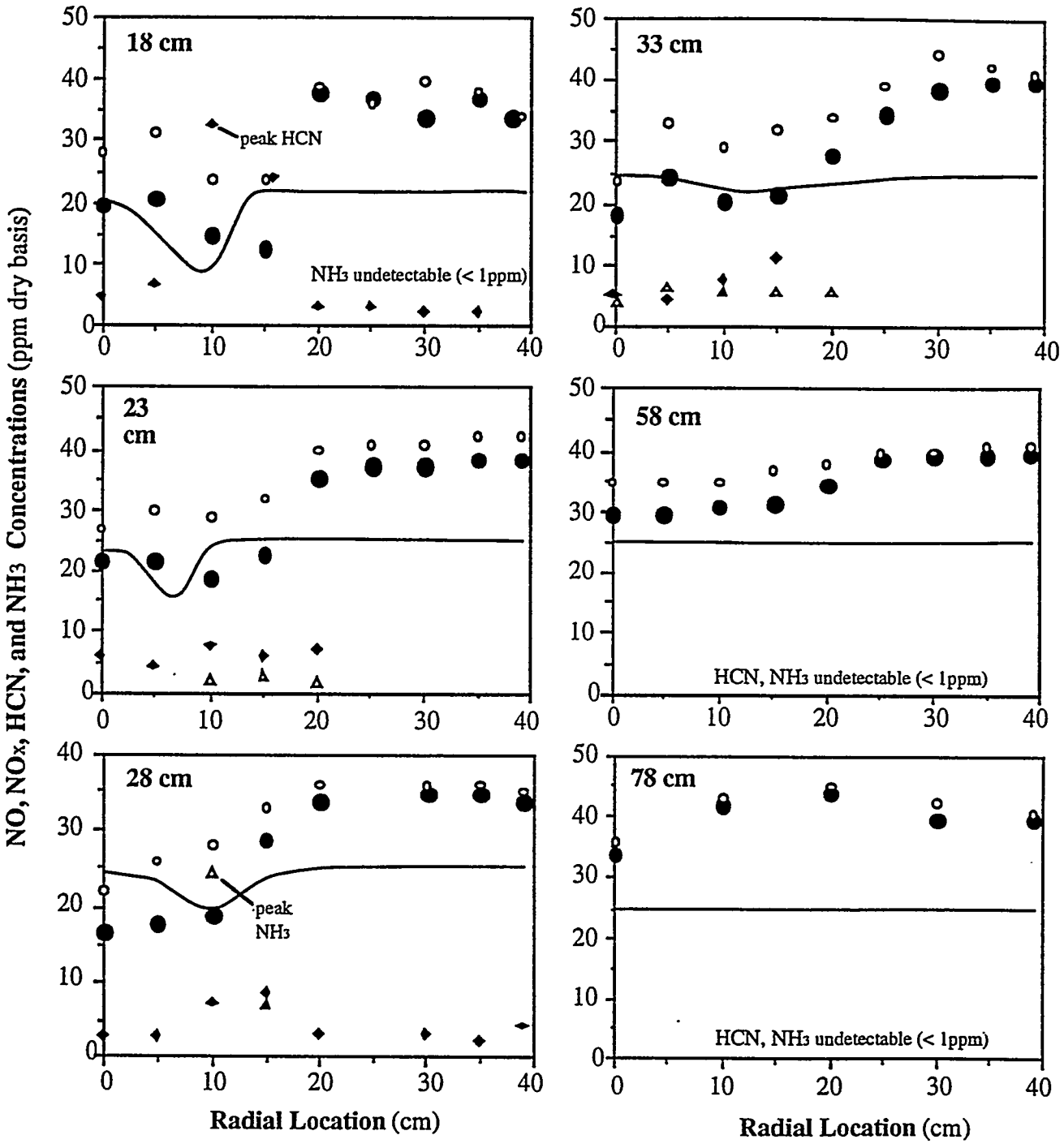

Figure II.G-9. Comparison of predicted thermal NO with measured NO for a 500,000 BTU/hr natural gas/air diffusion flame. Axial location of radial profiles listed in upper left corner. Other measured species (NO_x, HCN, and NH_3) are also shown. Data measured in a CPR reactor. Equivalence ratio=0.98; Secondary air swirl=1.5.

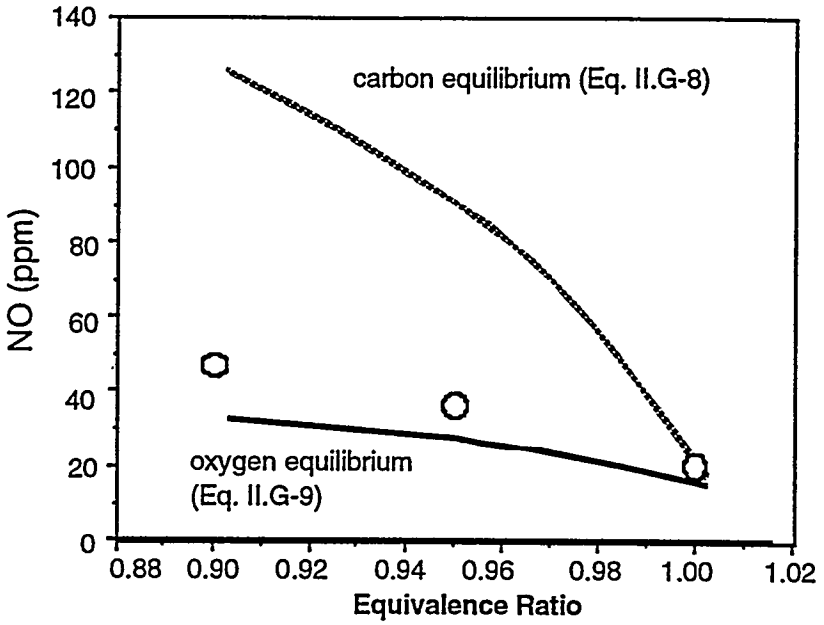

Figure II.G-10. Comparison of predictive methods used to estimate atomic oxygen concentrations with measured data (circles) for natural gas combustion in the ACERC controlled-profile reactor; Secondary swirl no. = 1.5; heating rate = 147 kW.

carbon equilibrium may give more accurate predictions. However, these results provide some guidance for using the NO model for practical burner conditions, which are normally fuel-lean. All NO_x model predictions in this study made use of the oxygen equilibrium expression. (Eqn. II.G-9)

Comparisons with Effluent Measurements - NO_x submodel computations were made to investigate the capability of the Zeldovich mechanism to predict the influence of swirl number. The predicted and measured NO concentrations are compared in Fig. II.G-11. Qualitative trend agreement is achieved for the larger primary tube while, for the smaller primary tube, the submodel fails to predict the correct trend at higher swirl numbers, though the magnitude of NO concentrations is about right. The differences between model predictions and measurements can be attributed to several factors, including the importance of other reactions not accounted for in the model. In addition, predictions of the governing flame structure, particularly the temperature field, were not evaluated and may have contributed to the differences. The NO_x submodel was more successful in predicting trends of decreasing overall fuel-to-air equivalence ratio as shown in Fig.II.G-10.

The evaluation of the Zeldovich mechanism showed NO concentration levels that were generally consistent with observations. However, some limitations of the NO model for predicting thermal NO concentrations in practical gas-fired combustors were noted. The relative importance of prompt NO and other reactions (i.e. NO_2 and N_2O chemistry) cannot be definitively determined from these predictions but appear to be significant at all values of swirl number for diffusion flames. Considerable sensitivity to the method used to predict radical oxygen concentration was demonstrated. Nevertheless, the qualitative agreement between the predicted and measured NO demonstrates that the model can be employed as a tool to aid in burner design procedures. When coupled with reliable data, its complementary role in gas-fired burner design will be enhanced. However, the absence of a comprehensive kinetic mechanism to predict nitrogen chemistry prevents the code from being able to predict quantitative NO emissions for complex gas-fired burners with established reliability.

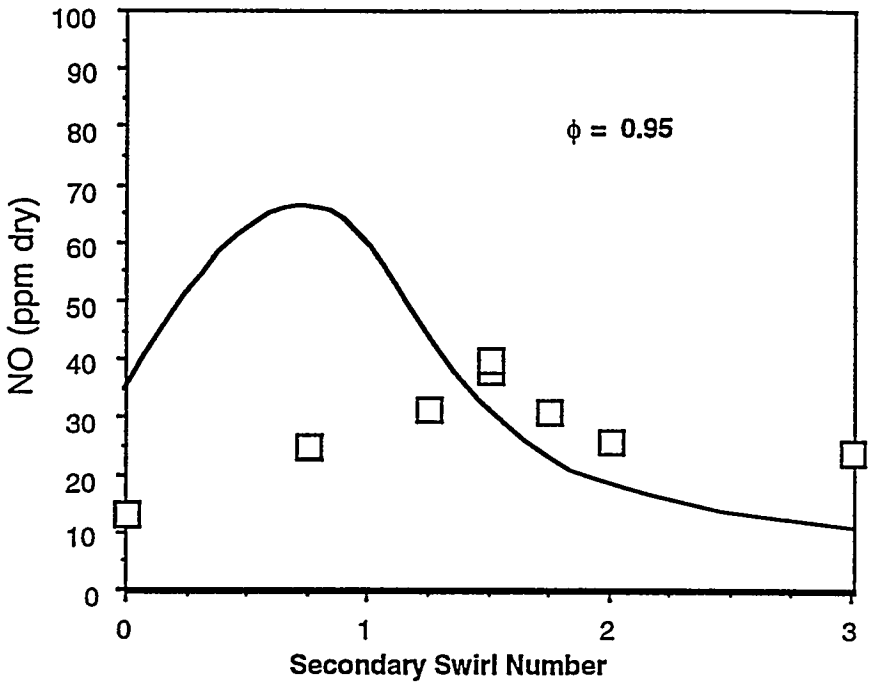

a.primary tube = 2.6 cm

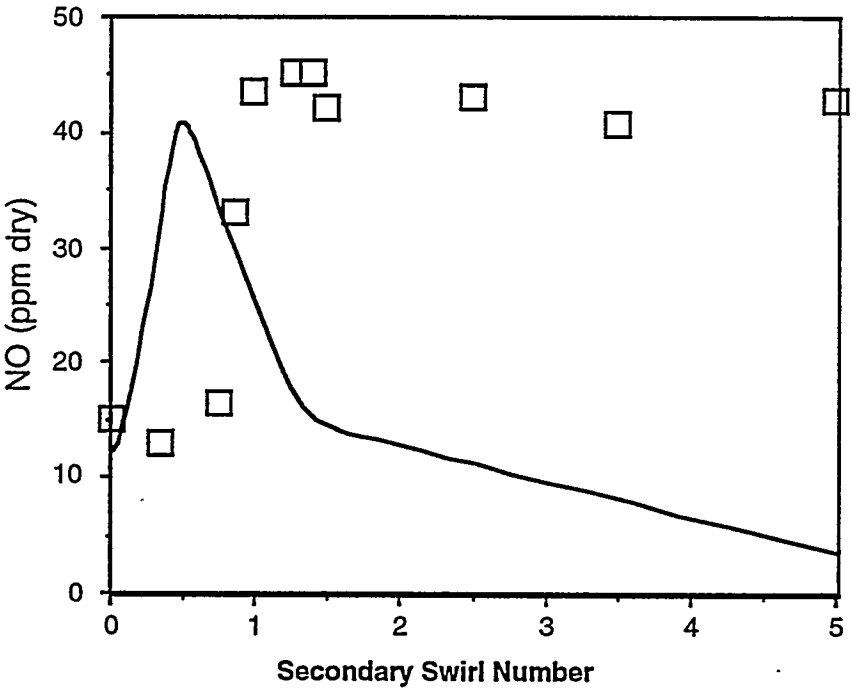

b.primary tube = 1.4 cm

Figure II.G-11. Comparison of predicted (curve and measured (symbols)) NO concentrations for systematic variation in secondary swirl number holding equivalence ratio constant. Data measured in the BYU/ACERC reactor for a 6,000 BTU/hr natural gas diffusion flame.

Comparisons in Fuel-Rich Systems - One of the objectives of this subtask was to consider the effects of fuel-rich conditions and high pressure on nitrogen chemistry in pulverized-fuel systems. The capability of the NO_x model to predict nitrogen pollutants during oxygen-blown, pulverized coal gasification was investigated for Utah bituminous coal and North Dakota lignite. Figure II.G-12 compares measured and predicted nitric oxide iso-contours for high pressure (5 atm) gasification of Utah bituminous coal.

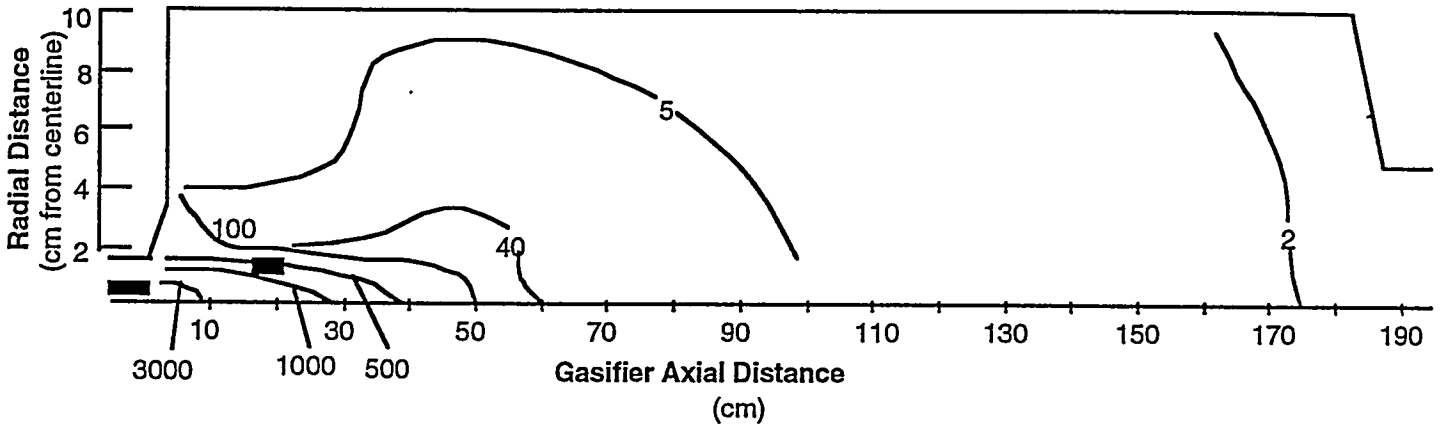

a. Measured NO (ppm-dry basis) Data are from Nichols (1985).

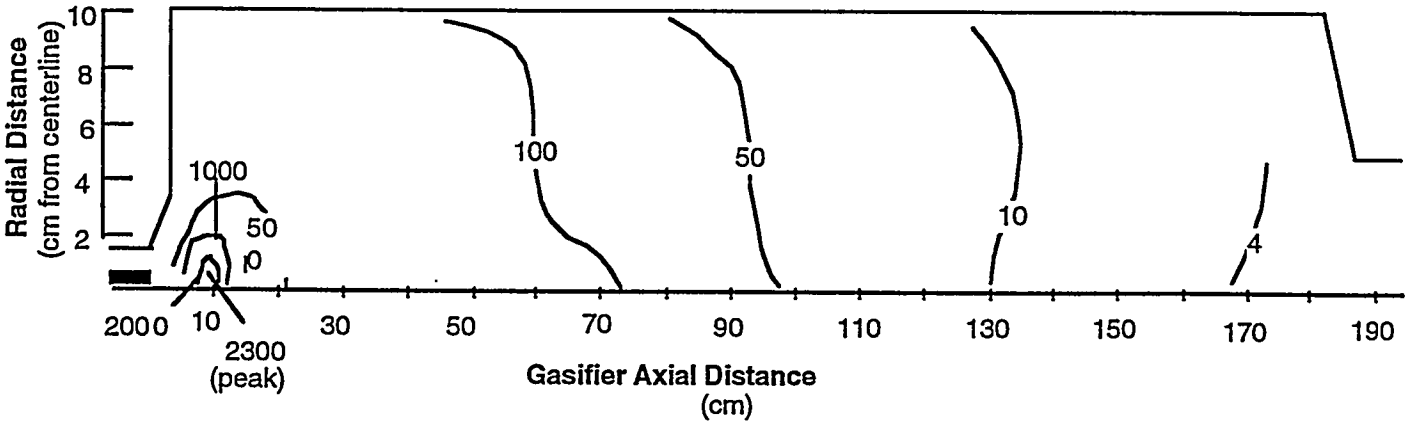

b. Predicted fuel NO (ppm-dry basis) not including thermal NO contributions.

Figure II.G-12 Comparison between measured and predicted NO concentration isopleths for pressurized Utah bituminous coal gasification.

Predictions compare quite well with measurements. However, predictions are initially lower than the measured NO concentrations, and the predicted concentrations do not decay quite as fast as the experimental data.

In these model predictions, thermal NO contributions were not included but were determined to be of possible importance for this case. In the experimental tests, nitrogen is used to blanket the coal in the coal feed hopper. Nichols (1985) speculated that this nitrogen was responsible for discrepancies in nitrogen mass balances. The NO_x model showed that even small amounts of nitrogen added to the primary inlet stream could convert to NO by thermal fixation in the oxygen - rich inlet where the maximum temperature is approximately 3000 K. Thus, with the inclusion of thermal NO in the model, and some amount of nitrogen added to the coal inlet stream to account for coal-hopper nitrogen, it was possible to account for the difference between measured and fuel NO predictions in the near-burner region. However, this also led to higher NO concentrations being predicted in the aft-burner region. The NO_x model is capable of predicting the formation of NO_x under extremely fuel-rich, high pressure conditions in detail in certain areas of the reactor.

It is speculated that the high sooting potential of bituminous coals could lead to soot-NO reduction in the post-burner region of the gasifier. This could explain the faster reduction of NO observed in the experiments. The model does not account for either soot formation or soot-nitrogen reduction. Cheng et al. (1989) showed that soot can destroy NO. Haussmann et al. (1989) have shown that bituminous coals have a large propensity for forming soot, especially when devolatilization is rapid and the local flame environment is fuel-rich. The gasification conditions meet these criteria; therefore, soot may have had some influence on the fast rate of NO reduction in the test reactor.

The prediction of nitrogen species for extremely fuel-rich gasification was considered in light of the fact that NH_3 may be an initial product of coal devolatilization. The data of Brown (1985) reveal substantial concentrations of NH_3 before HCN builds up in the reactor. This experimental observation was also exhibited for Wyoming subituminous coal gasification data but not for Illinois No. 6 or Utah bituminous coal (Brown, 1985). This evidence suggests that nitrogen release for low-rank coals at extremely fuel-rich conditions includes NH_3 as well as HCN.

The NO_x model was used to investigate the importance of NH_3 by varying the amount of coal nitrogen evolved directly as HCN and NH_3. Three cases were considered: 1) all nitrogen evolves at a rate proportional to total coal mass loss in the form of HCN; 2) all nitrogen evolves at a rate proportional to total coal mass loss in equal amounts of HCN and NH_3, and 3) nitrogen release is delayed until 20 percent of the total coal mass has been lost from the coal with the nitrogen being released in equal amounts of HCN and NH_3. Impetus for Case 3 comes from experimental observations that nitrogen release from low-rank coals occurs at a rate proportional to the volatiles release after an induction period during which approximately 20 percent of the initial coal volatiles is nitrogen-free (Haussmann et al., 1988; Pohl and Sarofim, 1977).

Case 1 results are shown in Fig. II.G-13. Here the predicted HCN concentrations are compared with the sum of measured HCN and NH_3 since the predicted HCN decays directly to NO. The agreement between predicted and measured NO concentrations is not good. Case 2 results are not shown but gave improved agreement between the predicted and measured effluent concentrations for all nitrogen species, although the predicted profiles still failed to match the experimental data. Case 3 resulted in the most favorable predictions (see Figure II.G-14) for all species, although the NO profile data are still not quantitatively predicted. The NO profile also suggests that the flame ignition was delayed, although attempts to delay the ignition by lowering the inlet stream enthalpy did not substantially improve the agreement between the NO predictions and measurements. Still, the model improvements are substantial and suggest that NH_3 may be evolved from lignite coal during extremely fuel-rich gasification

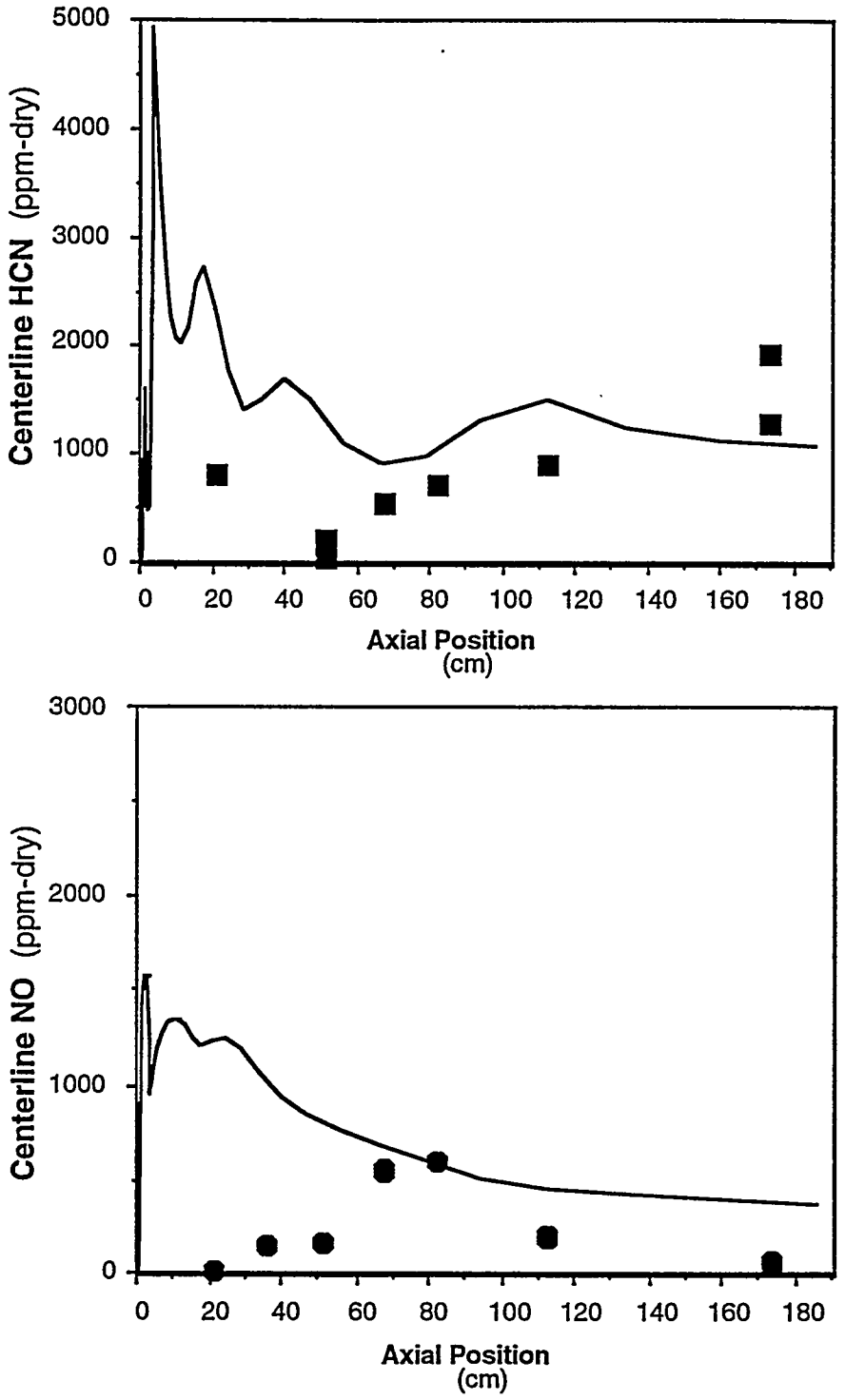

Figure II.G-13. Case-1: Comparison between predicted and measured NO and HCN centerline profiles for North Dakota lignite gasification. Predictions assume all coal nitrogen is released as HCN at a rate proportional to total coal mass loss. (Data from Nichols, 1985).

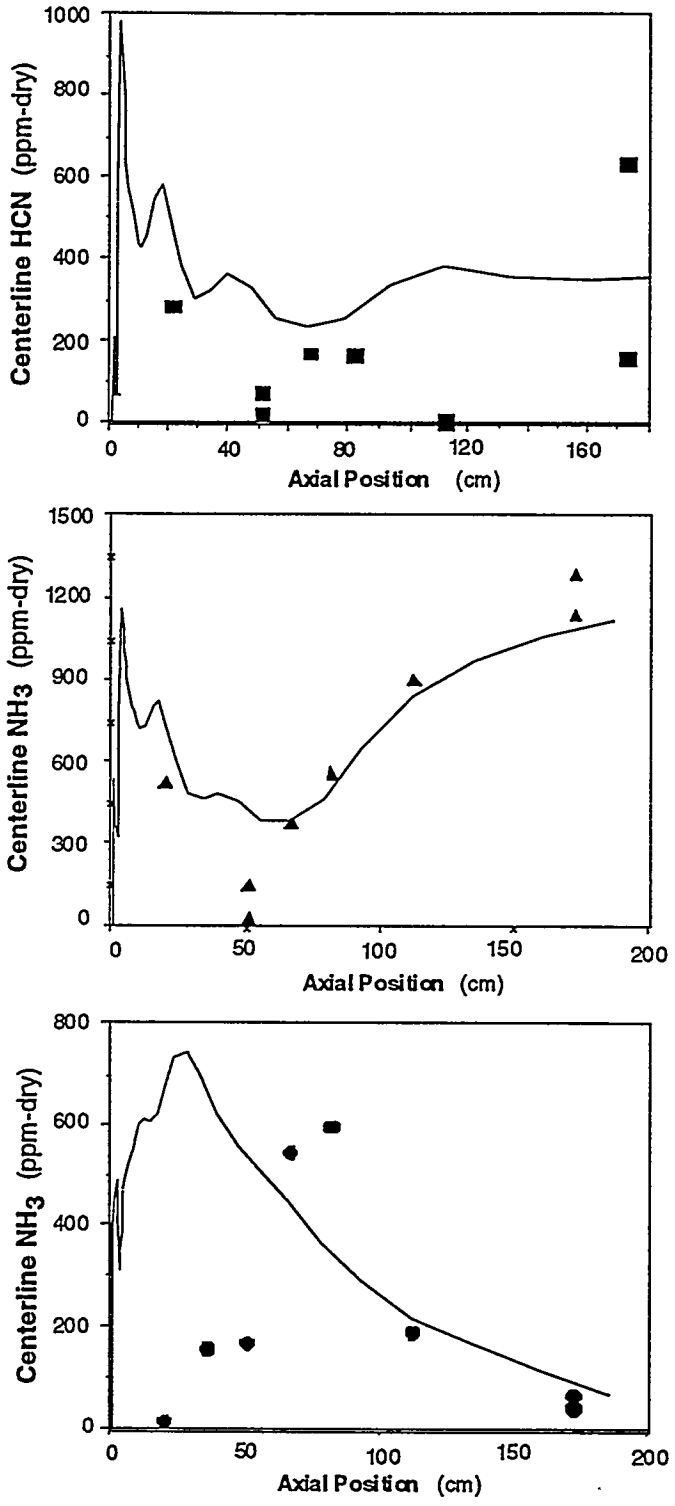

Figure II.G-14. Case 3: Comparison between predicted and measured nitrogen species centerline profiles for North Dakota lignite gasification. Predictions assume coal nitrogen is released after 20% of the coal matter is devolatilized. Nitrogen is released as equal amounts of HCN and NH_3. (Data from Nichols, 1985).

since the NO model predictions show improved agreement with the measured data. Also, need for an advanced nitrogen devolatilization model is evident. though accounting for turbulence effects in the gas chemistry will be complicated.

Joint Thermal/Fuel NO_x - Thermal NO increases production as the combustion temperature goes up. For the gasification cases, a small amount of diluent nitrogen (used to blanket the coal and also for sight window purging) leads to substantial thermal NO formation. Figure II.G-15 is one example where the contribution of thermal NO is significant in certain areas of the reactor. The relative importance of thermal NO in practical combustors, where the temperature exceeds that observed in experimental reactors, can be calculated using the revised NO model. Since prompt NO is far less significant in coal flames, the joint prediction of thermal and fuel NO may be adequate for modeling many coal flames.

SO_x/Sorbent Reactions Submodel

The work on this portion of the subtask was also conducted principally by Dr. Richard Boardman. Dr. Scott Brewster assisted with the integration, implementation, and evaluation of the submodel in PCGC-2. A publication based on this work is being prepared.

Theoretical Foundations - When hydrated lime [$Ca(OH)_2$] or limestone [calcium carbonate ($CaCO_3$)] is injected into a combustor, calcination occurs:

$$CaCO_3(s) \rightarrow CaO(s) + CO_2(g) \qquad \text{(II.G-11)}$$

$$Ca(OH)_2(s) \rightarrow CaO(s) + H_2O(g) \qquad \text{(II.G-12)}$$

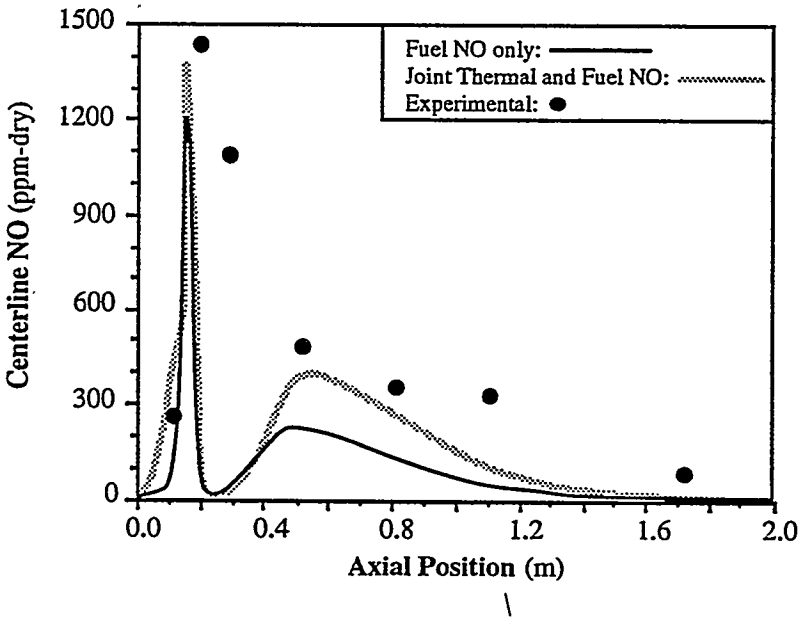

Figure II.G-15. Comparison between measured and predicted NO centerline concentrations for gasification of Utah bituminous coal at 1 atm. Predicted curves made with and without the thermal NO mechanism included in the calculation. Data are from Brown (1985).

Complete calcination of a $CaCO_3$ particle yields a particle of CaO with about 50 percent free pore volume. Scanning electron micrographs (SEM) reveal that the surface structure resembles overlapping spherical grains. For $Ca(OH)_2$-derived CaO, sheets or plates line the surface (Milne et al., 1990).

Once calcined material is produced, sulfur capture can occur, provided the temperature is conducive for sulfation reactions. The intrinsic heterogeneous kinetics for this process have been difficult to elucidate, because a solid product layer is formed through which the reactant must diffuse. The following simplified reactions are generally accepted to occur:

$$CaO(s) + 1/2\,O_2(g) + SO_2(g) \rightarrow CaSO_4(s) \qquad \text{(II.G-13)}$$

$$CaO(s) + H_2S(g) \rightarrow CaS(s) + H_2O(g) \qquad \text{(II.G-14)}$$

$$CaO(s) + SO_3(g) \rightarrow CaSO_4(s) \qquad \text{(II.G-15)}$$

The overall reaction process involves mass transfer of gaseous sulfur species (and oxygen in the case of SO_2 capture) to the calcined sorbent surface, diffusion through the intergranular pores, diffusion through the solid product layer, and finally reaction with CaO. Because the molar volume of $CaSO_4$ is greater than the molar volume of CaO, the capture of SO_2 decreases the pore radius and eventually closes off the pores. Thus, there is a limit to the extent of conversion possible when SO_2 is captured. The sulfation process for H_2S does not fill the pores as rapidly.

Two parameters which govern the effectiveness of calcium-based sorbent reactions are: 1) the effective surface area for reaction, which is a function of the sorbent type and its thermal history, and 2) the residence time of the calcined sorbent at temperatures favorable for sulfation. Significant sulfation occurs in a temperature window of 1140-1500 K (Borgwardt et al., 1987). Above 1500 K, sulfation is inhibited by particle sintering and grain growth. Below 1140 K, the sulfation kinetics are too slow. Thus, for maximum effectiveness, the sorbent should be injected into the combustor at a point where the longest residence time can be obtained at the optimum temperature conditions and where high temperatures that cause sintering are avoided. In addition, effective mixing with the sulfur-laden gas stream is needed.

A comprehensive combustion model that can accurately predict the combustor conditions and, subsequently, the mixing and reaction of injected sorbent particles would be a useful tool in applying this technology. The optimum location for sorbent injection that would maximize overall capture efficiency could then be determined for various sorbent chemical and physical properties, reactor geometries, etc.

A number of theoretical sulfation models have been developed for interpreting laboratory sorbent capture data. Most of the mathematical models assume that the solid particles are porous spheres composed of spherical grains or cylindrical pores. The more sophisticated models incorporate a distribution of grains or pores and account for void reduction as the sulfation reactions proceed. The structural parameters for these models are often based on nitrogen absorption and mercury penetration data for BET surface area and pore volume. The models generally fall into two categories: 1) models which are based on a material balance of the solid CaO, and 2) models that are based on a material balance in the pores. A mathematical description of these models is presented by Kocaefe et al. (1987) and Kramlich et al. (1989).

Sulfation Model - A shrinking-core grain model developed and evaluated by Silcox et al. (1985, 1989) was used as the basis for creating a sorbent reaction submodel in PCGC-2. This model assumes that calcined sorbent particles consist of an agglomeration of small spherical grains of CaO. Sulfation occurs by the following sequence of physical and chemical events:

(1) diffusion of reactants from the bulk gas to the particle surface,
(2) pore diffusion of reactants to the particle internal (i.e. grain) surface,

(3) solid-state diffusion through the solid product layer (except at the onset of reaction), and
(4) reaction with CaO.

As sulfation proceeds, the core of unreacted CaO shrinks while a layer of product builds up on the outside of individual grains. Because the molar volume of $CaSO_4$ is 2.7 times greater than the molar volume of CaO (see Table II.G-4), the void space between the grains is gradually filled and blocked. Thus, there is a practical limit to conversion which favors smaller particles. Figure. II.G-16 gives a conceptual view of the shrinking-core grain model for a sorbent particle with a radius of R_p. The enlargement of an area of grains at an internal radius of R (or a subshell) illustrates the band of reaction product (e.g. $CaSO_4$) with product radius of $r_{g'}$, extended beyond the original grain radius, r_g, and the core radius, r, of the unreacted, calcined material (CaO).

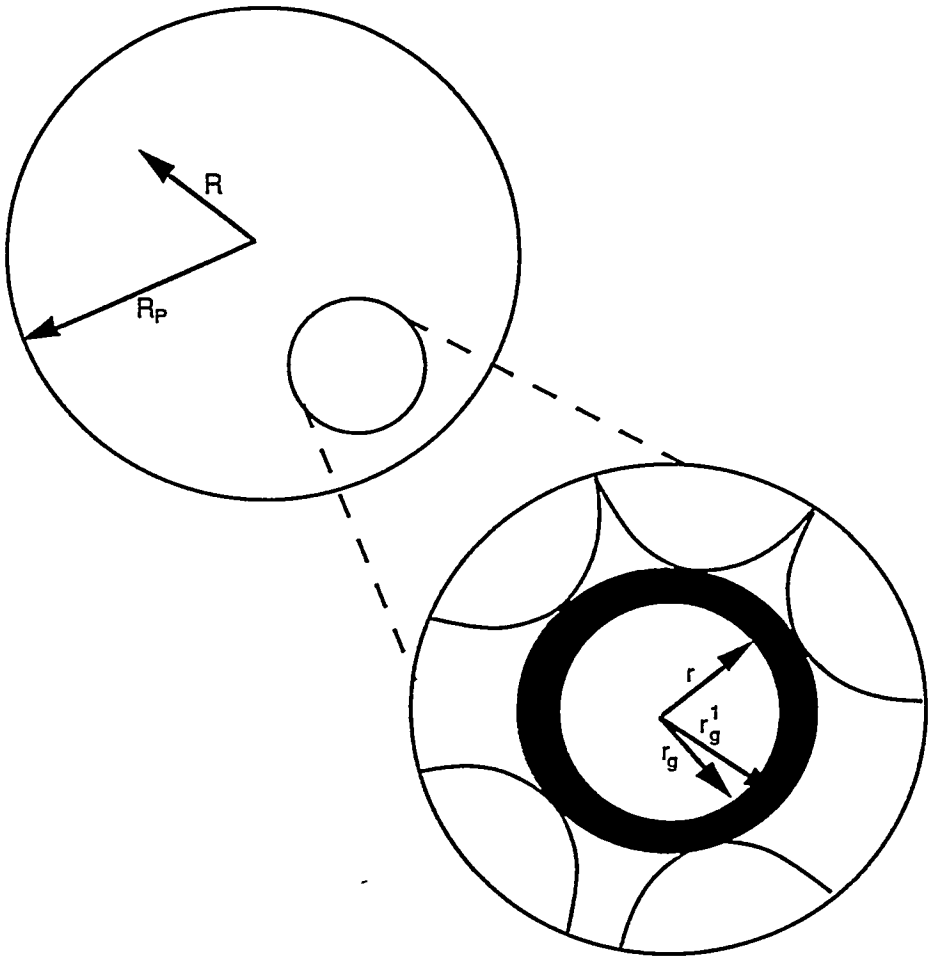

Figure II.G-16. A schematic of the grain model.
The enlarged view of the porous particle shows a dark band of product of raduis r_g, the initial grain radius r^1_g, and the radius of the unreacted core of reactant, r. (Adapted from Silcox, 1985).

TABLE II.G-4
SULFATION SUBMODEL PARAMETERS USED TO VALIDATE THE SORBENT REACTIONS SUBMODEL
(refs. given in the text)

Parameter	SO_2	H_2S
CaO molar volume, $cm^3 \cdot mol^{-1}$	16.91	16.91
$CaSO_4$ molar volume, $cm^3 \cdot mol^{-1}$	46.0	N/A
CaS molar volume, $cm^3 \cdot mol^{-1}$	N/A	25.8
BET surface area, $m^2\ g^{-1}$	100	100
Ca/S molar ratio in feed	3.2	3.0
Particle diameter, μm	8	8
Solid-state product diffusivity: $D_{sp} = D_o \exp(-E/RT)$, $cm^2 \cdot s^{-1}$		
D_o	0.0124	0.118
E/R	12,200	15,900
First-order reaction rate: $k = k_o \exp(-E/RT)$, $cm \cdot s^{-1}$		
k_o	291	67,700
E/R	7,510	19,566

For spherical sorbent particles, a material balance for the reacting gas in a concentric shell of the particle yields

$$\frac{d^2C}{dR^2} + \left(\frac{2}{R} + \frac{1}{D_{eff}}\frac{dD_{eff}}{dR}\right)\frac{dC}{dR} - \frac{N}{D_{eff}} = 0 \qquad \text{(II.G-16)}$$

where C is the SO_2 concentration, R is the radial coordinate of the sorbent, D_{eff} is the effective pore diffusivity, and N is the rate of reaction per unit volume of porous solid. The appropriate boundary conditions are

$$D_{eff}\frac{dC}{dR} = k_m(C_b - C) \quad \text{at } R = R_p \qquad \text{(II.G-17)}$$

$$\frac{\partial C}{\partial R} = 0 \quad \text{at } R = 0 \qquad \text{(II.G-18)}$$

Here, C_b is the reactant concentration in the bulk gas, and k_m is a mass transfer coefficient which can be obtained from the Sherwood number.

The reaction term, N, is given for reaction of order n with respect to the sulfur-containing reactant, by,

$$N = \frac{C^n}{\frac{1}{k_f} + \frac{r^2}{D_{sp}}\left(\frac{1}{r} - \frac{1}{r_g}\right)}(A), \quad \text{mol cm}^{-3}\ \text{s}^{-1} \qquad \text{(II.G-19)}$$

where k_f is the forward reaction rate (Eqn. II.G-13), D_{sp} is the diffusion coefficient of SO_2 in the solid product layer, and A is the interfacial area available for reaction per unit of volume. A complete equation set for the sorbent reaction submodel is given in Table II.G-5.

The sulfation grain model is solved at discrete time steps as the particle progresses through the combustor. Thus, the instantaneous sorbent particle conversion (sulfation) is dependent on the local gaseous properties (composition, temperature, etc.).

TABLE II.G-5

SORBENT-REACTION SUBMODEL EQUATION SET

Equation	Definition
$\frac{d^2[SO_2]}{dR^2} + \left(\frac{2}{R} + \frac{1}{D_{eff}}\frac{dD_{eff}}{dR}\right)\frac{d[SO_2]}{dR} - \frac{N}{D_{eff}} = 0$	Material balance on SO_2 in a spherical shell Used to calculate $[SO_2]$ at each sorbent particle subshell.
$@\ R = 0\ ;\ \frac{d[SO_2]}{dR} = 0$ $@\ R = R_p\ ;\ [SO_2]_{R_p} = [SO_2]_{xp,yp,dt}$	Boundary conditions
$N = k_{1/2} A [SO_2]^{\frac{1}{2}}_{r_{cor(i)}}$	Half-order volumetric consumption rate
$N = k_1 A [SO_2]^{1}_{r_{cor(i)}}$	First-order volumetric consumption rate
$A = 3z(1 - e_c)\frac{r^3}{r^3_{cor(i)}}$	Interfacial area available for reaction at ith subshell
$z = \left\{\frac{\rho_{CaO}}{\rho_{MgO}}\left(\frac{1}{W} - 1\right) + 1\right\}^{-1}$	Fraction of grains which are CaO
$W = \left\{1 + \left(\frac{1 - Y}{Y}\right)\left(\frac{M_{MgO} M_{CaCO_3}}{M_{MgCO_3} M_{CaO}}\right)\right\}^{-1}$	Weight fraction of CaO in the calcine on an "impurity-free" basis
$\frac{dr_{cor(i)}}{dt} = \left(\frac{-M_{CaO}}{\rho_{CaO}}\right) K_n [SO_2]^{n}_{r_{rear(i)}}$	Material balance on CaO at product-CaO interface for nth order reaction
$[SO_2]_{r_{rear(i)}} = \frac{D_{sp}[SO_2]_{R_{(i)}}}{D_{sp} + K_1 r_{cor(i)}\left(1 - \frac{r_{cor(i)}}{r_{ext(i)}}\right)}$	Interfacial concentration for ith subshell for first-order reaction rate
$[SO_2]_{r_{rear(i)}} = \frac{2[SO_2]_{R_{(i)}} - \alpha - \left(-4[SO_2]_{R_{(i)}}\alpha + \alpha^2\right)^{\frac{1}{2}}}{2}$ where, $\alpha = -\left(\frac{K_{1/2} r_{cor(i)}}{D_{sp}}\right)^2\left(1 - \frac{r_{cor(i)}}{r_{ext(i)}}\right)^2$	Interfacial concentration for ith subshell for half-order reaction rate
$r_{ext(i)} = \left\{\left(\frac{r_g^3 - r_{cor(i)}}{1 - e_s}\right)\left(\frac{\rho_{CaO} M_{CaSO_4}}{\rho_{CaSO_4} M_{CaO}}\right) + r^3_{cor(i)}\right\}^{\frac{1}{3}}$	Extended grain radius

TABLE II.G-5 (CONTINUED)

Equation	Definition
$r_g = \frac{3}{\rho_{CaO}\left(BET\ surface\ area\right)}$	Initial grain radius
$e_x = 1 - \left(1 - e_c\right)\left\{1 + \left(\frac{\left(\frac{a}{1-e_g} - 1\right)X}{1 + \frac{\rho_{CaO}\left(1-W\right)}{\rho_{MgO}W}}\right)\right\}$	Particle void fraction
$X_{R(i)} = 1 - \left(\frac{r_{cor(i)}}{r_g}\right)^3$	Extent of grain conversion at ith subshell
$X(t) = \frac{3}{R_p^3}\int_0^{R_p} R_{(i)}^2 X_{R(i)} dR$	Overall conversion of sorbent particle
$K_1 = 291\ exp\left(\frac{-7510}{T}\right)\ cm\ sec^{-1}$	First-order reaction rate constant
$K_{1/2} = 0.0307\ exp\left(\frac{-6970}{T}\right)\ gmol^{\frac{1}{2}} cm^{\frac{-1}{2}}\ sec^{-1}$	Half-order reaction rate constant
$D_{eff} = \left(\frac{1}{\frac{1}{D_M} + \frac{1}{D_K}}\right)e_x^2$	Effective diffusivity
$D_M = exp\left(1.66\ ln\left(T\right) - 11.3\right)\ \ cm^2\ sec^{-1}$	Bulk diffusivity for SO_2-air binary-pair
$D_K = 19,400\ \frac{e_e}{\rho_{CaO}\left(BET\ surface\ area\right)}\sqrt{\frac{T}{M_{SO_2}}}$ $cm^{-2}\ sec^{-1}$	Knudsen diffusion coefficient
$D_S = 0.0124\ exp\left(\frac{-12,000}{T}\right)\ \ cm^2\ sec^{-1}$	Product layer diffusion coefficient**

§ Equations reference number in Silcox (1985). Rate constants and diffusion coefficients derived by Silcox from experimental data as cited by Silcox (1985)
** Also see Table II.G-4 for product layer diffusion coefficient

The reaction rate parameters and solid-state diffusion rates which were used for the sulfation of SO_2 and H_2S were taken from Silcox (1985) and were listed in Table II.G-1. The solid-state diffusivity and reaction rate parameters were obtained by correlating experimental data of Borgwardt et al. (1984) the Borgwardt and Roache (1984). Other sorbent particle properties used to characterize the sorbent particles were based on values in the literature. The submodel was validated using a first-order reaction rate (with respect to SO_2 and H_2S). The reaction order with respect to SO_2 is generally believed to be ~0.6. A first-order reaction rate was used in these predictions to simplify the calculation procedure.

Integration into PCGC-2 - The proposed framework for the SO_x/sorbent reactions submodel in PCGC-2 is shown in Fig. II.G-17. An equilibrium approach was adopted for predicting the formation of gas-phase sulfur species. A justification for this approach is provided below. Any list of sulfur species can be calculated, and in the current study, SO_2, SO_3, H_2S, COS, and CS_2 were considered. SO_2 and SO_3 are the main species formed during fuel-lean pulverized coal combustion, while H_2S, COS, and CS_2 are also formed during fuel-rich combustion and gasification. Typically, SO_2 dominates the pool of sulfur-containing species during combustion while H_2S often dominates during fuel-rich combustion and gasification.

Use of the Equilibrium Approach - Simulations of atmospheric combustion Utah bituminous and Wyoming subbituminous coal were used to evaluate the equilibrium approach for predicting sulfur pollutant species. Simulations of high-pressure (5 atm) gasification of Utah bituminous coal and North Dakota lignite were also used. Both combustion cases were diffusion flames with an equivalence ratio of 1.0 and a secondary swirl number of 2.0, Fig. II.G-18 shows predicted and experimental radial profiles for SO_2 and H_2S concentration for the Utah coal. Predicted and measured concentrations of other sulfur species were less than 10 ppm. The centerline SO_2 concentration is lower than the measured data, while the H_2S concentration is higher, particularly in the near-burner region. The sum of the SO_2 and H_2S concentrations, however, agrees well with the data in the near-burner region, supporting the assumption that sulfur is evolved from the coal at a rate which is about proportional to the total particle weight loss.

Figure II.G-19 shows the corresponding results for Wyoming subbituminous coal. SO_2 is predicted fairly well throughout the entire reactor. H_2S is initially over-predicted. For this case, the equilibrium approach appears to be suitable for predicting SO_2 and H_2S concentrations, particularly in the aft-region of the reactor where sorbents are typically injected.

Figures II.G-20 to 23 show results for the high-pressure gasification cases. While there is large scatter among the experimental data, the predicted curves generally follow the magnitude of the measurements for both coal types. Thus, for the development and demonstration of a first-generation sulfur pollutants submodel, local gaseous equilibrium of SO_2 and H_2S was assumed to establish starting concentrations for sorption.

Code Solution - An information flow diagram for the sorbent reactions submodel is shown in Fig. II.G-24. First, the reacting coal particle/gas flowfield is solved without the sorbent particles. Second, the Eulerian number density for the sorbent particles is calculated. Third, the Lagrangian trajectories for the reacting sorbent particles are calculated,resulting in source terms for SO_2 or H_2S due to sorbent reaction. Fourth, the continuity equation for SO_2 or H_2S is calculated, using the source terms calculated in Step 3. Steps 3 and 4 are repeated until the sulfur species continuity equation is satisfied. Details of the code implementation such as required input data and definitions of variables and subroutines can be found in the user's manual which is being prepared.

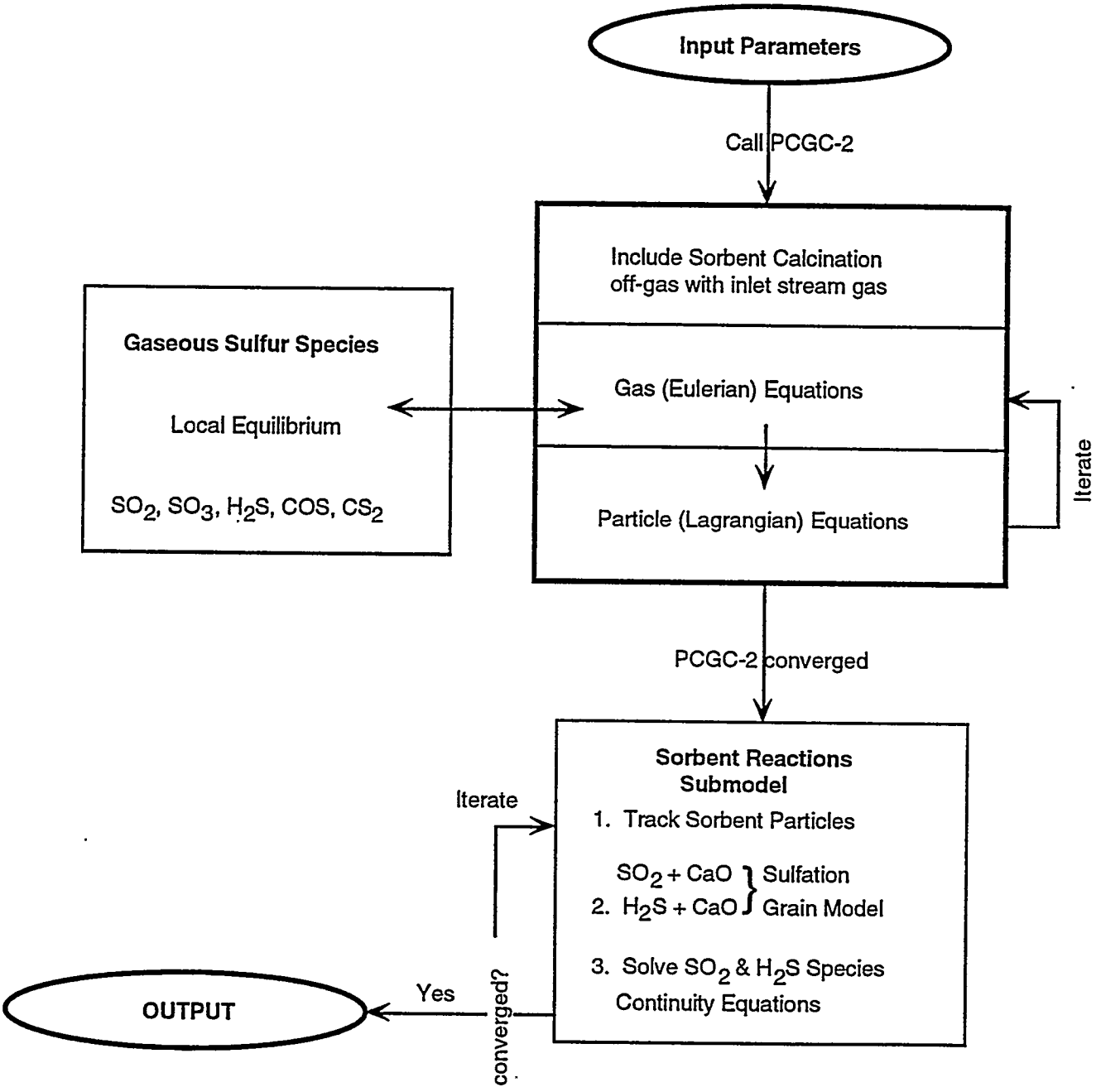

Figure II.G-17. SOx/sorbent-particle reaction submodel framework.

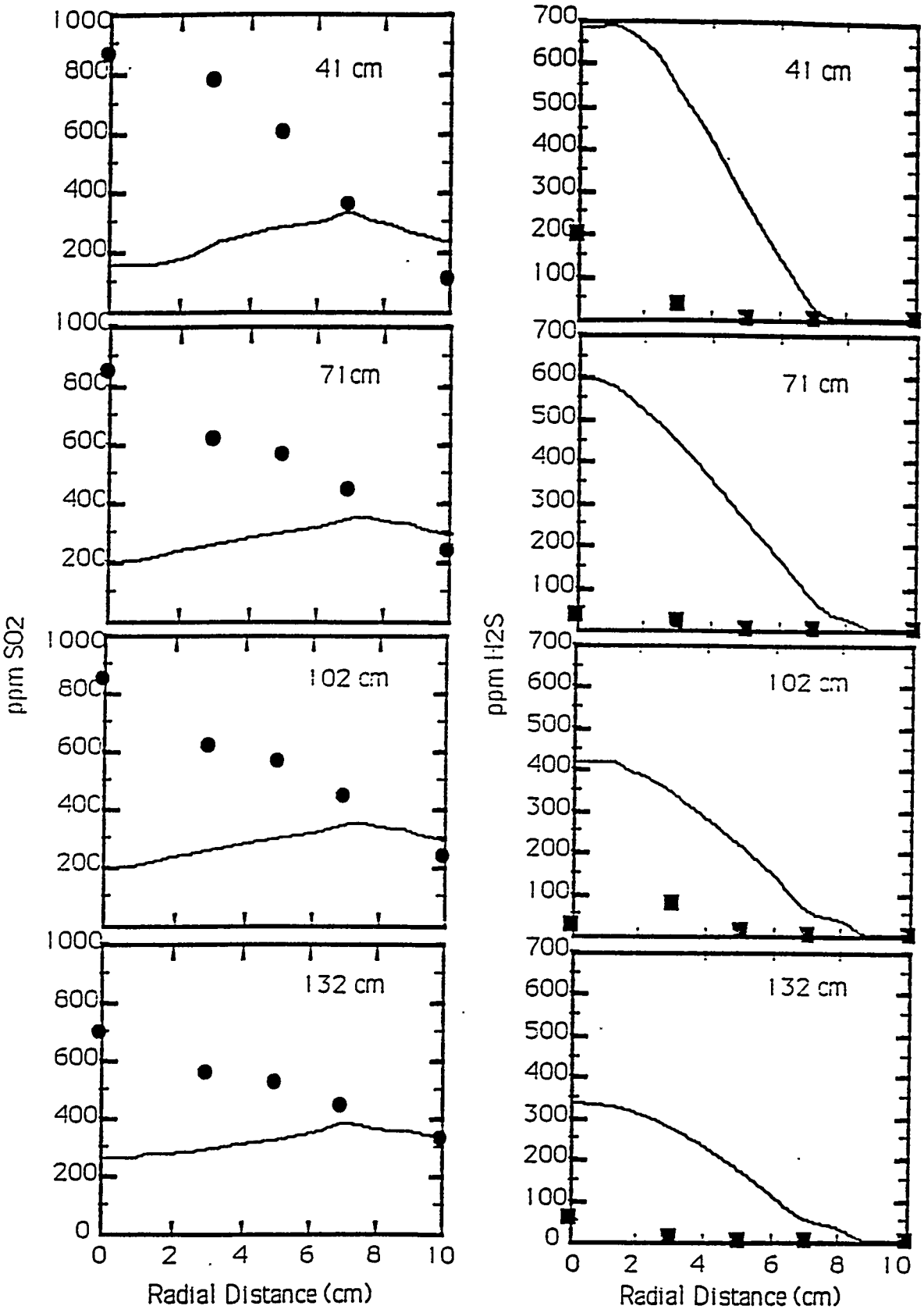

Figure II.G-18. Comparison of predicted and measured SO_2 and H_2S concentrations for combustion of Utah Bituminous coal; (S.R. = 1.0, Swirl No. = 2.2). Data from Zaugg (1984).

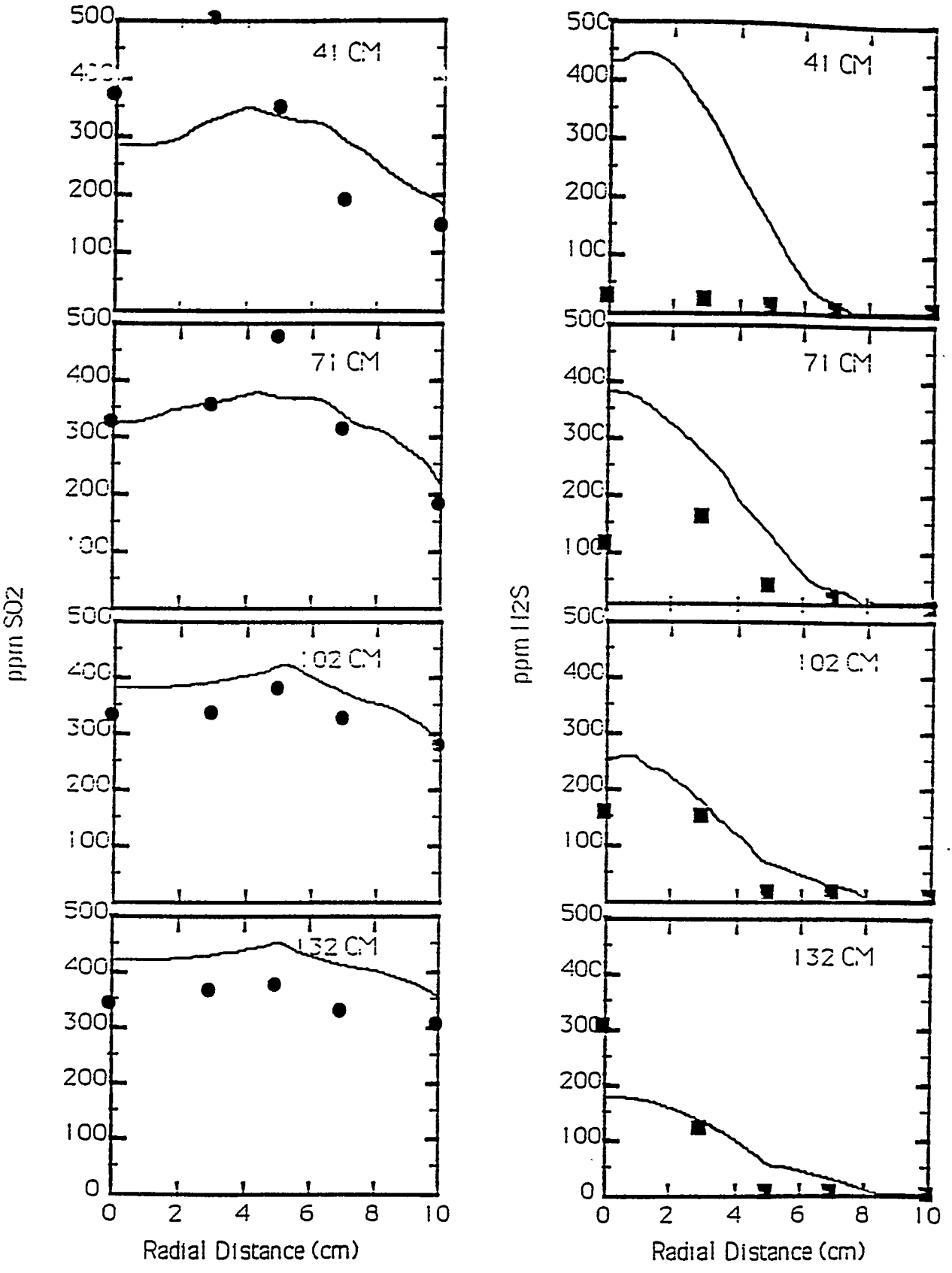

Figure II.G-19. Comparison of predicted and measured SO_2 and H_2S concentrations for combustion of Wyoming subbituminous coal; (S.R. = 1.0, Swirl No. = 3.0). Data from Zaugg (1984).

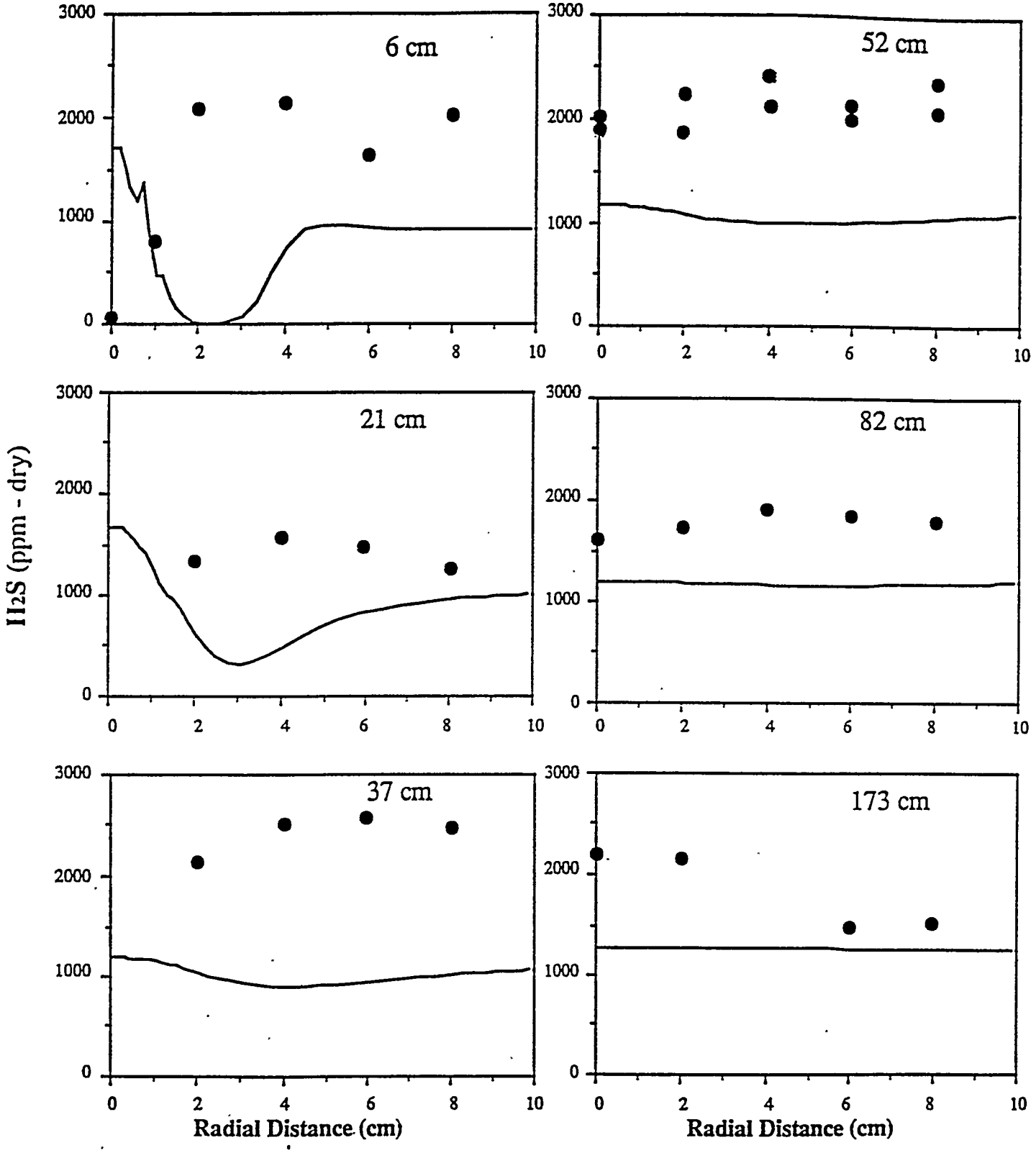

Figure II.G-20. Predicted and measured H_2S concentration for pressurized gasification 5 (atm) of Utah bituminous coal. Data from Nichols et al. (1989).

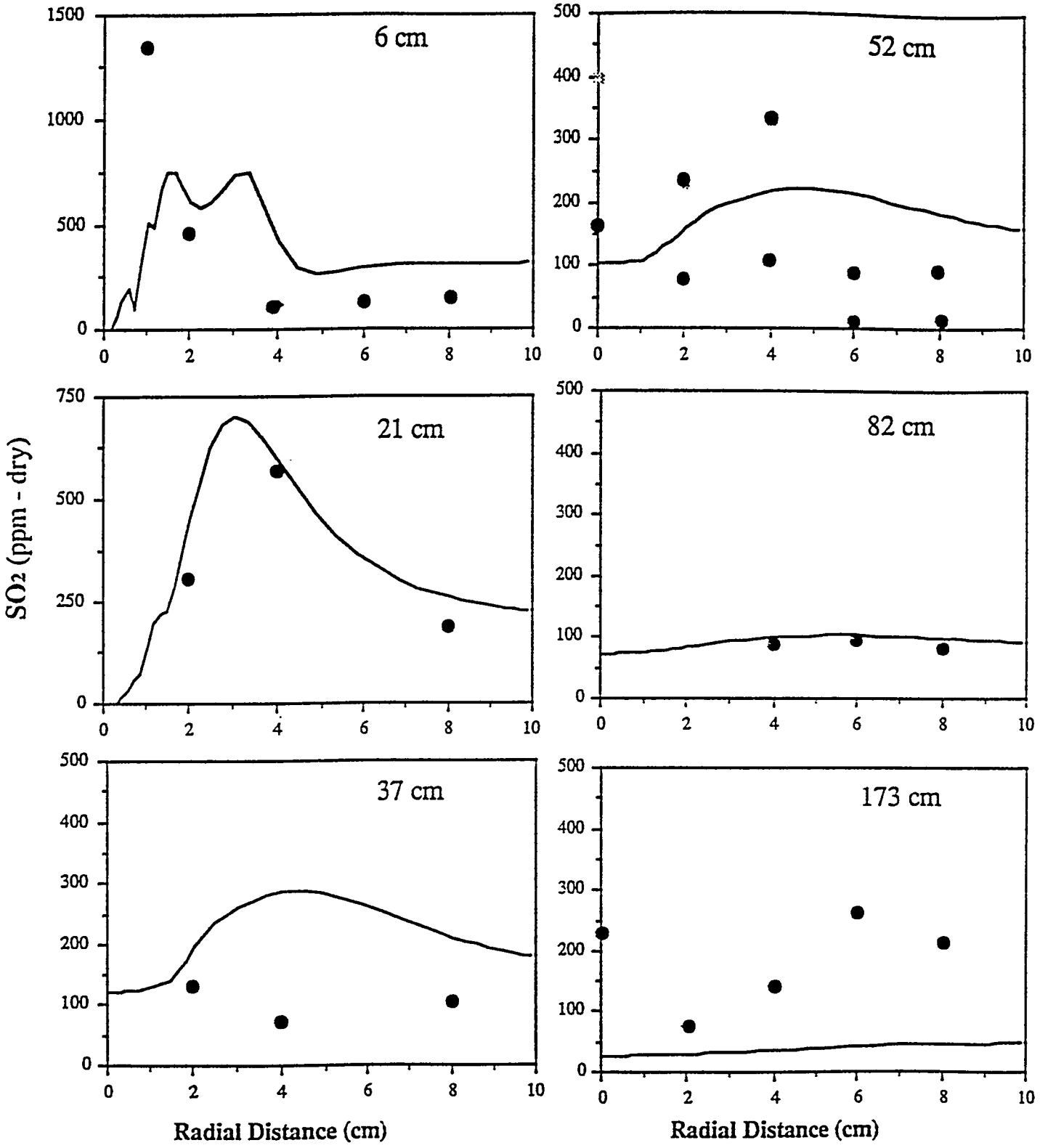

Figure II.G-21. Predicted and measured SO_2 concentration for pressurized gasification (5 atm) of Utah bituminous coal.

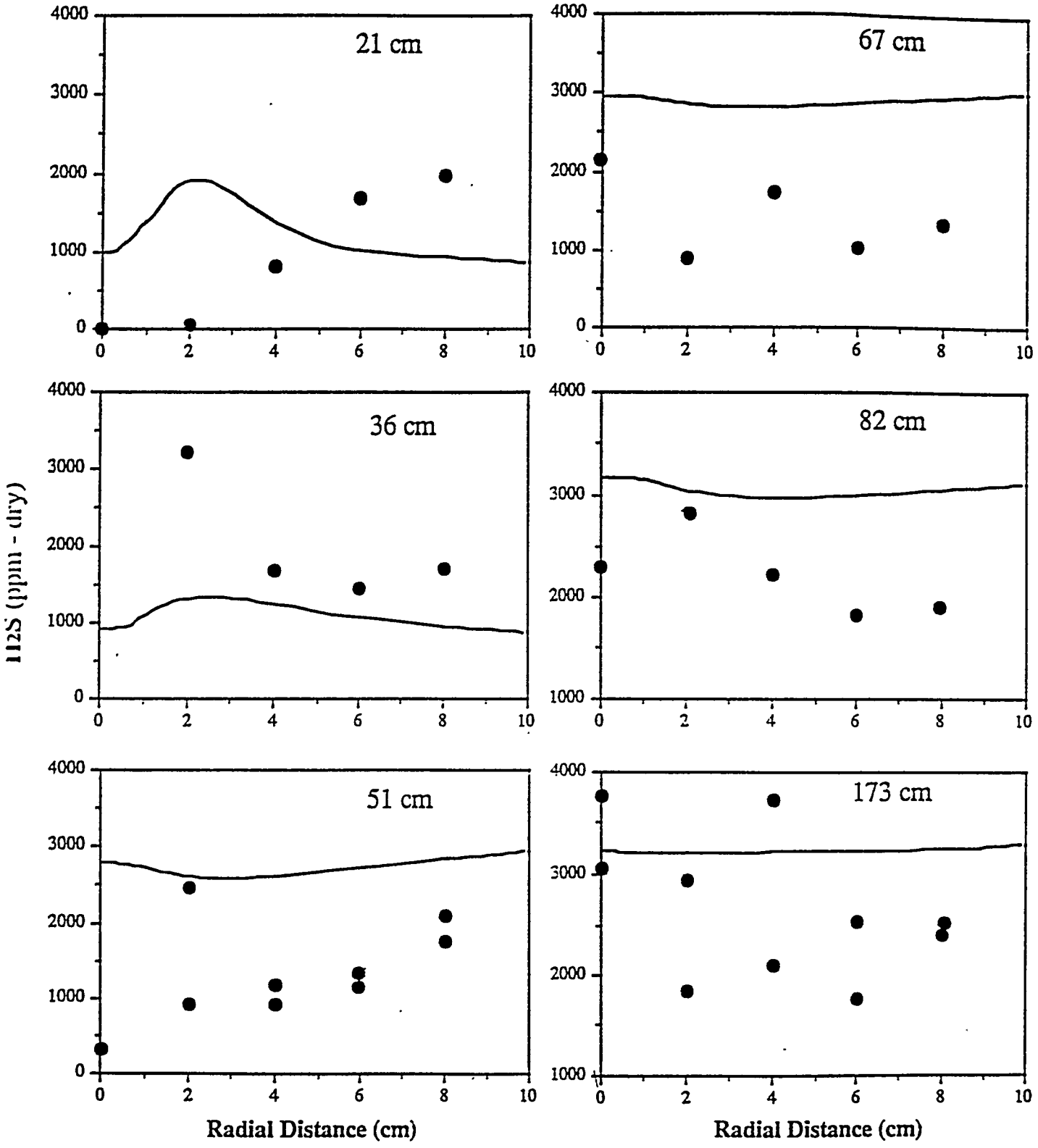

Figure II.G-22. Predicted and measured H_2S concentration for pressurized gasification of North Dakota lignite. Data from Brown (1985).

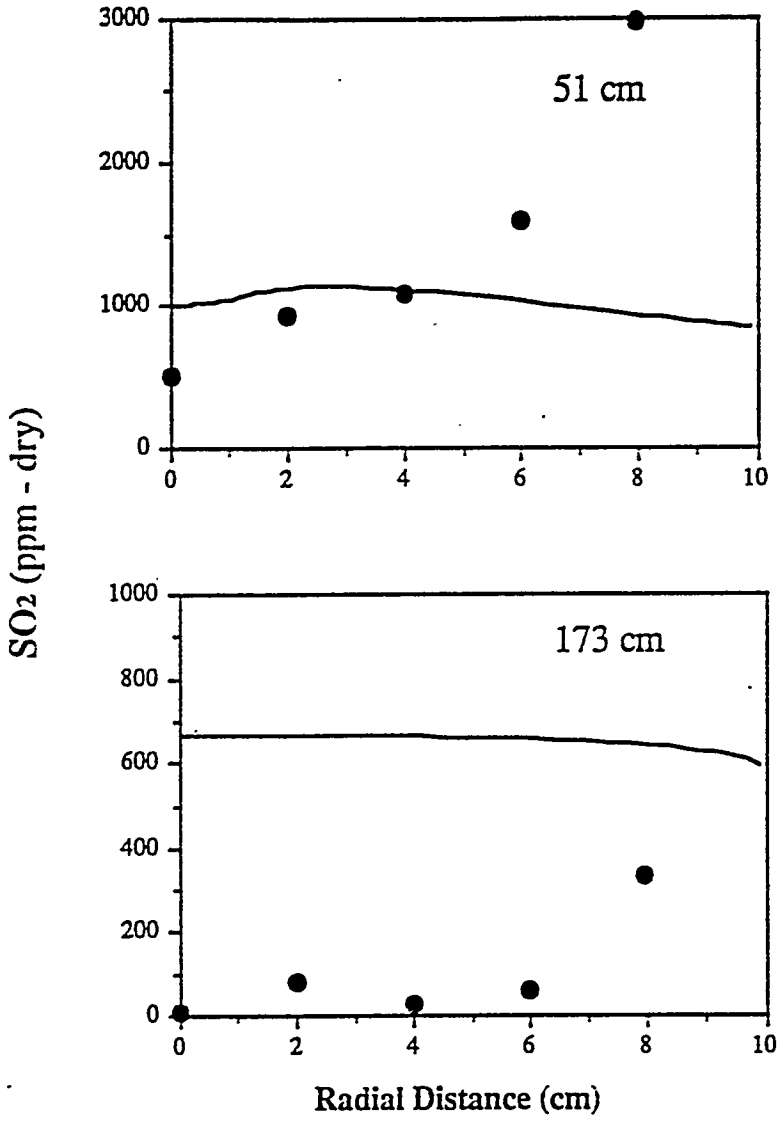

Figure II.G-23. Predicted and measured SO_2 concentration for gasification of North Dakota lignite.

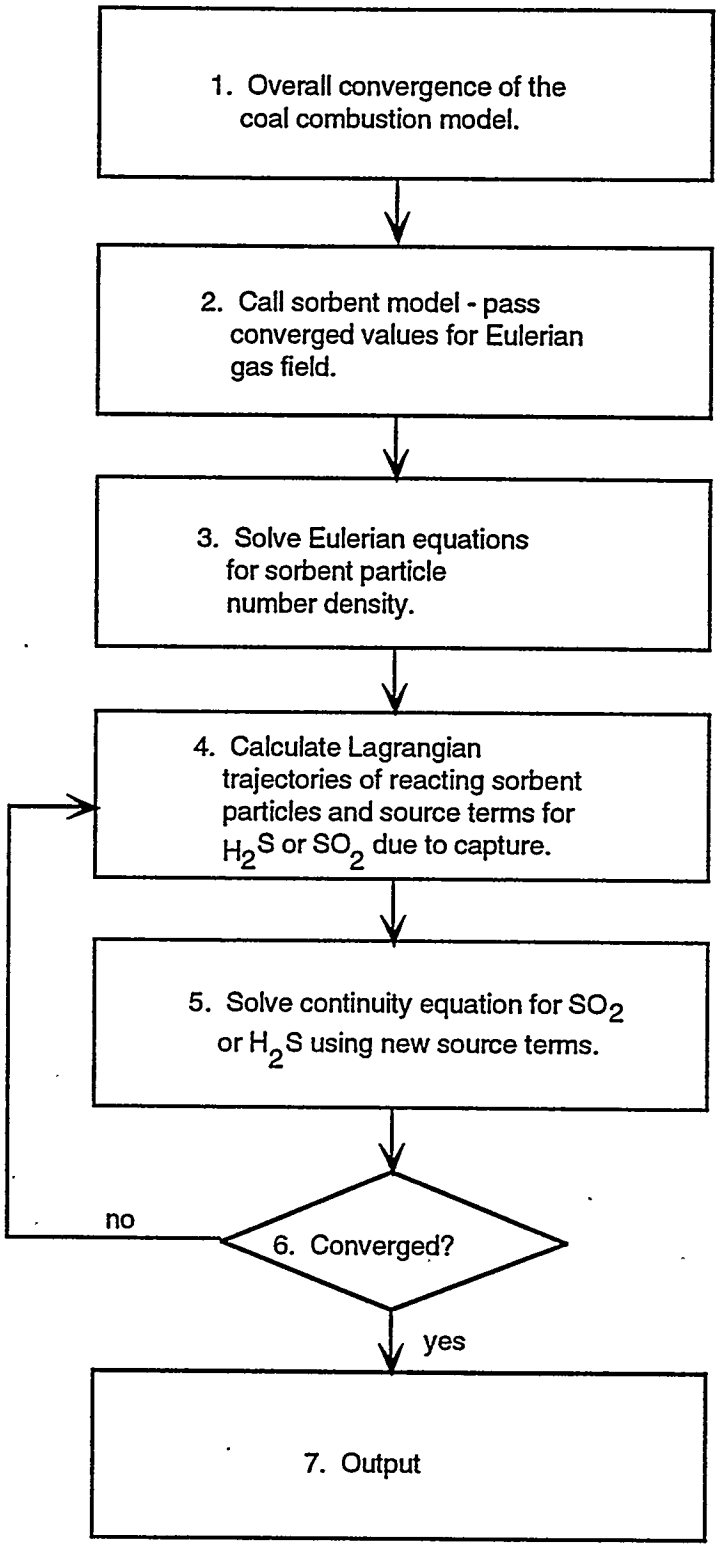

Figure II.G-24. Information flow diagram for sorbent reactions submodel.

The continuity equation solved in Step 4 is

$$\overline{W}_i = \overline{\rho}\tilde{u}\left(\frac{\partial \tilde{Y}_i}{\partial x}\right) + \overline{\rho}\tilde{v}\left(\frac{\partial \tilde{Y}_i}{\partial r}\right) - \frac{\partial}{\partial x}\left(\tilde{D}_Y \frac{\partial \tilde{Y}_i}{\partial x}\right) - \frac{1}{r}\left(\frac{\partial}{\partial r}\right)\left(r\tilde{D}_Y \frac{\partial \tilde{Y}_i}{\partial r}\right) \qquad \text{(II.G-20)}$$

$\overline{W}_i$ is the mean chemical reaction source or sink term for the species mass fraction, either SO_2 or H_2S, depending on the dominant species formed in the gas phase. The net source term for each finite-difference cell is comprised of two contributions: 1) the sink due to sorbent capture by particles passing through the cell, and 2) the contribution of sulfur released to the cell by reacting coal particles within the cell. The first contribution is calculated in Step 3. The second contribution is calculated from the total mass source term from the coal calculated in Step 1, with sulfur evolving from the coal at a rate proportional to the total coal weight loss and partitioning the evolved sulfur between SO_2 and H_2S.

This first-generation model does not allow for the conversion of SO_2 to H_2S or visa versa once it is formed. Therefore, if the local ratio of SO_2 to H_2S is used to partition the evolved sulfur between SO_2 and H_2S, the H_2S will be overpredicted at the exit and the SO_2 underpredicted at the exit in the fuel-lean case, and the opposite will occur in the fuel-rich case. This is because the model assumes that every SO_2 or H_2S molecule that is formed is frozen as such and can't reequilibrate to the other sulfur species when the local equivalence ratio changes. However, H_2S that is formed in oxygen-deficient regions of the fuel-lean case and SO_2 that is formed in oxygen-containing regions of the fuel-rich case are known to reequilibrate before reaching the reactor exit. Hence, in the current model, the partitioning between SO_2 and H_2S for the source term in the species continuity equation that is solved in Step 4 is determined from the ratio of SO_2 and H_2S in the reactor effluent that is predicted in Step 1 without sorbent.

The above approach overpredicts the SO_2 (in fuel-lean systems) or H_2S (in fuel-rich systems) in forward regions of the reactor where the equivalence ratio is different from the overall equivalence ratio, but does a reasonable job in the aft regions where most of the sulfur capture is supposed to occur. This limitation of the model can be alleviated by including the sorbent injection in Step 1 (a change which would greatly complicate the comprehensive model and which is, therefore, impractical) or by using the evolution rate of sulfur species predicted by the FG-DVC submodel and incorporating reaction kinetics for the sulfur species (similar to the manner in which NO_x reactions are modeled in PCGC-2). Unfortunately, the latter was beyond the scope of this project.

For the main combustion model (solved prior to the sorbent reactions submodel), sulfur release from the coal was also assumed to occur at a rate proportional to the coal weight loss. Local instantaneous equilibrium is assumed for the homogeneous chemistry; thus, the volatile sulfur is assumed to be locally equilibrated with the gas prior to capture by the sorbents.

The effects of the sorbent particles on the gas velocity and radiative fluxes are neglected. The particles are small (usually < 10 μm) and are assumed to follow the motion of the gas. In addition, the sorbent loading is light. Changes in the sulfur pollutant concentrations are considered to have negligible impact on the sulfur-free gas composition. This assumption is plausible since the sulfur pollutants are typically less than 0.5 percent of the gas. These assumptions, together with the assumption on the partitioning between SO_2 and H_2S for the source term discussed above, allow the sorbent predictions to be decoupled from the fluid mechanics and reacting coal predictions. Decoupling the sorbent calculations saves computational time. Another advantage is that an evaluation of the effects of sorbent injection can be made using restart files created by the simulation of the combusting flow field.

Other simplifying assumptions which were made in the sorbent reactions submodel are: 1) the sorbent particles are assumed to be instantaneously calcined to CaO; 2) the sorbent particles have no

internal temperature gradients and are in thermal equilibrium with the local gas; 3) sulfation is considered irreversible; and 4) sidewall injection of sorbents in cylindrical reactors can be modeled by an axisymmetric slit.

The assumption of instantaneous particle calcination deserves further comment. Silcox (1985) showed that this is a reasonable assumption for sorbents injected into high-temperature regions. Calculations showed that particle heat-up and calcination occur over a short period of time relative to the time required for sulfation by SO_2. Silcox noted that thermodynamic considerations rule out simultaneous calcination and sulfation if the sorbent is injected into the burner zone. If the sorbent is injected downstream of the burner zone in cooler flame regions, then simultaneous calcination and sulfation can occur. The model predictions presented in this paper account only for sulfation of calcined sorbents.

Sorbent Capture Predictions

Two test cases were simulated to illustrate the capability of the model. Each case required approximately 3 cpu-hr on a Convex C-2 computer. The first case was the combustion of Wyoming subbituminous coal in a down-fired, 0.2-m-inside-diameter reactor (Asay, 1982). Sorbent was not injected during this experimental study, but the effects of sorbent injection were investigated by simulation.

A second experimental study was conducted in an entrained-flow gasifier (down-fired with an internal diameter of 0.2 m) to investigate the effectiveness of injected sorbents for capturing H_2S (Huber, 1989). The data showed measurable capture for gasification of Illinois No. 6 bituminous coal with sidewall injection of sorbent.

The reaction rate parameters and solid-state diffusion rates which were used for the sulfation of SO_2 and H_2S were taken from Silcox (1985) and were listed in Table II.G-4. The solid-state diffusivity and reaction rate parameters were obtained by correlating experimental data of Borgwardt et al. (1984) and Borgwardt and Roache (1984). Other sorbent particle properties used to characterize the sorbent particles were based on values in the literature. The submodel was validated using a first-order reaction rate (with respect to SO_2 and H_2S). The reaction order with respect to SO_2 is generally believed to be ~0.6. A first-order reaction rate was used in these predictions to simplify the calculation procedure.

Fuel-Lean Case - In the simulation of the fuel-lean case, sorbent was injected in the primary stream with the coal. Ordinarily, sorbent would probably not be injected with the coal because it might sinter in the high-temperature, flame zone. However, it was injected with the coal for this illustrative calculation.

Predicted conversion and particle temperature are shown in Figs. II.G-25 and 26. The temperature is favorable for rapid calcination as the particles pass through the devolatilization and flame regions. The temperature then decays to the favorable window of 1190-1500 K for sorbent reactions to occur. The total sorbent particle residence time was approximately 3 seconds. Each particle trajectory is unique and has a slightly different conversion at the reactor exit.

The predicted SO_2 concentration with and without sorbent injection is shown in Fig. II.G-27. There is very little SO_2 capture near the flame zone where the SO_2 concentrations are stratified in the radial direction. Profiles in the mid and aft portions of the reactor show progressive SO_2 depletion by the sorbents. Sulfur capture is greatest near the combustor centerline, where the predicted sorbent particle concentration is highest. Integration of the percentage of SO_2 captured over the radial area indicated a total SO_2 capture of about 50 percent for this case.

Submodel Sensitivity Study - The sensitivity of the predicted sorbent conversion and sulfur capture to variations in key physical parameters was investigated further for the fuel-lean case. Figure II.G-

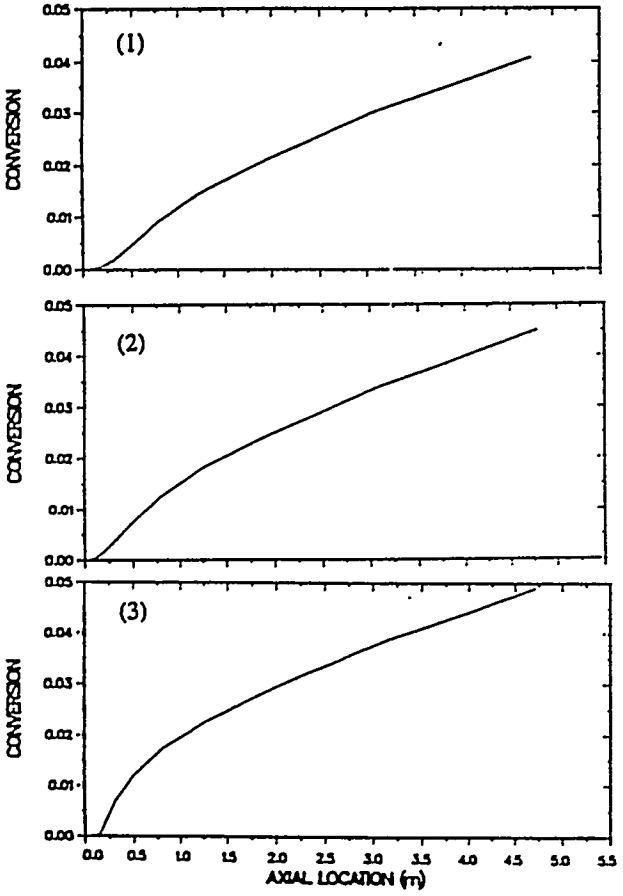

Figure. II.G-25. Predicted sorbent particle conversion for three starting locations for swirled, fuel-lean combustion of wyoming subbituminous coal = (mass O_2:coal:sorbent = 44:22:1).

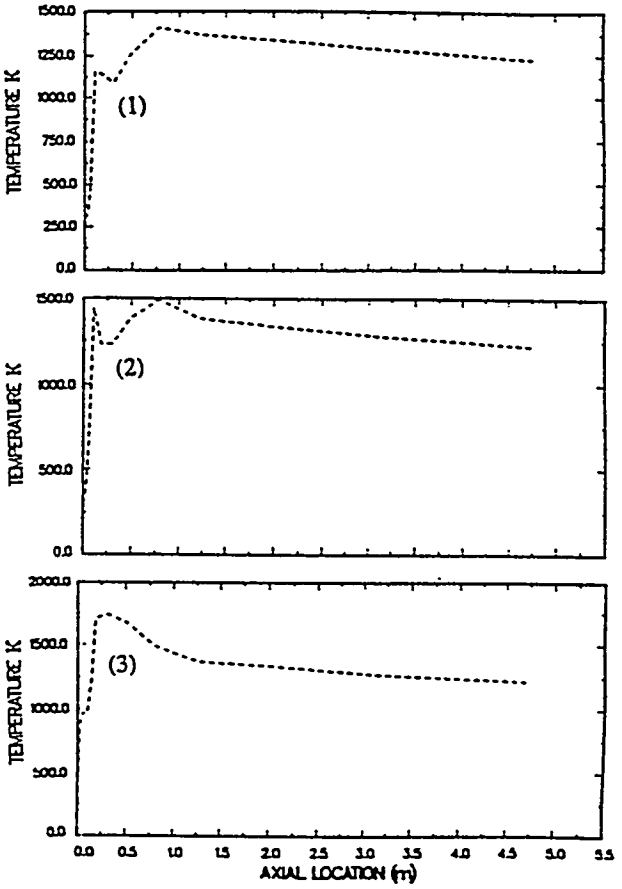

Figure II.G-26. Predicted sorbent particle temperature for the three particle trajectories whose conversion is depicted in Fig. III.G-25.

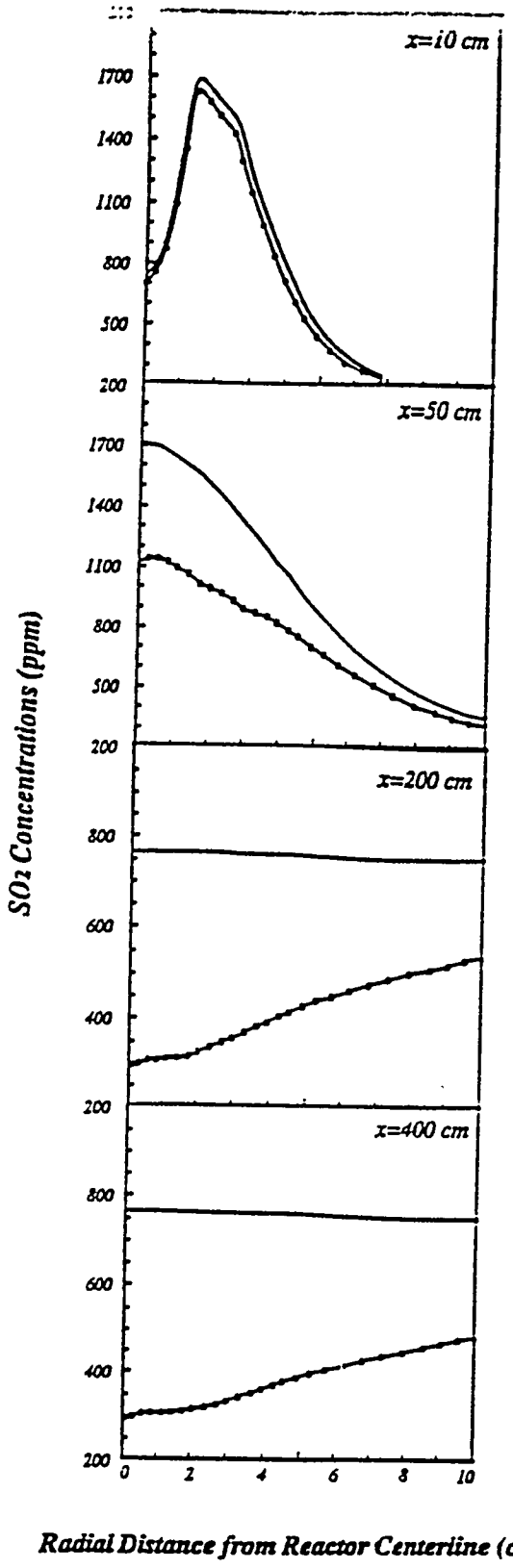

Figure II.G-27. Predicted SO_2 concentrations in fuel-lean case with (•—•—•) and without (————) sorbents injected. Axial distances are marked in the upper right handcorner of each frame.

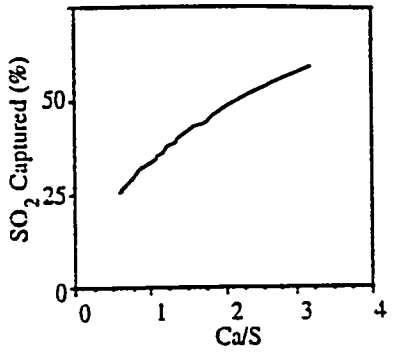

Figure II.G-28Predicted SO_2 capture dependence on sorbent loading. Ca/S is the molar ratio of CaO in the inlet and the amount of sulfur releasd to the gas from the reacting coal.

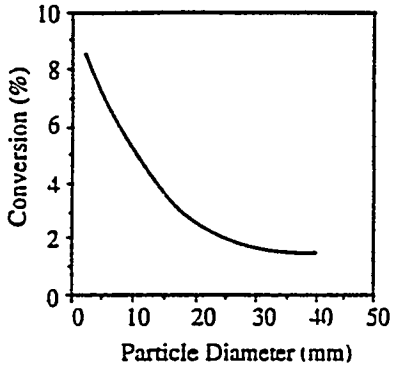

Figure II.G-29. Predicted sorbent particle conversion dependence on calcined sorbent particle diameter.

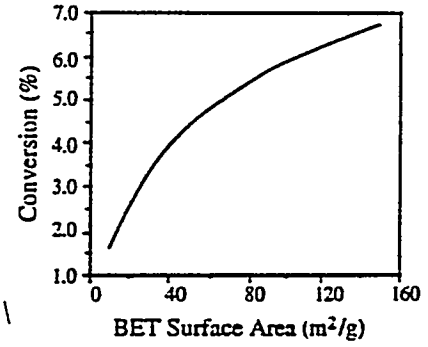

Figure II.G-30. Predicted sorbent particle conversion dependence on calcined sorbent particle reactive surface area.

28 shows that SO_2 capture increases with increasing Ca/S mole ratio for 8 μm diameter particles having a constant BET surface area of 100 m^2/g. The magnitude and trend of predicted sulfur capture agree generally with measurements of Newton et al. (1986).

The predicted particle conversion sensitivity on particle diameter is plotted in Fig. II.G-29 The particle diameter was varied from 2 to 40 μm for a constant BET surface area of 100 m^2/g. The predicted trend correctly reflects the resistance of mass transfer in the sorbent particle pores which is more significant for larger particles. The final particle conversion in this prediction is relatively low due to low gaseous SO_2 concentrations and a relatively short particle residence time in the combustor.

The predicted dependence of sorbent conversion on the BET surface area is shown in Figure II.G-30 for 8-μm-diameter particles. The BET surface area for calcined sorbents can vary significantly, depending on the sorbent type and calcination history. It is typically in the range of 2-30 m^2/g for calcium-based sorbents. The model results concur with experimental observations that the particle conversion is highly dependent on the surface area.

Fuel-Rich Case - In the fuel-rich case, sorbent particles of 8 μm size were injected through three ports spaced 120 degrees apart (simulated as an annular slit) on the side wall of the reactor located at a distance of 65 cm from the top. Argon was used as the sorbent carrier gas. The case was simulated with one sorbent particle size and a single starting location for sorbent trajectory calculation with uniform injection of sorbent around the cylindrical duct, to accommodate the 2-D nature of PCGC-2.

In the experiment, the crossflow jet was designed to penetrate to the reactor centerline. The gas flowrate was not reported, so it was adjusted in the simulation to get penetration of approximately two-thirds of the reactor radius. Full penetration to the centerline was impossible in the 2-D simulation because it would have completely blocked off the cross-section of the reactor and cut off the flow of primary and secondary gas.

Figure II.G-31 shows the sorbent particle trajectory, conversion, diameter, and temperature history. The sorbent particle trajectory penetrates about two-thirds of the reactor radius before turning and following the main stream. The particles heat up and attain the maximum temperature of about 1250 K before following the main stream. A sizable portion of the conversion takes place before the particles turn. This can also be seen in Fig. II.G-32, which shows the predicted H_2S capture. Radial profiles of H_2S concentration before and after sorbent injection are shown in the figure for four axial locations. The profiles without sorbent are almost flat, with about 9600 ppm H_2S. The total sulfur pollutant concentration (H_2S + SO_2) was predicted to be about 9800 ppm, which agrees with the experimentally observed value of ~10,000 ppm (Huber, 1989).

The model predicts substantially lower H_2S concentration with sorbent injection than without. At a distance of 100 cm from the top (35 cm from the injection ports), the average H_2S concentration is predicted to be about 2500 ppm. This means a capture of about 7000 ppm. The reason for such a high capture is attributed to the high conversion while the particle stream is penetrating radially. In the experiment, the sorbents were injected through three small ports of about 1.04-cm diameter. Therefore, it is possible that the sorbent particles came in contact with very little H_2S gas before they started moving with the main stream; hence, very little reaction presumably occurred at the axial location of injection. But in the axisymmetric simulation, the sorbents are injected through an annular slit which causes the sorbent particle stream to be like a thin sheet having much more surfacearea and contact with H_2S gas and thus substantially higher conversion. This is the drawback of modeling sidewall injection in two dimensions. This problem can be readily resolved through use of a three-dimensional combustion model. Independent work at this laboratory is under way to integrate the NO_x/SO_x submodels into the three dimensional combustion model, PCGC-3. Alternatively, a more realistic 2-D prediction might be obtained if

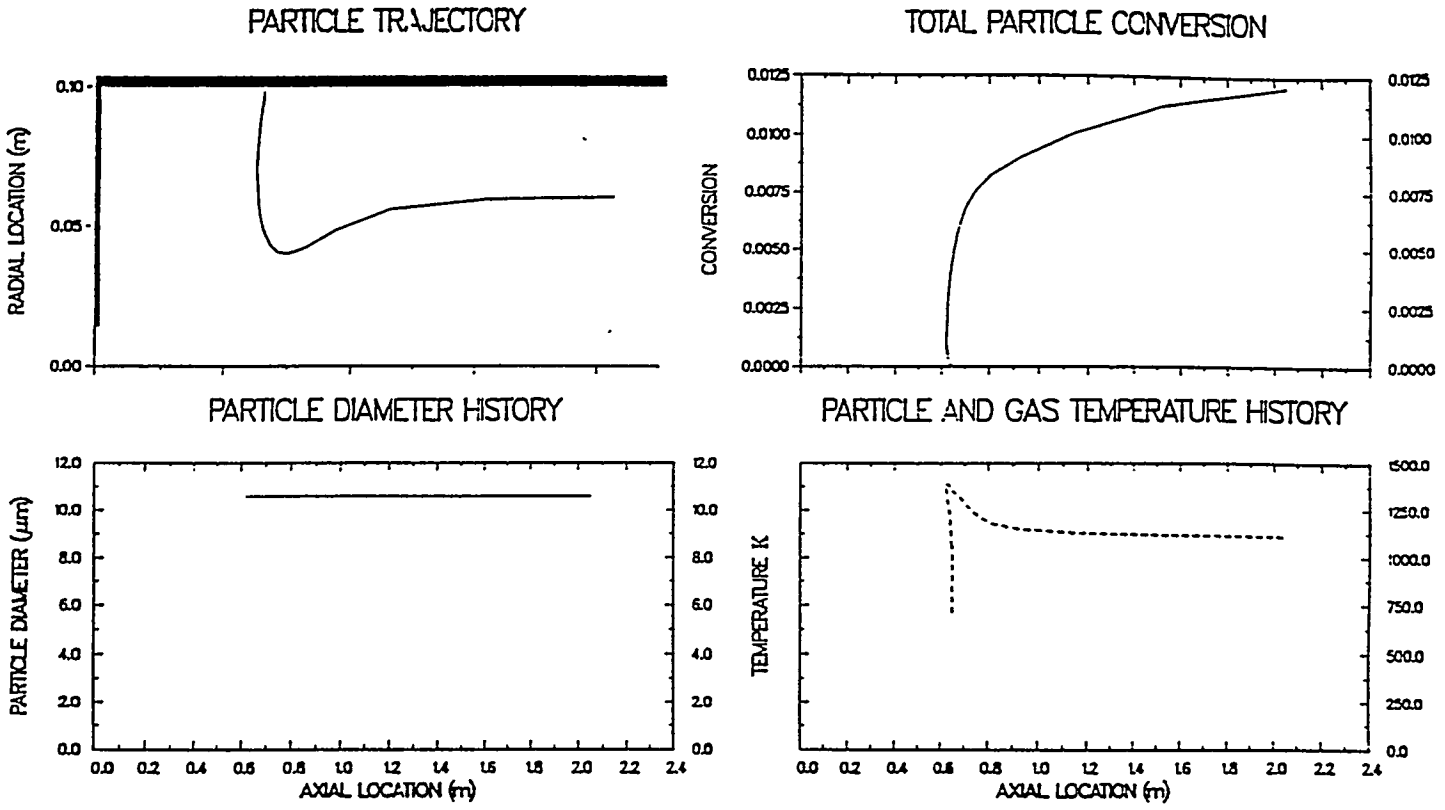

Figure II.G-31. Predicted sorbent particle trajectory, conversion, diameter and temperature for fuel-rich gasification of Illinois bituminous coal (mass O_2:coal:sorbent = 1:1.3:1.6).

the particle reactions were delayed until the particle turns and starts following the main flow. However, the axisymmetric simulation may change the flow patterns significantly and alter the sorbent particle trajectories from the 3-D case. In addition to the increased mixing rate that is apparently introduced by the 2-dimensionality of the model, neglecting the sorbent particle calcination kinetics may have also contributed to the high conversion at the point of injection.

The average predicted H_2S concentration decreases from about 2500 ppm at 100 cm to about 1000 ppm at 175 cm. This amount of capture is consistent with the measured extent of capture (Huber, 1989) of about 2000 ppm observed during the experimental tests. As expected, the radial profiles show lower values near the particles and higher values near the center and the walls.

Summary and Conclusions

NO_x Submodel

A joint thermal and fuel NO_x submodel has been developed, integrated into PCGC-2 and evaluated. Advances for this subtask, include; 1) development, incorporation and evaluation of an integrated thermal NO - fuel NO model within a comprehensive code, for combusting turbulent systems, 2) measurement of nitrogen pollutant concentration profiles throughout a gas-fired combustor (independent funding), 3) examination of the role of NH_3 during low-rank, fuel-rich coal gasification, and (4) the identification of a method to estimate oxygen atom concentration for fuel-lean systems.

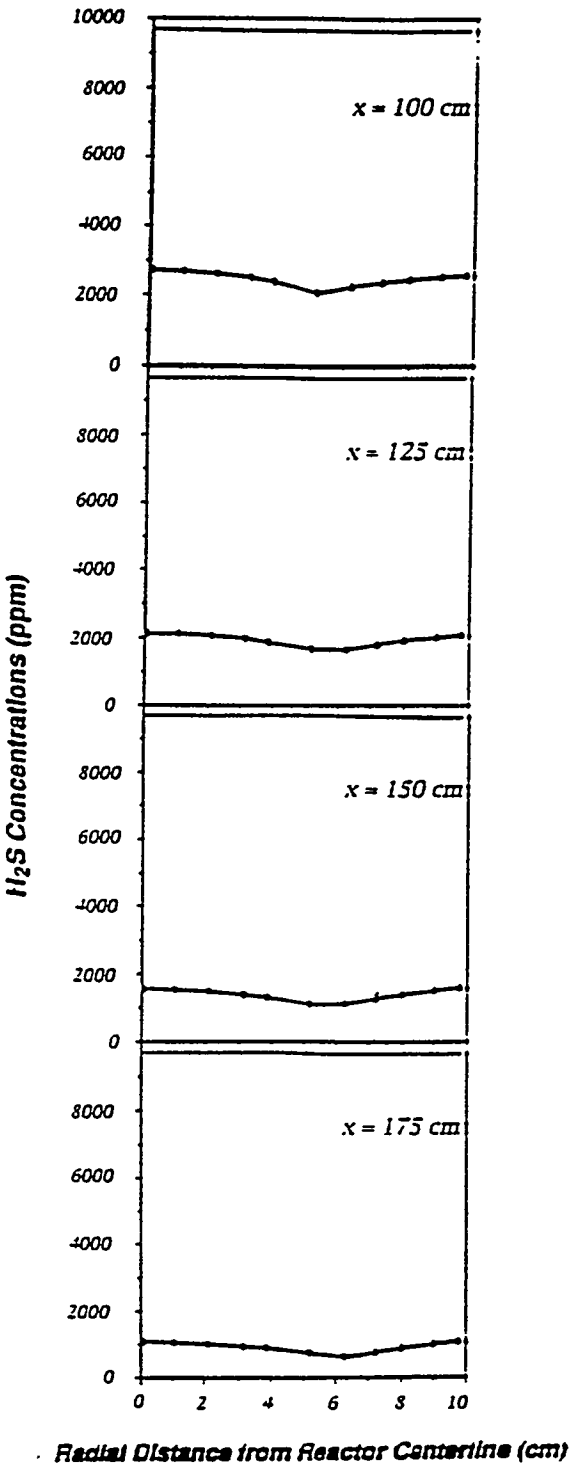

Figure II.G-32. Predicted H_2S concentrations in fuel-rich case with (•—•—•) and without (————) sorbent injection. Axial distances are marked in the upper right hand corner of each frame.

This generalized NO Model is based on global fuel-NO kinetics, and includes the Zeldovich mechanism to calculate thermal NO formation. The model framework allows global reaction rates which include any of the intermediate species, HCN, NH_3, NO, N_2 or C_bH_m, to be investigated. The model can also be used to investigate the relative importance of thermal NO during gaseous combustion and the formation of both fuel NO and thermal NO during pulverized coal combustion. The NO_x submodel has been evaluated by comparison with several sets of data. The results are qualitatively reasonable, and the model can be used with caution to supplement experimental investigations and to aid in burner design.

Experimental data were measured in a natural gas combustor and used to evaluate the predictive method for thermal NO formation. Pulverized coal combustor data obtained from previous experiments were used to evaluate the predictive method for fuel NO formation.

The formation of NO in turbulent natural gas diffusion flames depends on parameters other than swirl number and equivalence ratio, including primary-fuel inlet velocity and reactor wall temperatures. Predicted methods based on the three-step extended Zeldovich thermal NO mechanism were qualitatively reasonable in predicting total NO concentrations and NO trends for variation of swirl and equivalence ratio in natural gas flames. Measured NO concentrations for a small range of fuel-lean equivalence ratios were best predicted assuming atomic oxygen is in partial equilibrium with molecular oxygen. Thermal NO concentrations can be significant during coal combustion and gasification whenever high temperatures occur, even when N_2 and O_2 are present in only dilute concentrations. The importance of NH_3 as a nitrogen-species intermediate was suggested for a lignite coal gasification case.

SO_x/Sorbent Reactions Submodel

A shrinking-core grain sulfation model has been documented, implemented and used to predict sulfur/sorbent reactions and removal of sulfur species from the gas phase. An equilibrium approach has been used for predicting the initial concentrations of sulfur species in the gas phase, and has been evaluated by comparisons with experimental data. The sorbent reactions submodel described herein has been implemented as a post-processor to the comprehensive coal flame predictions, and shows promise for predicting sorbent particle conversion and sulfur pollutant capture in comprehensive combustion models. The overall conversion depends on the particle history and local gas properties. Optimum sorbent feedrate and injection location can be identified using the submodel in an appropriate comprehensive model (e.g. 2-D or 3-D). The optimum conditions will depend on the temperature and pollutant concentration fields.

The physical parameters for specific sorbents vary, depending on the origin of the calcium sorbents and the calcination history. Experimental or literature data which characterize the calcined sorbents and kinetic and diffusion rates is imperative to obtaining meaningful predictions. The predictions are sensitive to sorbent particle surface area and particle diameter. A calcination submodel may be necessary to predict the sorbent particle surface area and initial particle porosity. The supposition that the sorbent particle temperature is equal to the gas temperature also needs to be examined.

Limitations of the current model include: 1) The 2-D, axisymmetric model does not adequately simulate the 3-D aspects of sidewall injection and mixing of sorbent in cylindrical reactors. 2) Only a single sulfur species (i.e., SO_2 or H_2S) may be captured. 3) No interconversion between SO_2 and H_2S is allowed, once it is formed. 4) Sulfur is released from the coal at a rate proportional to its total weight loss and forms SO_2 and H_2S in a ratio equal to that of the reactor exit gas without sorbent injection. 5) Calcination of the sorbent is assumed to be instantaneous, neglecting the rate processes. 6) Sintering is neglected.

References for Subtask 2.g.

Asay, B. W., Effects of Coal Type and Moisture Content on Burnout and Nitrogenous Pollutant Formation, Ph.D. dissertation, Brigham Young University, Provo, UT (1982).

Baulch, D. L., Drysdale, P. D., Home, D. G. and Lloyd, A. C., Evaluated Kinetic Data for High Temperature Reactions, Homogeneous gas phase reactions of the H_2-O_2-N_2 systems, Butterworth, London (1973).

Boardman, R. D., Development and Evaluation of a Combined Thermal and Fuel Nitric Oxide Predictive Model, Ph.D. dissertation, Brigham Young University, Provo, UT (1990).

Borgwardt, R. H., Surface Area of Calcium Oxide and Kinetics of Calcium Sulfide Formation, Env. Prog., 3, 129 (1984).

Borgwardt, R. H. and Roache, N. F., Reaction of H_2S and Sulfur with Limestone Particles, Ind. Eng. Chem. Process Des. Develop., 23, 742 (1984).

Borgwardt, R. H., Bruce, K. R. and Blake J, An Investigation of Product-Layer Diffusivity for CAO Sulfation, IEC Res., 26, 1993-1998 (1987).

Brown, B.W., Effects of Coal Type on Entrained Gasification, Ph.D. Dissertation, Department of Chemical Engineering, Brigham Young University, Provo, UT (1985).

Cheng, M.T., Kirsch, J.M., and Lester, T.W., Reaction of Nitric Oxide with Carbon at Flame Temperatures, Brief Communication, Combustion and Flame, **77**, 213 (1989).

de Soëte, G. G., Overall Reaction Rates of NO and N_2 From Fuel Nitrogen, Fifteenth Symposium (International) on Combustion, The Combustion Institute, Pittsburgh, PA, 1093 (1975).

Drake, M. C., Pitz, R. W., Correa, S. M. and Lapp, M., Nitric Oxide Formation for Thermal and Fuel-Bound Nitrogen Sources in a Turbulent Nonpremixed Syngas Flame, Twentieth Symposium (International) on Combustion, The Combustion Institute, Pittsburgh, PA, 1983 (1984).

Drake, M. C., Correa, S. M., Pitz, R. W., Shyy, W. and Fenimore, C. P., Superequilibrium and Thermal Nitric Oxide Formation in Turbulent Diffusion Flames," Combustion and Flame, 69, 347 (1987).

Eatough, C. N., Controlled Profile Reactor Design and Combustion Measurements, Ph.D. Dissertation, Brigham Young University, Provo, UT (1991).

Fenimore, C. P., Formation of Nitric Oxide in Pre-Mixed Hydrocarbon Flames, Thirteenth Symposium (International) on Combustion/The Combustion Institute, Pittsburgh, PA, 373 (1971).

Haussmann, G.J. and Kruger, C.H., Evolution and Reaction of Fuel Nitrogen During Rapid Coal Pyrolysis and Combustion, Western States Section, The Combustion Institute, Livermore, CA (1989).

Hill, S. C., Smoot, L. D. and Smith, P. J., Prediction of Nitrogen Oxide Formation in Turbulent Coal Flames, Twentieth Symposium (International) on Combustion, The Combustion Institute, Pittsburgh, PA, 1391 (1984).

Huber, A. M., Effect of Sorbent on Sulfur Pollutant Species in an Entrained-Flow Coal Gasifier," M.S. thesis, Brigham Young University, Provo, Utah (1989).

Iverach, D., Basden, K. S. and Kirov, N. Y., Formation of Nitric Oxide in Fuel-Lean and Fuel-Rich Flames, Fourteenth Symposium (International) on Combustion/The Combustion Institute, Pittsburgh, PA, 767 (1973).

Kocaefe, D., Karman, D. and Steward, F. R., Interpretation of the sulfation rate of CaO, MgO, and ZnO with SO_2 and SO_3, AIChE J., 23, 1835 (1987).

Kramlich, J. C., Seeker, W. R., Sarofim, A. F., Longwell, J. T., Ham, D. and Simons, G. A., Kinetics of Sulfur and Nitrogen Reactions in Combustion Systems, in Volume II: Kinetics of sulfur reactions, Progress rept. DOE/PC170771-T10-VOL.2, Energy and Environmental Research Corp., Irvine CA (1989).

Malte, P. C., Smidt, S. C. and Pratt, D. T., Hydroxyl Radical and Atomic Oxygen Concentrations in High-Intensity Turbulent Combustion, Sixteenth Symposium (International) on Combustion, The Combustion Institute, Pittsburgh, PA, 145 (1977).

Miller, J. A. and Bowman, C. T., Mechanism and Modeling of Nitrogen Chemistry in Combustion, Prog. Energy Combust. Sci., 15, 287 (1989).

Milne, C. R., Silcox, G. D., Pershing, D. W. and Kirchgessner, D. A., Calcination and Sintering Models for Application to High-Temperature, Short-Time Sulfation of Calcium-Based Sorbents," Industrial & Engineering Chemistry Research, 29, 139 (1990).

Mitchell, J. W. and Tarbell, J. M., A Kinetic Model of Nitric Oxide Formation During Pulverized Coal Combustion," AIChE J., 28, 302 (1982).

Muzio, L.J., Arand, J.K. and Teixeira, D.P., Gas Phase Decomposition of Nitric Oxide in Combustion Products, Sixteenth Symposium (International) on Combustion, The Combustion Institute, Pittsburgh, PA, 199 (1977).

Newton, G. H., Harrison, D. J., Silcox, G. D. and Pershing, D. W., Control of SO_x Emissions by In-Furnace Sorbent Injection: Carbonates vs. Hydrates, Environ. Prog., 5, 140 (1986).

Nichols, K.M., The Effects of Elevated Pressure on Nitrogen and Sulfur Pollutant Formation During Coal Gasification, Master's Thesis, Department of Chemical Engineering, Brigham Young University, Provo, UT (1985).

Nichols, K.M., Hedman, P.O., Smoot, L.D. and Blackham, A.U., Fate of Coal-Sulphur in a Laboratory -Scale Coal Gasifier, Fuel, 68, 243-248 (1989).

Peck, R. E. and Glarborg, P., Modeling Gas-Phase Nitrogen Chemistry in One-Dimensional, Pulverized-Coal Flames, Western States Section/The Combustion Institute, University of Arizona, Tucson, AZ (1986).

Peck, R. E., Glarborg, P. and Johnsson, J. E., Kinetic Modeling of Nitrogen Oxide Formation in One-Dimensional, Pulverized-Coal Flames, Western States Section/The Combustion Institute, Dana Point, CA (1988).

Peters, N. and Donnerhach, S., Structure and Similarity of Nitric Oxide Production in Turbulent Diffusion Flames, Eighteenth Symposium (International) in Combustion, The Combustion Institute, Pittsburgh, PA, 33 (1981).

Sadakata, M., Fujioka, Y. and Kunii, D., Effects of Air Preheating on Emissions of NO, HCN and NH_3 From a Two-Stage Combustion, Eighteenth Symposium (International) on Combustion, The Combustion Institute, Pittsburgh, PA, 65 (1981).

Sarofim, A. F. and Pohl, J. H., Kinetics of Nitric Oxide Formation in Premixed Laminar Flames, Fourteenth Symposium (International) on Combustion, The Combustion Institute, Pittsburgh, PA, 739 (1973).

Sawyer, R. F., The Formation and Destruction of Pullutants in Combustion Processes: Clearing Air on the Role of Combustion Research, 18th Symposium (International) on Combustion, The Combustion Institute, Pittsburgh, PA, 1 (1981).

Semerjian, H. and Varnos, A., NO_x Formation in Premixed Turbulent Flames, Eighteenth Symposium (International) on Combustion, The Combustion Institute, Pittsburgh, PA, 169 (1981).

Silcox, G. D., Analysis of the SO_2-Lime Reaction System: Mathematical Modeling and Experimental Studies Emphasis on Stoker Applications," Ph.D. dissertation, The University of Utah (1985).

Silcox, J. D., Kramlich, J. C. and Pershing, D. W., The Mathematical Modeling for the Flash Calcination of Dispersed $CaCO_3$ and $Ca(OH)_2$ Particles, Ind. Eng. Chem., 28, 155 (1989).

Singh, S., Grosshandler, W., Malte, P. C. and Crane, J. R. W., Oxides of Nitrogen Formed in High-Intensity Methanol Combustion, Seventeenth Symposium (International) on Combustion, The Combustion Institute, Pittsburgh, PA, 689 (1978).

Smith, P. J., Hill, S. C. and Smoot, L. D., Theory for NO Formation in Turbulent Coal Flames, 19th Symposium (International) on Combustion, The Combustion Institute, Pittsburgh, PA, 1263 (1982).

Smoot, L. D., Smith, P. J., Brewster, B. S. and Baxter, L. L., eds., Revised User's Manual, Pulverized Coal Gasification or Combustion--2-Dimensional (87-PCGC-2), eds., Brigham Young University, Provo, UT (1988).

Solomon, P.R., Serio, M.A., Hamblen, D.G., Smoot, L.D., and Brewster, B.S., Measurement and Modeling of Advanced Coal Conversion Processes, 14th Quarterly Report under DOE/METC Contract No. DE-AC21-86MC23075, Advanced Fuel Research, Hartford, CT (1990).

Song, Y. H., Blair, D. W., Siminski, V. J. and Bartok, W., Conversion of Fixed Nitrogen to N_2 in Rich Combustion, Eighteenth Symposium (International) on Combustion, The Combustion Institute, Pittsburgh, PA, 53 (1981).

Takagi, T., Ogasawara, M., Fujii, K. and Daizo, M., A Study on Nitric Oxide Formation in Turbulent Diffusion Flames," Eighteenth Symposium (International) on Combustion, The Combustion Institute, Pittsburgh, PA, 1051 (1981).

Tang, S. and Churchill, S. W., The Formation of Thermal and Fuel NO_x for Radiantly Stabilized Combustion, Eighteenth Symposium (International) on Combustion, The Combustion Institute, Pittsburgh, PA, 73 (1981).

Thompson, D., Brown, T. D. and Beér, J. M., Formation of NO in a Methane-Air Flame, Eighteenth Symposium (International) on Combustion, The Combustion Institute, Pittsburgh, PA, 787 (1981).

Westenberg, A.A., Kinetics of NO and CO in Lean, Premixed Hydrocarbons Air Flows, Combust. Sci. and Technol., 9, 4:59 (1971).

Zaugg, S.D., Measurement of Sulfur Pollutants in an Entrained Coal Combustor, Ph.D. dissertation, Brigham Young University, Provo, UT (1984).

Zeldovich, Y. B., Sadovnikov, P. Y. and Frank-Kamentskii, D. A., *Oxidation of Nitrogen in Combustion*, (translated by Shelef), Academy of Sciences of USSR (1947).

II.H. SUBTASK 2.H. - SO_x/NO_x SUBMODEL EVALUATION

Senior Investigator - Paul O. Hedman

Student Investigators - David Braithwaite, Aaron Huber
Laren Huntsman, Gregg Shipp

Objectives

The objectives of this subtask were: 1) to obtain detailed turbulence measurements for radial cross-jet injection of sorbent particles in a cold-flow facility designed to replicate the geometry of a 2-D combustor/gasifier, 2) to obtain concentration profile data for sulfur and nitrogen pollutant species from laboratory-scale, coal reaction tests at atmospheric and elevated pressure with and without sulfur sorbents, and 3) to investigate the effect of pressure on the effectiveness of sorbent injection in capturing sulfur pollutants. These data were obtained so that sorbent-flow and sulfur-capture information would be available for sorbent submodel evaluation in Subtask 3.a.

Accomplishments

The cross-flow injection and mixing of sorbent were studied in a cold-flow facility, and the results were used to modify an existing entrained-flow gasifier for sorbent injection. Sulfur-capture studies were then carried out at pressure with limestone and four coals of varying sulfur content. Three methods were used to investigate the sorbent mixing in cold-flow: 1) Smoke injection for visualization, 2) tracer gas injection and sampling, and 3) laser-Doppler anemometry (LDA). The results at relatively low jet-to-free-stream momentum ratios showed that such flows are slower to mix with the free stream than flows with sufficient energy to impinge on the opposite wall. In such cases, increasing the number of cross-flow injectors was found to enhance the mixing. Three injection ports were therefore used in the gasifier. Sight windows were installed to permit optical access, and FT-IR data were obtained with the assistance of AFR. There was no significant sulfur capture for three of the coals, and only a small effect with the highest-sulfur coal. The major cause of the low capture is believed to be the high temperature in the gasifier. Temperatures determined by FT-IR ranged from approximately 1510 to 2480 K. Also, slag samples taken at various axial locations indicated that interactions between the slag, sulfur, and sorbent were occurring, probably reducing the amount of sorbent available for sulfur capture. Work conducted under this subtask was previously reported in its entirety in the 3rd Annual Report for this contract and is not repeated here.

SECTION III. TASK 3. COMPREHENSIVE MODEL DEVELOPMENT AND EVALUATION

Objectives

The objective of this task was to integrate advanced chemistry and physics submodels into a comprehensive two-dimensional model of entrained-flow reactors (PCGC-2) and to evaluate the model by comparing with data from well-documented experiments. Approaches for the comprehensive modeling of fixed-bed reactors were reviewed and evaluated and a comprehensive fixed-bed code was developed.

Task Outline

This task was performed in three subtasks. The first covered the full 84 months of the program and was devoted to the development of the entrained-bed code. The second subtask was for fixed-bed reactors and was divided into two parts. The first part (12 months) was devoted to reviewing the state-of-the-art in fixed-bed reactors. This led to the development of the research plan for fixed-bed reactors, which was approved. The code development was done in the remaining 72 months of the program. The third subtask was to generalize the entrained-bed code to fuels other than dry pulverized coal and was performed during the last 48 months of the program.

III.A. SUBTASK 3.A. - INTEGRATION OF ADVANCED SUBMODELS INTO ENTRAINED-FLOW CODE, WITH EVALUATION AND DOCUMENTATION

Senior Investigators - B. Scott Brewster and L. Douglas Smoot
Brigham Young University
Provo, UT 84602
(801) 378-6240 and 4326

Research Assistants - Ziaul Huque[1] and Susana K. Berrondo

Objectives

The objectives of this subtask were to 1) integrate FG-DVC and PCGC-2, 2) incorporate additional submodels and improvements, particularly those developed under Task 2, 3) evaluate the improved code, 4) improve user-friendliness and robustness, and 5) document the code.

Accomplishments

An advanced two-dimensional model for predicting pulverized coal combustion and gasification has been developed by integrating advanced submodels for coal reactions and pollutant formation and reactions into 87-PCGC-2 (Pulverized Coal Gasification or Combustion - 2 dimensional). The new code is referred to as 93-PCGC-2. 93-PCGC-2 contains several improvements over 87-PCGC-2, including a generalized coal reactions submodel with a database of coal reaction parameters for the eight coals in the Argonne Premium Coal Sample Program, improved energy equation solution, an extended pollutant submodel, generalized solids feeding with capability for sorbent injection and sulfur capture, a laminar-flow option and laminarization with turbulence, effects of gas buoyancy, improved robustness and user-friendliness, and improved code graphics. 93-PCGC-2 was evaluated by comparing code predictions with selected laboratory data. The theory and operation of the code is described in a new user's manual (Brewster et al., 1993). Under a closely related, but independent study, improvements were made to the radiation submodel, and enthalpy balance closure was realized.

FG-DVC Submodel Integration

FG-DVC was integrated into 93-PCGC-2 as an optional submodel for predicting particle weight loss due to devolatilization. This option provides a useful alternative to the simple, empirical weight-loss model in 93-PCGC-2. The FG-DVC submodel requires several additional input files that are available for each of the eight coals in the Argonne Premium Coal Sample Program. In addition to weight loss, FG-DVC predicts volatiles enthalpy, which varies with burnout. Coal offgas enthalpy does not vary with burnout for the simple, empirical submodel option. Elemental composition of the coal offgas is assumed to be constant and independent of extent of burnout for both the FG-DVC and empirical devolatilization options.

Advantages of FG-DVC - Besides predicting coal offgas enthalpy as a function of burnout, the FG-DVC submodel provides several other current and potential advantages compared with the simple, empirical model. First, due to its more fundamental nature, it is more generally applicable to a wide variety of coal types and heating rates. Its broad base of input data for a variety of coal types provides a foundation for predicting behavior of coal types which are not specifically included in the database. Procedures to interpolate the database to predict behavior of other coals are being developed. Second, the FG-DVC submodel provides a fundamental basis for predicting particle properties, such as swelling and reactivity, specifically for each coal type and as functions of burnout. These enhancements are also

[1]Now with Mech. Eng. Dept., Prairie View A&M University, Prairie View, TX 77446.

under development, and have not yet been fully implemented. And third, FG-DVC predicts the evolution rates of individual gas species, not just the total weight loss. Although PCGC-2 cannot make full use of this information at the present time, some limited use by the acid rain precursor (SO_x/NO_x) submodel may be practical in the near future.

Submodel Description - The version of FG-DVC currently used in 93-PCGC-2 is based on rank-dependent kinetics and uses two-sigma percolation theory to model the statistics of the coal polymer network decomposition. A complete description of the submodel is given in the user's manual which was produced for this contract.

The initial integration of FG-DVC into PCGC-2 was performed at AFR during the second year of the study, with assistance from BYU. The submodel was integrated as a "black box" to preserve the integrity of the FG-DVC subroutines and minimize the changes in PCGC-2. This approach allowed the FG-DVC routines to remain under AFR control and new versions of the submodel to be "plugged in" by BYU whenever available. Several new versions of the submodel have been implemented over the course of the study in this manner.

Several problems with the submodel and its integration were encountered during the course of the study. Some of these problems led to significant improvements in the submodel, such as the incorporation of percolation theory. A primary concern from the very beginning has been the computer time requirement. Another has been stability and robustness. Considerable effort has been made to provide a robust, stable model that requires a reasonable amount of computer time on a workstation. It is not the purpose of this final report to give a detailed, historical account of these developments. Such an account is given in the numerous quarterly and annual reports, and the interested reader is referred particularly to the annual reports. Neither is it the purpose of this report to give detailed instructions on how to use the submodel. A separate user's manual is being developed under a separate contract for that purpose (Brewster et al., 1993).

Pollutant Predictions - For nitrogen pollutant predictions, it is important to know the individual evolution rates of the pollutant precursors (e.g. HCN, NH_3) as functions of burnout. The HCN/NH_3 ratio is currently an empirical input to the NO_x model, and the model predictions are sensitive to that parameter. The NO_x predictions are also sensitive to the rate of nitrogen evolution, since nitrogen evolved in the presence of oxygen forms NO_x rather than N_2. Once it is formed, NO_x is difficult to reduce because the kinetics are slow, even at high temperature. The comprehensive model currently assumes that all elements, including nitrogen, evolve at equivalent rates. The FG-DVC submodel would therefore allow a more accurate prediction of the NO_x that gets formed by predicting the rate at which nitrogen evolves as a function of burnout as well as the form (e.g. HCN/NH_3 ratio) in which it evolves. Similar improvements might also be realized in the sulfur pollutant predictions, although the importance is not quite as great, because the homogeneous sulfur reactions are faster and are currently assumed to be in equilibrium. Therefore, the exact location of sulfur evolution and chemical form does not matter as much. Of course, there must be some sensitivity of the capture predictions to the location of sulfur evolution, but this effect is probably minor.

Chemistry/Turbulence Interactions - The current theory for modeling the effects of chemistry/turbulence interactions in PCGC-2 provides two independent gas composition variables for tracking mixing. These variables are referred to as progress variables or mixture fractions. One progress variable is used to track mixing of inlet gas (e.g. primary and secondary) and another is used to track mixing of coal offgas, which is defined as the total material evolving from the coal due to devolatilization and heterogeneous reaction of the char. With only a single variable tracking the mixing of coal offgas, the offgas composition must be assumed to be constant and independent of extent of burnout. Hence, simple, empirical weight-loss devolatilization models are adequate for PCGC-2.

Since FG-DVC predicts evolution rates of individual gas species, as well as total weight loss, the current theory for chemistry/turbulence interactions was generalized to an arbitrary number of progress variables and tested for two progress variables tracking coal offgas. Two schemes were investigated for partitioning the coal offgas. In one scheme, one progress variable was used to track the volatiles and the other was used to track the carbon evolving through char oxidation. In the other scheme, one progress variable was used to track hydrogen and the other was used to track all other variables. The generalized theory and results of the above test were described in detail in quarterly and annual reports and in a publication by Brewster et al. (1988). The results indicated that effects of variability in coal offgas, as allowed for by two progress variables, are significant. However, adding an additional, fluctuating progress variable to the model was judged to be computationally impractical at this time. Therefore, the assumption of constant coal offgas composition was retained in 93-PCGC-2 for the FG-DVC submodel.

Other Submodels and Improvements

Many other improvements were made to PCGC-2 over the course of the study, including a robust, user-friendly energy equation option, a laminar option, an equilibrium algorithm that allows for condensed phases, and inclusion of the effects of gas buoyancy and centrifugal force on particles. Many numerical improvements were also made and diagnostics were added. Most of the improvements have been adequately documented in the annual reports. Two improvements which have not been so documented are described below.

Particle Momentum Coupling - A problem with the gas-particle momentum coupling was uncovered by independent work performed under a DOE-sponsored Phase II SBIR program (Grant No. DE-FG05-90ER80877), where 93-PCGC-2 is being modified by AFR and applied to mild gasification in a transport reactor. The problem became apparent in the densely-loaded system of the transport reactor, where the momentum coupling term is significant. The problem was that the entire change in particle momentum in a computational cell was being attributed to interaction with the gas, in agreement with the original paper on the particle-source-in-cell (PSI-CELL) technique published by Crowe et al. (1977). However, changes in particle momentum due to gravitational forces should not be attributed to the gas; only the drag effects in the particle momentum equation in PCGC-2 should be included in the momentum coupling with the gas. This conclusion was confirmed through a telephone call to Prof. Clayton Crowe, and his suggestion for splitting the drag term into two parts, an "S_p" term that gets multiplied by the gas velocity and which is always negative (for stability in the SIMPLE algorithm used in PCGC-2) and an "S_u" term that contains the rest of the momentum coupling, was implemented in 93-PCGC-2.

Condensed-Phase Equilibrium Algorithm - A new equilibrium algorithm was integrated and tested in 93-PCGC-2. The new algorithm is based on the METCEC code (METC Equilibrium Code) (Nicoletti, 1986a, 1986b) that was obtained with the help of Dr. Thomas J. O'Brien at METC. The new algorithm is similar to the CREE (Chemical Reaction Equilibrium for Elements) algorithm (Smoot and Smith, 1985) that existed previously in 87-PCGC-2, but it allows for condensed phases. It was developed from the well-known NASA-Lewis equilibrium code that also formed the basis of CREE. The CREE routine was retained in 93-PCGC-2 and modified to work with the new routines taken from METCEC, which consist of a routine named SPECE and all of the routines that it calls. The old algorithm also had a routine named SPECE, so the integration mainly consisted of replacing the old SPECE with the new SPECE and adding all the new routines which it calls. The new algorithm was shown to correctly predict chemical equilibrium with solid carbon for a test case that previously failed with the old algorithm.

Radiation Submodel and Mass/Enthalpy Balance Closure - Under an independent study, an option was added to the code to routinely perform an overall mass and enthalpy balance calculation as a part of each simulation. The enthalpy balance is further broken down into balances around the gas phase, the radiation field, and the particle phase. The results of this mass and enthalpy balance calculation are printed in the log file at the conclusion of the simulation. Under the same independent study, modifications were also made to the manner in which the particle radiation absorption and scattering

coefficients are calculated. Previously, they were based on Eulerian particle density. Now they are based on Lagrangian particle information. These changes were necessary to achieve overall enthalpy balance closure, which is now possible to within a few percent.

Code Evaluation

The code was evaluated by comparison with data from five reactors: the AFR transparent wall reactor (TWR), the BYU/ACERC controlled-profile reactor (CPR), the Imperial College reactor, the BYU gasifier, and the Combustion Engineering (CE) drop-tube furnace.

AFR Transparent Wall Reactor (TWR) - The TWR and experimental data obtained by AFR for three near-laminar coal flames (North Dakota lignite, Montana Rosebud subbituminous, and Pittsburgh bituminous) are described under Subtask 2.c. Data were also obtained for non-reacting flow (air only; no coal). In order to adequately model the TWR, 93-PCGC-2 was modified to include options for upflow (counter-gravity), laminar flow, turbulent flow with laminarization, and gas buoyancy effects. Comparisons of measured and predicted particle velocity, gas and particle temperatures, and particle burnout were presented in the 3rd and subsequent annual reports (Solomon et al., 1989-91). Both laminar and turbulence effects, as well as gas buoyancy, were important in modeling this reactor.

Comparisons of model predictions with detailed flame data obtained by E/T FT-IR tomography led to the following observations:

1. Predicted particles heat more rapidly than the measured particles near the edge of the coal stream.

2. Measured particles seem to jump more quickly in temperature when they ignite. (Temperature increases of nearly 1000 K between ignited and unignited particles were observed at the same location.)

3. At the observed ignition point, the predicted core is still fairly cool (1000 K) and the particles are unignited, while tomography data indicate 20 percent of the particles are ignited on the centerline.

Modeling deficiencies which might account for these discrepancies include neglecting direct energy feedback from (1) volatiles combustion in the vicinity of devolatilizaing coal particles, and (2) CO_2 formation in the vicinity of oxidizing char particles. Both possibilities were investigated. The feedback from volatiles combustion was of particular interest, since volatiles flames were observed in the TWR. Also, energy feedback from volatiles flames would occur during the early stages of particle heatup (i.e. during devolatilization), where the major discrepancies in particle temperature were observed. Calculations illustrating the effects of direct enthalpy feedback from volatiles combustion and heterogeneous CO_2 formation were presented in the 5th Annual Report (Solomon et al., 1991). The calculations varying volatiles enthalpy feedback were continued during the last year, and are summarized in Fig. III.A-1. Including feedback increased the heating rate of the particles and reduced the spread in particle temperature. However, even with 100 percent feedback, the model did not predict the "jump" in particle temperature of approximately 1000 K at ignition that was observed experimentally. Also, the discrepancy in predicted and measured gas temperatures in the pre-ignition zone is even greater with the increased feedback.

The predicted temperature is well over 1000 K higher than measured at a radius of 2-4 mm when the enthalpy feedback is 100 percent. This discrepancy is probably due to neglecting the intracellular mixing and combustion kinetics of the volatiles. Particle weight loss is predicted to begin at approximately 6 cm, in good agreement with experimental data. The model assumes that the volatiles mix with the bulk gas and react to equilibrium instantaneously. Shaw et al. (1991) measured global kinetics of volatiles

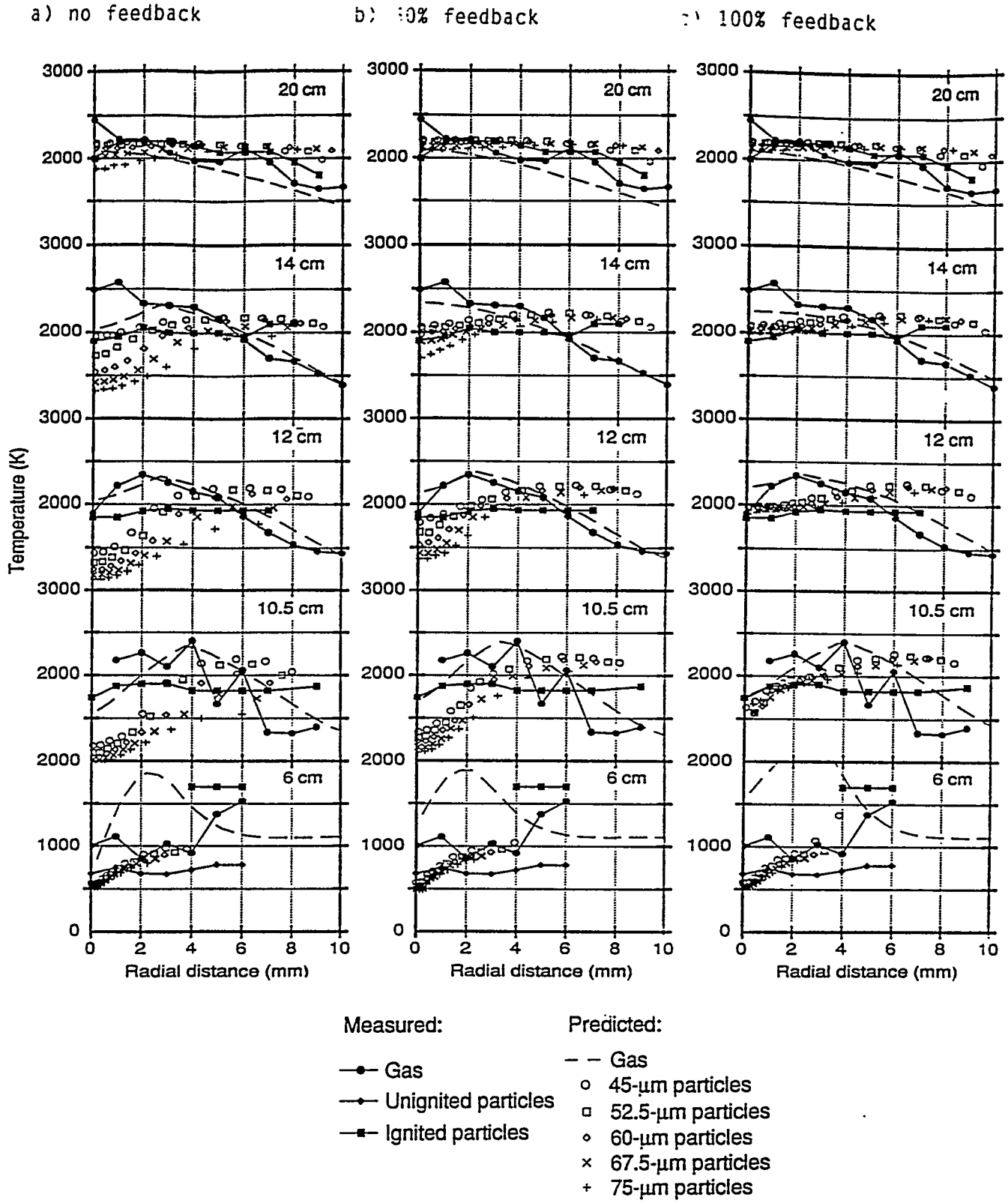

Figure III.A-1. Effect of direct volatiles flame enthalpy feedback on measured and predicted particle and gas temperatures for combustion of Rosebud subbituminous coal ("fast flame" conditions) in the transparent wall reactor.

combustion. Taking average values of 11.5 kcal/mol and 12.85 for activation energy and ln k_o (k_o is in $m^3kg^{-1}s^{-1}$), respectively, the time constant (time for the concentration to decay to e^{-1} of the original concentration) for the first-order decomposition of volatiles (oxygen concentration remains constant) is 0.01 s at 1000 K. For a gas velocity of 1.4 m/s, this time constant represents a distance of 1.4 cm for the volatiles concentration to decay to e^{-1} of its original value. If the mixing delay were also considered, the distance from volatiles evolution to the resulting temperature increase from combustion would be even greater. Hence, in the region of volatiles evolution, the predicted gas temperature rises instantaneously, but the measured gas temperature rise is delayed and more gradual. At 10.5 cm, when volatiles evolution is essentially complete, the predicted and measured gas temperatures agree quite closely.

Based on the TWR modeling and comparisons, the following conclusions can be made:

1. With the inclusion of both laminar and turbulence effects, as well as gas buoyancy, 93-PCGC-2 did an acceptable job of predicting the fluid flow and mixing in the TWR.

2. Including the effects of direct enthalpy feedback from combusting volatiles to devolatilizing particles did not account for the jump in particle temperature that was observed at ignition.

3. Including the effects of heterogeneous CO_2 formation can have a significant effect on maximum particle temperature, and should be retained in the model. However, this mechanism also failed to explain the significant jump in particle temperature for assumed reasonable values of CO_2/CO ratio (15 percent CO_2).

4. The effects of finite rate of mixing and reaction of the volatiles with the bulk gas appear to be important, and methods of incorporating these effects into the model should be developed.

5. Including soot radiation from the flame would have improved the agreement between model predictions and experimental data. While the onset of soot can be predicted from equilibrium, the decay appears to be controlled by kinetics.

BYU/ACERC Controlled-Profile Reactor (CPR) - A diagram of the CPR and results of gas flame simulations were given in the 5th Annual Report (Solomon et al., 1991). Input conditions for the simulation of Utah bituminous coal combustion are shown in Table III.A-1. Predictions were originally made using a swirl no. of 0.8 rather than the reported value of 1.4, consistent with the recommendations of Harding (1980) for theoretical and measured swirl numbers. Use of the reported swirl no. resulted in the particles travelling along the front wall of the reactor, due to an incorrectly predicted external recirculation zone. It was later found that the external recirculation zone could be predicted reasonably well at the reported swirl no. (1.4) if a finer grid were used.

Figure III.A-2 shows a plot of the predicted velocity vectors with particle trajectories superimposed on it. The plot distinctly shows the external and internal recirculation zones. The directions of both recirculation zones are qualitatively correct. As expected, the particles experience a reversal in direction near the inlet due to the inlet secondary swirl. The maximum penetration of the particles was about 0.3 m. The burnout at the exit was predicted to be about 76 percent as shown in Figure III.A-3. Devolatilization was essentially complete at an axial distance of about 0.2 m from the inlet, followed by char oxidation. Figure III.A-4 shows the comparison of the predicted radial temperature profile with the measured values. The predicted profile becomes flat rather early in the reactor, at an axial distance of 0.55 m from the inlet. The reason may be due to the predicted bigger internal recirculation zone which causes good mixing of the gases around that axial location as can be seen from Figure III.A-2.

TABLE III.A-1

PCGC-2 EVALUATION CASES FOR COAL COMBUSTION AND GASIFICATION

A. Coal Combustion

	Coal type	Diameters (m)			Chamber length (m)	Mass flow rates (kg/s)			Swirl number	
		Pri.	Sec.	Cham.		Pri.	Sec.	Solids	Pri.	Sec.
Imperial College										
Case A	UK Geddling [1]	.0222	.056	.60	3.0	.00785	.02872	.00305	0	0.78 [3]
Case F	IL Oakdale [2]	.0222	.056	.60	3.0	.01067	.03886	.00400	0	1.45 [3]
BYU/CPR										
	Utah Blind Canyon	.0266	.098	.80	2.65	.00412	.03528	.00288	0	1.40

B. Coal Gasification (BYU) [Soelberg (1983), Brown (1984)]

	Coal type	Diameters (m)			Chamber length (m)	Mass flow rates (kg/s)			Swirl number	
		Pri.	Sec.	Cham.		Pri.	Sec.	Solids	Pri.	Sec.
	Wyoming subbituminous	.0131	.0287	.20	2.0	.0066	0.0	.00616	0	0
	N.D. lignite	.0131	.0287	.20	2.0	.00774	0.0	.00776	0	0
	Illinois #6 bituminous	.0131	.0287	.20	2.0	.0092	.000667	.00822	0	0

[1]Simulated by Wyoming subbituminous coal.
[2]Simulated by Pocahonatas low-volatile bituminous coal.
[3]Simulated by half the reported swirl no.

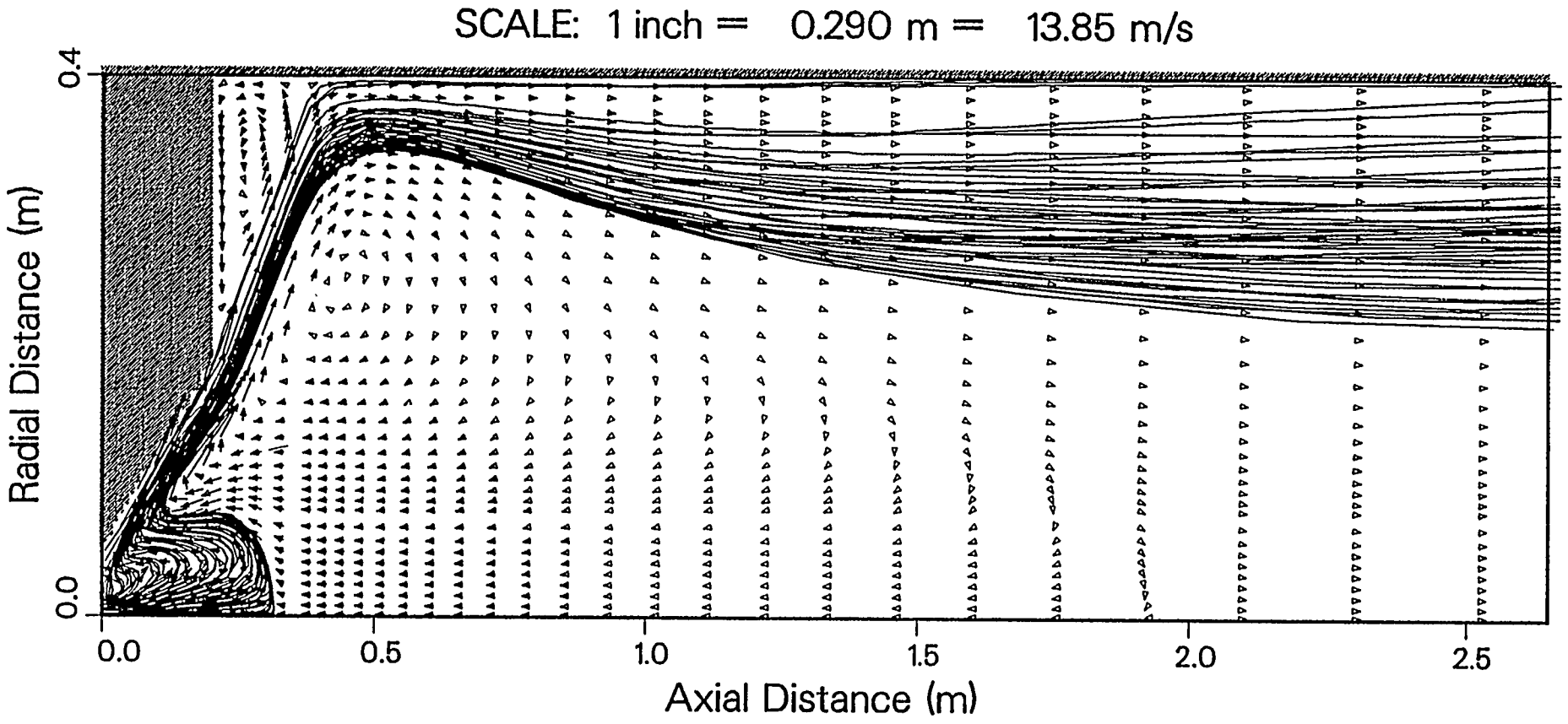

Figure III.A-2. Predicted velocity vectors and particle trajectories for combustion of Utah bituminous coal in the CPR. (Secondary swirl no. = 1.4)

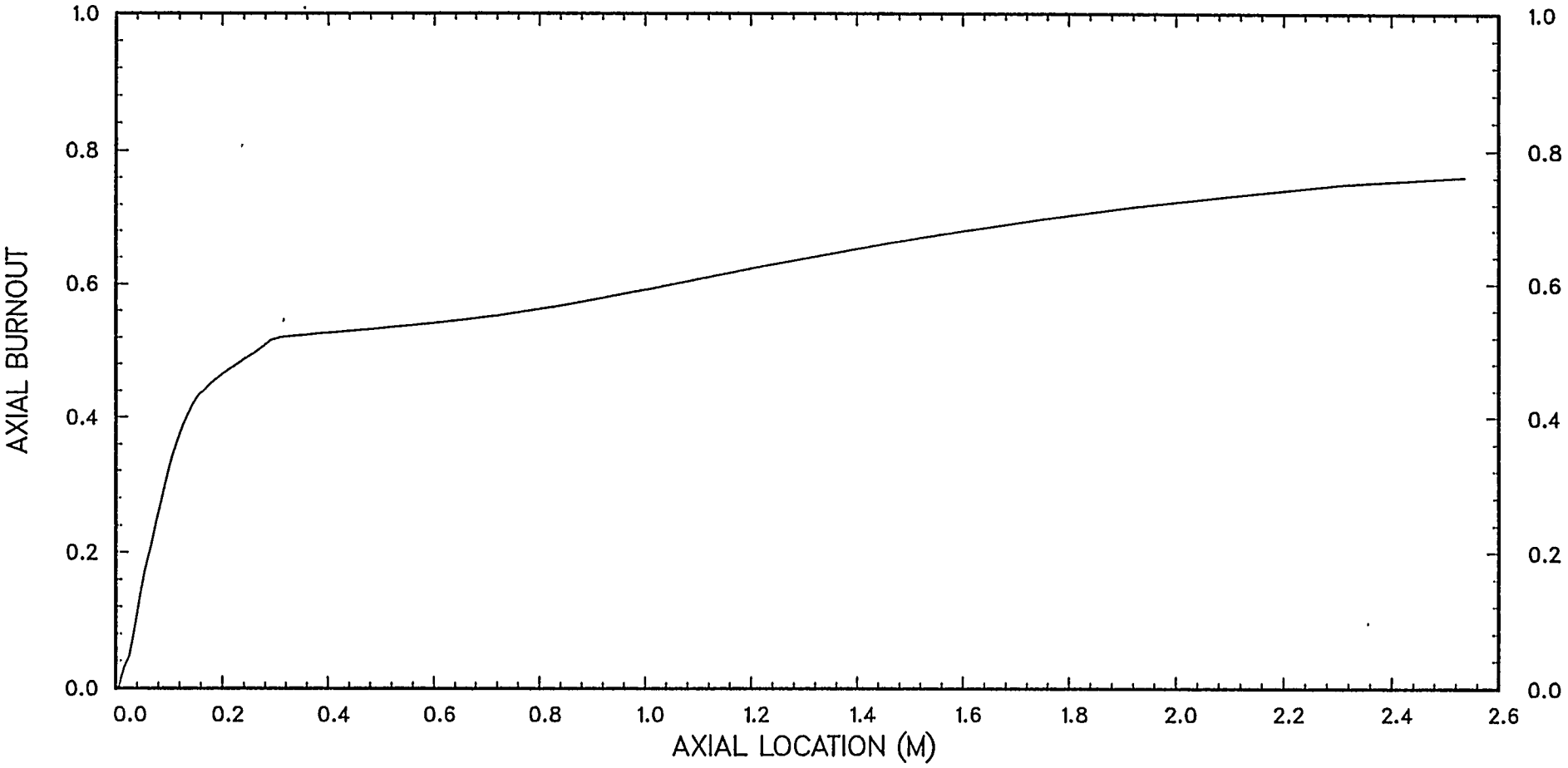

Figure III.A-3. Predicted burnout for combustion of Utah bituminous coal in the CPR. (Secondary swirl no. = 1.4)

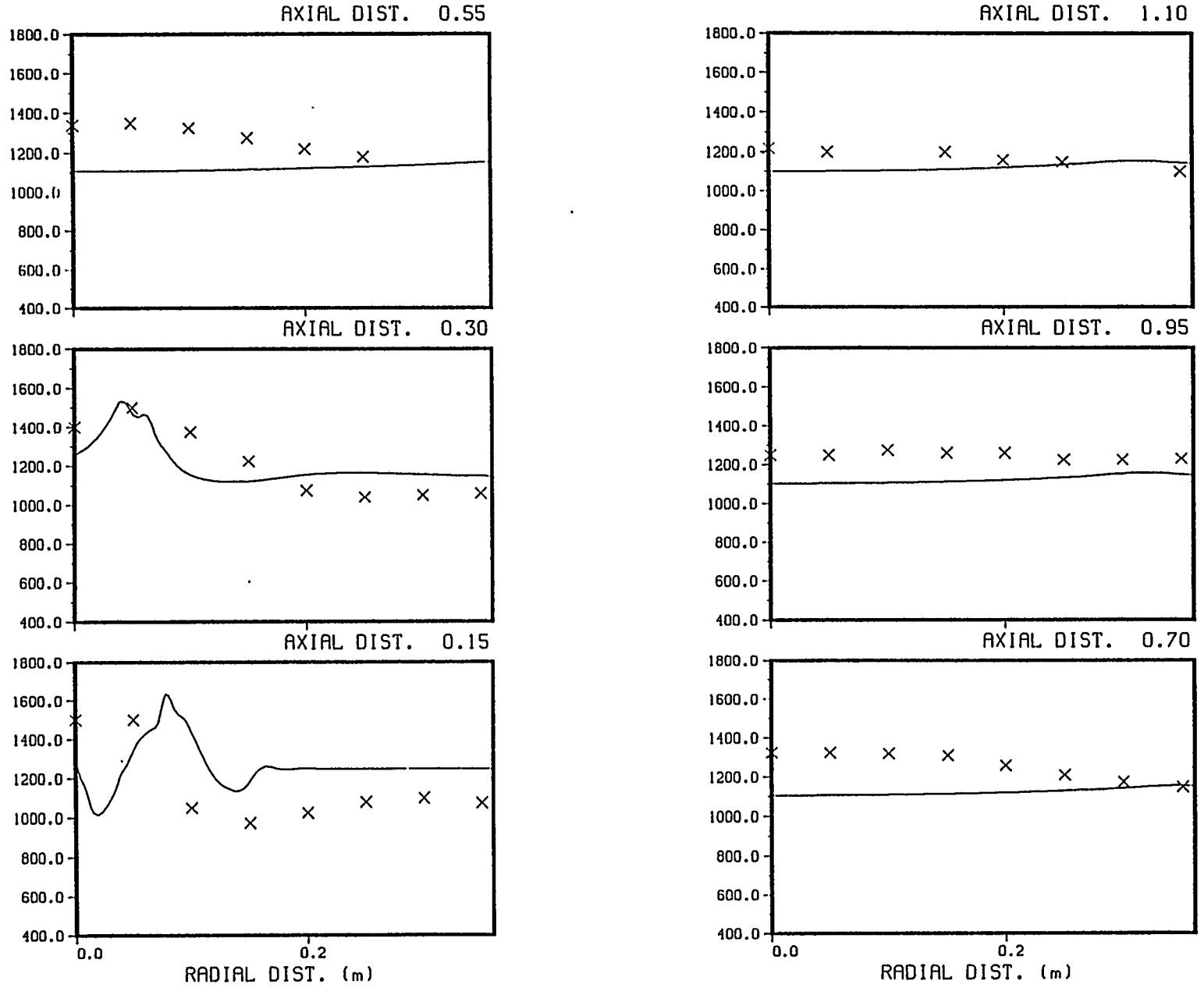

Figure III.A-4. Measured and predicted radial temperature profiles for combustion of Utah bituminous coal in the CPR. (Secondary swirl no. = 1.4)

Imperial College Reactor - A description of available data sets for the axisymmetric, Imperial College reactor was given in the 5th Annual Report (Solomon et al., 1991). A schematic diagram of the reactor is shown in Figure III.A-5. In the 5th Annual Report, it was reported that the directions of both the internal and external recirculation zones were incorrectly predicted. No flow reversal was seen on the centerline near the inlet. Flow reversal was finally predicted at swirl numbers greater than approximately 0.35, using a finer grid. However, the internal recirculation zone was overpredicted. In order to reduce this effect, the simulations were performed at half the reported swirl numbers.

Two cases were simulated, one with Wyoming subbituminous coal and the other with Pocahontas low-volatile bituminous coal. These two coals were chosen to represent the high-volatile UK Geddling coal and low-volatile UK Oakdale coal that were used in the experiments.

Predicted velocity vectors and particle trajectories for combustion of the high-volatile coal are shown in Figure III.A-6. Some of the larger particles do not experience a reversal in axial direction. The maximum penetration of the particles which experience a reversal in direction is about 0.5 m. After reversal, the particles flow along the side wall, suggesting that the external recirculation zone is still not predicted correctly.

Figures III.A-7 and III.A-8 show the comparison of the predicted radial profiles of oxygen and carbon dioxide concentrations, and Figure III.A-9 shows the comparison of the predicted radial temperature profiles with the experimental data at several axial locations. Predicted trends of radial oxygen concentration profiles are found to reproduce the observed trends except at locations near the burner. The prediction shows early ignition which was not observed experimentally. This may be due to the assumptions of instantaneous mixing of the volatiles and instantaneous reaction in the prediction. This early ignition was also observed by Costa et al. (1990) in their prediction of the same case.

The radial temperature profiles are found to be in good agreement near the side wall, but temperature is underpredicted near the centerline up to an axial distance of 0.5 m. The low temperature is due to the scarcity of oxygen in that region, as shown in Figure III.A-7. A sizeable portion of the incoming, oxygen-containing stream gets diverted and flows along the wall, making oxygen less available near the centerline and close to the inlet. According to Figure III.A-7, oxygen gets properly mixed and the oxygen profile is well-predicted at an axial distance of about 0.72 m. Temperature profiles are also expected to be predicted well at this location, but there are no experimental data with which to compare. Carbon dioxide concentration profiles also show behavior similar to the temperature profiles up to an axial distance of about 0.72 m. Carbon dioxide predictions are quite good near the end of the reactor.

Figure III.A-10 shows the velocity vector and particle trajectory plots for the low-volatile coal combustion case. All the particles are found to experience the reversal in axial direction and flow along the side wall of the reactor. This may be due to the higher secondary swirl number involved in this case compared to the high-volatile coal case. Figures III.A-11 and III.A-12 show the comparisons of oxygen and carbon dioxide concentration profiles, and Figure III.A-13 shows the comparison of radial temperature profiles with the experimental data. Early ignition was also predicted for this case, similar to the high-volatile coal case. Radial profiles are found to flatten out rather early in the reactor. Oxygen and carbon dioxide predictions are reasonable at the downstream end of the reactor, but the temperatures are found to be substantially overpredicted near the downstream end of the reactor. This discrepancy is attributed to improper prediction of the fluid dynamics, i.e., the code predicts a large internal recirculation zone with an almost non-existing external recirculaton zone. As a result, the particles are predicted to flow along the sidewall and get dispersed from the top as they move downstream in the reactor.

BYU Gasifier - A description of the BYU gasifier was given in the 3rd Annual Report (Solomon et al., 1989) under Subtask 2.h. Three cases of coal gasification with oxygen and steam were simulated by 93-PCGC-2. Table III.A-1 shows the list of cases with some important input parameters. Because most of the current gasification data are either incomplete, proprietary or measured in systems incompatable with 93-PCGC-2 (e.g. fluidized bed), all three gasification cases that were simulated originated at the BYU

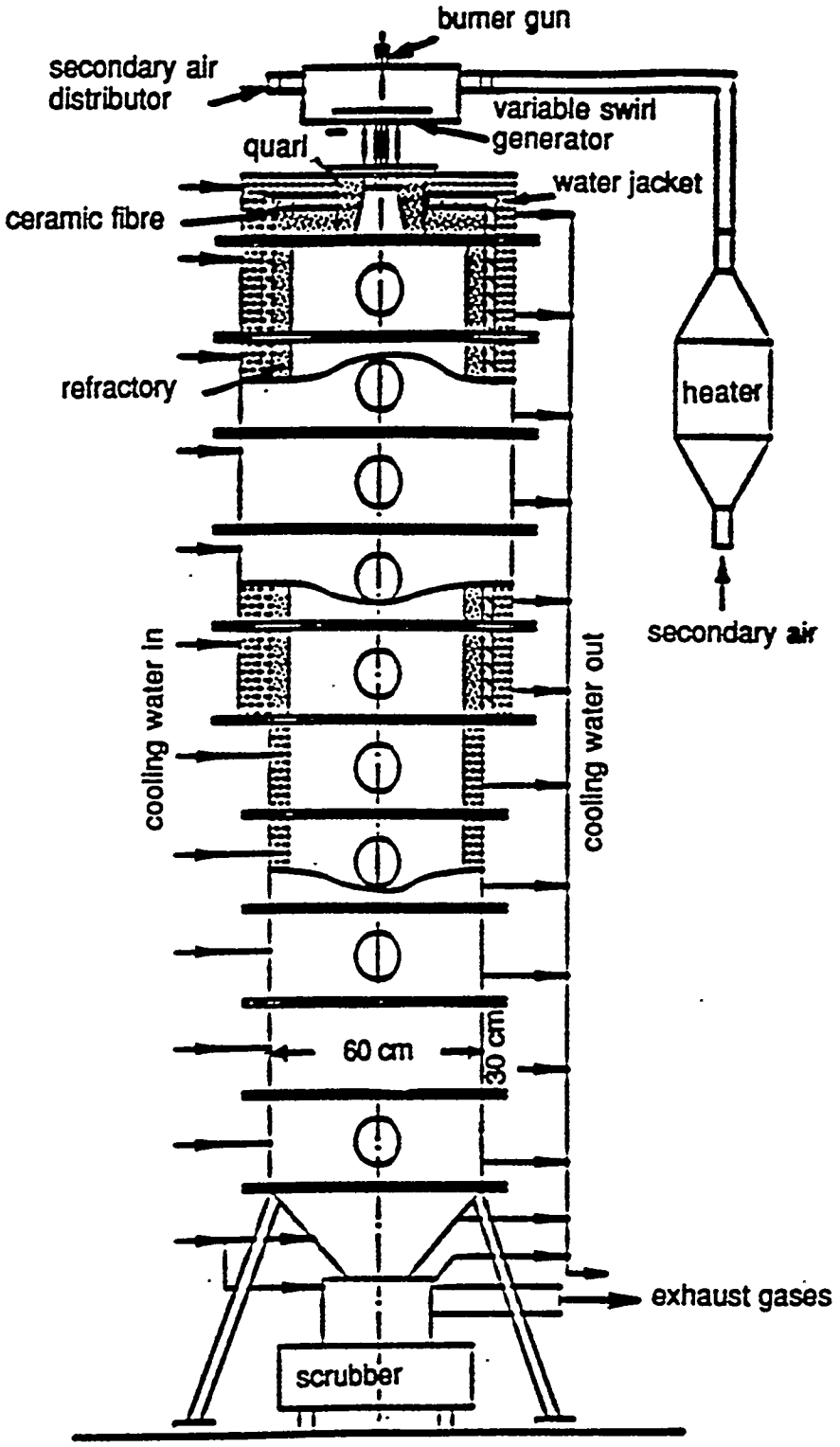

Figure III.A-5. Schematic diagram of the Imperial College reactor. (From Costa et al., 1991).

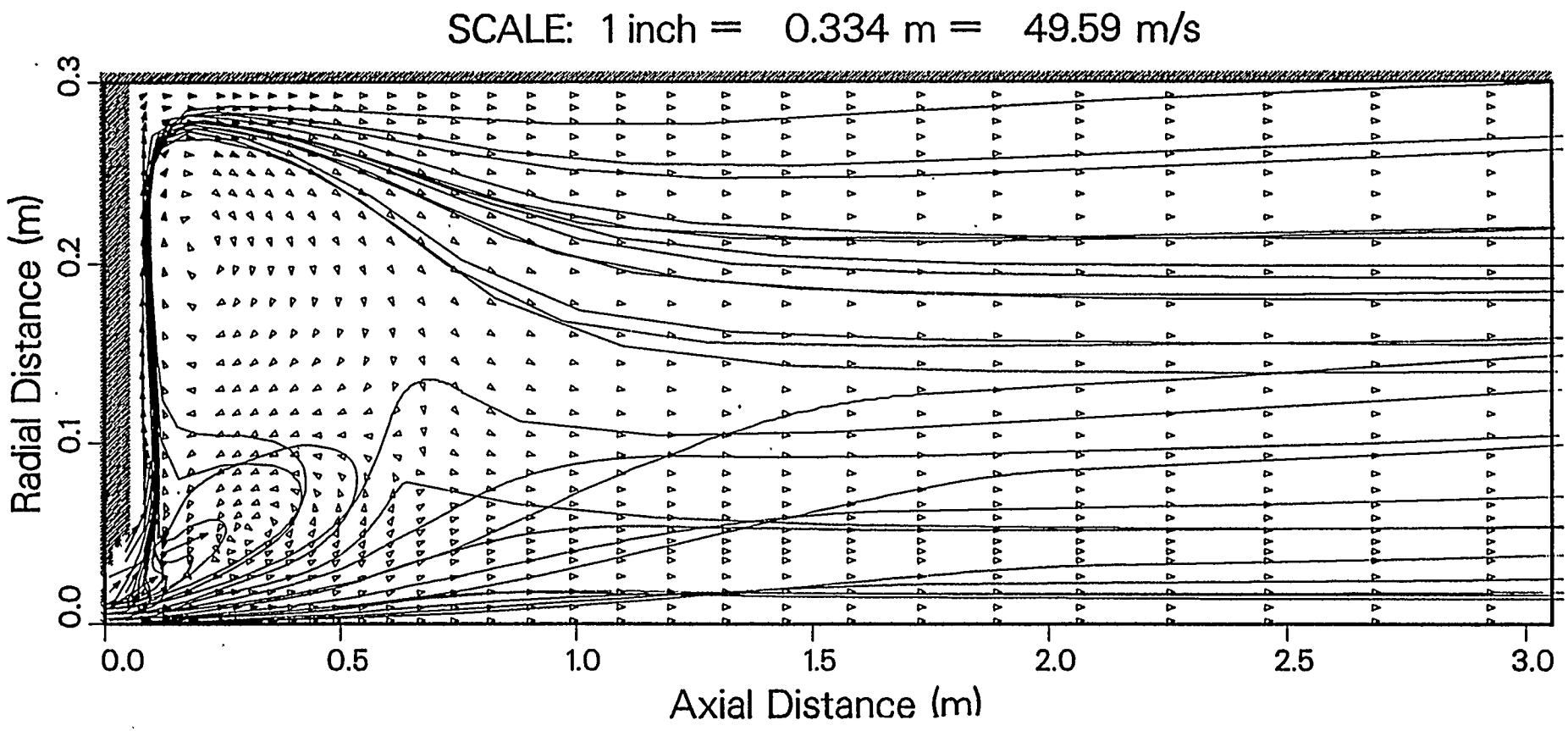

Figure III.A-6. Predicted u-v velocity reactors and particle trajectories for combustion of Wyoming subbitumious coal in the Imperial College reactor. (Secondary swirl no. = 0.4).

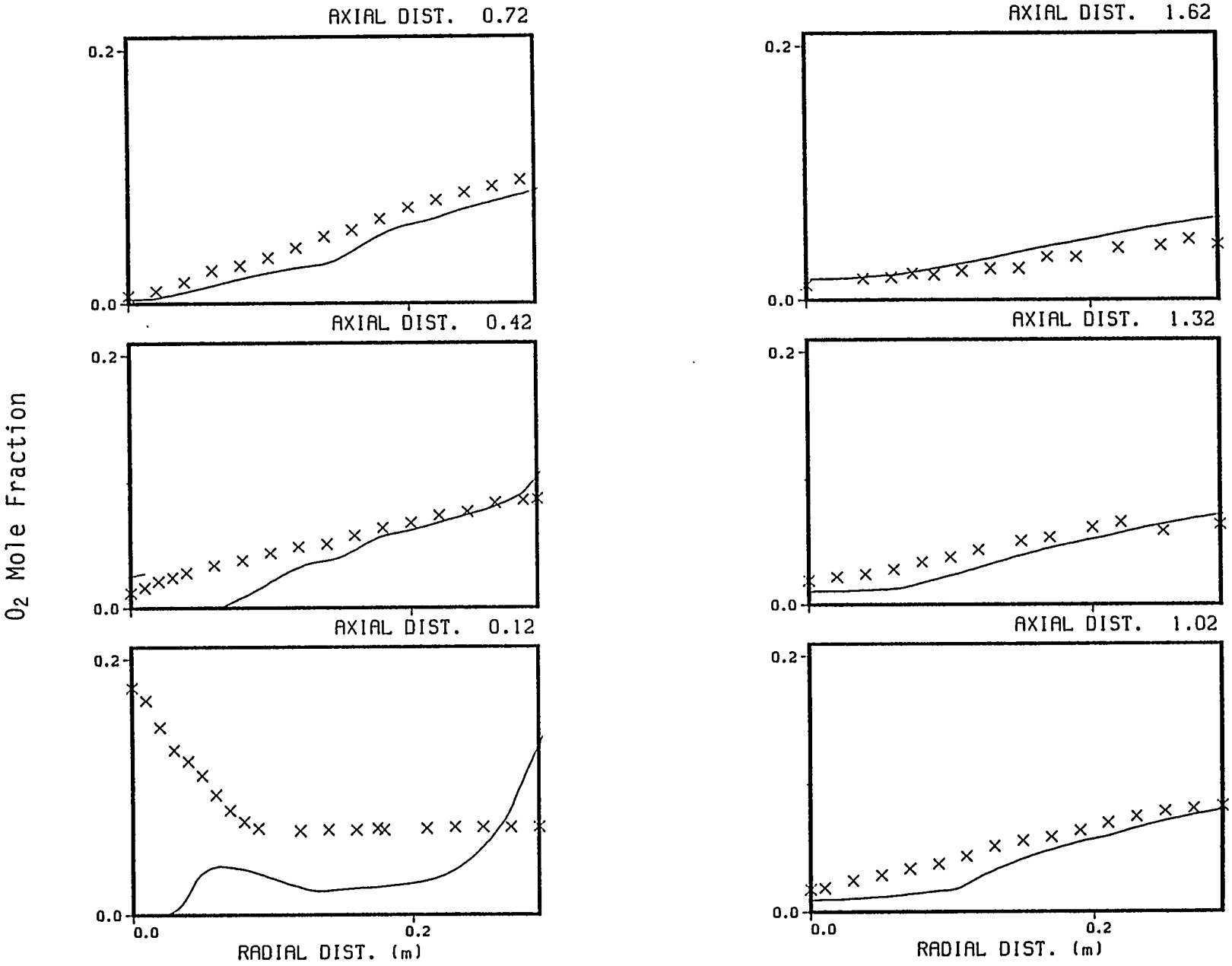

Figure III.A-7. Predicted and measured radial profiles of oxygen concentration for combustion of Wyoming subbituminous coal in the Imperial College reactor. (Secondary swirl no. = 0.4)

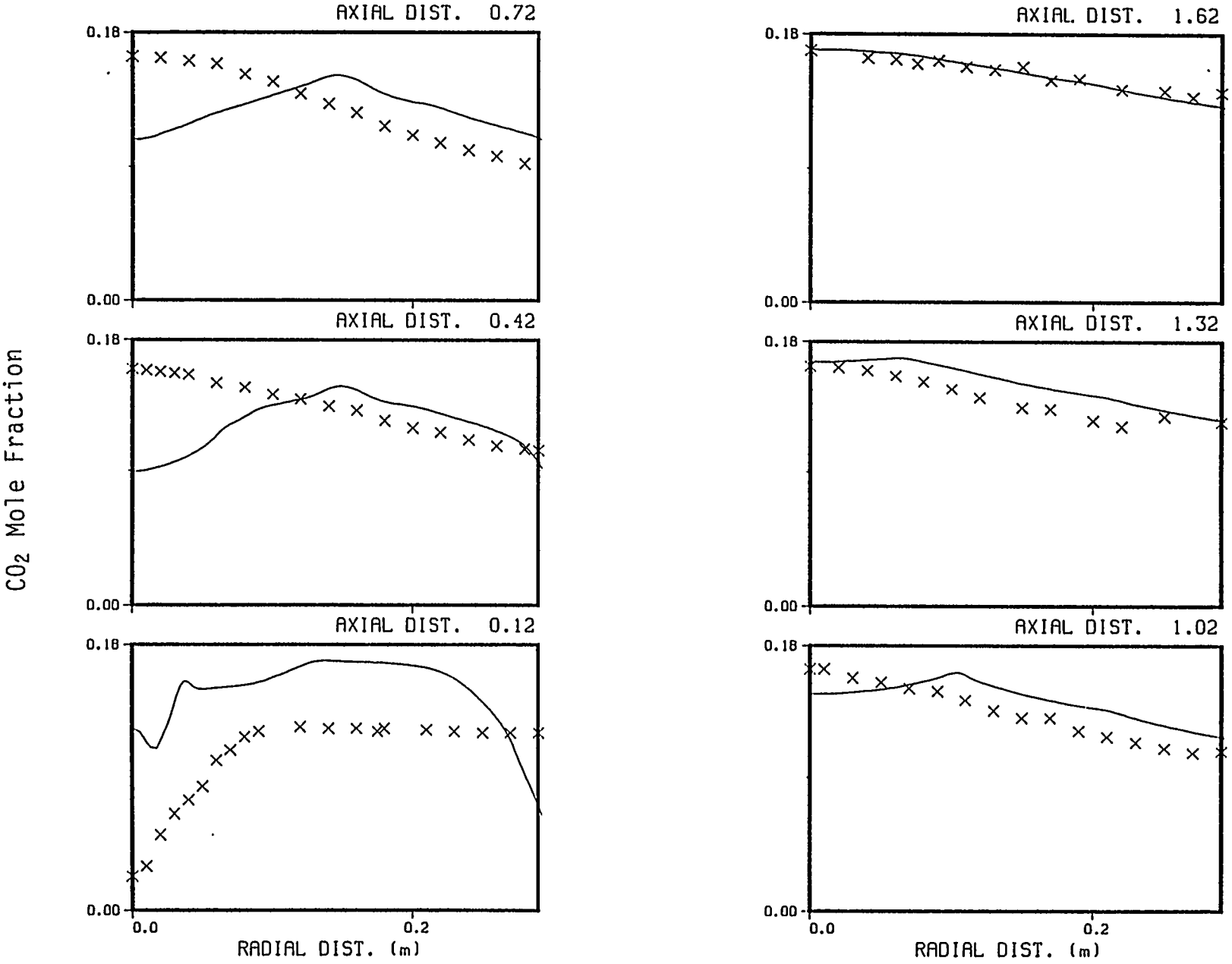

Figure III.A-8. Predicted and measured radial profiles of carbon dioxide concentration for combustion of Wyoming subbituminous coal in the Imperial College reactor. (Secondary swirl no. = 0.4)

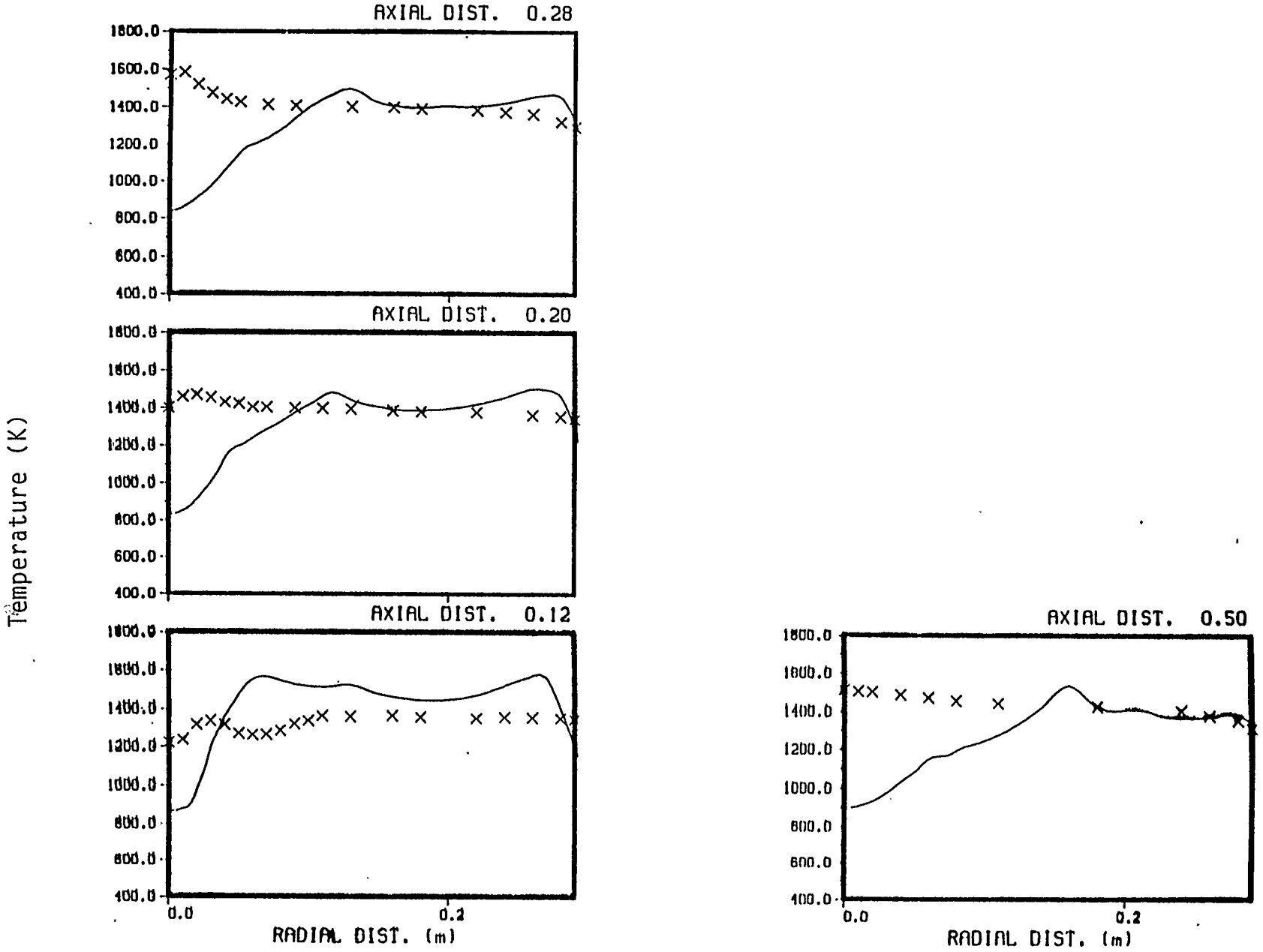

Figure III.A-9. Predicted and measured gas temperature for combustion of Wyoming subbituminous coal in the Imperial College reactor. (Secondary swirl no. = 0.4)

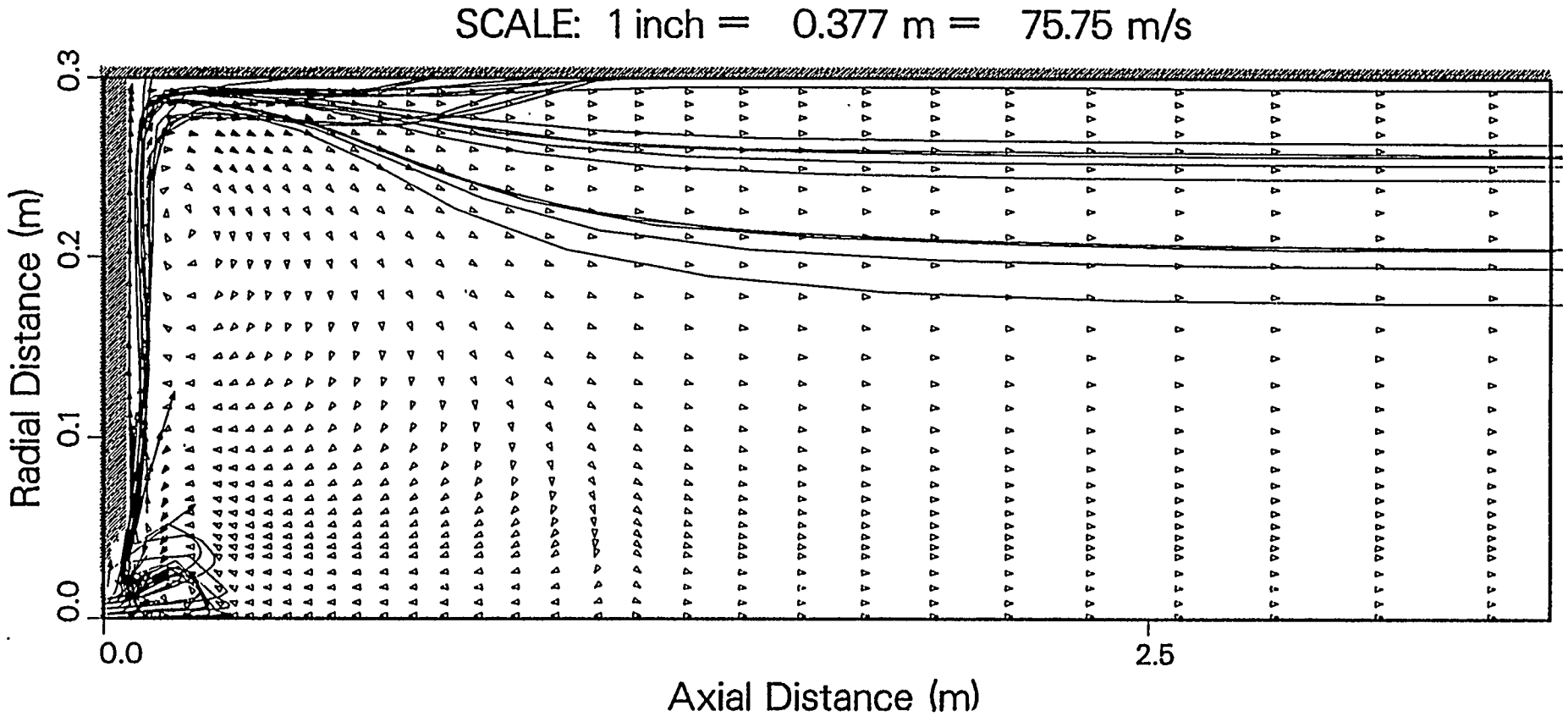

Figure III.A-10. Predicted u-v velocity vectors and particle trajectories for combustion of Pocahontas low-volatile coal in the Imperial College reactor. (Secondary swirl no. = 0.7)

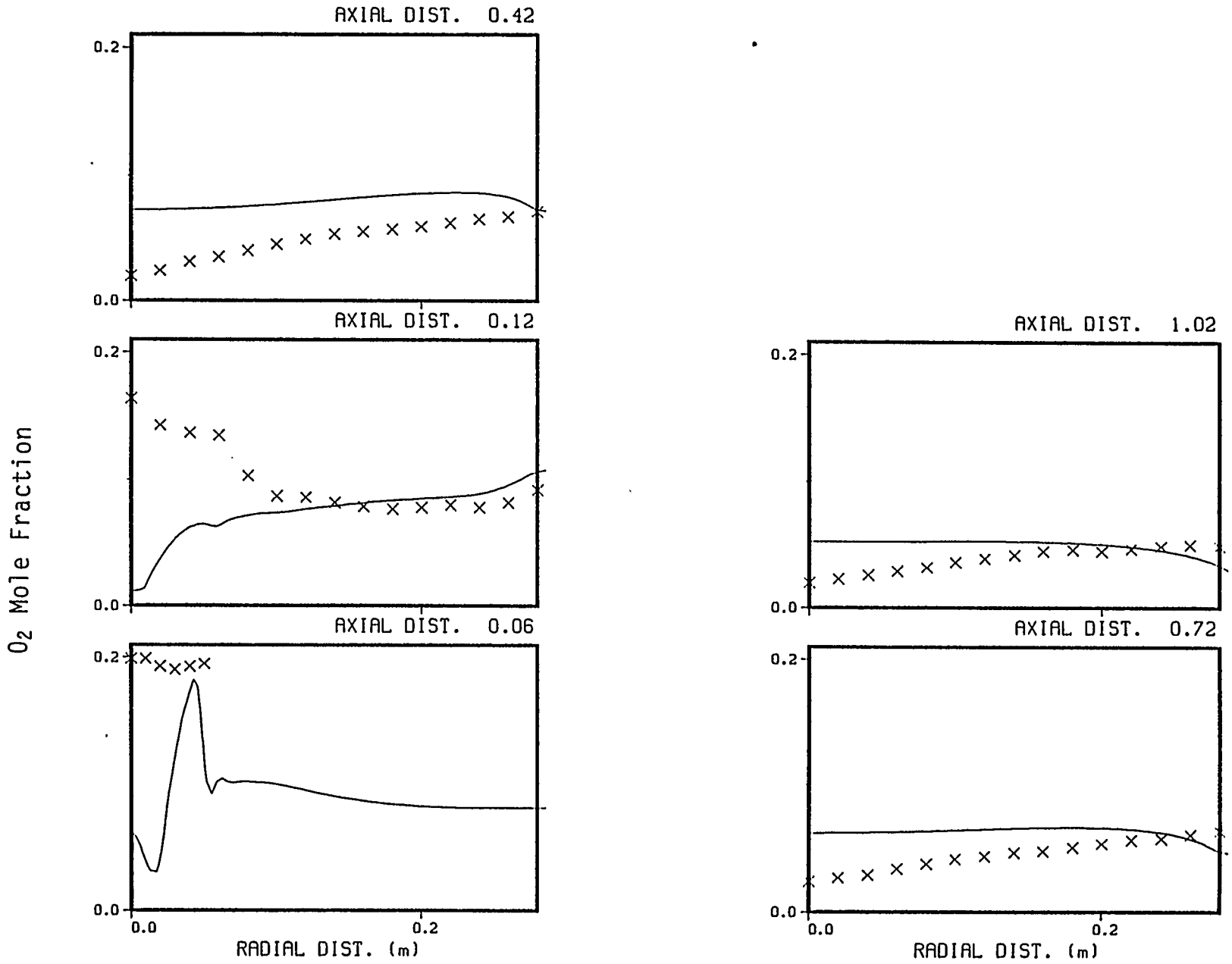

Figure III.A-11. Predicted and measured radial profiles of oxygen concentration for combustion of Pocahontas low-volatile coal in the Imperial College reactor. (Secondary swirl no. = 0.7)

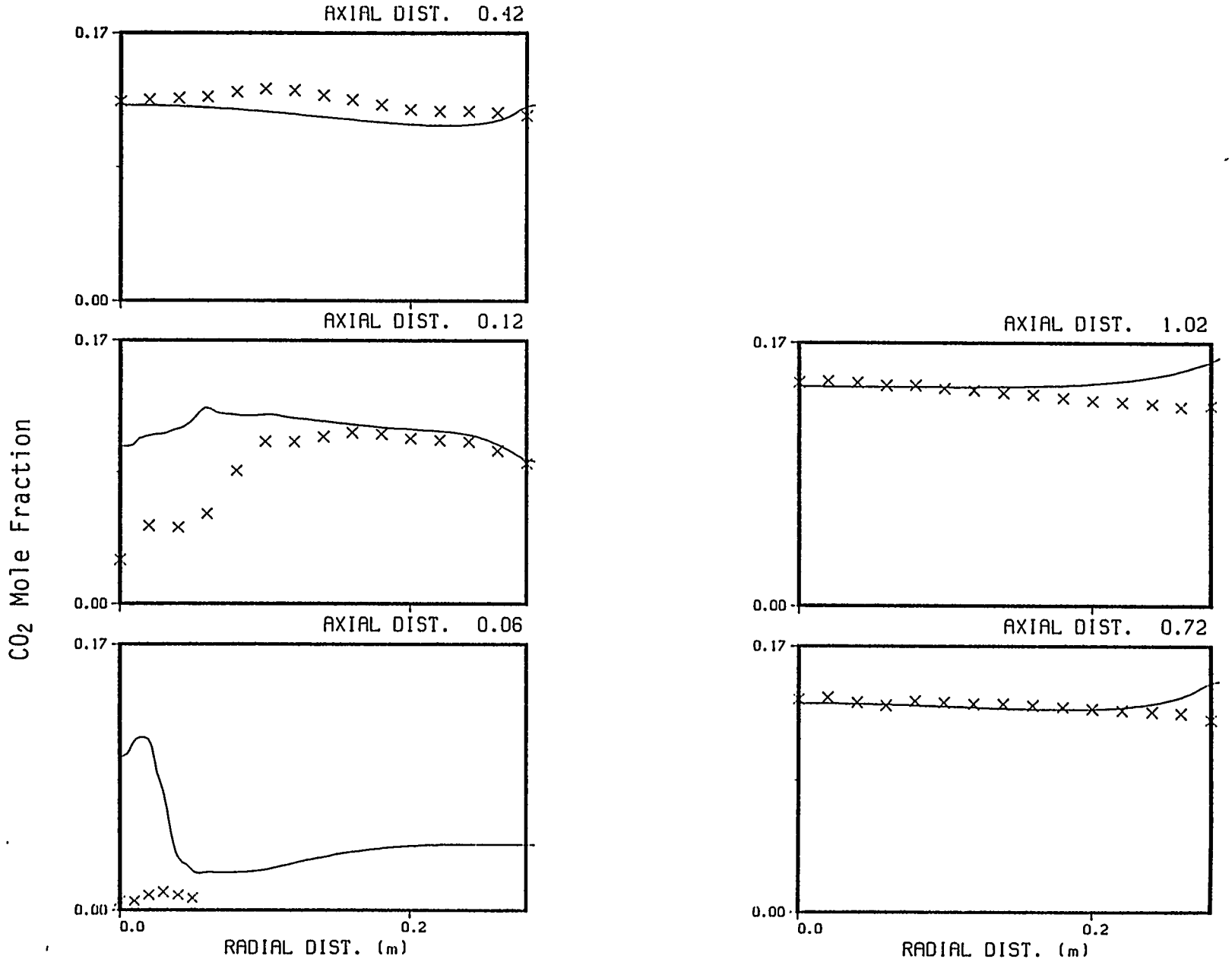

Figure III.A-12. Predicted and measured radial profiles of carbon dioxide concentration for combustion of Pocahontas low-volatile coal in the Imperial College reactor. (Secondary swirl no. = 0.7)

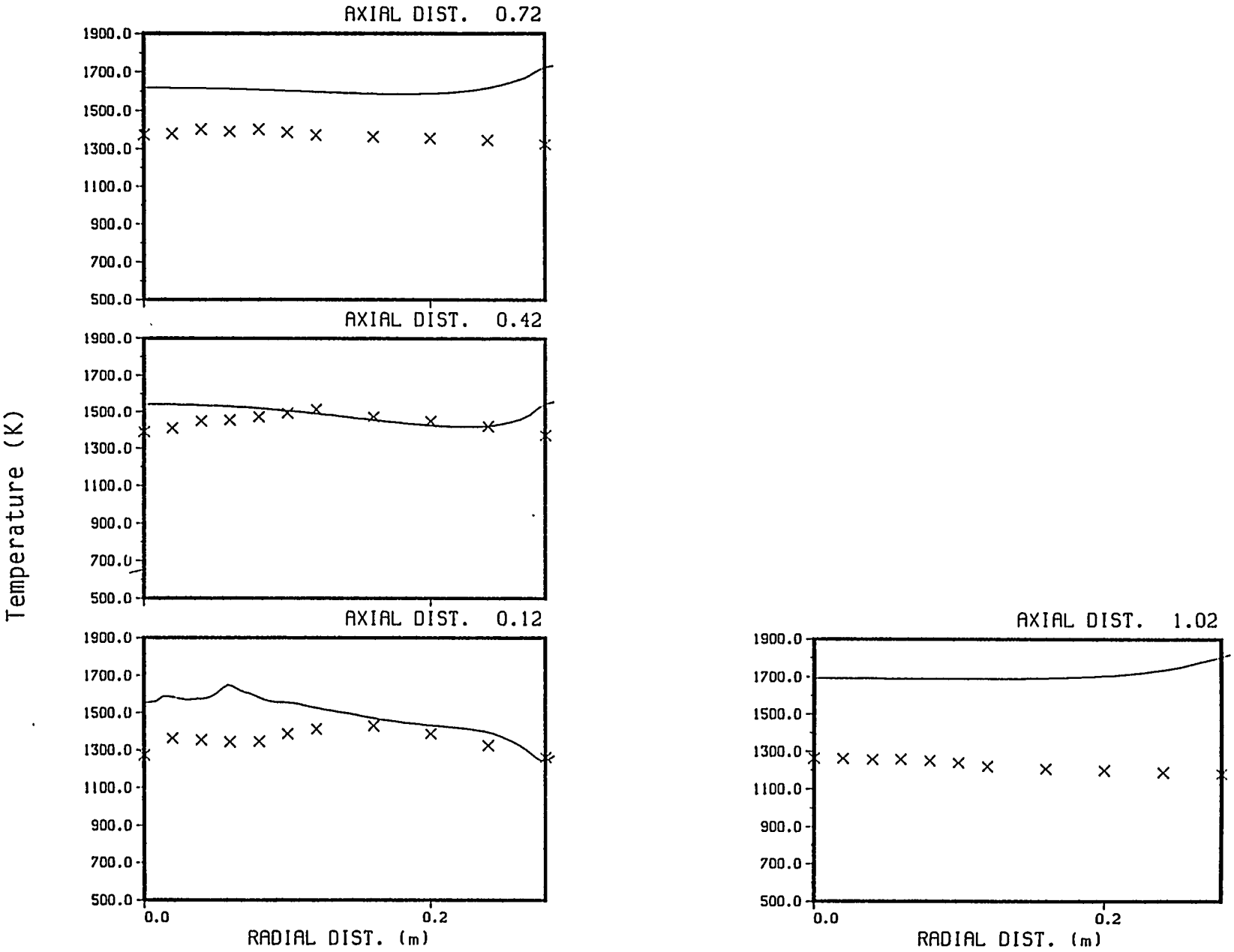

Figure III.A-13. Predicted and measured gas temperature for combustion of Pocahontas low-volatile coal in the Imperial College reactor. (Secondary swirl no. = 0.7)

gasification facilities. The cases differ with coal type and inlet conditions. For all the cases, the FG-DVC submodel was used, and heterogenous reactions of oxygen, carbon dioxide, and steam with char were considered. All three cases have non-swirling inlets.

The first case is gasification of Wyoming subbituminous coal. Figure III.A-14 shows the velocity vector plot with particle trajectories. Because of the non-swirling inlet condition, the particle radial dispersion is slow, and the external recirculation zone is relatively big. Figure III.A-15 shows the history of a particle of size 17 μm starting at a location half way between the reactor centerline and the primary inlet wall. The figure shows the particle trajectory, its diameter and mass history and the temperature history of both the particle and the gas along the trajectory. Devolatilization is completed at a distance of about 0.1 m from the inlet, followed by a very slow char oxidation reaction. Gas temperature reaches a maximum value of about 2600 K with particle temperature reaching a value of 2000 K. This high value of temperature is typical of gasification processes.

Predicted oncentration profiles for hydrogen, carbon monixide, and carbon dioxide are shown in Figs. III.A-16, 17, and 18. Predictions compare reasonably well with the data in the downstream end of the reactor. In the near-burner region, the code overpredicts hydrogen and carbon monoxide and underpredicts carbon dioxide. It substantially overpredicts hydrogen and underpredicts carbon dioxide at an axial distance of 0.36 m. All predicted radial profiles become more flat in shape earlier than the data, suggesting that mixing might be occurring faster in the predictions than it is during experiment.

In the second case, studies were performed on gasification with North Dakota lignite. Predicted and measured radial profiles of hydrogen, carbon monoxide, and carbon dioxide concentration (not shown here) where compared. Hydrogen predictions showed good agreement with the data. Predictions of carbon monoxide were also found to agree reasonably well with the measured values, with a slight overprediction. But the code substantially overpredicted carbon dioxide concentration. Overprediction of both carbon monoxide and carbon dioxide is most likely due to overpredicting burnout. Burnout predictions could not be compared because no data were available.

Illinois #6 bituminous coal was used in the third case. Unlike the other two cases, there was a small secondary flow of air with no swirl. Figures III.A-19 and 20 show the comparisons between the predictions and experimental data of the radial concentration profiles of carbon monoxide and carbon dioxide. Again, carbon monoxide is slightly overpredicted, and carbon dioxide is slightly underpredicted. But in general, the near-burner predictions of all three species are found to predict the trends observed in the experiment. At an axial location of 0.21 m from the inlet, the code correctly predicted the radial location where the carbon dioxide concentration is maximum. Likewise, it also predicted the correct radial location of the minimum values of hydrogen (not shown) and carbon monoxide, at the same axial location.

Combustion Engineering (CE) Drop-Tube Furnace System (DTFS) - A description of the ABB CE drop tube furnace system (DTFS) was given by Nsakala et al. (1986). A schematic diagram of the reactor was shown in the 5th Annual Report (Solomon et al., 1991) and is repeated here in Fig. III.A-21 to add a detail not shown previously. Rather than being entrained in primary gas and fed through a 0.27-cm-diameter tube as shown in the previous figure, the coal is injected on the centerline of the 0.27-cm-diameter tube through a 0.084-cm-i.d. hypodermic tube. Sheath gas is fed at room temperature through the annulus between the hypodermic tube and the larger tube. The coal injection was simulated with two starting locations, one of which was in the annular region of the injection nozzle; the difference in predicted burnout between the two starting locations was insignificant.

Eleven cases were simulated as shown in Table III.A-2. Gas flowrates were constant, while coal flowrate varied. The sheath, carrier, and secondary gas streams were all 6.5 percent oxygen in argon at 1755 K. The single-step kinetics of Solomon et al. (1986) were used for devolatilization. Coal C cases were also simulated with the FG-DVC submodel. Char kinetics were supplied by ABB CE for Coals A and B. For Coal C, the kinetics reported by Smith and Smoot (1989) obtained from refitted ABB CE kinetic data (Goetz et al., 1982) were used. The Field et al. (1967) kinetics were also tested. The kinetics of de

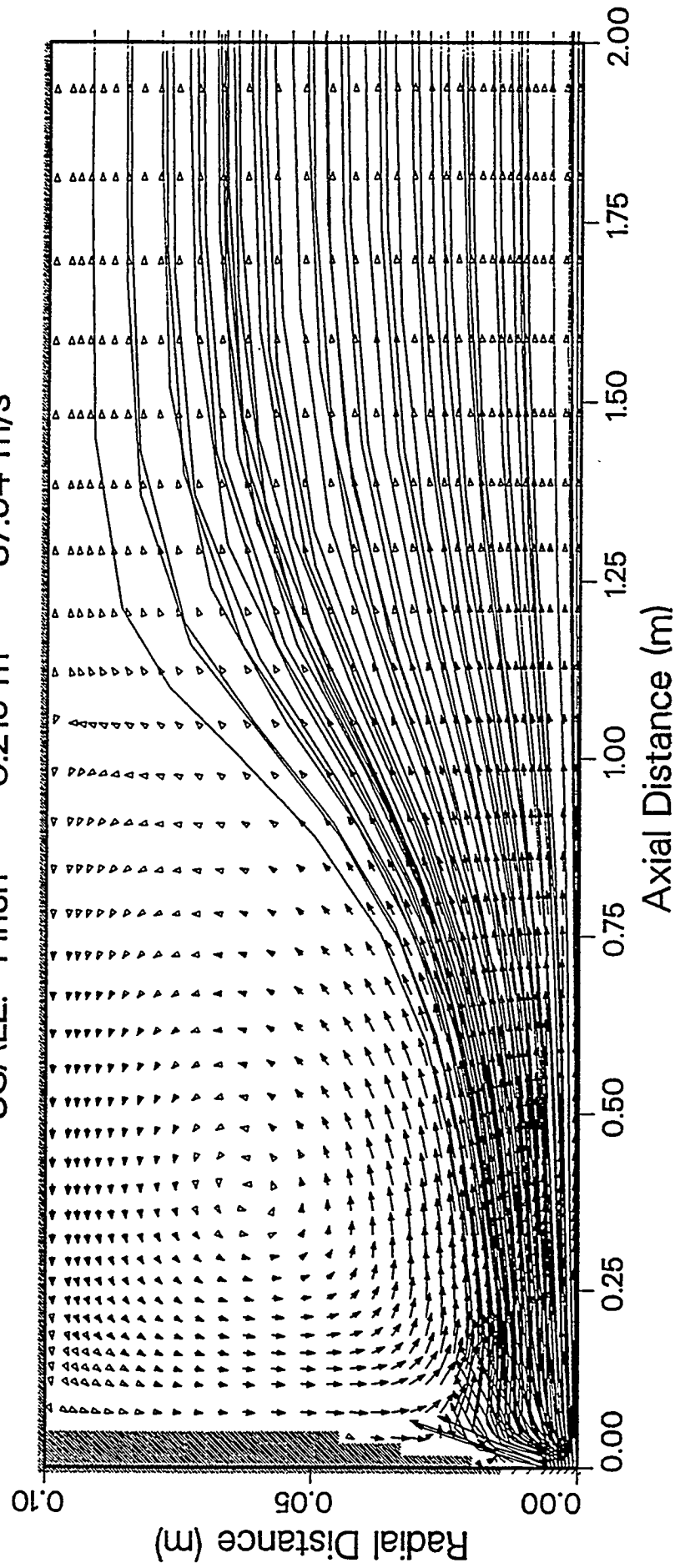

Figure III.A-14. Predicted u-v velocity vectors and particle trajectories for oxygen-blown gasification of Wyoming subbituminous coal in the BYU gasifier.

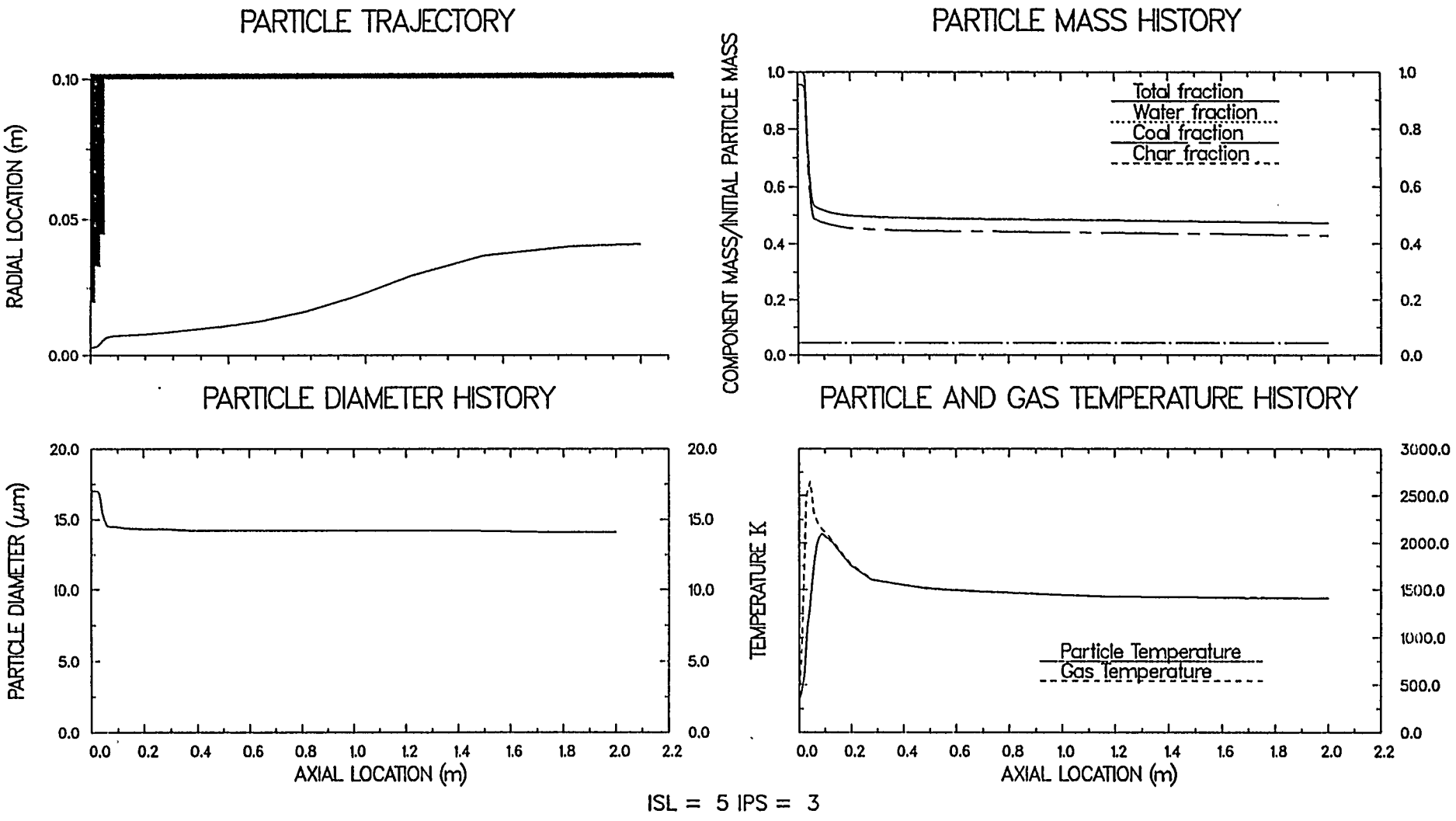

Figure III.A-15. Predicted particle properties for a 17-μm particle in the oxygen-blown gasification of Wyoming subbituminous coal in the BYU gasifier.

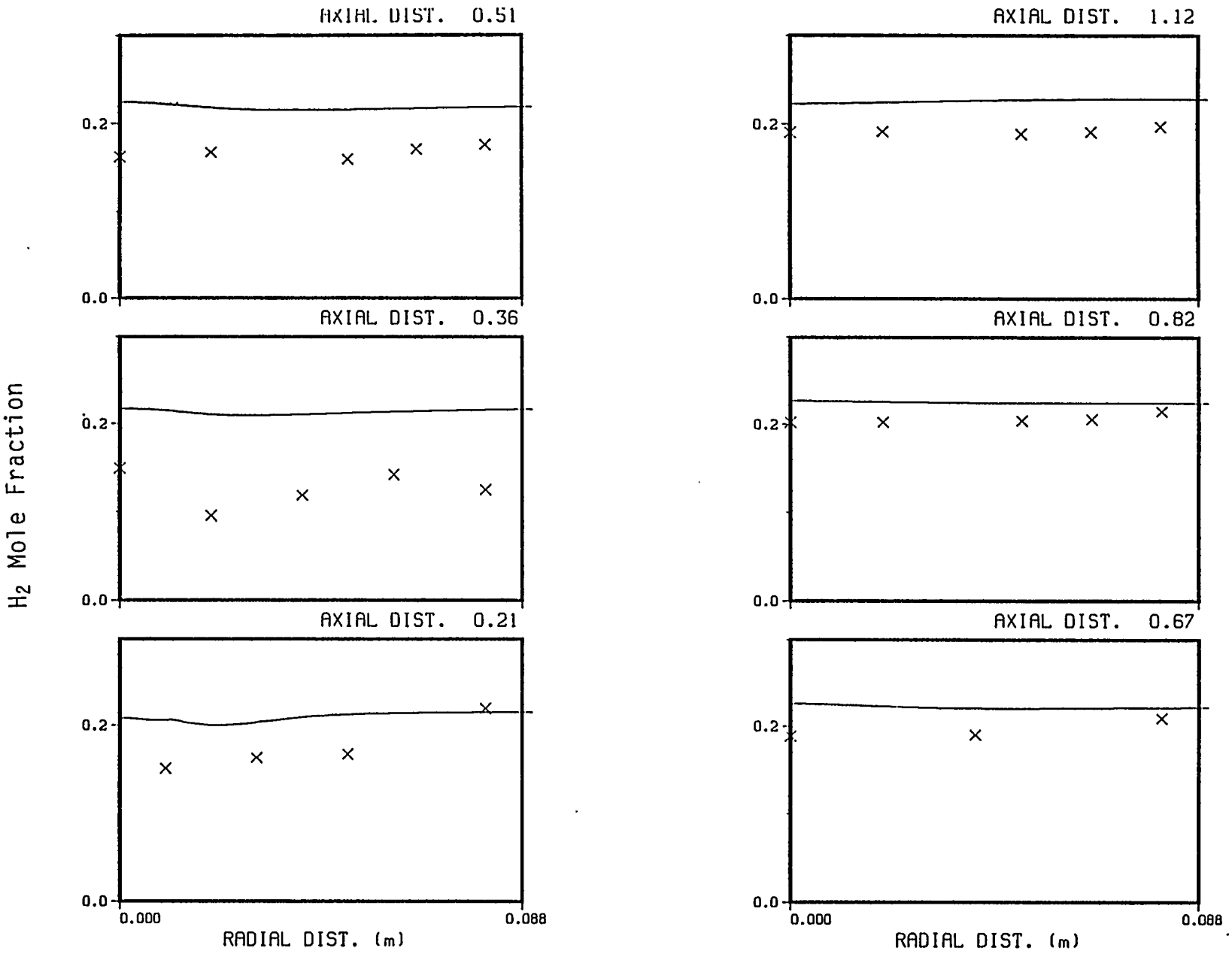

Figure III.A-16. Predicted and measured radial profiles of hydrogen concentration for oxygen-blown gasification of Wyoming subbituminous coal in the BYU gasifier.

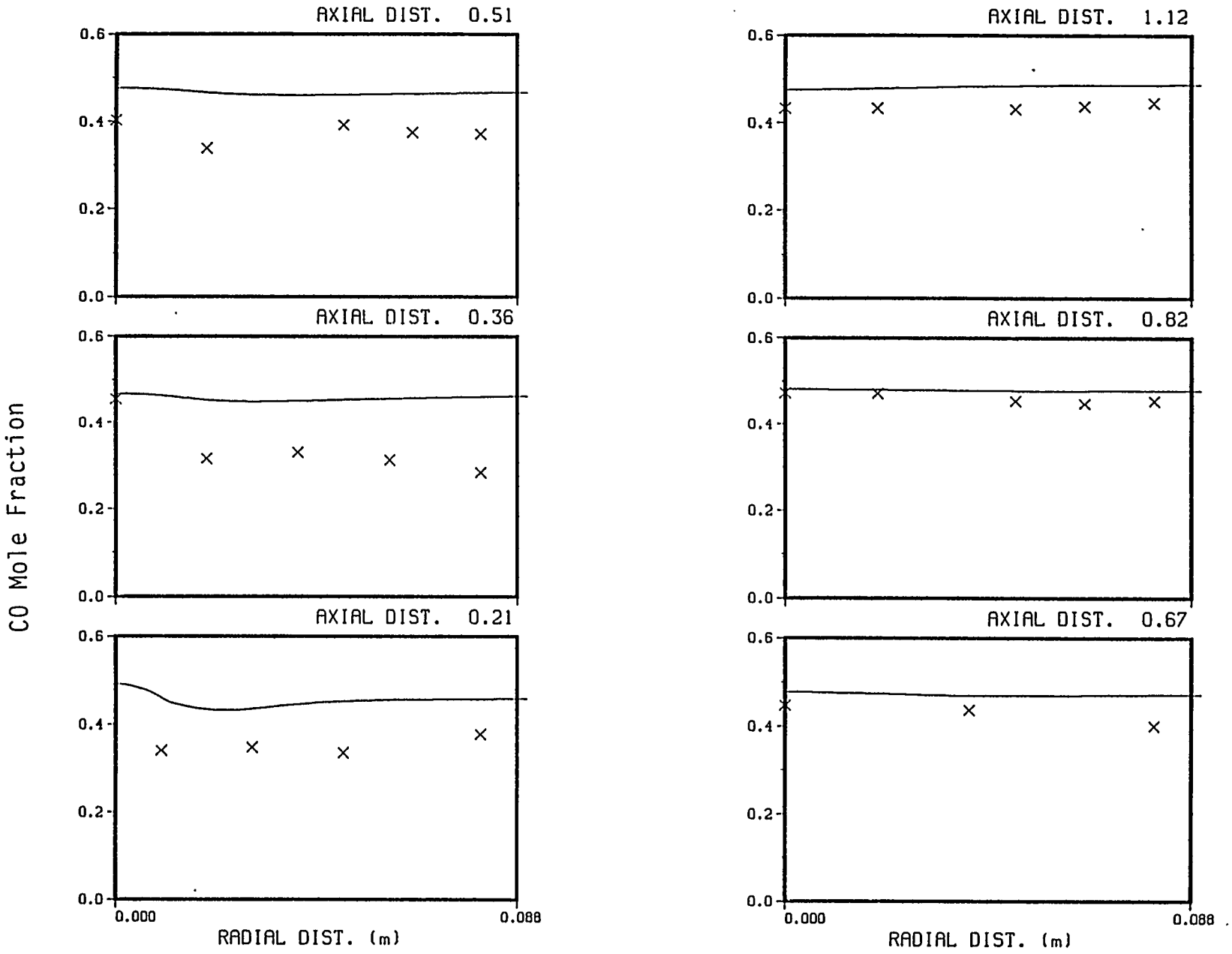

Figure III.A-17. Predicted and measured radial profiles of carbon monoxide concentration for oxygen-blown gasification of Wyoming subbituminous coal in the BYU gasifier.

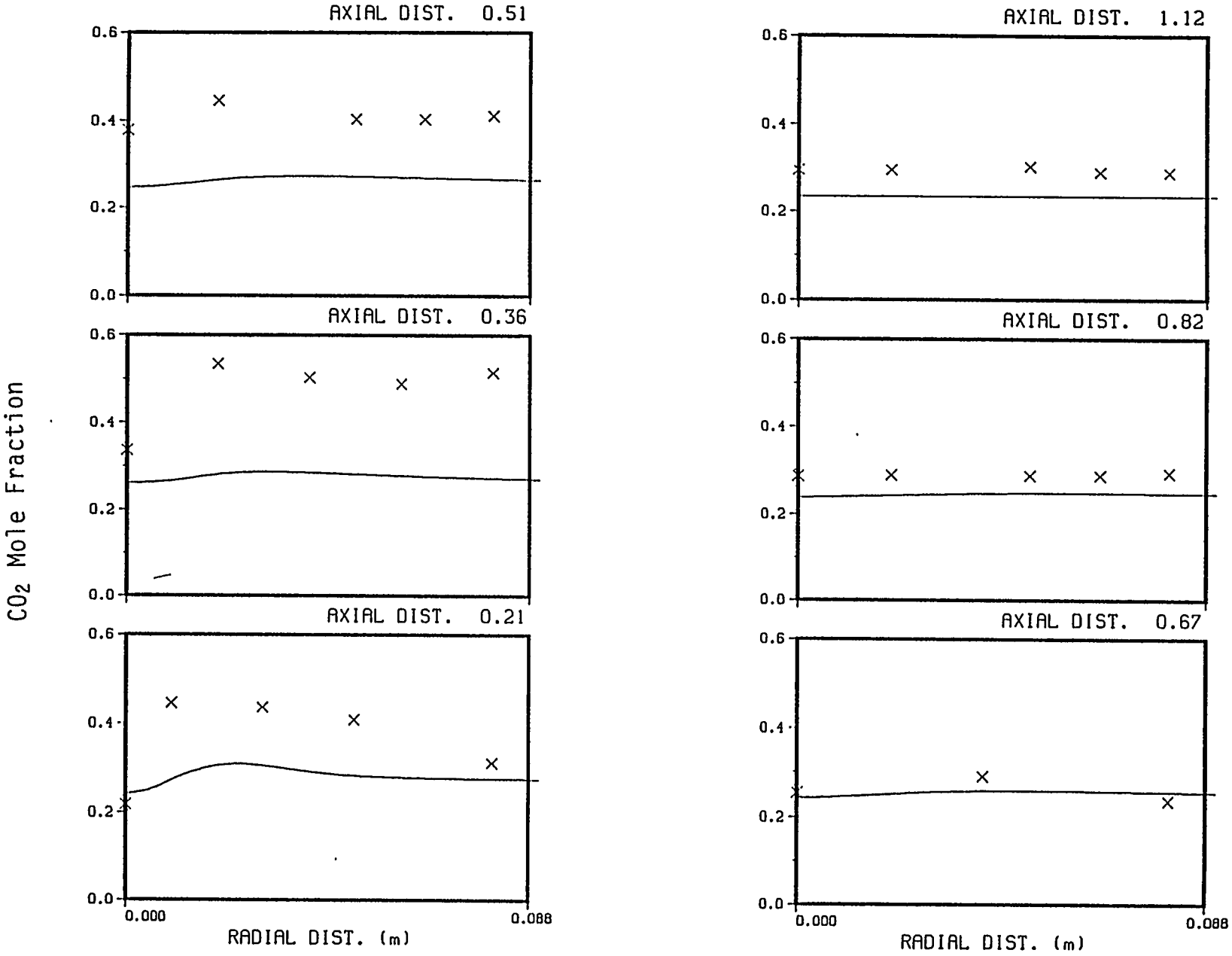

Figure III.A-18. Predicted and measured radial profiles of carbon dioxide concentration for oxygen-blown gasification of Wyoming subbituminous coal in the BYU gasifier.

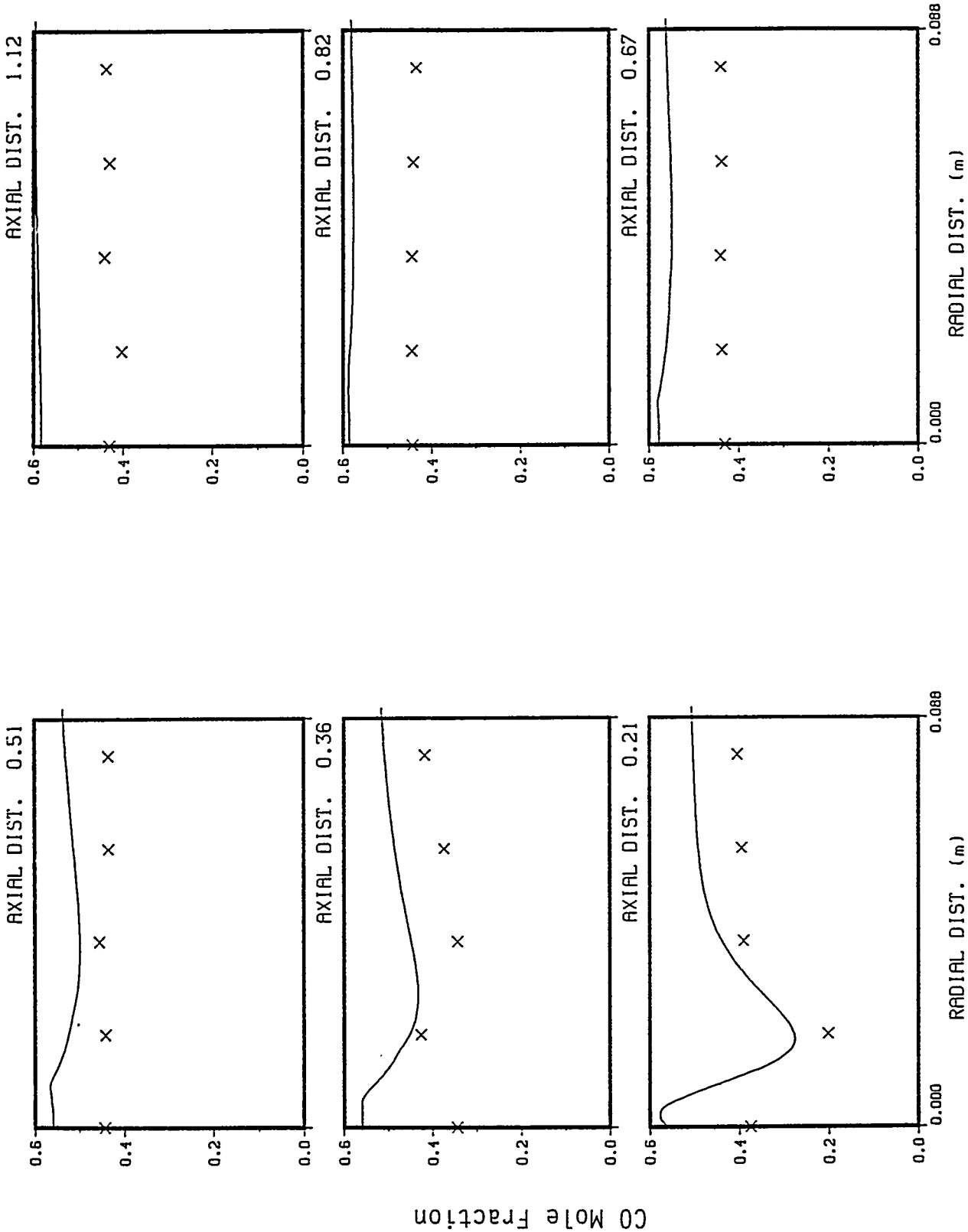

Figure III.A-19. Predicted and measured radial profiles of carbon monoxide concentration for gasification of Illinois #6 bituminous coal in the BYU gasifier.

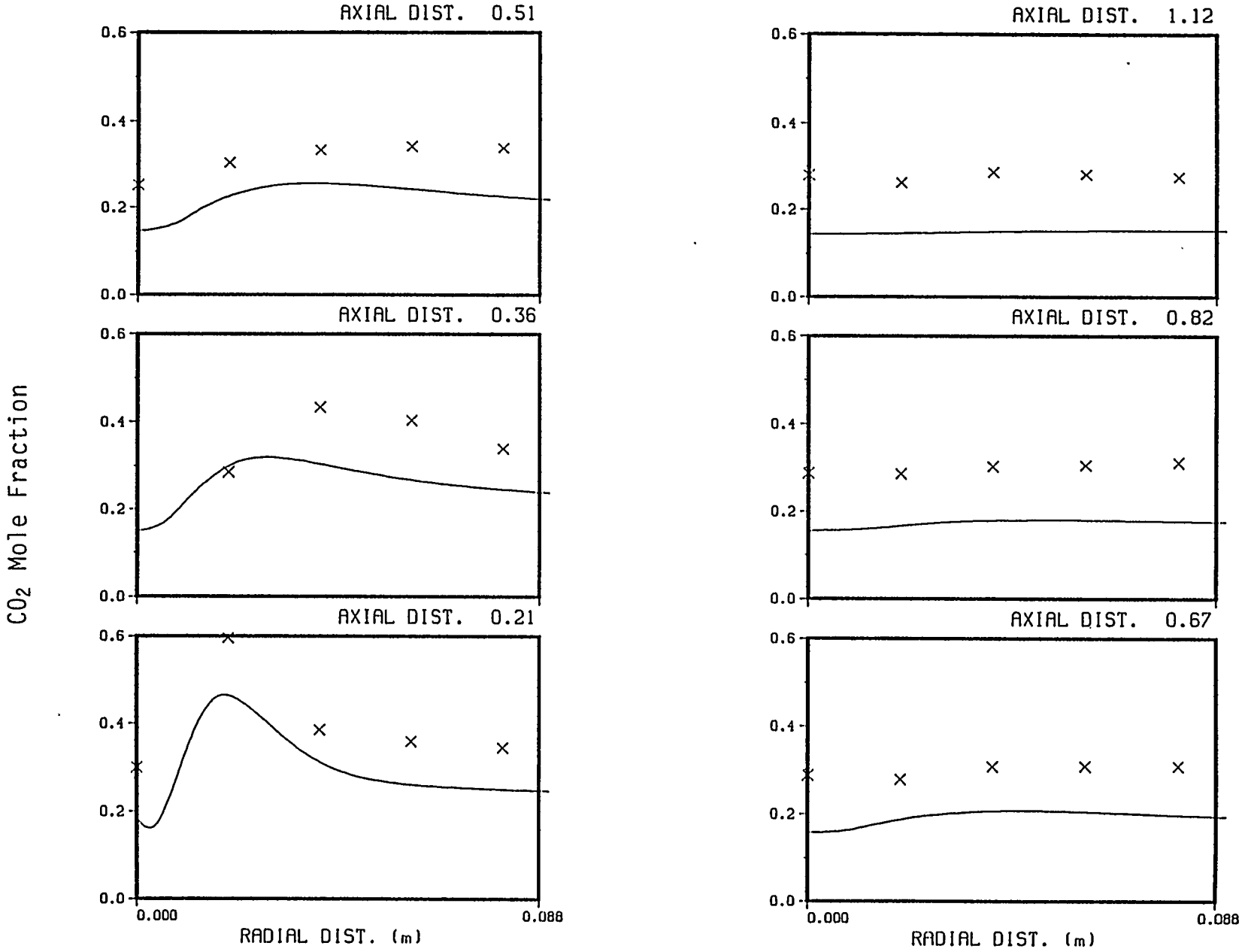

Figure III.A-20. Predicted and measured radial profiles of carbon dioxide concentration for gasification of Illinois #6 bituminous coal in the BYU gasifier.

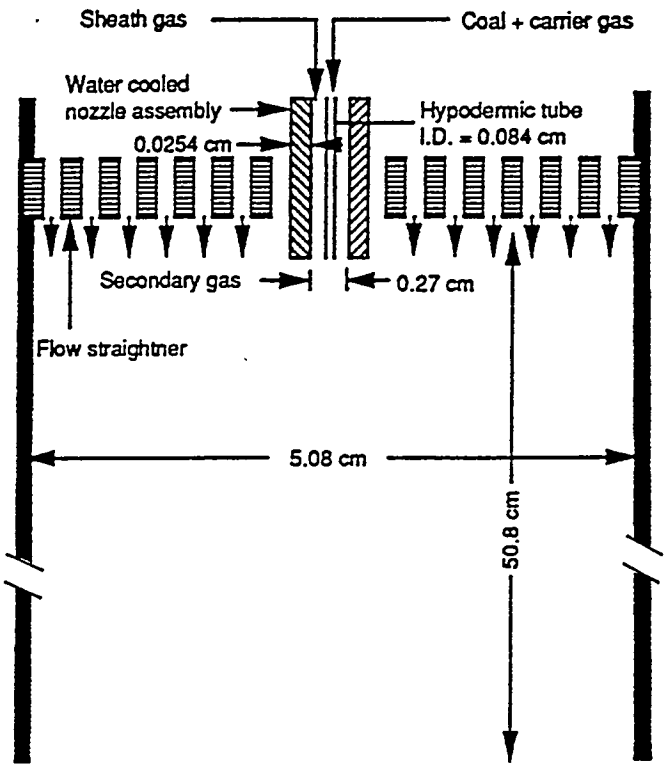

Figure III.A-21. Burner region of ABB Combustion Engineering drop-tube reactor.

TABLE III.A-2

MEASURED AND PREDICTED NO_x CONCENTRATION AT THE EXIT OF THE ABB CE DROP TUBE FURNACE

Coal Type	Coal feed rate (g/min)	O_2/coal ratio	Measured NO_x(ppm)	Predicted NO_x(ppm)	% difference
Coal A	0.91	1.59	115	93	19
(Bituminous)	0.62	2.35	131	109	17
	0.44	3.30	152	122	20
	0.26	5.59	151	133	12
Coal B	0.92	1.57	156	108	31
(Bituminous)	0.68	2.12	219	138	37
	0.48	2.99	274	166	39
	0.27	5.35	251	205	18
Coal C	0.77	1.88	79	97	-23
(subbituminous)	0.61	2.39	86	112	-27
	0.39	3.69	95	122	-28

Soëte (1975), Wendt and coworkers (Wendt et al., 1989; Bose et al., 1988), and Mitchell and Tarbell (1982) were used for fuel NO formation. Coal nitrogen was assumed to partition equally between HCN and NH_3 upon devolatilization for all three coals, although a value of unity is probably more appropriate for bituminous coals (Boardman, 1990). Convergence was difficult to achieve as the partitioning factor approached pure HCN and the predictions moved farther away from from the data.

Figure III.A-22 shows the predicted and measured NO_x concentrations at the reactor exit. Since the inlet gas mixture is argon and oxygen, the NO_x is formed from fuel nitrogen. The Coal C predictions were obtained with the single-step devolatilization kinetics and the char kinetics reported by Smith and Smoot (1989) for subbituminous coal. The latter gave results which agreed more closely with the experimental data than the kinetics of Field et al. (1967). The char kinetic rates are compared in Fig. III.A-23a for all three coals. Fuel NO was predicted with the de Soëte kinetics in all three cases. The predictions are strongly dependent on the assumptions of HCN/NH_3 partitioning and the fuel NO kinetics. Convergence was marginal with the Wendt kinetics and not achieved with the Mitchell and Tarbell kinetics. Further work is needed to improve robustness with the various kinetics options and to correlate the HCN/NH_3 partitioning factor with coal type, heating rate, etc.

As shown by both the predictions and the data, the effluent concentration of NO_x increases at a decreasing rate with decreasing coal flowrate. The data for Coal B even indicate a decrease in NO_x concentration at low coal flowrate. This trend may be explained as follows: Predicted fractional burnout of the coal increases with decreasing coal flowrate (Fig. III.A-23b). However, the product of burnout and coal flowrate (total amount of coal that has reacted) decreases with decreasing coal flowrate (Fig. III.A-23c). Since nitrogen evolution is proportional to the coal mass loss, the total nitrogen in the exit gas should also decrease with decreasing coal flowrate, and this is indeed the case (Fig. III.A-23c). Therefore, total nitrogen in the effluent gas decreases with decreasing coal flowrate, but NO_x concentration increases. The reason can be seen in Fig. III.A-23d. The formation of NO depends on the availability of oxygen. As coal flowrate is increased, oxygen is depleted for an increasingly longer distance at the reactor centerline, due to char combustion. Although less nitrogen is evolved at lower coal flowrate, more NO is formed because of the increased availability of oxygen. At sufficiently high coal flowrate, the availability of fuel

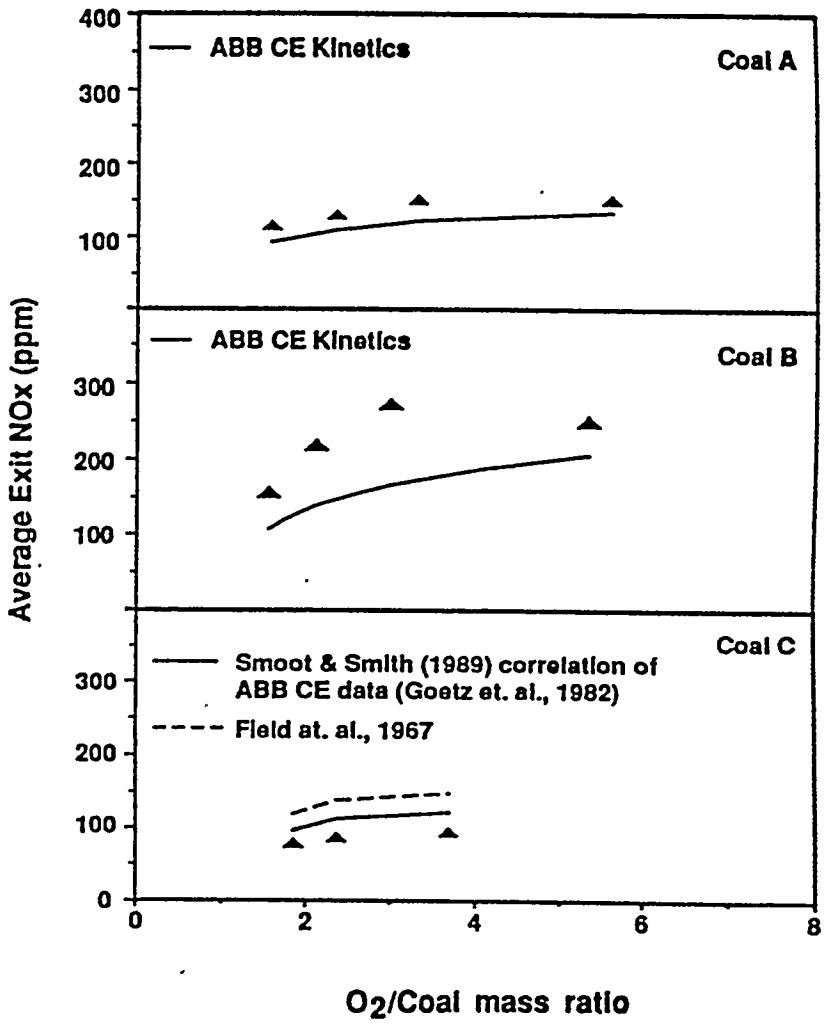

Figure III.A-22. Predicted (—) and measured (▲) NO_x at the outlet of the ABB CE drop tube furnace for three coal types.

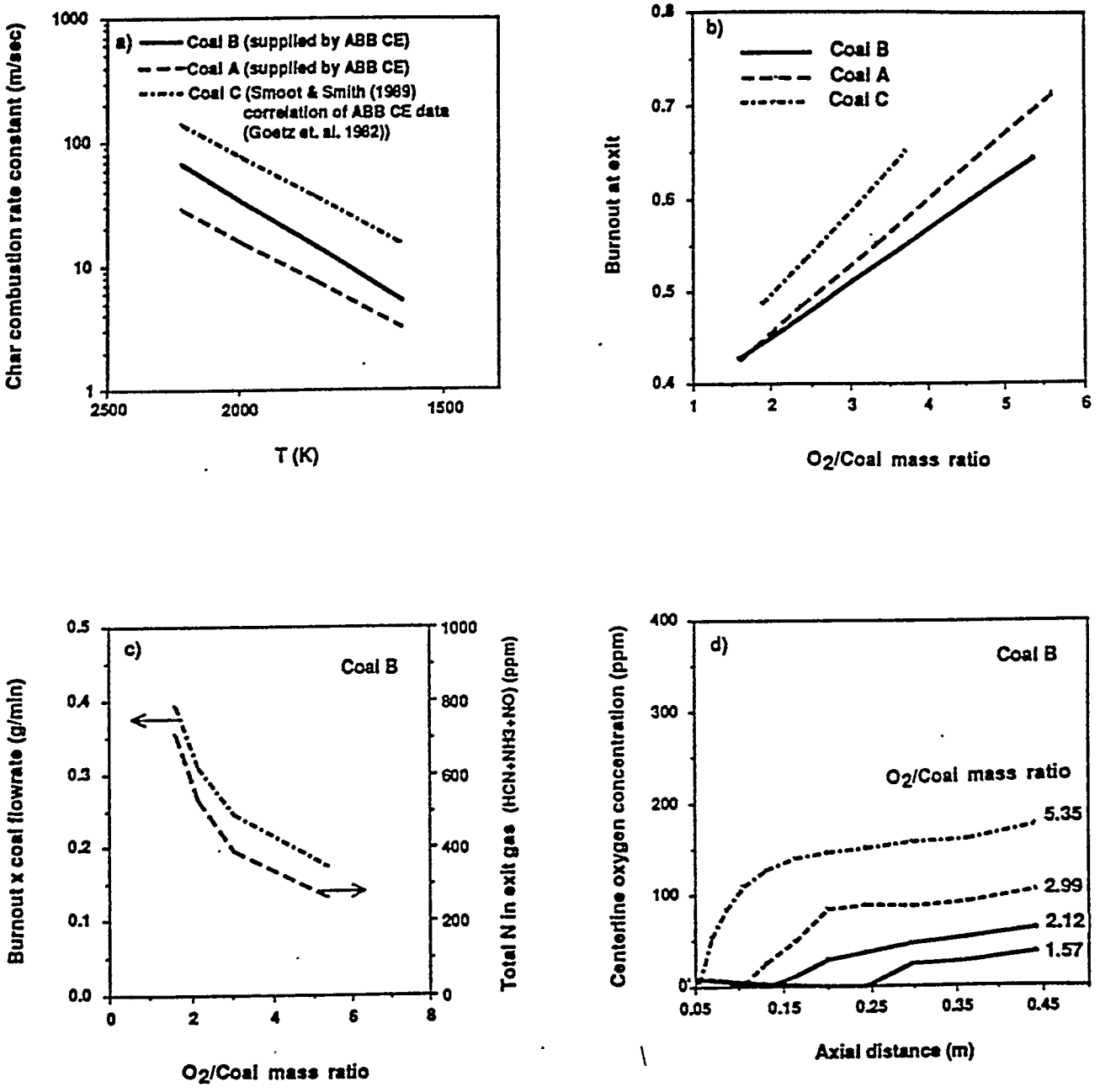

Figure III.A-23. Predictions for coal combustion in the ABB CE drop tube reactor.

nitrogen becomes the limiting factor, and NO_x decreases. This explanation was tested theoretically with the model, which predicted a maximum in NO_x concentration at an O_2/coal ratio of approximately 12.

User-Friendliness and Robustness

Considerable effort was expended to make 93-PCGC-2 user-friendly and robust. Diagnostics were added to the code for many of the the more common input errors to tell the user how to change his input. Two graphics packages were developed to assist with preparing code input and viewing of code output.

A graphical user interface (GUI) for preparing code input was developed. The GUI uses the CQUEL.BYU graphics software, which runs under the X windows system and is available on many platforms. A portion of the window for specifying primary stream data is shown as an example in Fig. III.A-24. The GUI is intended to allow both the inexperienced and experienced users of 93-PCGC-2 to quickly prepare code input for new cases. Its focus is on the standard coal combustion case with simple geometry. It is not intended to provide access to all of the code options; these can be accessed from the input data files once they are created. A detailed explanation of the GUI and its use is contained in the 93-PCGC-2 user's manual (Brewster et al., 1993).

The graphics for code output uses the DISSPLA software. A menu-driven program provides the interface between DISSPLA and the plotting files of 93-PCGC-2. A spreadsheet option is provided for users that don't have access to DISSPLA. With this option, code output can be viewed in any spreadsheet package with plotting options. The DISSPLA post-processor is described in detail in the user's manual (Brewster et al., 1993).

Code Documentation

A new user's manual was prepared to document 93-PCGC-2 with the FG-DVC submodel (Brewster et al., 1993). The user's manual contains a description of the code theory, the numerical solution, how to use the code, and how to install the code on a computer system.

Summary and Conclusions

A 2-D pulverized coal combustion and gasification code (82-PCGC-2) was extended to include the FG-DVC submodel for devolatilization, laminar flow effects, gas buoyancy effects, a user-friendly energy equation option, and a condensed-phase equilibrium algorithm. The improved model (93-PCGC-2) was evaluated using data from five reactor systems. The evaluation results support the following observations:

1. The code (93-PCGC-2) was applied to five very different systems, ranging from near-laminar combustion to strongly swirling, turbulent flow combustion to high-pressure gasification. Comparison of predictions with measurements was often good, with exceptions noted below.

2. 93-PCGC-2 often predicts ignition prematurely, presumably because of the assumptions of instantaneous mixing and reaction of volatiles with the bulk gas.

3. The code has trouble giving reasonable predictions for highly swirling systems with little or no quarl, presumably because of inadequacies in the turbulence submodel.

4. A clear advantage of the FG-DVC submodel is coal generality.

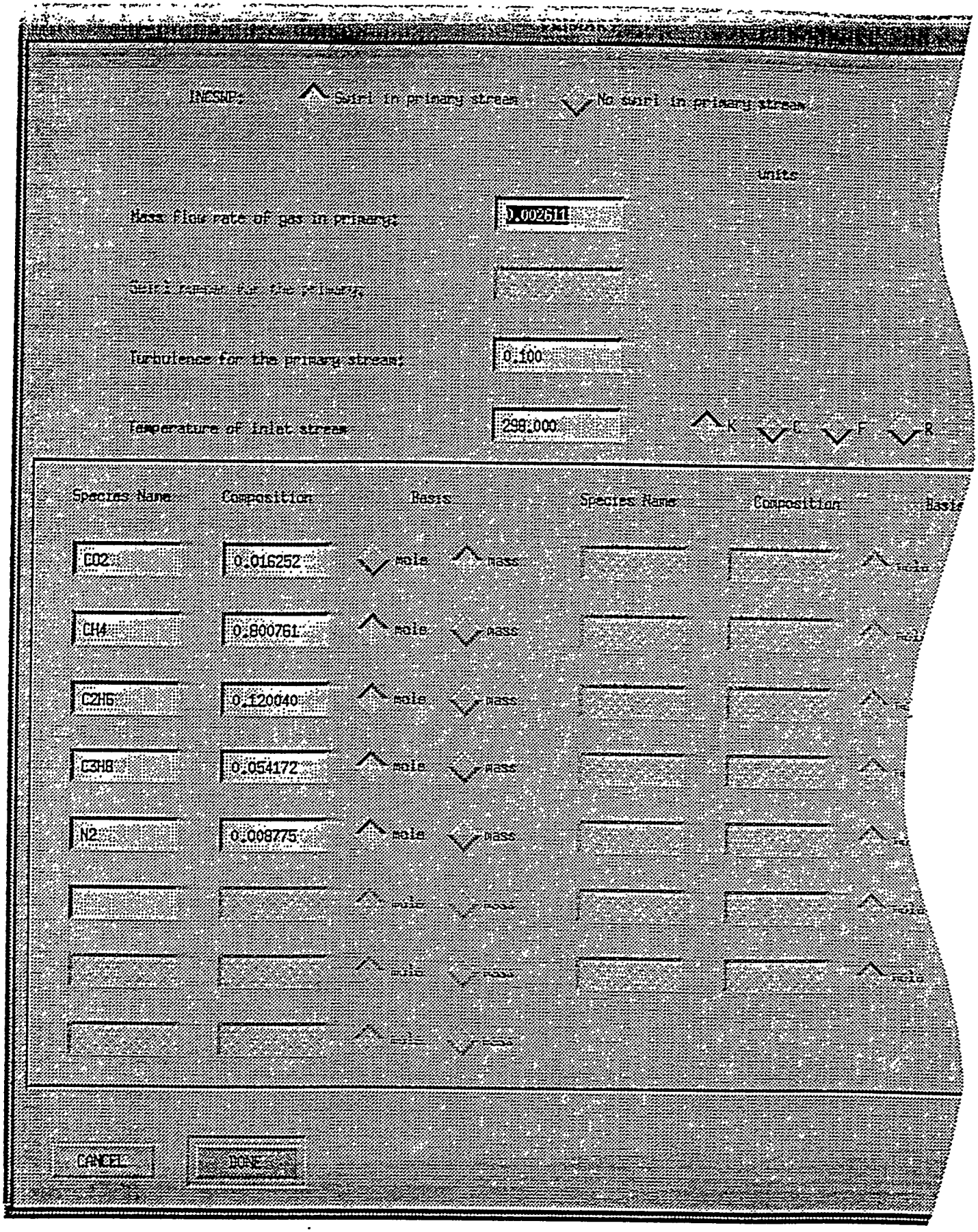

Figure III.A-24. Graphical User Interface window for specifying primary stream data.

5. FG-DVC has potential for contributing in areas of ignition, swelling, char reactivity, rate of evolution of pollutant precursors, and non-equilibrium processes related to tar formation (e.g. mild gasification and soot formation)

6. Including soot radiation would probably improve the agreement bertween experimental data and predictions significantly.

Graphics programs and code diagnostics were developed to improve user-friendliness, and the code theory and operation were documented in a user's manual. Although much more user-friendly and robust than before, the code still requires significant understanding and experience on the part of the user for reliable application. User interaction is often required to achieve convergence and results must be evaluated carefully. However, for the engineer who makes the necessary investment of time to understand the code and learn its operation, it provides a valuable design and analysis tool.

References for Subtask 3.a.

Boardman, R. D., Development and Evaluation of a Combined Thermal and Fuel Nitric Oxide Predictive Model, Ph.D. dissertation, Brigham Young University, Provo, UT (1990).

Bose, A. C., Dannecker, K. M. and Wendt, J. O. L., Coal Decomposition Effects on Mechanisms Governing the Destruction of NO and Other Nitrogenous Species During Fuel-Rich Combustion, Energy & Fuels, 2, 301 (1988).

Brewster, B. S., Baxter, L. L. and Smoot, L. D., Treatment of Coal Devolatilization in Comprehensive Combustion Modeling," Energy & Fuels, 2, 362-370 (1988).

Brewster, B. S., Huque, Z., Berrondo, S., Smoot, L. D., Zhao, Y. and Solomon, P. R., 93-PCGC-2 User's Manual, developed for the Department of Energy/Morgantown Energy Technology Center under Contract No. DE-AC21-86MC23075, Vol. II, final report (1993).

Costa, M., Costen, P. and Lockwood, F. C., Pulverized-Coal and Heavy-Fuel-Oil Flames - Large-Scale Experimental Studies at Imperial-College, London, Journal of the Institute of Energy, 64, 64-76 (1991).

Costa, M., Costen, P. and Lockwood, F. C., Data Package for the Validation of a Mathematical Model of the Imperial College Large-Scale Pulverized-Fuel Furnace, Report no. FS/90/08, Imperial College of Science, Technology and Medicine, London (1990).

Crowe, C. T., Sharma, M. P. and Stock, D. E., The Particle-Source-in-Cell (PSI-CELL) Model for Gas Droplet Flows, J. Fluids Eng., Trans. of the ASME, 99, 325-332 (1977).

de Soëte, G. G., Overall Reaction Rates of NO and N_2 From Fuel Nitrogen, Fifteenth Symposium (International) on Combustion/The Combustion Institute, Pittsburgh, PA, 1093 (1975).

Field, M. A., Gill, D. W., Morgan, B. B. and Hawksley, P. G. W., *Combustion of Pulverized Coal*, The British Coal Utilization Research Association, Leatherhead, Surrey, England (1967).

Goetz, G. J., Nsakala, N. Y., Patel, K. L. and Lao, T. C., Combustion and Gasification Kinetics of Chars From Four Commercially Significant Coals of Varying Rank, Second Annual Conference on Coal Gasification, EPRI, Palo Alto, CA, October (1982).

Harding, N. S., Effects of Secondary Swirl and Other Burner Parameters on Nitrogen Pollution Formation in a Pulverized Coal Combustor, Ph.D. dissertation, Brigham Young University, Provo, UT (1980).

Mitchell, J. W. and Tarbell, J. M., A Kinetic Model of Nitric Oxide Formation During Pulverized Coal Combustion, AIChE J., 28, 302-311 (1982).

Nicoletti, P. A., METCEC - Program Logic Manual, Final Report, Work performed under Contract No. DE-AC21-85MC21353, EG&G WASC, Morgantown, WV (1986).

Nicoletti, P. A., METCEC - User's Manual, Final Report, DOE-METC Contract No. DE-AC21-85MC21353, EG&G WASC, Inc., Morgantown, WV (1986).

Nsakala, N., Patel, R. and Borio, R., An Advanced Methodology for Prediction of Carbon Loss in Commercial Pulverized Coal-Fired Boilers, 1986 JPGC, Portland, OR, October 19-23 (1986).

Shaw, D. W. and Essenhigh, R. H., Temperature Fluctuations in Pulverized Coal (P.C.) Flames, Comb. Flame, 86, 333-346 (1991).

Smith, P. J. and Smoot, L. D., Brigham Young University, Detailed Model for Practical Pulverized Coal Furnaces and Gasifiers. Volume 1. General Technical Report, Brigham Young University, Provo, UT (1989).

Smoot, L. D. and Smith, P. J., *Coal Combustion and Gasification*, Plenum, New York (1985).

Solomon, P. R., Serio, M. A., Hamblen, D. G., Smoot, L. D. and Brewster, B. S., eds., Measurement and Modeling of Advanced Coal Conversion Processes, Quarterly and Annual technical reports, eds., work performed for the U.S. Department of Energy under contract no. DE-AC21-86MC23075 (1986-1993).

Solomon, P. R., Serio, M. A., Carangelo, R. M. and Markham, J. R., Very Rapid Coal Pyrolysis, Fuel, 65, 182-194 (1986).

Wendt, J. O. L., Bose, A. C. and Hein, K. R. G., Fuel Nitrogen Mechanisms Governing NO_x Abatement for Low and High Rank Coals, 1988 Joint Symposium on Stationary Combustion NO_x Control, San Francisco, CA, March 609 (1989).

III.B. SUBTASK 3.B. - COMPREHENSIVE FIXED-BED MODELING REVIEW, DEVELOPMENT, EVALUATION, AND IMPLEMENTATION

Senior Investigators - Predrag T. Radulovic and L. Douglas Smoot
Brigham Young University
Provo, Utah 84602
(801) 378-3097 and (801) 378-4326

Research Assistants - M. Usman Ghani, Michael L. Hobbs, and Sung-Chul Yi

Objectives

The objectives of this subtask are: (1) to develop an advanced, fixed-bed* model incorporating the advanced submodels being developed under Task 2, particularly the large-particle submodel (Subtask 2.e.), and (2) to evaluate the advanced model.

Accomplishments

Although direct utilization of coal (i.e. combustion) currently dominates industrial and residential applications, a number of technologies based on coal gasification are emerging as cost-competitive. These include integrated coal gasification combined cycles (IGCC) for electricity generation, fixed-bed gasification for SNG production, gasification for synthesis of fuels and chemicals, and gasification for fuel cells. In order to support the development of these technologies, a recent panel of experts has listed the following as a priority research and development area (Penner, 1987): "Develop comprehensive (numerical) models for gasifiers based on our best scientific knowledge of chemical and physical phenomena and validate and improve these models by performing laboratory and field measurements."

Based on a review of existing models and recommendations of expert consultants, an advanced model for fixed-bed coal gasification has been developed. The rationale for this decision is as follows: (1) the past level of effort in fixed-bed modeling has been modest; (2) there is currently no generalized, robust, well-documented code for fixed-bed coal gasification or combustion available; (3) the proposed advanced model has been reviewed by expert consultants and has received a positive recommendation; (4) there has been little evaluation and application of fixed-bed models; (5) fixed-bed technology is of current interest in high pressure, combined cycle power generation, synthesis gas production, liquids production (mild gasification), and fuel gas production; and (6) the importance of fixed-bed technology was specifically noted in an evaluation of gasification research needs (Penner, 1987). The report by Penner specifically recommends development of fixed-bed process models.

The main accomplishments of this subtask are: (1) review of fixed-bed combustion and gasification processes, test data, and models; (2) development of an advanced fixed-bed coal combustion, gasification, and devolatilization model, MBED-1, with a functional group devolatilization model, FG; and (3) development of an advanced fixed-bed coal combustion, gasification, and devolatilization model, FBED-1, with a functional group-depolymerization, vaporization, crosslinking model, FG-DVC.

During the course of this study, two fixed-bed models were necessarily developed. The first, MBED-1 (Moving-Bed, 1-dimensional) was developed initially when only part of the planned submodels from AFR were available. In this version more empirical information, particularly regarding tar, was required. The second, FBED-1, (Fixed-Bed-1 dimensional) incorporated other AFR submodels, which were subsequently made available.

*The term "fixed-bed" is in common usage, although the bed is often slowly moving. "Fixed-bed" and "moving-bed" are used here interchangeably.

The results of this subtask have been published in our previous reports (Solomon et al., 1987-1991), in a dissertation resulting from this project (Hobbs, 1990), in two chapters contributed to a book on coal combustion (Radulovic and Smoot, 1993; Brewster et al., 1993), and in peer-reviewed journals (Hobbs et al., 1992 a and b). The results have also been presented at three conferences (Yi et al., 1988; Hobbs et al., 1990; Ghani et al., 1993). A review paper on fixed-bed combustion and gasification of coal is being prepared (Radulovic et al., 1993).

Reviews, Data Collection and Plans

Combustion and Gasification Processes

Fixed-bed systems are simple and reliable, have high thermal efficiency, and require minimal pretreatment of feed coal. Combustion and gasification of coal in fixed or slowly moving beds of packed coal particles are of commercial interest. Such beds can be operated at high pressure, providing opportunity for increased power generation efficiency through combined cycle processes. Fixed beds are also a popular choice for mild gasification since, by their countercurrent nature, the liquids can be quickly removed before being altered by substantial reaction. A schematic of the typical atmospheric fixed-bed gasifier is shown in Fig. III.B-1.

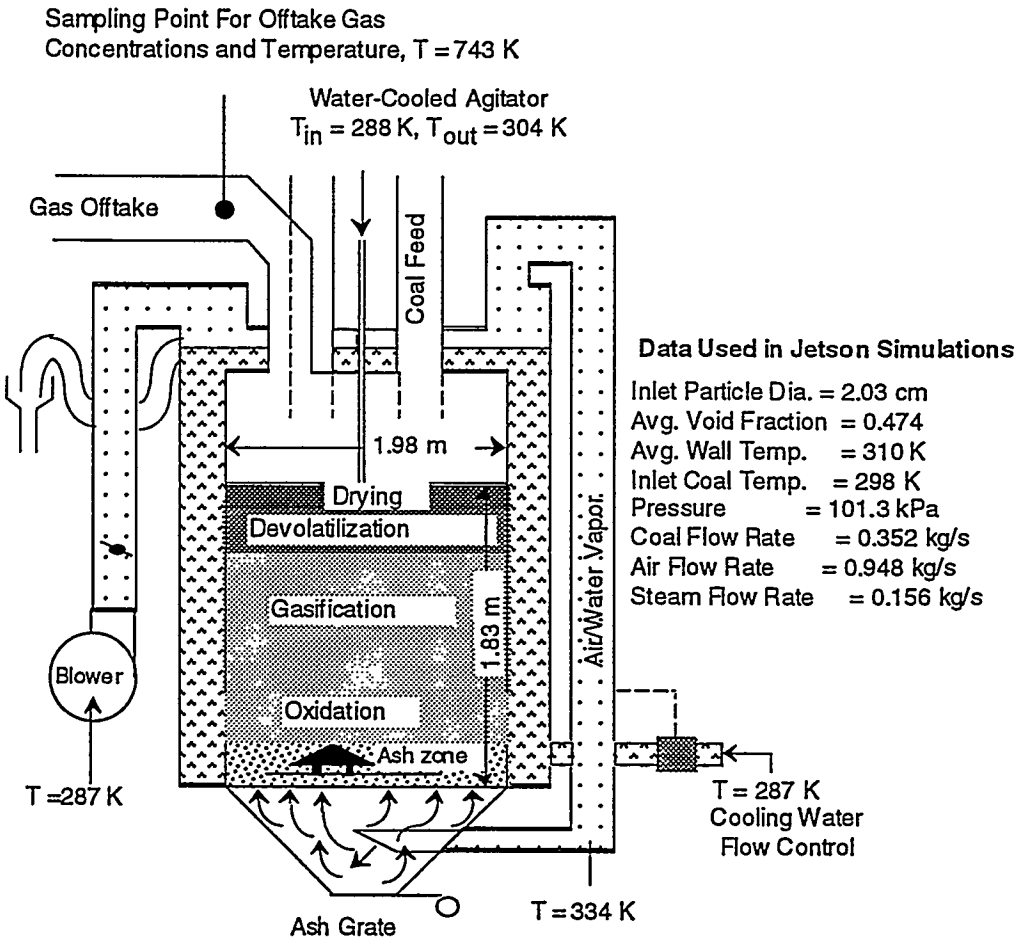

Figure. III.B-1. Schematic of typical atmospheric fixed-bed gasifier (Wellman-Galusha). Temperatures shown are for gasification of Jetson coal with air. Configuration and data taken from Thimsen *et al.* (1984).

The coal is fed to the top of the reactor and moves downward under gravity, countercurrent to the rising gas stream. The dry or slagging ash is removed at the bottom of the reactor. The feed gas is commonly composed of air or oxygen and steam. The excess steam is supplied to the gasifier to control the ash temperature. As the coal slowly descends, the hot gases produced in the gasification and combustion zones exchange energy with the colder solid. The water vapor and, subsequently, the volatile matter are released when the coal reaches sufficiently high temperatures. After the drying and the devolatilization zones, the char enters the gasification zone, where carbon reacts with steam, carbon dioxide, and hydrogen. The endothermic reactions in this section produce carbon monoxide and hydrogen. The slightly exothermic reaction of hydrogen with carbon produces methane. Differentiation between the "combustion zone" and the "gasification zone" is based on the presence or absence of free oxygen. Combustion and gasification reactions can occur simultaneously in the "combustion zone." Combustible gases such as carbon monoxide or hydrogen may react with oxygen. The exothermic combustion reactions provide the necessary energy for the endothermic gasification reactions and drying. The blast gas, which is composed of steam and air (or oxygen), is preheated by the hot ash.

The solid residence times in the drying, devolatilization, gasification, and oxidation zones may be on the order of several hours. The residence time in the ash zone may be even higher, depending on the thickness of this zone. The gas residence time is on the order of seconds. The solid and gas temperature gradients are highest in the devolatilization and oxidation zones.

Fixed-bed combustion and gasification processes and technologies are treated in more detail in our previous reports (Solomon et al., 1987, 1988), in our contribution to a book on coal combustion (Radulovic and Smoot, 1993) and in our review (Radulovic et al., 1993).

Design and Test Data

Fixed-bed gasifiers may be conveniently divided into commercial, demonstration, development, and laboratory units, as shown in Table III.B-1. Design and test data from open literature were obtained for some of the fixed-bed gasifiers shown in Table III.B-1. Particular attention was paid to mild gasification data. Detailed profile data of particle temperature and composition as well as gas temperature, pressure, and composition in fixed-beds are needed for testing and validation of fixed-bed models. Unfortunately, only limited detailed data are available, at least in open literature. There are no published data available for separate gas and solids temperatures and only one set of data for gas composition in the bed. Effluent gas composition and temperature as well as available temperature and pressure profiles were also used for model validations.

In order to obtain all the data potentially available for testing and validation of fixed-bed models a world-wide survey of fixed-bed design and test data was carried out. A list of more than two hundred names and addresses of individuals, companies, universities, and research laboratories, involved in fixed- or moving-bed gasification and combustion research or in research on non-reacting fixed- or moving-beds was compiled. A request for fixed-bed design and test data was sent to all of them. Ninety answers were received, forty-one were positive, and twenty-five sets of data were obtained. Some of the important data sets were proprietary and thus not available.

The most comprehensive design and test data, including temperature and pressure profiles, are available for an atmospheric Wellman-Galusha gasifier in Minneapolis, Minnesota (Thimsen et al., 1984, 1985). Very comprehensive test data, but without temperature and pressure profiles, are also available for a medium pressure METC gasifier in Morgantown, West Virginia (Pater, Jr., 1984, 1985, 1986; Stopek 1984a, 1984b) and a high pressure Lurgi gasifier in Westfield, Scotland (Woodall-Duckham, 1974; Elgin and Perks, 1973, 1974). The Wellman-Galusha test data were used to validate the fixed-bed models developed in this project; the models were also applied to the METC and Lurgi gasifiers. Fixed-bed design and test data are presented in more detail in our previous reports (Solomon et al., 1987-1990) and in our review (Radulovic et al., 1993).

TABLE III.B-1
FIXED-BED REACTORS

COMMERCIAL

1. LURGI Dry Ash
   - Sasolburg and Secunda (SASOL), South Africa
   - Westfield, Scotland
   - Beulah (Great Plains), North Dakota

DEMONSTRATION

1. BGC/LURGI Slagging Ash - Westfield, Scotland
2. KILnGAS - Wood River Station, Illinois
3. ENCOAL* - Gillette, Wyoming

DEVELOPMENT

1. METC - Morgantown, West Virginia
2. CTC MGU* - Bristol, Virginia
3. WELLMAN-GALUSHA - Minneapolis, Minnesota
4. GEGAS - Schenectady, New York
5. GFETC - Grand Forks, North Dakota
6. RUHR 100 - Dorsten, West Germany
7. KGN - Hueckelhoven, West Germany

LABORATORY

1. Washington University - St. Louis, Missouri
2. Pennsylvania State University - University Park, Pennsylvania
3. METC-SHRODR* - Morgantown, West Virginia
4. CTC* - Bristol, Virginia
5. LLNL* - Livermore, California
6. BNL* - Upton, New York

*Mild gasification

Models

Modeling of fixed-bed coal combustion and gasification processes has received continuing attention during the last decade, Yet, model development has not reached the point where significant use is made in process development for coal utilization. In the past, comprehensive modeling of coal combustion and gasification processes was restricted by lack of computer speed and capacity and by difficulties in describing essential model elements. Elliott (1981) edited a comprehensive review of the chemistry of coal utilization which presents information on coal origins, characteristics, and reactions. However, comprehensive modeling of coal combustion and gasification was not addressed.

More recently, Smoot (1984) and Smoot and Smith (1985) reviewed modeling of coal combustion and gasification processes, including fixed-bed processes. Six fixed-bed models were identified and all six were one-dimensional models, while two of the six considered transient effects. All models emphasized countercurrent, fixed-bed gasification systems. No models for combustion systems, such as coal stokers, were found. Comparisons of predicted to measured effluent values, even though encouraging, were considered insufficient to gain significant confidence in the models. Comparisons of predicted to measured temperature, pressure, and composition profiles were needed, but were

hampered by lack of available data, and only one set of measurements by Eapen et al., (1976) was identified for this purpose. Only one comparison of predicted to measured profile data by Barriga and Essenhigh (1980) was found. Still, the question of model reliability was identified as central to model utility.

As part of this project Yi, Brewster, and Smoot (1987), Smoot, Brewster, and Yi (1987) and Radulovic, Yi, and Smoot (1988) reviewed fixed-bed gasifier models in terms of their level of complexity, method of mathematical solution, extent of validation with experimental data, and availability of computer code and documentation. The models were found to have potential for providing detailed reactor simulations. However, a more general, accurate, and detailed model that could be used as a reliable design and development tool was found to be needed. Hobbs (1990) reviewed fixed-bed coal combustion and gasification models with an emphasis on one-dimensional models. A comprehensive review of fixed-bed models has recently been provided by Brewster, Hill, Radulovic, and Smoot (1993). Of the thirty-seven models, six are zero-dimensional, twenty-seven are one-dimensional, and four are two-dimensional. Twenty-one of the models are listed as heterogeneous, which implies separate solid and gas temperatures. The important limitations common to most of the models are presented in Table III.B-2. Some of the simplifying assumptions from Table III.B-2 have been removed in the fixed-bed models developed in this project.

TABLE III.B-2
COMMON LIMITATIONS OF TYPICAL FIXED-BED GASIFICATION MODELS

- Single particle size
- No momentum transport for gas and solid phase
- Axially and radially uniform gas and solid-phase flow
- Axially and radially uniform bed void fraction
- Heat and mass transport for nonreacting fixed beds
- Instantaneous drying
- Instantaneous or simplified devolatilization with yields from proximate analysis
- Char or carbon combustion (O_2) and gasification (CO_2, H_2O, H_2) with kinetic parameters for small particles
- Fixed combustion product distribution (CO/CO_2)
- Simplified gas phase chemistry usually reduced to water-gas shift equilibrium
- Two-point boundary-value problem reduced to initial-value problem and solved by shooting method
- Limited sensitivity analysis and validation

Fixed-bed models are treated in substantial detail in our previous reports (Solomon et al., 1987, 1988; Smoot et al, 1987), in a dissertation resulting from this project (Hobbs, 1990), in our contribution to a book on coal combustion (Brewster et al., 1993), and in our review (Radulovic et al., 1993).

Initial Planning

Planning fixed-bed research was a substantial effort. A preliminary fixed-bed research plan was prepared as a part of the master research plan (Solomon and Smoot, 1986). A detailed fixed-bed research plan was formulated based on the review of fixed-bed combustion and gasification processes and technologies, the survey of fixed-bed design and test data, the review of fixed-bed models, and the recommendations of expert consultants (Smoot et al., 1987). The principal areas of focus were: (1) generalizing coal reaction processes particularly devolatilization; (2) extending treatment of gas phase species; (3) including treatment of pollutants; (4) improving treatment of gas and solid flows; and (5) improving validation of the model with available experimental data. The rationale for developing an advanced model for fixed-bed coal gasification includes the following: (1) the past level of effort in fixed-bed modeling has been modest; (2) there was no generalized, robust, well-documented code for fixed-bed coal gasification or combustion available; (3) the proposed advanced model was reviewed by expert consultants and received positive recommendations; (4) there was little evaluation and application of fixed-bed models; (5) fixed-bed technology is of interest in high pressure, combined cycle power generation, synthesis gas production, liquids production (mild gasification), and fuel gas production; and (6) the importance of fixed-bed technology was specifically noted in an evaluation of gasification research needs (Penner, 1987). The report by Penner specifically recommended development of fixed-bed process models.

An updated fixed-bed research plan for phase II of this project was prepared as part of the master research plan for phase II (Solomon and Smoot, 1989).

Development and Evaluation of MBED-1 Code

The initial version of the fixed-bed model, MBED-1, is a one-dimensional, steady-state model of countercurrent, fixed-bed coal gasification. This model considers separate gas and solid temperatures, axially variable solid and gas flow rates, variable bed void fraction, coal drying, devolatilization based on chemical functional group composition, oxidation and gasification of char, and partial equilibrium in the gas phase. A generalized treatment of gas phase chemistry and accounting for variable bed void fraction were necessary to predict realistic axial temperature, concentration and pressure profiles. The model evaluation includes the sensitivity of axial temperature profiles to model options, model parameters, and operational parameters. Model results have been compared to experimental data obtained from commercial-scale gasifiers. Reasonable agreement with the experimental temperature and pressure profile data for the gasification of eight coal types ranging from lignite to bituminous has been obtained.

Development of MBED-0 Submodel

Motivation for developing the two-zone partial equilibrium submodel, MBED-0, was to provide an initial estimate of effluent compositions and temperatures. These estimates are essential for solving the nonlinear equation set for the one-dimensional model. The two-zone model uses a coal-independent devolatilization submodel. Effluent gas composition can be determined in terms of any number of species. Tar production can be predicted and tar recycle can be considered. The key assumption for the two-zone model is that oxidation and gasification occur at relatively high temperature compared to the colder devolatilization and drying zones. The temperature difference provides a natural division of the process into two zones. High temperatures in the oxidation/gasification section favor total equilibrium in the gas phase. Lower temperature in the devolatilization zone favors partial equilibrium. Limitations to the two-zone model are the need to specify burnout, uncertainty in wall heat loss, and lack of a reliable method to estimate the tar yield.

The two-zone, partial equilibrium model predictions demonstrate that the ultimate volatiles distribution and coal gas composition depend strongly on coal rank. The ultimate volatiles distribution is more sensitive to the potential tar-forming fraction than to the temperature. The coal gas composition is not very sensitive to either. This emphasizes the importance of predicting accurate volatiles distribution into tar, coal gas, and chemical water as opposed to the coal gas composition. The predicted tar yields using the specified tar-forming fractions from literature correlations for various coal types are high in comparison to the values measured in commercial-scale, fixed-bed gasifiers. A more rigorous method for predicting tar, depending on coal structure, DVC, was, at the time, under development at AFR.

Effluent gas compositions predicted with the two-zone, partial equilibrium model compared well with experimental data for gasification of thirteen coal types in two commercial-scale, fixed-bed gasifiers. Effluent compositions and temperatures were predicted with reasonable accuracy for a wide range of coal types by treating devolatilization/drying and char oxidation/gasification as two separate temperature zones. The two-zone model provides an acceptable, initial estimate of fixed-bed effluent temperature and composition. Coal burnout must be specified and an estimate of wall heat loss is required. The two-zone, partial equilibrium model may also be adequate as a standalone model when only effluent temperatures and compositions are required and computational times must be minimized as in large process optimizations.

The two-zone, partial equilibrium model, MBED-0, is presented in more detail in our previous reports (Solomon et al., 1989, 1990), in a dissertation resulting from this project (Hobbs, 1990), and in our paper (Hobbs et al., 1992a, Appendix D).

Development of MBED-1 Code

Conservation Equations - The conservation equations for mass and energy form the foundation of the model. The derivation of the two-phase conservation equations can be found in Smoot and Pratt (1979). The source terms in the continuity and energy equations are described by physical and chemical submodels. Input parameters are reactor dimensions, operating conditions, inlet solid and gas temperatures, pressure, concentrations, flow rates, and wall temperature. Calculated quantities include axial variation in gas temperature, solids temperature, pressure, species concentration, gas flow rate, solid flow rate and wall heat loss. Plug flow is assumed in both the solid and gas phases with variable axial velocities. Gas phase pressure drop is calculated with the Ergun equation for packed beds (Ergun, 1952). An effective heat transfer coefficient is used for heat loss to the wall, including both stagnant and dynamic contributions for convective and radiative heat transfer. Large coal particle devolatilization is allowed to occur simultaneously with char oxidation and gasification. Shell progressive (SP)or ash segregation (AS), shrinking core char submodels describe oxidation and gasification. Chemical equilibrium is used to calculate gas concentration and temperature. Turbulence is not treated formally in the slowly moving bed with low gas velocities, but is included implicitly through correlations such as the effective heat transfer coefficient. Primary assumptions for the one-dimensional fixed bed model include negligible aerodynamic drag, ideal gases, and particles locally isothermal throughout; one particle size and type exists in the feed coal. The conservation equations and boundary conditions for the one-dimensional, fixed bed model are given in Table III.B-3. These can be classified as gas and solid overall continuity, gas and solid energy equations, and gas and solid species or elemental continuity equations. The constitutive relations for solid flow have been proposed only recently and no solution for these equations has been attempted (Gray and Stiles, 1988). Thus, only differential equations for continuity and energy are treated in the model described herein. Hobbs (1990) provides a detailed discussion of these equations.

Auxiliary Equations - Pressure Drop - The pressure drop in the reactor is calculated from Ergun's equation (Ergun, 1952), since Reynolds numbers are typically less than 500 in fixed bed coal gasifiers. The small pressure drop in the reactor is sensitive to the bed void fraction, ε. Void fractions of the feed coal at the bed top and the product ash at the bed bottom are estimated based on coal and ash bulk and apparent density measurements.

TABLE III.B-3

DIFFERENTIAL EQUATION SET AND BOUNDARY CONDITIONS FOR MBED-1

Overall Gas Species Continuity	$\frac{dW_g}{dz} = A\sum_{i=1}^{n} r_i$	(1)
Overall Solid Species Continuity	$\frac{dW_s}{dz} = -A\sum_{i=1}^{n} r_i$	(2)
Gas Phase Energy	$\frac{dW_g h_g}{dz} = A\left(Q_{sg} - Q_{gw} + \sum_{i=1}^{n} r_i h_{ig}\right)$	(3)
Solid Phase Energy	$\frac{dW_s h_s}{dz} = A\left(-Q_{sg} - Q_{sw} - \sum_{i=1}^{n} r_i h_{ig}\right)$	(4)
Solid Species Continuity		
Moisture	$\frac{dW_{moisture}}{dz} = -A r_{moisture}$	(5)
Non-volatile Carbon	$\frac{dW_{Non\text{-}vol\ C}}{dz} = -A r_{Non\text{-}vol\ C}$	(6)
Non-volatile Sulfur	$\frac{dW_{Non\text{-}vol\ S}}{dz} = -A r_{Non\text{-}vol\ S}$	(7)
Organic Functional Groups	$\frac{dy_i}{dz} = -\frac{1}{U_s} k_i y_i$	(8-26)
Tar Fraction	$\frac{dx}{dz} = -\frac{1}{U_s} k_x x$	(27)
Gas Phase Elemental Continuity[a]	$\frac{dW_g \omega_j}{dz} = A\sum_{i=1}^{n} r_{i,j}$	(28-32)
Gas Phase Tar Species Continuity	$\frac{dW_{tar}}{dz} = A\sum_{i=1}^{n} r_i^{tar}$	(33)
Gas Phase Tar Elemental Continuity[a]	$\frac{dW_{tar}\omega_{tar,j}}{dz} = A\sum_{i=1}^{n} r_{i,j}^{tar}$	(34-38)
Boundary Conditions		
Feed Coal/Gas Mass Flow Rate	Feed Coal/Gas Enthalpy or Temperature	
Proximate and Functional Group Analysis of the Coal	Feed Gas and Tar Composition	

[a]The subscript "j" represents carbon, hydrogen, nitrogen, oxygen, and sulfur.

Gas Phase Chemistry - Gas temperature is determined by assuming all gas species to be in thermal equilibrium and partial or total chemical equilibrium. Gas phase composition is determined by Gibbs free energy minimization. Partial equilibrium refers to a gaseous mixture where at least one species is held out of chemical equilibrium. Hobbs et al. (1992a) investigated three options regarding equilibrium: total equilibrium, partial equilibrium where tar was held out of chemical equilibrium, and partial equilibrium where all gases in the drying and devolatilization zone were assumed to be nonreactive. Since gas phase kinetic models for coal systems are complex, the one-dimensional fixed bed model assumes partial equilibrium by holding tar out of chemical equilibrium.

Mass and Heat Transfer - Mass and heat transfer processes in fixed-bed gasifiers are affected by complex solids flow and chemical reactions. Coarsely crushed coal settles while undergoing heating, drying, devolatilization, gasification and combustion. Coal particles change in diameter, shape and porosity. Non-ideal behavior may result from coal bridges, gas bubbles and channels. Variable bed void fraction may also change heat and mass transport properties. Correlations for solid-gas heat transfer coefficients are questionable, since they are typically obtained under ideal conditions. Mass transfer occurs by diffusion and convection. Heat transfer is by conduction, convection and radiation in the gas and solid phases.

Several physical properties of the gas and particle phases are required to obtain mass and heat transfer coefficients needed to solve the differential equation set in Table III.B-3. Chapman-Enskog theory has been used to calculate multicomponent gas mixture viscosity and diffusivity (Bird et al., 1960). Euken's formula is used to calculate the conductivity of individual gaseous species. Furthermore, the gaseous tar diffusivity is assumed to be 0.1 cm^2/s at standard temperature and pressure (Suuberg et al., 1978). The pressure and temperature dependences for the tar diffusivity are assumed to follow Chapman-Enskog theory. The JANAF tables were used to provide values for calculating gas-phase enthalpy, entropy, and heat capacity (Stull and Prophet, 1971). Dulong's formula (Perry and Chilton, 1973) was used for heating value of the char, Merrick's correlations (1983) were used for char enthalpy and heat capacity, and the Kopp-Neumann rule was used for ash heat capacity (Mills and Rhine, 1989). The solid-gas heat transfer coefficent was taken from Sen Gupta and Thodos (1963) but adjusted by a factor accounting for chemical reactions in the bed (0.1 to 0.5). A summary of the heat and mass transfer correlations used in the one-dimensional model is presented in Table III.B-4.

Coal Drying and Devolatilization - Coal reaction source terms represent drying, devolatilization, char oxidation and gasification. These chemical and physical processes are shown in Fig. III.B-2 which depicts a conceptual coal particle divided into various functional groups, including moisture and ash. The ash is taken to be inert and drying is assumed to be diffusion-limited.

As shown in Fig. III.B-2, devolatilization is described by assuming that the organic portion of the coal particle is composed of various functional groups: carboxyl, hydroxyl, ether, nitrogen, etc. A functional group (FG) model has been used to describe the devolatilization process (Solomon et al., 1988; Serio et al., 1987; Section 2a of this report). The kinetics for functional group evolution are considered to be independent of the type of coal used. The x and y values (Eqns. 8-27 in Table III.B-3) represent the two-dimensional description of coal. The y dimension is divided into fractions according to the chemical composition of the coal. The initial fraction of a particular functional group component is represented by y_i^o, and the sum of y_i^o's equals 1. The evolution of each functional group into the gas is represented by the first order decay of the y dimension, $dy_i / dt = - k_i y_i$. The x dimension represents non-tar-forming char, tar-forming char, and tar. The evolution of tar is represented by the first-order decay of the x dimension, $dx / dt = - k_x x$. Normally distributed Arrhenius rate coefficients for 19 functional groups, k_i, and tar, k_x, were obtained from Solomon *et al.* (1988) for the organic functional groups depicted in Fig. III.B-2. The potential tar-forming fraction, x^o, was calculated with the semi-empirical correlation of Ko *et al.* (1988).

A more rigorous method that depends on coal structure for better tar predictions was being developed under Subtask 2a of this study. Publications in this direction include Solomon *et al.* (1988,

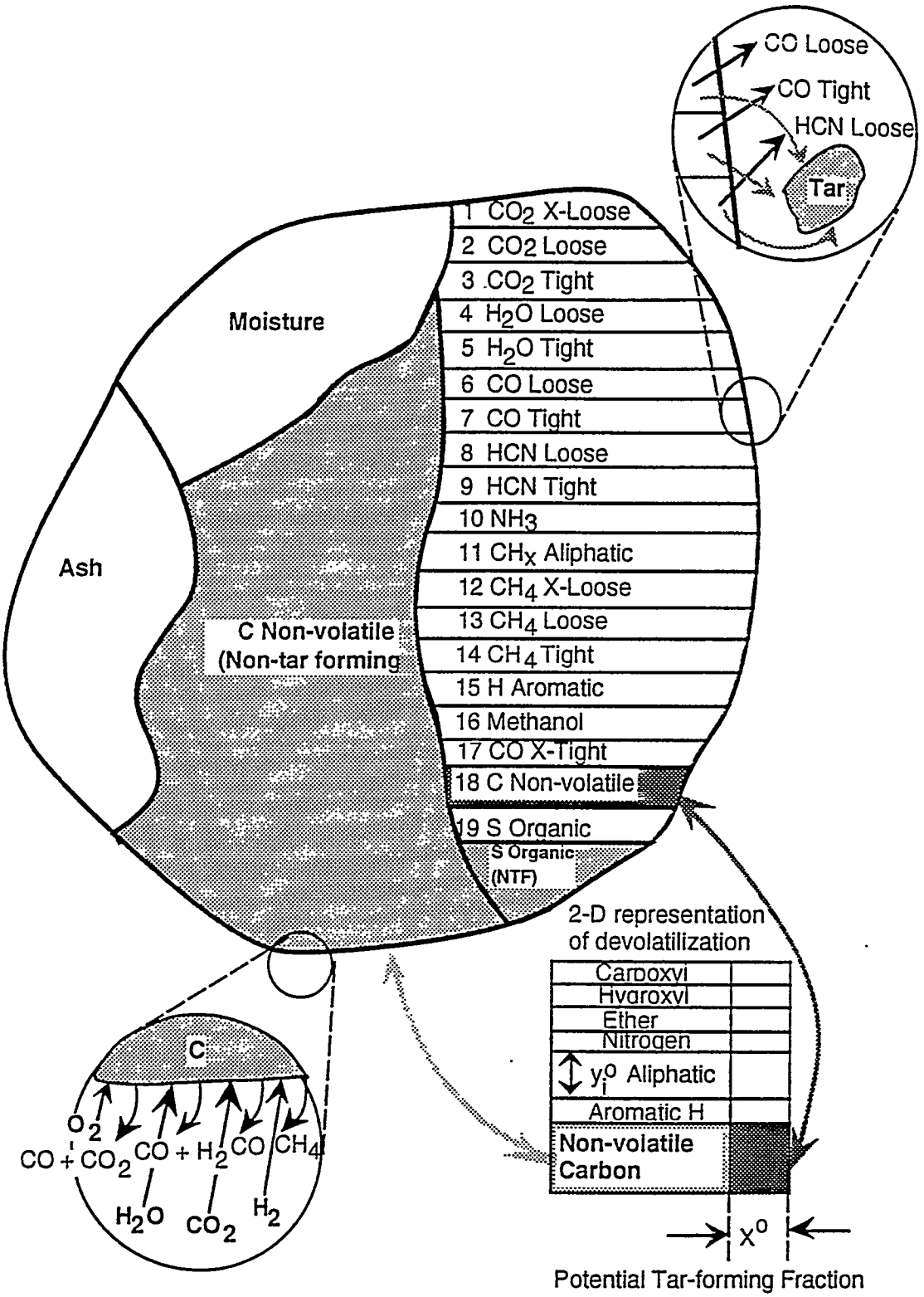

Figure III.B-2. Schematic of coal particle with devolatilization model based on chemical functional group (Solomon et al., 1988). The potential tar-forming fraction of the non-volatile carbon functional group evolves as tar. The non-tar-forming C and S organic groups evolve via heterogeneous char oxidation or gasification.

TABLE III.B-4

HEAT AND MASS TRANSPORT CORRELATIONS USED IN MBED-1

Bed-wall heat transfer coefficient (Froment and Bischoff, 1979)	$hw = 2.44\, k_g^{\dagger}\, D^{-4/3} + 0.033\, k_g \cdot Pr \cdot Re \cdot d_p^{-1}$	(1)
Gas-wall heat transfer coefficient (DeWasch and Froment, 1971)	$h_{gw} = h_w k_{rg} / \left(k_{rg} + k_{rs} \right)$	(2)
Solid-wall heat transfer coefficient (DeWasch and Froment, 1971)	$h_{sw} = h_w k_{rs} / \left(k_{rg} + k_{rs} \right)$	(3)
Static effective radial conductivity (Froment and Bischoff, 1979)	$k_r^o = k_g \epsilon \left(1 + \frac{d_p h_{rv}}{k_g} \right) + \frac{k_g (1-\epsilon)}{\left(\frac{1}{\phi} + \frac{h_{rs} d_p}{k_g} \right)^{-1} + \frac{2}{3\kappa}}$	(4)
Gas effective radial conductivity (Froment and Bischoff, 1979)	$k_{rg} = k_g \left\{ \epsilon \left(1 + \frac{d_p h_{rv}}{k_g} \right) + 0.14\, PrRe / \left[1 + 46 \left(\frac{d_p}{D} \right)^2 \right] \right\}$	(5)
Solid effective radial conductivity (Froment and Bischoff, 1979)	$k_{rs} = k_g (1-\epsilon) / \left[\left(\frac{1}{\phi} + \frac{h_{rs} d_p}{k_g} \right)^{-1} + \frac{2}{3\kappa} \right]$	(6)
Solid conductivity (Merrick, 1983)	$k_s = \left(\rho_s^t / 4511 \right)^{3.5} \sqrt{T_s}$	(7)
Void-void radiation coefficient (Froment and Bischoff, 1979)	$h_{rv} = 2.27 \times 10^{-7}\, T_g^3 / \left[1 + \frac{\epsilon}{2(1-\epsilon)} \left(\frac{1-\epsilon'}{\epsilon'} \right) \right]$	(8)
Solid-solid radiation coefficient (Froment and Bischoff, 1979)	$h_{rs} = 2.27 \times 10^{-7} \left(\frac{\epsilon'}{2-\epsilon'} \right) T_s^3$	(9)
Packing parameter (Kunii and Smith, 1960)	$\phi = \begin{cases} \phi_2 + \left(\phi_1 - \phi_2 \right) \frac{\epsilon - 0.260}{0.476 - 0.260} & \text{if } \epsilon_1 \geq \epsilon \geq \epsilon_2 \\ \phi_1 & \text{if } \epsilon > \epsilon_1 = 0.476 \\ \phi_2 & \text{if } \epsilon < \epsilon_2 = 0.260 \end{cases}$	(10)
Loose packing parameter (for ϵ_1) (Kunii and Smith, 1960)	$\phi_1 = \frac{0.3525 \left(\frac{\kappa - 1}{\kappa} \right)^2}{\ln[\kappa - 0.5431(\kappa-1)] - \frac{0.4569\,(\kappa-1)}{\kappa}} - \frac{2}{3\kappa}$	(11)

TABLE III.B-4 (CONTINUED)

Dense packing parameter (for ϵ_2) (Kunii and Smith, 1960)	$\phi_2 = \dfrac{0.07217\left(\frac{\kappa-1}{\kappa}\right)^2}{\ln[\kappa-0.9250(\kappa-1)] - \frac{0.07498(\kappa-1)}{\kappa}} - \dfrac{2}{3\kappa}$	(12)
Solid-gas heat transfer coefficient (Sen Gupta and Thodos, 1963)	$h_{sg} = \dfrac{2.06\,Cp_g\,G}{\epsilon} Re^{-0.575}\, Pr^{-2/3}$	(13)
Mass transfer coefficient (Sen Gupta and Thodos, 1963)	$k_m = \dfrac{2.06\,G}{\epsilon\rho_g} Re^{-0.575}\, Sc^{-2/3}$	(14)
Reynolds, Prandtl and Schmidt numbers	$Re=d_pG/\mu_g$, $Pr=Cp_g\mu_g/k_g$, $Sc_i=\mu_g/r_gD_{im}$	(15)
Conductivity ratio	$\kappa = k_s/k_g$	(16)
Bed void fraction	ϵ = void volume/bed volume	(17)
Emissivity (Perry and Chilton, 1973)	$\epsilon' = 0.85$	(18)

1990). Solomon *et al.* (1988, 1990) completed the development of a depolymerization, vaporization, and crosslinking (DVC) model and combined it with their functional group (FG) model to provide a general coal devolatilization model (FG-DVG).

To introduce mass transport effects, transport resistances through the film and particle were added. The mass transfer resistances used herein for devolatilization are identical to the mass transfer resistances used in the oxidation and gasification submodel.

Oxidation and Gasification - Oxidation and gasification reactions consume the char which is assumed to be composed of nonvolatile functional groups. As shown in Fig. III.B-2, three gasification agents were considered: steam, carbon dioxide, and hydrogen. Light gases and tar evolve competitively, resulting in char. Both tar and char were treated as single species that have variable compositions depending on the location in the reactor.

The two most common char oxidation submodels used in fixed-bed coal gasification are the shell progressive (SP) model and the ash segregation (AS) model. The differences between the two models are in the description of the ash. The ash in the SP model remains intact. The oxidant is required to diffuse through the gas film boundary layer and the ash layer. The ash in the AS model is assumed to crumble and fall away from the char particle with the oxidant required to diffuse only through the gas film boundary layer. The submodels assume that the reactions are global, based on the external particle surface area, and first order in oxidizer concentration. The SP or AS submodels are used to obtain the rates of char oxidation and gasification. Oxidation and gasification kinetic rate constants are given in Table III.B-5. It was assumed, based on the available data (Yoon et al., 1978; Wen et al., 1982; Wen and Chaung, 1979; and Walker et al., 1959), that the steam gasification rate was the same as the carbon dioxide gasification rate. Based on the same data, the hydrogen gasification rate was taken to be three orders of magnitude smaller than the carbon dioxide rate. Although the parameters shown in Table III.B-5 were derived from small-particle experimentation, the kinetic rate constants were assumed to be

TABLE III.B-5

OXIDATION AND GASIFICATION KINETIC RATE CONSTANTS

(adapted from Hedman *et al*., 1987)

$$k = A\,T^{n}\exp\left(-\frac{E}{RT}\right)\frac{m}{s}$$

Reaction		$A\ (\frac{m}{sK^n})$	n	$\frac{E}{R}$ (K)		Source of Correlation	Source of data
$C+0.5O_2 \rightarrow CO$							
All ranks	a	2.30×10	0	1.11×10	4	Baxter (1987)[b]	Field *et al* (1967)
HVBA		1.03×10	0	9.01×10	3	Baxter (1987)	Goetz *et al* (1982)
HVBC		5.00×10	-1	6.31×10	3	Baxter (1987)	Goetz *et al* (1982)
SUBC		1.04×10	1	1.12×10	4	Baxter (1987)	Goetz *et al* (1982)
Lignite A		1.22×10	0	1.03×10	4	Nsakala *et al* (1985)	Nsakala *et al* (1985)
$C+CO_2 \rightarrow 2CO$							
All ranks	a	5.89×10	2	2.68×10	4	Hobbs *et al* (1992b)[c]	Goetz *et al* (1982)
HVBA		1.16×10	3	3.12×10	4	Baxter (1987)	Goetz *et al* (1982)
HVBC		4.89×10	3	3.13×10	4	Baxter (1987)	Goetz *et al* (1982)
SUBC		6.19×10	3	2.89×10	4	Baxter (1987)	Goetz *et al* (1982)
Lignite A		3.42×10	0	1.56×10	4	Baxter (1987)	Goetz *et al* (1982)

a Base case parameters used in sensitivity analysis.

b Baxter's (1987) rate constants were obtained by nonlinear analysis of Field's *et al* . (1967) and Goetz' *et al* . (1982) data.

c Hobbs' *et al* . (1992b) rate constants for all ranks were obtained by averaging Baxter's (1987) rate constants for four coal ranks.

applicable to large-particle oxidation and gasification. Large-particle oxidation and gasification data are scarce. Although chemical rates for small particles may be different from large-particle rates, film diffusion and internal diffusion dominate, at least for oxidation. Additional experimental data are needed to make the same conclusion for the gasification reactions. Thus, shrinking-core models using effective internal diffusion may be adequate.

Walker *et al.* (1959) and Laurendeau (1978) discuss methods for calculating effective diffusivities. Park and Edgar (1987) show the effect of a developing ash layer on the burning rate of a core sample of coal. The core burning rate can be predicted by using an effective diffusivity based on the molecular diffusivity multiplied by a constant ($D_{eff}=\phi D_m$). The constant, ϕ, is based on the porosity of the developing ash layer. Thorsness and Kang (1985) have used 0.35 for ϕ. Wang and Wen (1972) have measured porosity of a fire clay ash which varied from 0.4 to 0.8. Laurendeau (1978) shows that ϕ can be estimated by the ash porosity divided by the tortuosity, which was taken to be 2.0. Using Wang and Wen's values for the ash porosity (0.4 to 0.8), ϕ should range between 0.2 and 0.4. However, lower values of ash porosity were determined for ash originating from the Lurgi and Wellman-Galusha gasifiers (Hobbs, 1990). Porosities for these ashes ranged from 0.06 to 0.60, indicating a lower range for ϕ of 0.03 to 0.3 for fixed-bed gasifiers.

The heterogeneous oxidation of carbon produces both CO and CO_2 as primary products. Carbon monoxide may be favored at higher temperatures if CO is formed at carbon edges and CO_2 is formed at inorganic sites. Lower temperatures may favor CO_2 due to catalytic activity. The CO/CO_2 ratio has been correlated by Arrhenius-type dependence on temperature with constants taken from Laurendeau (1978). Section 2b of this report provides a furthur discussion of the CO/CO_2 ratio together with measured values for small particle oxidation for a range of pressures.

Solution Technique - The set of equations with boundary conditions summarized in Table III.B-3 describes a split boundary value problem. The term "split boundary" has been used to describe the partially known and unknown boundary conditions at both the top and the bottom of the moving-bed reactor. Although split-boundary-value problems have been solved satisfactorily for homogeneous models (equal solid and gas temperatures), heterogeneous models are more difficult. In this study, iterative methods were used to satisfy temperature boundary conditions. The 38 ordinary differential equations listed in Table III.B-3 were integrated simultaneously from the top to the bottom of the reactor with LSODE (Livermore Solver for Ordinary Differential Equations; Hindmarsh, 1983).

MBED-0 (Hobbs, 1992a) was used to provide initial estimates of the effluent gas composition and temperature. However, the gas exit temperature predicted by the two-zone model is generally high due to the assumption that the devolatilization zone is at a uniform temperature. Likewise, the effluent solid temperature is high due to the well-mixed assumption. Thus, after integrating from the top to the bottom of the reactor, the calculated feed gas temperature will be higher than the input feed gas temperature. Therefore, a new effluent gas temperature must be estimated which is smaller than the temperature predicted by the two-zone model. This procedure can be repeated in an iterative manner until the calculated feed gas temperature is equal to the input feed gas temperature. Typically, 2-4 iterations through the gasifer are required for convergence. Hobbs (1990) provides details on the computational algorithm. Calculation times for one sweep through the reactor using an engineering workstation for the two-zone model, MBED-0, and the one-dimensional model, MBED-1, are on the order of seconds and minutes, respectively.

Sensitivity Analysis - The parametric sensitivity analysis was divided into three major categories: (1) model options, (2) model parameters, and (3) operational parameters. Four model options: tar vapor reaction equilibrium, volatiles mass transport, char ash layer formation, and combustion product distribution were investigated. Six model parameters: solid-gas heat transfer coefficient, effective diffusivity, wall heat transfer coefficient, potential tar-forming fraction, functional group composition, and oxidation and gasification kinetic parameters were also examined. Furthermore, eight operational parameters were examined: feed gas temperature, reactor pressure, coal mass flow rate, steam mass flow rate, air mass flow rate, proximate ash content of the feed coal, coal particle diameter, and bed void fraction.

The response to parametric changes in input parameters can be observed in various output parameters such as solid temperature, gas temperature, gas concentrations, or pressure drop. Solid temperature was chosen as the primary response variable for all parametric simulations herein, since it is indicative of the extent of heterogeneous reaction. The base case for the parametric sensitivity simulations was gasification of Jetson bituminous coal in an air-blown Wellman-Galusha gasifier, Fig. III.B-1. The gasification of Jetson coal was part of an extensive experimental program carried out by Thimsen et al. (1984). Operational data for the Jetson case are given in Table III.B-6. The sensitivity of temperature to the solid-gas heat transfer coefficient was completed for eight different cases rather than just the Jetson case. Input parameters for these eight cases are also reported in Table III.B-6.

The sensitivity analysis has helped in the selection of model options and model parameters; it has also provided valuable insights into the fixed- bed coal gasification processes. Based on the sensitivity analysis and other available information, the following model options were selected: tar out of equilibrium, volatiles mass transport included, shell progressive reactions, and temperature dependent CO/CO_2 ratio.

TABLE III.B-6.

OPERATING PARAMETERS FOR THE WELLMAN-GALUSHA GASIFIER TESTS

Coal Type	Absaloka subbitum.	Benton lignite	Elkhorn bituminous	Jetson bituminous	Kemmer subbitum.	Leucite subbitum.	Rosebud subbitum.	Utah B.C.[b] bituminous
Proximate, weight %								
Ash	6.3	6.4	4.7	4.3	5.7	9.0	11.8	11.1
Fixed carbon	40.7	25.9	53.7	49.5	42.4	44.9	40.1	43.9
Moisture	23.5	32.8	4.6	6.3	16.8	17.4	21.3	6.1
Volatile	29.6	34.9	36.9	39.9	35.1	28.8	26.8	38.9
Ultimate, weight %								
Carbon	76.3	73.7	82.5	81.4	77.5	78.1	78.7	80.3
Hydrogen	5.1	6.2	5.7	5.1	5.6	5.0	4.9	6.2
Nitrogen	0.8	1.0	1.6	1.8	1.2	1.9	1.1	1.2
Sulfur	0.4	0.9	0.9	1.6	1.0	0.6	1.3	0.6
Oxygen	17.4	18.2	9.3	10.2	14.7	14.7	14.0	11.7
Operating Parameters								
Chamber diameter, m	1.98	1.98	1.98	1.98	1.98	1.98	1.98	1.98
Chamber length, m	2.11	2.13	2.13	1.83	2.13	2.00	2.00	1.90
Chamber pressure, kPa	101.3	101.3	101.3	101.3	101.3	101.3	101.3	101.3
Inlet coal temperature, K	298	298	298	298	298	298	298	298
Feed gas temperature, K	332	340	331	334	332	334	336	335
Wall temperature, K	310	310	310	310	310	310	310	310
Coal mass flow, kg/s	0.420	0.749	0.324	0.352	0.284	0.293	0.179	0.337
Air mass flow, kg/s	0.764	0.931	0.789	0.948	0.573	0.532	0.335	0.673
Steam mass flow, kg/s	0.114	0.231	0.113	0.156	0.0881	0.0883	0.050	0.119
Jacket steam mass flow, kg/s	0.0034	0.051	0.0082	0.134	0.0030	0.0620	0.0174	0.0261
Wall heat loss, MW[a]	0.155	0.226	0.260	0.416	0.167	0.291	0.169	0.295

[a]Heat loss calculated from reported jacket steam and cooling water heat loss. Adapted from Thimsen *et al.* (1984).
[b]B.S. is Blind Canyon.

Several model parameters were found to have significant impact on predictions, particularly the solid-gas heat transfer coefficient, the effective ash diffusivity, and the bed void fraction. These parameters are, at the same time, difficult to obtain experimentally and subject to substantial uncertainty. The solid-gas heat transfer coefficient for a reactive system may be 0.02 to 0.1 times that for a nonreactive system (Van Fredersdorff and Elliott, 1963). The observed difference may be due to unsteady heat transfer (Dzhapbyev et al., 1986). Vigorous reactions as well as nonsphericity and transpiration cooling may also contribute to this difference. Based on the sensitivity analysis, a solid-gas heat transfer correction factor of 0.1 was recommended. The effective ash diffusivity can be measured or estimated from the ash porosity. The ash porosities ranged from 0.06 to 0.60 for ash obtained from fixed bed gasification. A value of 0.5 was recommended. The bed void fraction was assumed to vary linearly between the top and the bottom of the bed as supported by data from Krishnudu *et al.* (1989). The values at the top and the bottom of the bed were based on experimental data.

Sensitivity of solid temperature to operational parameters is shown in Fig. III.B-3. Operational parameters that can be changed readily are the feed gas temperature, the reactor pressure, the coal mass flow rate, the steam mass flow rate, and the air mass flow rate. Other operational parameters are not as easily modified during gasifier operation. Such parameters include the proximate ash content, coal particle diameter, and the bed void fraction. Coal pretreatment such as washing or crushing may be necessary to change these parameters.

Validations - While effluent gas composition is predicted by MBED-1, comparison of these predicted and measured values does not provide a strong evaluation of a generalized fixed-bed model. Once coal burnout is established, which is often near unity, and tar production is estimated, effluent gas composition can be estimated without recourse to a generalized fixed bed model (Hobbs et al., 1992a). Thus, evaluation of MBED-1 was performed by comparison with measured axial profiles of temperature and pressure in fixed beds. No data for composition profiles were located for this purpose and experimental temperature and pressure profiles within laboratory or commercial-scale fixed bed gasifiers are limited. Eight atmospheric pressure, air-blown Wellman-Galusha cases (Thimsen et al., 1984), were simulated. Operating parameters were presented in Table III.B-6.

Predicted axial variations in temperature and pressure profiles are compared to measurements for gasification of the eight coals in the Wellman-Galusha gasifier in Figs. III.B-4 and 5. Profile comparisons for both temperature and pressure are considered to be quite good for all but the lignite case. Measurements for the Jetson case indicate the location of the maximum temperature. Predicted axial variations in temperature, pressure drop, gas concentration, oxidation/gasification carbon consumption rate, burnout, and particle diameter for atmospheric gasification of the Jetson bituminous coal are shown in Fig. III.B-6. This case is presented in detail since it was used as the base case in the sensitivity analysis. In the Jetson case, burnout (daf) was predicted to be unity as shown in Fig. III.B-6. Thus, carbon is not available for oxidation in the ash zone. The ash zone temperature remains approximately 550 K. Carbon becomes available for oxidation approximately 0.5 meters from the bottom of the reactor where oxidation begins. The highly exothermic oxidation reaction increases the solid temperature dramatically. The oxidation reaction occurs before the steam gasification reaction, as shown by the carbon consumption rates in Fig. III.B-6E. Once initiated, the endothermic steam gasification reaction causes the positive solid temperature gradient to decrease. This competition between exothermic and endothermic reactions describes the initial step in the temperature profile going from the ash zone to the oxidation zone. The temperature is highest at the end of the oxidation zone and starts to decrease due to predominantly endothermic gasification reactions of carbon with steam and carbon dioxide in the gasification zone.

Steam gasification overlaps oxidation as shown in Fig. III.B-6E. For example, at 0.65 meters from the reactor bottom, the carbon consumption rate due to steam gasification is approximately 0.05 kg/s m^3. At this location in the reactor, steam is reacting with carbon to produce hydrogen and carbon monoxide. However, no depletion of steam is observed at this reactor location as shown in Fig. III.B-6C. Steam is being replenished by the homogeneous oxidation of hydrogen. Also, carbon monoxide produced from both oxidation and steam gasification is being oxidized in the presence of oxygen to produce carbon

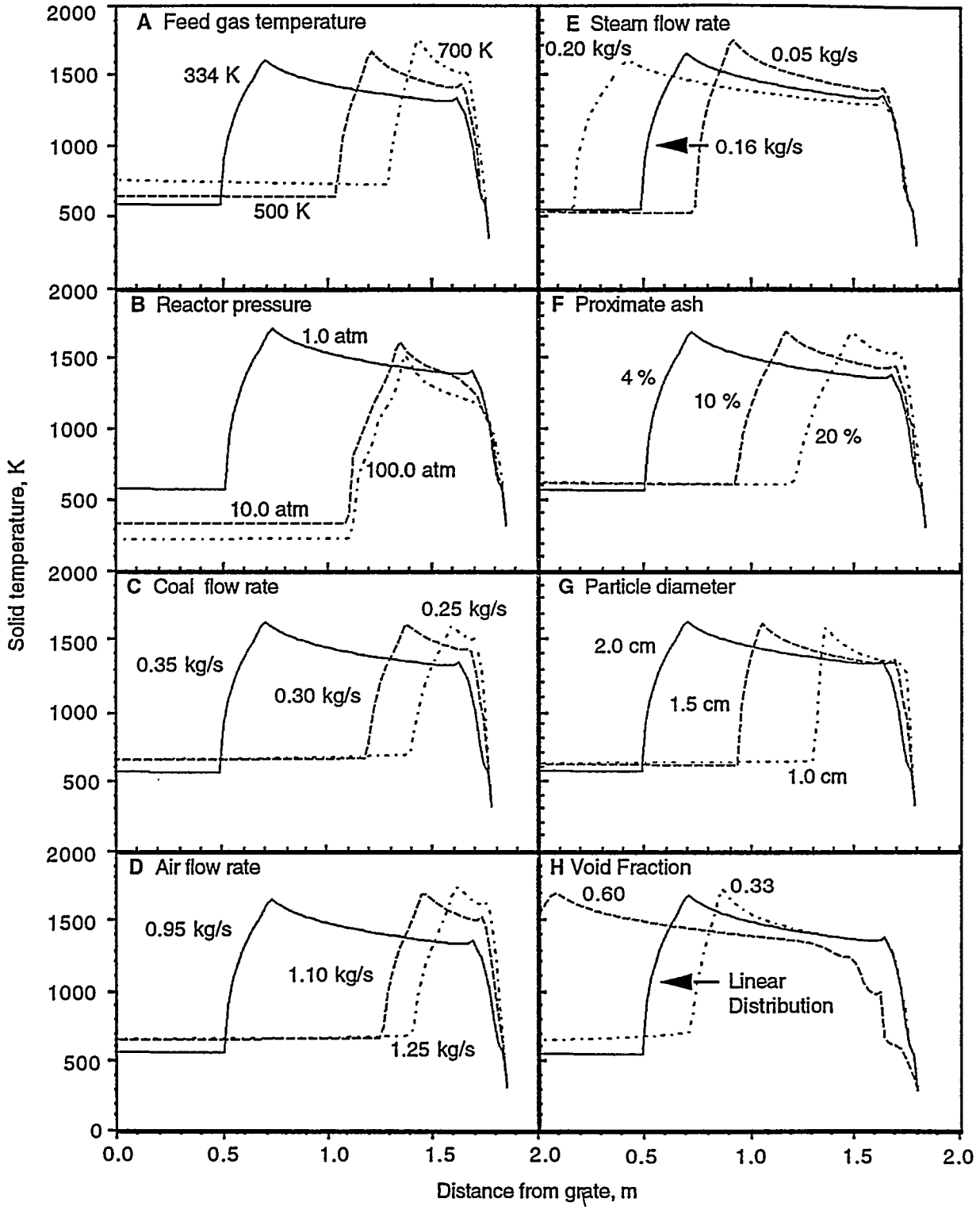

Figure III.B-3. Predicted sensitivity of axial solid temperature to A) feed gas temperature, B) reactor pressure, C) feed coal mass flow rate, D) feed air mass flow rate, E) feed steam mass flow rate, F) feed coal proximate ash content, G) feed coal mean particle diameter, and H) bed void fraction. Input conditions are for atmospheric gasification of Jetson bituminous coal in an air-blown Wellman-Galusha gasifier. Input conditions given in Table III.B-6.

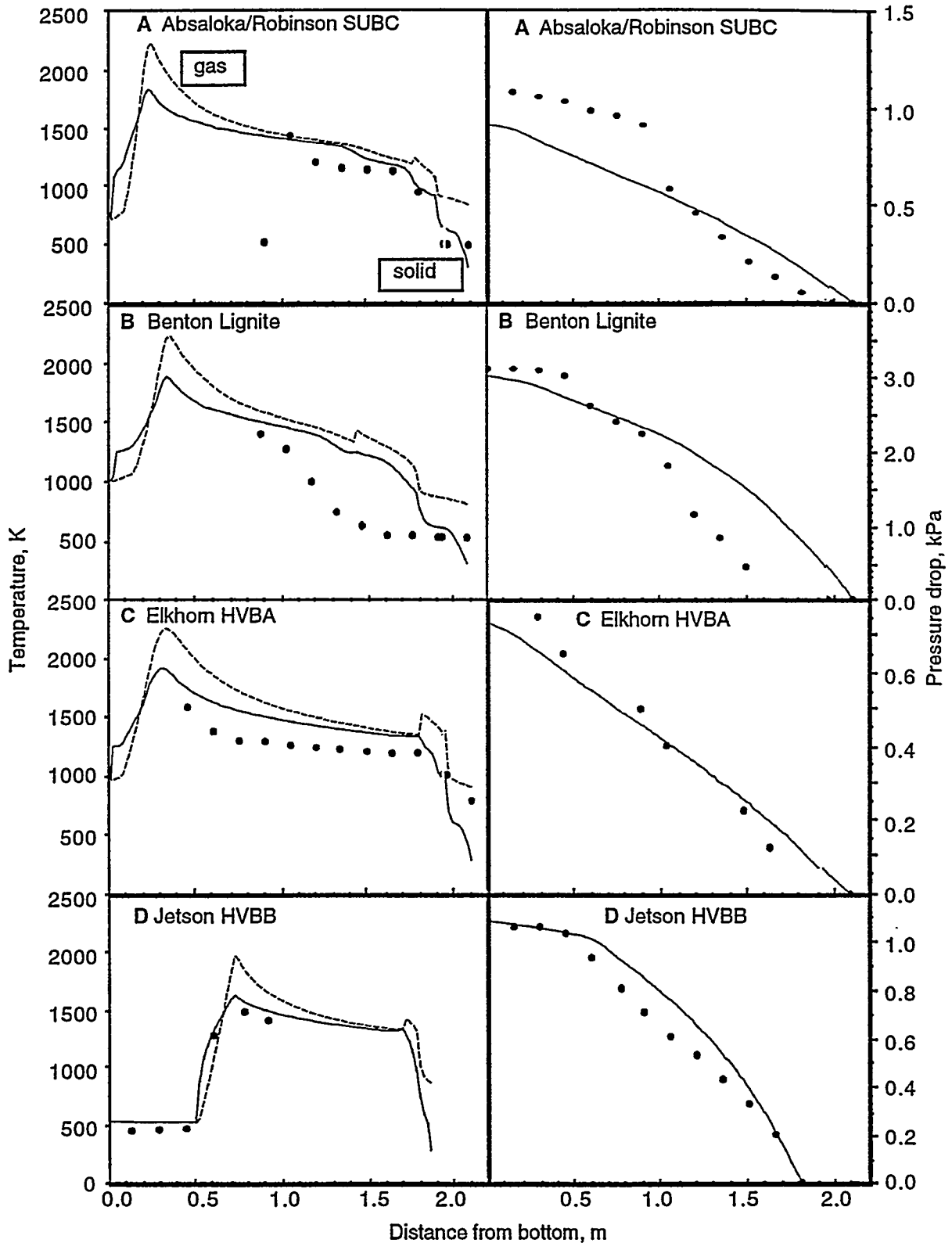

Figure III.B-4. Predicted and measured axial variations in temperature and pressure drop during gasification of A) Absaloka/Robinson subbituminous, B) Benton lignite, C) Elkhorn bituminous, and D) Jetson bituminous coal in an air-blown, atmoshperic Wellman-Galusha gasifier. Measurements are from Thimsen *et al.* (1984). Input parameters given in Table III.B-6.

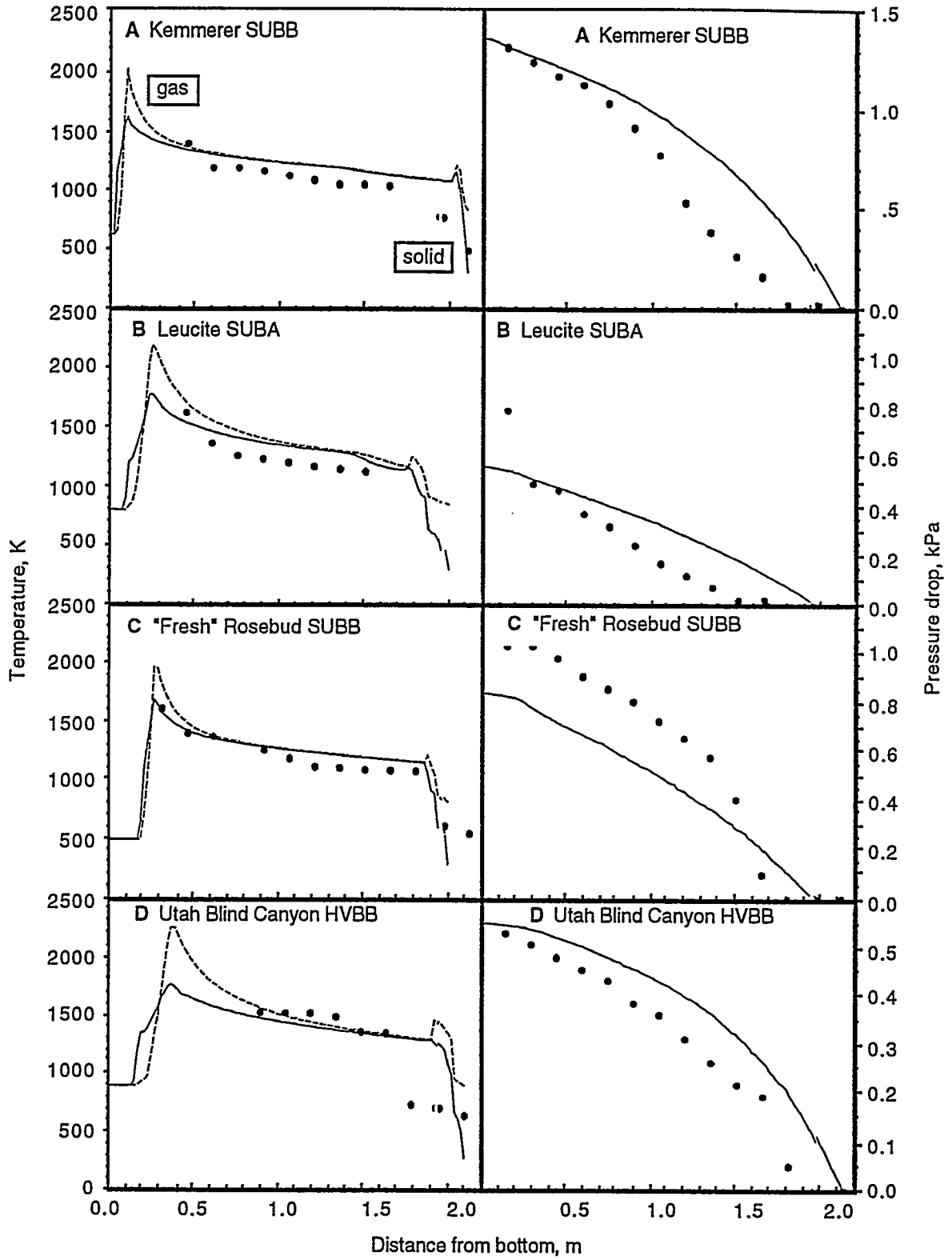

Figure III.B-5. Predicted and measured axial variations in temperature and pressure drop during gasification of A) Kemmerer subbituminous, B) Leucite subbituminous, C) "fresh" Rosebud subbituminous, and D) Utah Blind Canyon bituminous coals in an air-blown, atmospheric Wellman-Galusha gasifier. Measurements are from Thimsen et al. (1984). Input parameters given in Table III.B-6.

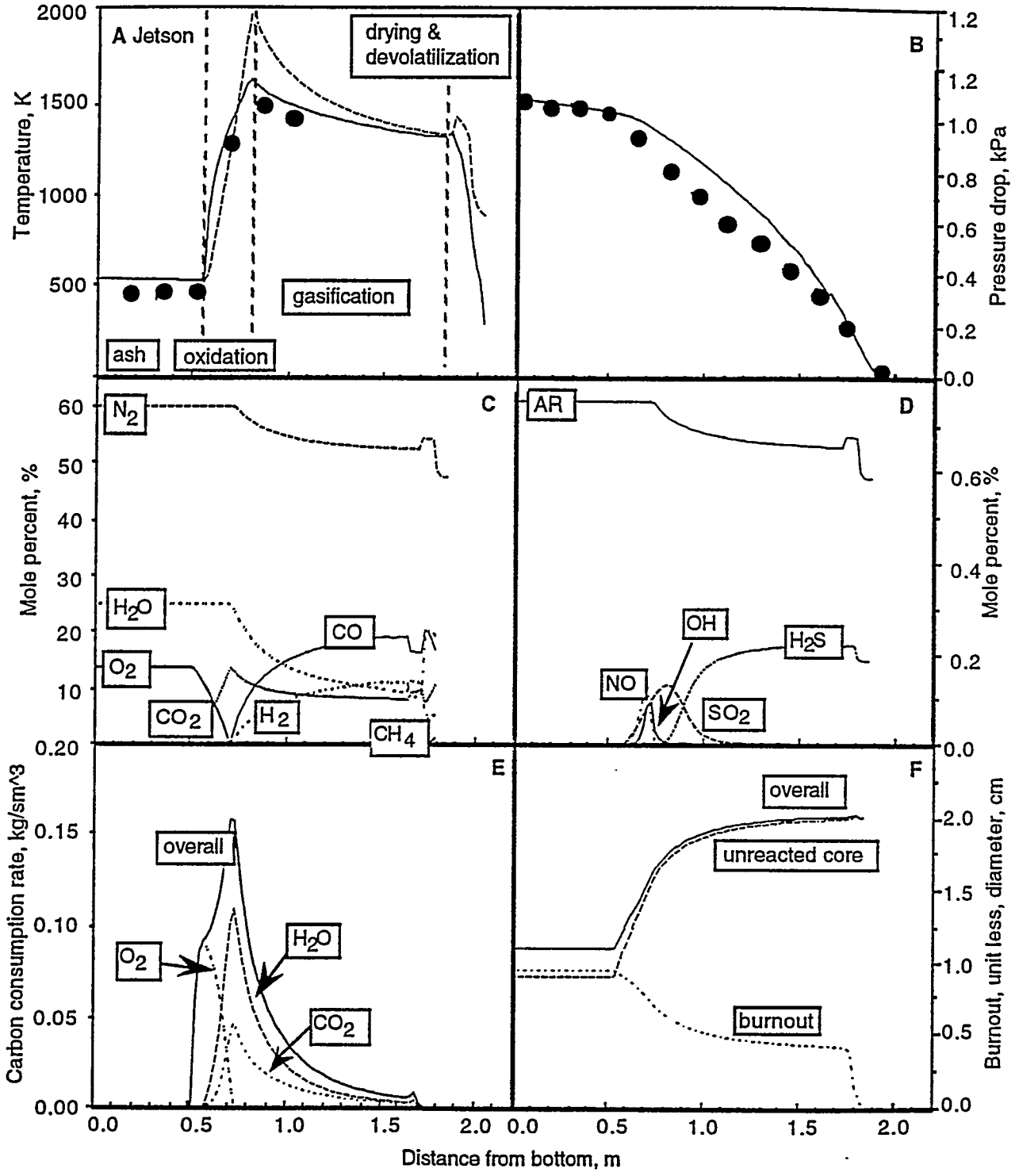

Figure III.B-6 Predicted axial A) temperature, B) pressure drop, C) major species concentration, D) minor species concentration, E) oxidation/gasification carbon consumption rate, F) burnout, overall and unreacted particle diameter in an atmospheric, air-blown Wellman-Galusha gasifier fired with Jetson bituminous coal. Input parameters given in Table III.B-6. Measurements are from Thimsen *et al.* (1984).

dixoide. Carbon dioxide reaches a maximum at the end of the oxidation zone and decreases in the gasification zone. In the gasification zone, carbon dioxide reacts heterogeneously with carbon to produce carbon monoxide. Carbon monoxide is not present in the gas phase until oxygen is depleted. As with carbon monoxide, hydrogen does not appear in the gas phase until oxygen is depleted. Although agreement between the predicted and measured pressure profiles was acceptable, the void distribution may not be linear throughout the reactor. For example, the measured pressure profile in Fig. III.B-6B indicated that the void fraction changed markedly near the ash zone.

The predicted increase in the particle diameter at the top of the reactor was attributed to coal particle swelling. Swelling was assumed to be proportional to the extent of devolatilization. For the Jetson case, the predicted particle diameter of the ash was about 0.9 centimeters. The measured geometric mean diameter of the ash was 1.02 centimeters as reported by Thimsen et al. (1984). The excess nitrogen and high temperatures caused the equilibrium quantities of NO and OH to form in the oxygen-rich, high temperature zone of the reactor. These quantities decayed to zero as temperature decreased. Sulfur dioxide also formed in the presence of oxygen, and was converted to H_2S in the colder, fuel-rich regions of the gasifier.

The one-dimensional, fixed-bed model, MBED-1, is presented in more detail in our previous reports (Solomon et al, 1989, 1990, 1991), in a dissertation resulting from this project (Hobbs, 1990), and in our paper (Hobbs, et al., 1992b, Appendix E).

Development and Evaluation of FBED-1 Code

The final version of the fixed-bed code, FBED-1, addresses the deficiencies of MBED-1 code and builds on it. It aims at the following: (1) improved predictions of product gas composition and temperature; (2) improved prediction of tar flow rate; (3) integration of the devolatilization submodel, FG-DVC; (4) modifications in the iteration scheme to satisfy the gas phase boundary conditions at the bottom of the gasifier; (5) improved modularity, code structure and user friendliness; and (6) improved graphics output. All these objectives were successfully achieved. While maintaining the original style of MBED-1, the overall structure of the code was modified and the governing equations were grouped separately for the zero-dimensional and the one-dimensional portions of the code. A number of subroutines were rewritten and broken into smaller subprograms to enhance the modularity. Dynamic length arrays were used to allow for variable number of functional groups and gas phase species. The new structure of FBED-1 code allows the addition or deletion of dependent variables with only minor changes. The final version of the fixed-bed code, FBED-1, has been written to accommodate a maximum of 27 functional groups and 22 gas phase species. In the final implementation, 27 functional groups and 22 gas phase species were considered. The total number of differential equations has risen from 38 for MBED-1 to 191 for FBED-1. A routine to calculate the overall and species mass balances and overall enthalpy balance has been added in FBED-1.

Development of FBED-0 Code

The system of equations for the fixed-bed model constitutes a split boundary-value problem due to countercurrent gas and solid flows. The initial conditions for the coal stream are known at the top of the gasifier bed. The initial conditions for the gas stream are known at the lower boundary, i.e., at the bottom of the gasifier. Following the solution method of MBED-1, integration in FBED-1 was also implemented from the top to the bottom of the reactor. The initial values for the gas stream are provided by the zero-dimensional model, FBED-0. FBED-0 is similar to MBED-0 with the following differences: (1) the advanced devolatilization submodel FG-DVC has been fully integrated; (2) the gas phase decomposition of tar is modeled; and (3) the recycled tar is allowed to decompose to gas in the equilibrium zone. In MBED-0, the tar-forming fraction was either computed with Ko's correlation (1988) or specified as an input by the user. This led to algebraic expressions for determining the composition of the devolatilized products as well as the tar yield. In the final version, which is based on the FG-DVC submodel, the tar

evolution is computed by the DVC portion of the devolatilization submodel and is not known *a priori*. The resulting system of equations is comprised of 153 first order, coupled, ordinary differential equations. The system is solved using the sparse version of Lawrence Livermore ODE Solver, LSODES.. Due to the differential nature of the system, the CPU time increased from seconds to minutes. The details of integration of FG-DVC and tar decomposition submodel are discussed in the next section.

Development of FBED-1 Code

FG-DVC Submodel - Coal devolatilization in the first version of the fixed-bed code, MBED-1, was based on the functional group (FG) model along with computation of the tar yield based either on Ko's correlation (1988) or specified by the user. The simulation results showed a significant effect of tar yield and demonstrated the need for a more rigorous devolatilization model. A major improvement in the final version of the fixed-bed code, FBED-1, is the integration of the FG-DVC devolatilization submodel which computes the tar yield based on the coal structure. The FG-DVC submodel, as integrated in FBED-1, is formulated as a differential system, which is a significant refinement over the previous version formulated as an algebraic system. The FG-DVC devolatilization submodel takes into account 27 functional groups. The rates of evolution of mass from char to gas and tar are computed with rank-dependent, Arrhenius-type kinetics. The evolution of char phase functional groups into gas and tar phase functional groups is tracked. To preserve compatibility with MBED-1, the FG-SET submodel with 19 functional groups and rank-independent kinetics is also included as an option in the FBED-1 code.

FG-DVC Input Data - The input data for the FG-DVC submodel include the initial functional group composition of the coal, the rank-dependent kinetic parameters, percolation submodel data for bond population, and probability distribution for the tar mass bins. Eight data files with the input values for a set of standard (Argonne premium) coals are provided. Three options are provided in the code to select or provide an appropriate data file for the coal-dependent parameters for the devolatilization submodel. The first option allows the program to select the standard coal which is closest, on a oxygen/carbon-hydrogen/carbon plot, to the feed coal. The second option allows the user to specify a standard coal based on specific considerations e.g., the geographical origin of the feed coal. The third option allows the user to provide the data for the feed coal. With the first two options, the functional group composition of the standard coal is adjusted to match the ultimate composition of the feed coal to account for any differences.

Heat of Devolatilization - The simulation results from MBED-1 and preliminary versions of FBED-1 showed instantaneous devolatilization with extremely steep temperature gradients. This was caused by coal/char and gas phase enthalpies which were not internally consistent. New, improved expressions to calculate internally consistent coal/char and gas phase enthalpies were derived and a new procedure to simulate the energy exchange effects between the solid and the gas phases during devolatilization was incorporated into the code. The new algorithm is based on the model proposed by Merrick (1983). Merrick's model, which considers 9 species including tar, was extended to accommodate 27 functional groups of the FG-DVC devolatilization submodel. Figure III.B-7 shows the results of the simulations made with the previous and the new formulations. Figure III.B-7A

shows the steep temperature gradient during devolatilization which is caused by heat exchange effects due to high devolatilization rates as shown in Fig. III.B-7B. The simulations made with the new submodel show reasonable temperature gradients for the solid during devolatilization as shown in Fig. III.B-7C. The sharp devolatilization spike observed during the previous simulations is eliminated as shown in Fig. III.B-7D.

Gas Phase Decomposition of Tar - The tar yield predicted by MBED-1 was consistently higher for all the coals simulated. This was attributed to the lack of tar repolymerization mechanism and gas phase decomposition of tar. The fixed-bed model, FBED-1, was, therefore, extended to account for the decomposition of tar in the gas phase. The tar cracking submodel is based on the following assumptions: (1) the *i-th* functional group in tar evolves to the *i-th* functional group in gas; (2) the

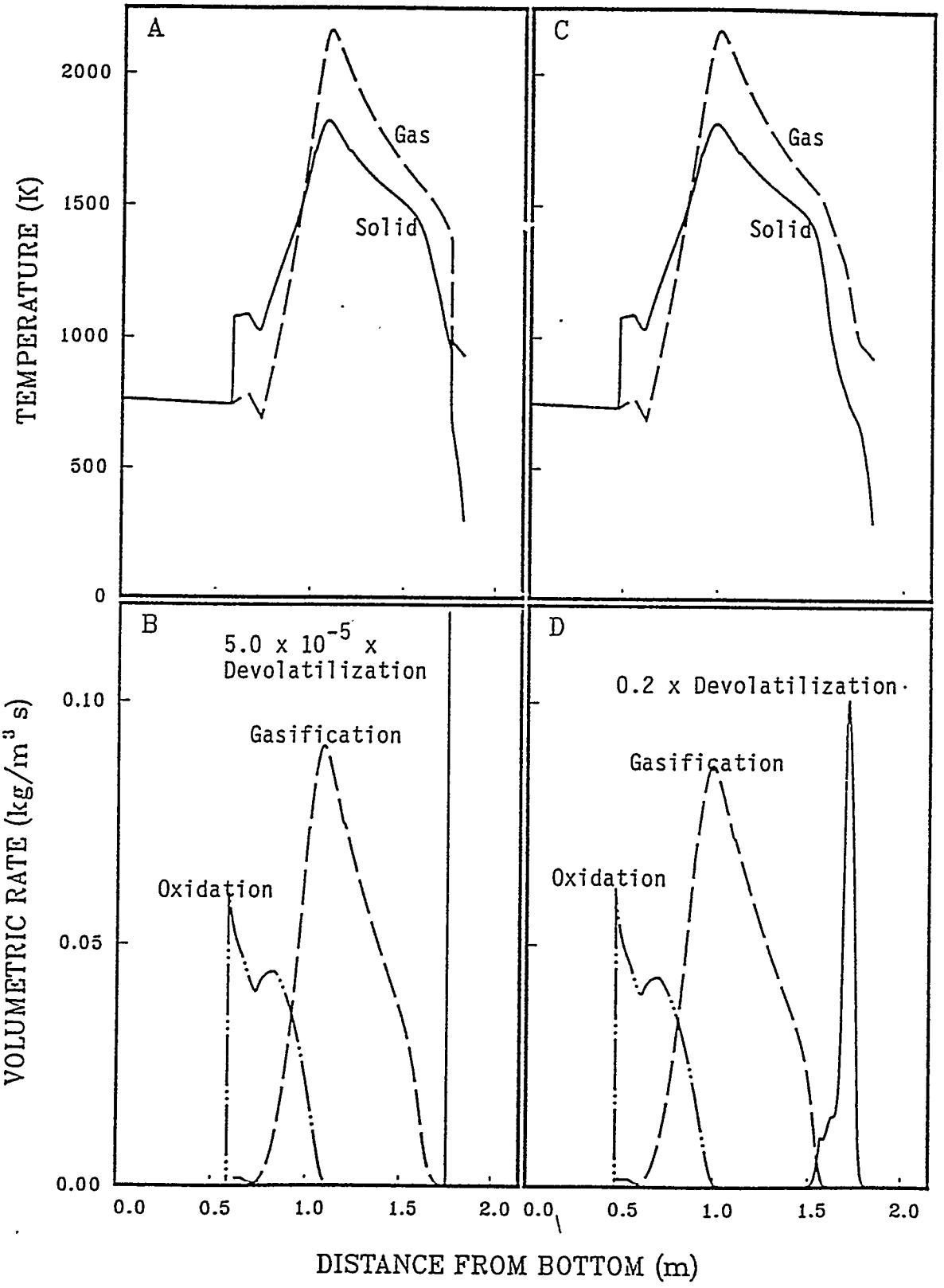

Figure III.B-7. Comparison of temperature and volumetric rate profiles: A) temperature profiles with the old devolatilization energy exchange formulation, B) volumetric rate profiles with the old devolatilization energy exchange formulation, C) temperature profiles with the new devolatilization energy exchange formulation, D) volumetric rate profiles with the new devolatilization energy exchange formulation.

decomposition of tar follows the same kinetics as that of gas evolution from the char, and (3) the evolution of gas from tar takes place at the gas temperature. The kinetic rates for the gas phase decomposition of tar are determined using a variable cut-off point for the distributed activation energy model.

Product Gas Composition - The product gas composition as predicted by the previous version of the model did not compare well with the experimental values for the Wellman-Galusha gasifier. This was especially true for the high moisture coals, where the model overpredicted H_2, CH_4, and CO_2 and underpredicted CO and H_2O. In order to improve the predictions for the product gas composition, an option to switch between full gas phase equilibrium and non-reactive gas phase was implemented. In this option, during the downward integration pass, the evolved gases are considered to be non-reactive but in thermal equilibrium until the gas-phase temperature attains a specified value, usually 1200K. At that temperature and onward the gas phase is considered to be in chemical and thermal equilibrium. During the upward integration pass, the order is reversed and full gas phase equilibrium is assumed till the gas temperature equals or falls below the switch temperature. After the switch is made, the gases are taken to be non-reactive and the gas phase composition is updated by accounting for the generated gases by heterogeneous reactions and solid decomposition. The product gas composition predicted using this option is significantly improved and compares well with the experimental data for both low moisture and high moisture coals.

Conservation Equations - The conservation equations for mass and energy form the foundation of the FBED-1 model. The gas and solid phase equations are coupled through the source terms. These source terms account for the release of mass from the solid phase to the gas phase, and energy exchange between the two phases. Tar is considered to be a pseudophase in FBED-1 formulation. The two-phase conservation equations have been reported by Crowe and Smoot (1979). The set of governing differential equations is listed in Table III.B-7. In the one-dimensional model, all 191 equations are solved, whereas only 153 differential equations listed are solved in FBED-0. During the upward integration pass, only 35 equations for the gas and the tar phase are solved. It is also pointed out that the gas phase species continuity equations are solved only when the gas phase is assumed not to be in chemical equilibrium.

Auxiliary Equations - The set of auxiliary equations for FBED-1 is essentially the same as that for MBED-1. Since plug flow is assumed for both the solid and the gas phase, the gas phase momentum equation is solved to calculate the gas phase pressure drop. Ergun's equation is used to calculate the friction factor and the bed void fraction is assumed to vary linearly between the feed coal and the product ash void fractions. At temperatures higher than the user-specified value, usually 1200K, the gas phase is assumed to be in chemical and thermal equilibrium and its composition and temperature are computed by Gibbs free energy minimization. The option to keep tar either in or out of chemical equilibrium is preserved in FBED-1. The heat and the mass transfer coefficients and the transport and the thermodynamic properties of gas and tar phases are based on the same correlations as in MBED-1.

Solution Method - In MBED-1, the system of the governing differential equations was integrated from the top to the bottom of the gasifier using the MBED-0 results as the initial conditions for the gas phase. The predicted gas phase quantities at the bottom of the gasifier did not satisfy the feed gas boundary conditions. In order to improve on these predictions and satisfy the boundary conditions for both the solid and the gas stream, a split back-and-forth integration scheme was implemented in FBED-1. By this method, the complete set of the differential equations is solved during the downward integration pass. In the upward integration pass, only the gas phase equations are integrated. The solid phase variables are held constant and the solid-gas exchange quantities are calculated from the values predicted during the downward integration pass. This yields a new guess for the gas phase quantities at the top of the gasifier which is then used for the next downward integration sweep. This improves the predictions and the downward integration sweep closely satisfies the feed gas boundary conditions except for the temperature. Finally, to satisfy the feed gas temperature, the split back-and-forth integration was coupled with the shooting method with the product gas enthalpy as the iteration variable.

TABLE III.B-7
DIFFERENTIAL EQUATION SET FOR FBED-1

Overall Gas Continuity	$\frac{dW_g}{dz} = A\sum_{i=1}^{6} r_i$	(1)
Overall Solid Continuity	$\frac{dW_s}{dz} = -A\sum_{i=1}^{6} r_i$	(2)
Gas Phase Energy	$\frac{dW_g h_g}{dz} = A\left(Q_{sg} - Q_{gw} + \sum_{i=1}^{6} r_i h_{ig}\right)$	(3)
Solid Phase Energy	$\frac{dW_s h_s}{dz} = A\left(-Q_{sg} - Q_{sw} - \sum_{i=1}^{6} r_i h_{ig}\right)$	(4)
Gas Phase Elemental Continuity	$\frac{dW_g \omega_{g,j}}{dz} = A\sum_{i=1}^{6} r_{v_{i,j}}$	(5-9)
Overall Tar Continuity	$\frac{dW_{tar}}{dz} = A\sum_{k=1}^{nfg=27}\left(r_{d_{tar,k}} - r_{c_{tar,k}}\right)$	(10)
Tar Elemental Continuity	$\frac{dW_{tar}\omega_{tar,j}}{dz} = \omega_{tar,j}(z)\frac{dW_{tar}}{dz}$	(11-15)
Moisture Continuity	$\frac{dW_{moisture}}{dz} = -Ar_{drying}$	(16)
Gas Phase Species Continuity	$\frac{dW_{g,1}}{dz} = \sum_{k=1}^{nfg} F_{k1} W^{\circ}_{s,daf} r_{d_{gas,k}} + A\sum_{\substack{i=1 \\ i\neq 2}}^{6} G_{i1}\upsilon_{i1}\frac{M_1}{M_c} r_i$	(17-38)
Gas Functional Groups	$\frac{dW_{g,k}}{dz} = \frac{W^{\circ}_{sv,daf}}{V_s}\left(r_{d_{gas,k}} + r_{c_{tar,k}}\right)$	(39-65)
Tar Functional Groups	$\frac{dW_{tar,k}}{dz} = \frac{W^{\circ}_{sv,daf}}{V_s}\left(r_{d_{tar,k}} - r_{c_{tar,k}}\right)$	(66-92)

TABLE III.B-7 (CONTINUED)

Char Functional Groups

$$\frac{dW_{char.k}}{dz} = \frac{1}{V_s}\left(W^{\circ}_{sv,daf}\ r_{d_{char.k}} - \frac{\sum_{i=3}^{6} W_{char.k} r_i}{W^{\circ}_{sv,daf} \sum_{k=1}^{nfg} W_{char.k}} \right) \quad (93\text{-}119)$$

Lower Bound for E_k^m

$$\frac{dE_k^m}{dz} = \frac{1}{V_s}\left(\langle k_k(T_s) \rangle \frac{\int_{E_k^m}^{\infty} f_k(E)dE}{f_k(E_k^m)} \right) \quad (120\text{-}146)$$

Lower Bound for E_B^m

$$\frac{dE_B^m}{dz} = \frac{1}{V_s}\left(\langle k_B(T_s) \rangle \frac{\int_{E_B^m}^{\infty} f_B(E)dE}{f_B(E_B^m)} \right) \quad (147)$$

Labile Bridge Fraction

$$\frac{dp_L}{dz} = \frac{1}{V_s}\left(-2\langle k_B(T_s) \rangle p_L \right) \quad (148)$$

Total Bridge Fraction

$$\frac{dp}{dz} = \frac{1}{V_s}\left(-\langle k_B(T_s) \rangle p_L \right) \quad (149)$$

Cross-link Fraction

$$\frac{dq}{dz} = \frac{1}{V_s}\left(\sum_{CO_2,CH_4} r_{d_{gas.k}} \frac{X_i}{M_k \sum_{k=1}^{nfg} W_{char.k}} \right) \quad (150)$$

Tar in Mass Bins

$$\frac{dW_{tar.n}}{dz} = \frac{1}{V_s}\left(P_n \chi_n \frac{\sum_{k=1}^{nfg} r_{d_{gas.k}}}{P_o + \Delta P + \sum_{n=1}^{nbins=13} P_n \chi_n} \right) \quad (151\text{-}163)$$

Tar Forming Fraction

$$\frac{d\chi^{o}}{dz} = \frac{1}{V_s} \langle k_{tar}(T_s) \rangle \Big|_{DVC} \quad (164)$$

TABLE III.B-7 (CONTINUED)

Lower Bound for E_{TC}^m

$$\frac{dE_{TC}^m}{dz} = \frac{1}{V_s}\left(\langle k_k(T_g)\rangle \frac{\int_{E_{TC}^m}^{\infty} f_k(E)dE}{f_k\left(E_{TC,k}^m\right)}\right) \qquad (165\text{-}191)$$

Definitions

Char devolatilization $\quad r_{d_{char,k}} = -r_{d_{gas,k}} - r_{d_{tar,k}}$

Gas evolution from char $\quad r_{d_{gas,k}} = \langle k_k(T_s)\rangle\left(W_{char,k} + i^{th}\ W_{tar,k}\right)$

Tar evolution from gas $\quad r_{d_{tar,k}} = \langle k_{tar}(T_s)\rangle \Big|_{DVC} \frac{W_{char,k}}{\sum_{k=1}^{nfg} W_{char,k}}$

Gas evolution from tar cracking $\quad r_{c_{tar,k}} = \langle k_k(T_g)\rangle W_{tar,k}$

i^{th} = 1, if tar (within char) is allowed to form gas
0, otherwise.

F_{kl} = 1, if k^{th} functional group contributes to l^{th} gaseous species
0, otherwise.

G_{il} = 1, if i^{th} reaction contributes to l^{th} gaseous species
0, otherwise.

υ_{il} = Stoichiometric coefficient for the l^{th} species in the i^{th} reaction.

i = 1-6 represents drying, devolatilization, CO_2, H_2, H_2O gasification, and oxidation reactions, respectively.

j = 1-5 represents elements C, H, O, N,S, respectively.

k represents 27 functional groups considered in FBED-1.

l represents 22 gaseous species considered in FBED-1.

n represents 13 mass bins considered in FG-DVC submodel.

$$W_{s,daf}^{\circ} = W_{coal}^{\circ}\left(1 - \Omega_{ash}^{\circ} - \Omega_{H_2O}^{\circ}\right)$$

$$W_{sv,daf}^{\circ} = \rho_{coal}^{\circ}\left(1 - \varepsilon_{coal}^{\circ}\right)\left(1 - \Omega_{ash}^{\circ} - \Omega_{H_2O}^{\circ}\right)$$

In this scheme, the product gas enthalpy is varied, while all other gas phase quantities are held constant, and the complete set of equations is integrated from the top to the bottom of the gasifier. Once the feed gas temperature is converged within the specified tolerance, an upward pass is taken to compute the final product gas composition and temperature. Convergence is typically obtained in 8-10 iterations and CPU time is typically around one hour on a mini super computer.

A full back-and forth integration method, in which both the solid and the gas phase equations were integrated not only downward but also upward, was also tried. However, the numerical problems in the upward integration of this highly non-linear, full set of differential equations were substantial and the effort had to be put on hold for now.

Figure III.B-8 shows the results obtained using the solution method discussed above. Both the predicted and the measured values for the Wellman-Galusha gasifier fired with the Jetson bituminous coal are presented. The predicted values are shown for the first solution which is based on the initial guess provided by FBED-0, as well as for the final converged solution. The first solution does not satisfy the feed gas composition and temperature. It overpredicts the amount of H_2O in the feed gas stream and the product tar flow rate, and underpredicts the amount of O_2 in the feed gas stream, the wall heat loss and the feed gas temperature. Since the feed gas temperature was not reported, it was estimated to be 560 K to allow for the heat exchange between the ash and the feed gas below the gasifier bed. The product gas composition also does not compare well with the experimental values. It is pointed out that these concentrations were determined assuming the gas phase to be in equilibrium in FBED-0. Only marginal improvements were observed in the product gas composition when the devolatilized gases were kept out of equilibrium in the drying and devolatilization zone. Both the first solution and the converged solution predict complete burnout of char. The converged solution satisfies the feed gas composition and temperature. The product gas composition, the product tar flow rate and the wall heat loss also show marked improvement and compare well with the experimental data. The predicted pressure profiles for both the first and the final solution compare well with the experimental data. The difference between the two predicted profiles is due to the integration procedure which requires an initial guess for the gasifier top pressure. The subsequent integration passes improve on this guess and thereby improve the pressure predictions. The solid and the gas temperature profiles show increases in the peak temperatures. This is caused by the higher amount of O_2 and lower amount of H_2O available which lead to higher oxidation rate and thus higher temperatures. The final solid temperature profile, even though it overpredicts the peak temperature, compares well with the experimental data. Finally, the product gas temperature for both of these solutions does not compare well with the experimental data. It should be noted that the reported effluent gas temperature is at the gas off-take location whereas our predicted temperatures are at the gasifier bed top. A proper submodel to account for the heat exchange in the free-board zone should improve these predictions.

Graphics - The output of the FBED-1 code is provided in a form suitable for use with popular spreadsheet packages. The user can use a spreadsheet package available at his/her site and generate the plots of the quantities of interest by importing the output files to the spreadsheet. In addition, two computer programs, written in FORTRAN, are provided to be used with the DISSPLA graphics package. The first program generates the temperature, pressure, composition, char consumption and burnout profiles. The second program generates a plot which compares the available experimental data with the predictions. These comparisons include the feed gas properties (i.e., the temperature and the composition for the species of interest), the product gas properties, the temperature and pressure profiles, the burnout, the product tar flow rate and the wall heat loss. Figs. III.B-8 and III.B-9 of this report were generated using these two programs.

Sample Simulation - In this section, the simulation of the atmospheric, air-blown, dry-ash Wellman-Galusha gasifier fired with the Jetson bituminous coal is discussed in detail. This case was selected because the experimental temperature profile shows reliable measurements in the ash zone. For other cases, either no or little data are available for the ash zone. The FBED-1 predicted results are

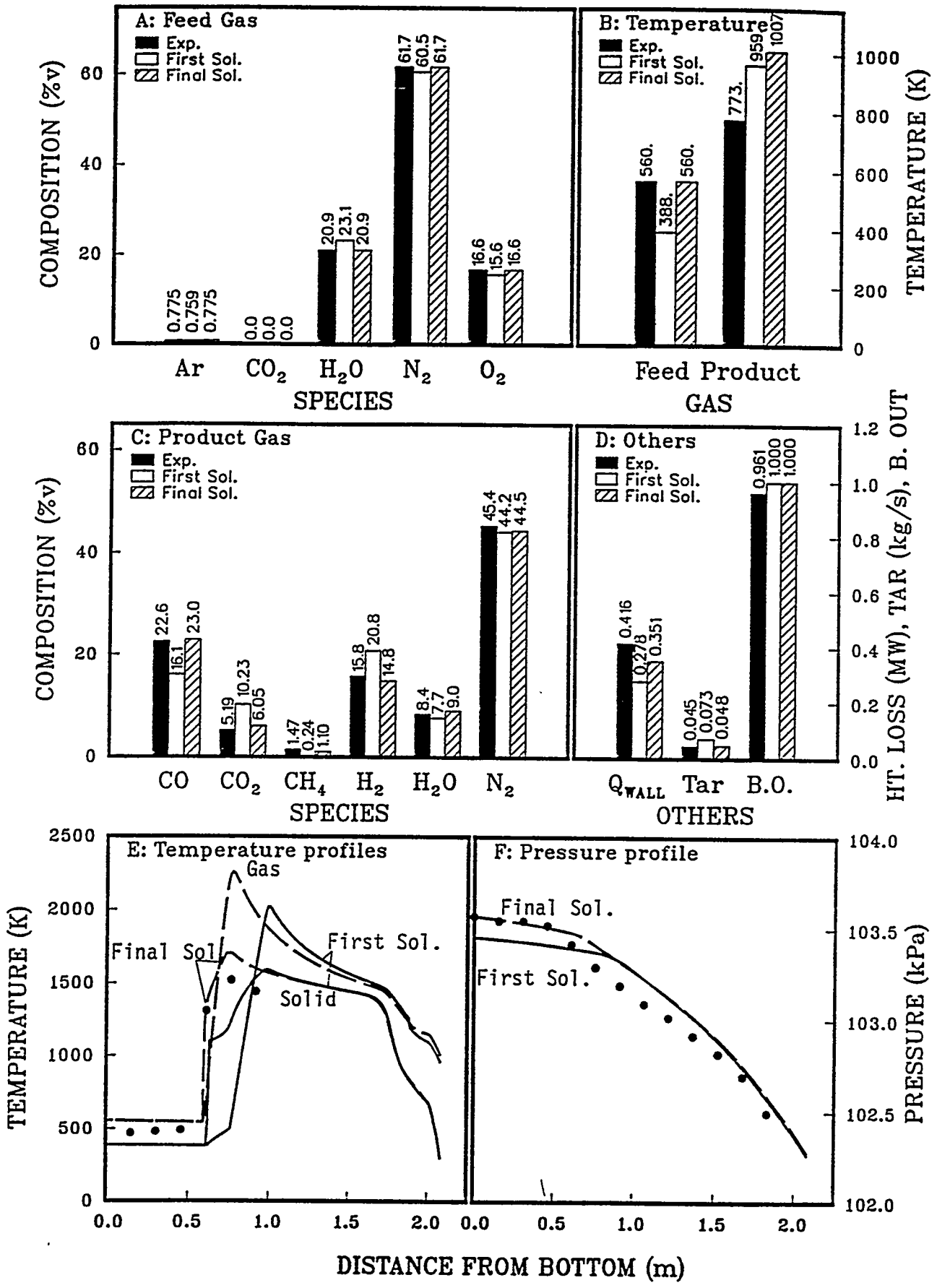

Figure III.B-8. Comparison of FBED-1 predictions with experimental data for the first and the final solution.

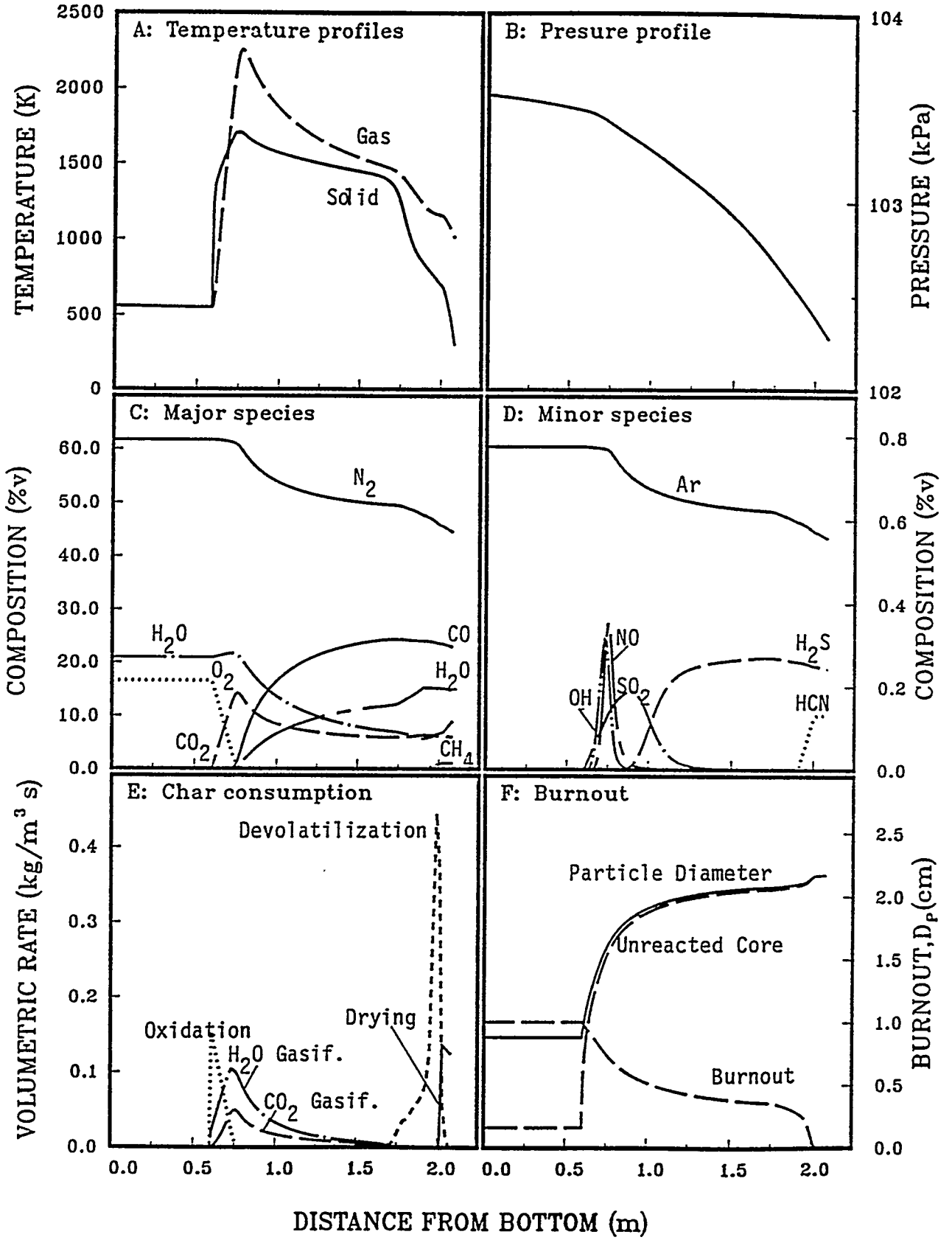

Figure III.B-9. FBED-1 predictions for the atmospheric, air-blown, dry-ash Wellman-Galusha gasifier fired with the Jetson bituminous coal.

shown in Fig. III.B-9. The predicted profiles are shown for temperature, pressure, major and minor species composition, char consumption, and burnout. Both the solid and the gas temperatures show rapid change in the drying and devolatilization region. This is associated with the rapid addition of the devolatilized mass to the gas phase. In FBED-1, all coal conversion processes, namely drying, devolatilization, gasification and oxidation, are allowed to occur simultaneously. The results show that for atmospheric gasifiers, very little gasification occurs before devolatilization is complete, mainly due to the low solid temperatures.

Oxidation and gasification reactions overlap in the region where oxygen is available. Due to high temperature in this zone, oxidation is dominant. The peak solid and gas temperatures occur when the oxygen becomes available to the char. The heat evolved due to the exothermic oxidation reaction causes the rapid heat-up of the gas stream. The temperatures drop sharply as soon as all the char is consumed and remain almost constant in the ash zone. CO and H_2 are not observed in the oxidation zone due to chemical equilibrium in the gas phase which causes all carbon and hydrogen to form CO_2 and H_2O. In the oxidation zone, H_2O concentration also shows some increase due to the reaction of char oxygen and hydrogen which is assumed to be proportional to the overall char consumption rate. Char consumption by hydrogen gasification reaction is insignificant in comparison with CO_2 and H_2O gasification reactions. Increase in H_2O near the gasifier top is due to the release of moisture during the drying of feed coal.

CH_4 appears only in the low temperature devolatilization zone where the gas phase is assumed to be out of chemical equilibrium. Char sulfur is reacted to form H_2S in the oxygen free zone and is converted to SO_2 when the oxygen becomes available. NO and OH are observed only in the high temperature oxidation region. In addition, substantial amounts of HCN are observed in the product gas with practically no amounts of NH_3 and NO. All of HCN is released in the devolatilization zone through HCN tight and extra-tight functional groups. This indicates a need for a nitrogen pollutants submodel to adequately predict the amounts of NO, NH_3 and HCN in the product gas. The burnout profiles show rapid change in the devolatilization zone followed by a gradual change in the gasification and oxidation zone. The particle size shows a very rapid decrease in the oxidation zone due to the high char consumption rates. Finally, the pressure profile show a small drop in the ash zone followed by a gradual change in the reactive zones of the gasifier. The small change in the ash zone is attributed to the higher bed void fraction offering little resistance to the gas flow.

Cocurrent Option - The modifications needed in the FBED-1 model to simulate novel configurations and additional flow patterns were formulated. These configurations include staged gasification and multiple inlets and outlets. The flow patterns include cocurrent and crosscurrent flows.

Sensitivity Analysis

This section presents the effects of model parameters on the predictions of FBED-1. These parameters include solid-gas heat transfer, ash diffusion, oxidation and gasification kinetics, wall heat loss, and switch temperature for gas phase equilibrium. The effect of feed gas temperature, which is an operational variable, is also studied. The sensitivity to these parameters is demonstrated by simulating the atmospheric, air-blown, Wellman-Galusha gasifier fired with the Jetson bituminous coal. The changes in the gas and solid temperature fields and the product gas composition of major species are analyzed to understand the effect of these parameters. Figures III.B-10 to III.B-12 show the predicted effect of these parameters on solid temperature, gas temperature and product gas composition. It is pointed out that the sensitivity analysis reported using the earlier version of the model, MBED-1, was only qualitative as some of the boundary conditions were not satisfied in those simulations. The sensitivity analysis presented here is quantitative since the boundary conditions for both the coal and the gas stream are satisfied. The variations in these parameters were explored over wide ranges. However, the results presented here are only for the values which yielded converged solutions. This resulted in a narrow range for some parameters, especially for gas-solid heat transfer and kinetics.

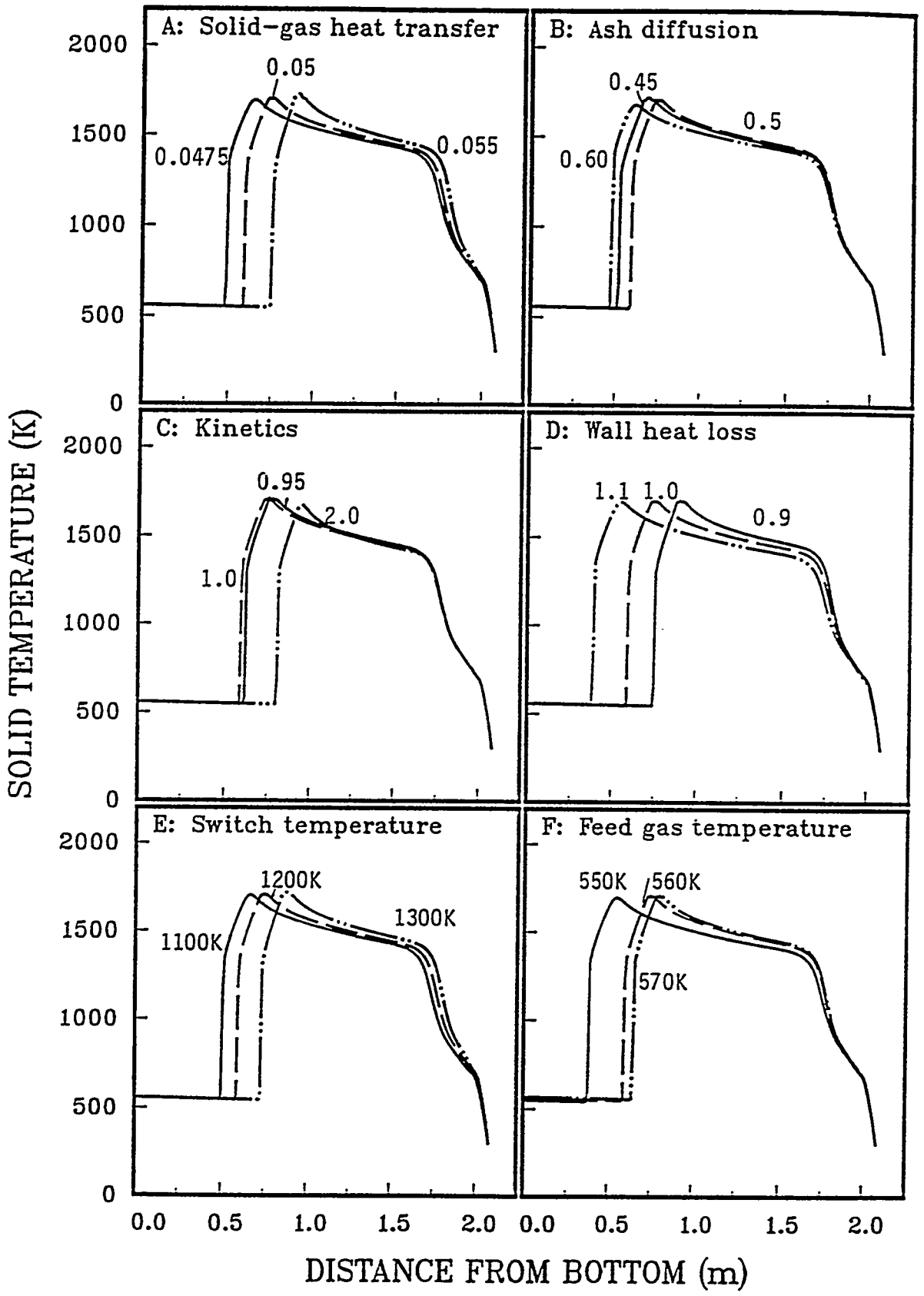

Figure III.B-10. Predicted sensitivity of solid temperature to model parameters and operational variables.

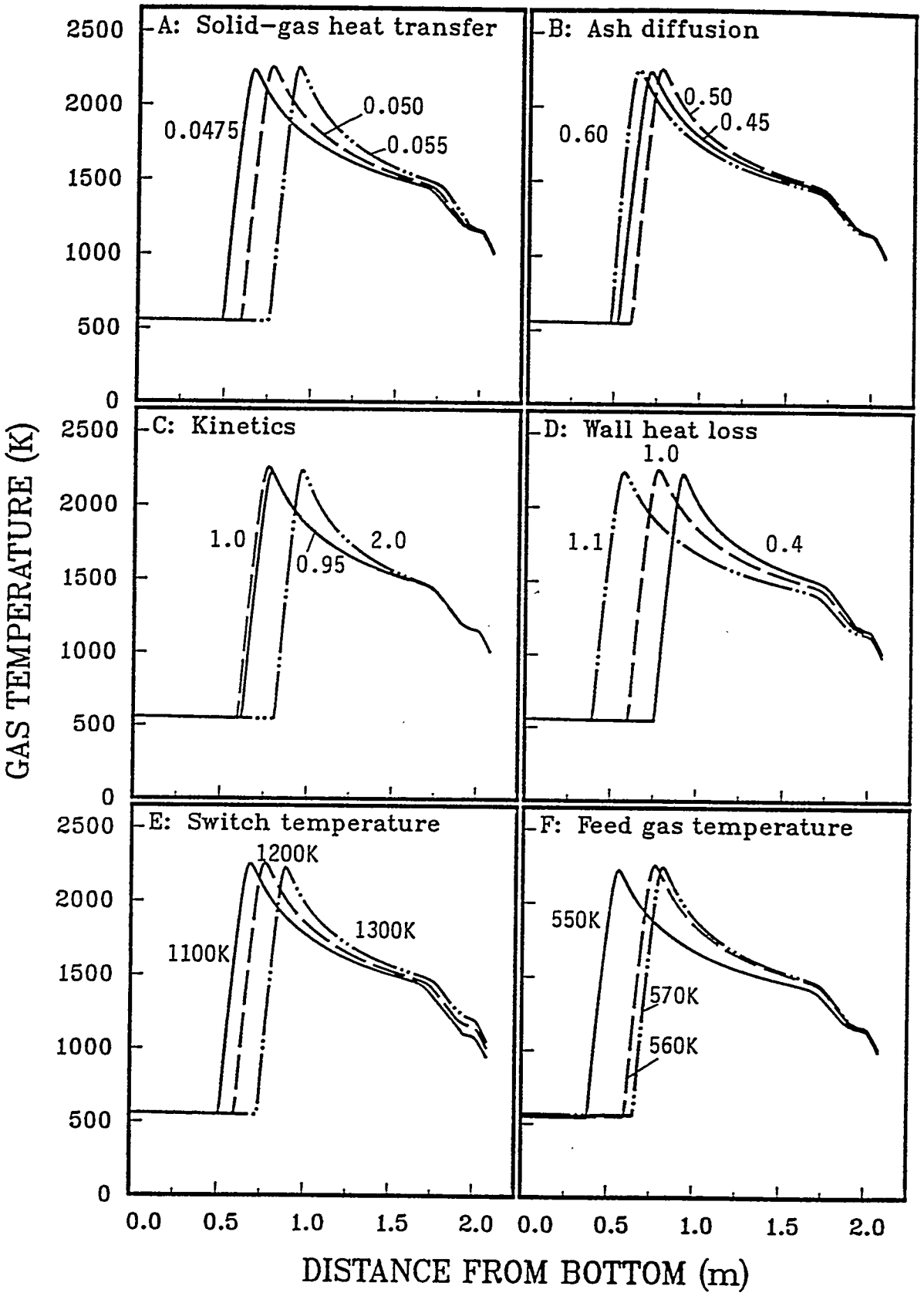

Figure III.B-11. Predicted sensitivity of gas temperature to model parameters and operational variables.

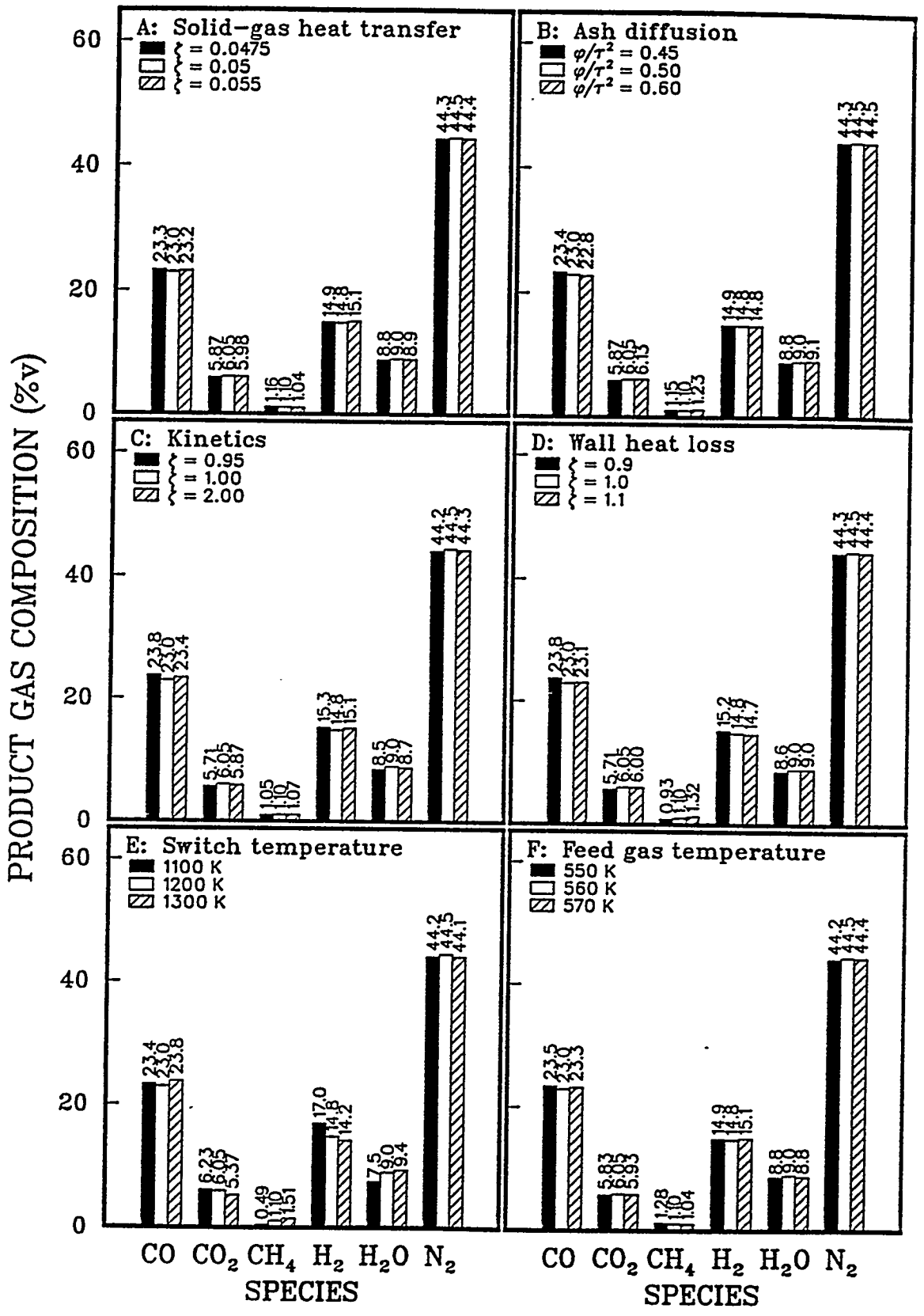

Figure III.B-12. Predicted sensitivity of product gas composition to model parameters and operational variables.

Wall Heat Loss - The effect of wall heat loss is shown in Figs. III.B-10D, 11D and 12D. A ten percent decrease in the wall heat transfer coefficient decreases the heat loss by 17.5%. The product gas temperature increases by 20K. This leads to a shorter reaction zone due to the additional available energy. Similarly, a 10% increase in wall heat transfer coefficientincreases the wall heat loss by about 22% showing a non-linear behavior. The product gas temperature is also lowered by 20K. This results in a longer reaction zone and a shorter ash zone. The peak solid temperatures do not show any significant deviations from the base case. Higher product gas temperature yields larger amounts of CO and H_2, and lower amounts of CO_2, CH_4, and H_2O.

Switch Temperature - The switch temperature above which the gas phase is considered to be in chemical and thermal equilibrium shows a significant effect on solid and gas temperatures as well as on product gas composition. A lower switch temperature yields significantly lower amounts of CH_4 and H_2O, and larger quantities of H_2 as shown in Fig. III.B-12E. The amount of CO_2 in the product gas also increases. The effluent gas temperature decreases as the switch temperature is lowered, as shown in Fig. III.B-11E, leading to an extended reaction zone. These results are consistent with the observed behavior for the wall heat loss. Furthermore, these results indicate that the product gas is not in chemical equilibrium at the low effluent temperatures. This is especially true for high moisture coals which yield higher quantities of H_2 and CH_4 and smaller quantities of H_2O when the gases are allowed to react to equilibrium.

Feed Gas Temperature - The effect of feed gas temperature is shown in Figs. III.B-10F, 11F, and 12F. The lower feed gas temperature gives the lower gas peak temperature. The solid peak temperature, on the other hand, does not show any significant change. The effect of lowering the feed gas temperature by 10K is more pronounced than increasing the temperature by 10K. This is attributed to the much lower product gas temperature resulting from the lower feed gas temperature. The product gas composition does not show any significant change.

Validations

In order to evaluate and validate the final version of the fixed-bed code, FBED-1, its predictions are compared with the available data for the atmospheric, air-blown, dry-ash, Wellman-Galusha gasifier (Thimsen et. al., 1984). The experimental data include the temperature and pressure profiles, and the product gas composition. Following Barriga and Essenhigh (1980), the experimental temperature profile is assumed to represent the solid temperature. The comparisons for two coals, Jetson bituminous and Rosebud subbituminous, are presented. The simulation results are shown in Figs. III.B-13 and 14. The feed gas composition and temperatures are satisfied exactly. The product gas composition, the product tar flow rate and the wall heat loss predicted by the model are in close agreement with the experimental data. The predicted pressure profile for the Jetson case shows good agreement with the experimental data. The Rosebud case, although predicts the proper trend, does not simulate well the pressure in the drying zone. This is also true for the temperature field which shows steep change in the drying zone. The predicted temperatures are slightly higher but the trends in the devolatilization, gasification and oxidation zone are properly predicted. The overall mass and energy balances close within 1%. The elemental mass balances close typically within 5%. Overall, the comparison between the experimental and the predicted values is good.

Summary and Conclusions

Although direct utilization of coal (i.e. combustion) currently dominates industrial and residential applications, a number of technologies based on coal gasification are emerging as cost-competitive. These include integrated coal gasification combined cycles (IGCC) for electricity generation, fixed-bed gasification for SNG production, gasification for synthesis of fuels and chemicals, and gasification for fuel cells. In order to support the development of these technologies, a recent panel of experts has listed the following as a priority research and development area (Penner, 1987): "Develop comprehensive

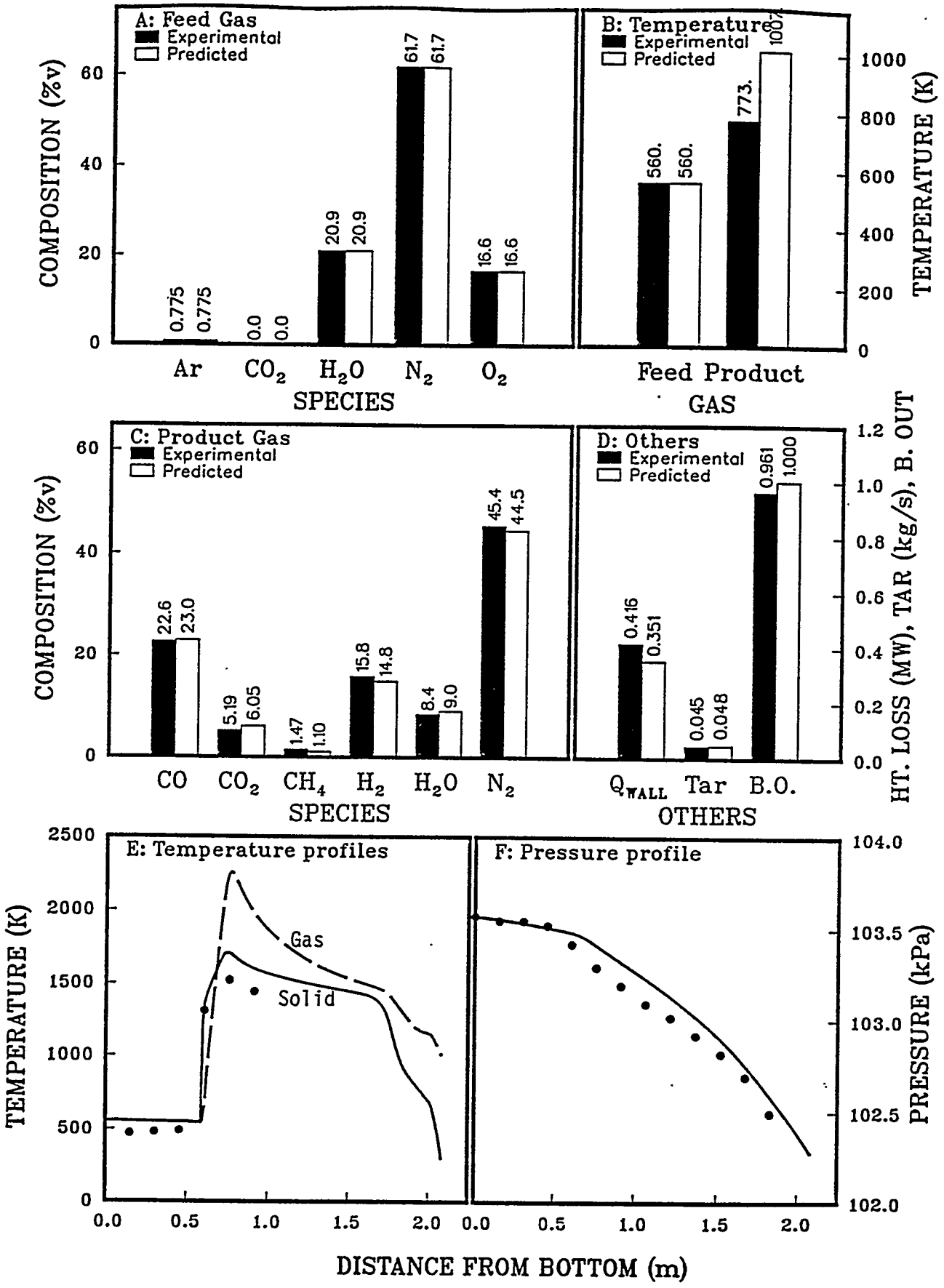

Figure III.B-13. Comparison of FBED-1 predictions with experimental data for the gasification of the Jetson bituminous coal in the atmospheric, air-blown, dry-ash Wellman-Galusha gasifier.

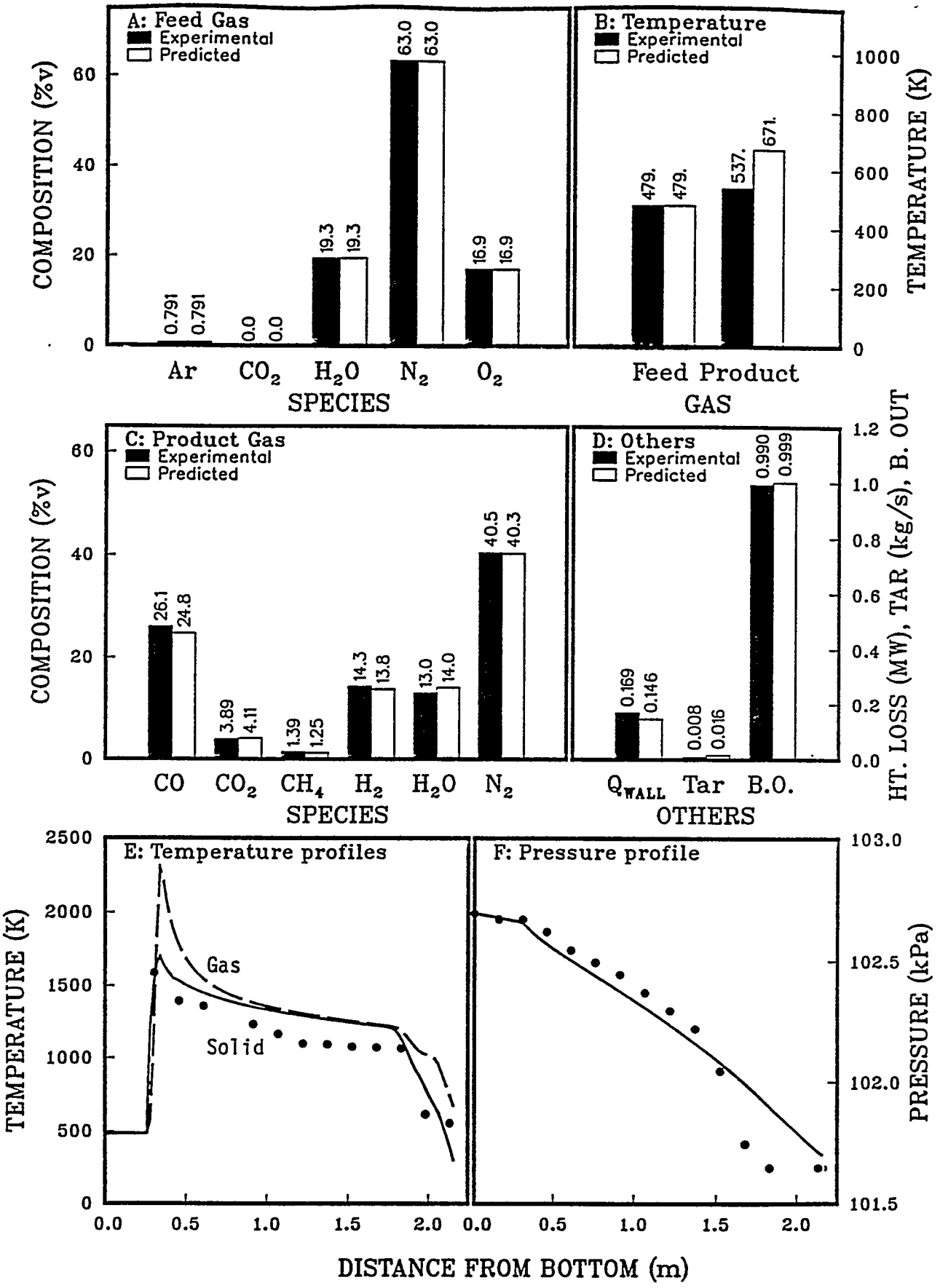

Figure III.B-14. Comparison of FBED-1 predictions with experimental data for the gasification of the Rosebud subbituminous coal in the atmospheric, air-blown, dry-ash Wellman-Galusha gasifier.

(numerical) models for gasifiers based on our best scientific knowledge of chemical and physical phenomena and validate and improve these models by performing appropriate laboratory and field measurements."

Based on a review of existing models and recommendations of expert consultants, an advanced model for fixed-bed coal gasification has been developed. The rationale for this decision has been as follows: the past level of effort in fixed-bed modeling has been modest; there was no generalized, robust, well-documented code for fixed-bed coal gasification or combustion available; the proposed, advanced model has been reviewed by expert consultants and has received positive recommendations; there has been little evaluation and application of fixed-bed models; fixed-bed technology is of interest in high pressure, combined cycle power generation, synthesis gas production, liquids production (mild gasification), and fuel gas production; and the importance of fixed-bed technology was specifically noted in an evaluation of gasification research needs (Penner, 1987). The report by Penner specifically recommended development of fixed-bed process models.

The principal objective of this project was to develop, evaluate and apply an advanced, steady-state, one-dimensional model of countercurrent, fixed-bed coal combustion and gasification. Improvements include advanced treatment of devolatilization, separate gas and coal temperatures, axially variable solid and gas flow rates, variable bed void fraction, generalized treatment of gas phase chemistry, and SO_X/NO_X pollutants. The initial fixed-bed model, MBED-1, was evaluated through sensitivity analysis and comparisons to experimental data. The predicted temperature and pressure profiles were found to agree reasonably well with the measured values. In MBED-1, gas evolution rates are determined by the functional group (FG) submodel and tar evolution rate is determined by the semi-empirical tar (SET) correlation. The MBED-1 results brought out the significant effect of tar yield on predictions and the need for a more rigorous devolatilization model.

The most important improvement in the final version of the fixed-bed model, FBED-1, is the inclusion of the advanced devolatilization submodel, FG-DVC. In this submodel gas evolution rates are determined by the functional group (FG) submodel and tar evolution rate by the depolymerization-vaporization-crosslinking (DVC) submodel. The final version of the fixed-bed code, FBED-1, also provides improved predictions of product gas composition and temperature, improved prediction of tar production, modifications in the iteration scheme to satisfy the gas phase boundary conditions at the bottom of the gasifier, improved modularity, code structure, and use friendliness, and improved graphics output. The final fixed-bed model, FBED-1, was also evaluated through sensitivity analysis and comparisons to experimental data. The predicted effluent composition and temperature as well as the predicted temperature and pressure profiles were found to agree very well with the measured values. A user's manual for FBED-1 is provided as Volume III of this final report.

The advanced, one-dimensional model of fixed-bed coal gasification, FBED-1, has been developed, evaluated, and applied to a number of test cases. Many advances have been made: advanced treatment of devolatilization, generalized gas phase chemistry, equilibrium SO_x/NO_x, variable and overlapping coal reaction zones, variable bed porosity and solid velocity, ash layer effects, and tar production. Comprehensive comparisons of temperature and pressure profiles with experimental data have also been made. Still, further research is needed on a number of issues. Three such important issues are large particle devolatilization, large particle combustion and gasification, and advanced fixed-bed coal gasification model to treat a variety of novel and complex configurations and modes of operation. Other important issues are gas phase kinetics, pollutant kinetics, improved heat and mass transfer rates for reacting fixed-beds, improved initial estimates of effluent properties, and full back-and-forth iteration method.

References for Section 3.b.

Bird, R.B., Stewart, W.E. and Lightfoot, E.N., *Transport Phenomena*, John Wiley and Sons,New York, NY (1960).

De Wasch, A.P.and Froment, G.F., A Two Dimensional Heterogeneous Model for Fixed Bed Catalytic Reactors, Chem. Eng. Sci., 26, pp.629-634 (1971).

Dzhapbyev, K., Miropol'ski, A.L. and Mal'kovskii, V.J., Investigation of Unsteady Heat Transfer in a Packed Bed of Spheres Swept by Gas, Therm. Eng., 33 (1986) pp. 159-162, English translation of Teploenergentika, 33 (1986) pp. Ed., Chemistry of Coal Utilization, Supplementary Volume, John Wiley & Sons, New York, NY, pp. 892-1022 (1963).

Ergun, S., Fluid Flow through Packed Columns, Chem. Eng. Prog., 48, pp. 89-94 (1952).

Froment, G.F. and Bischoff, K.B., *Chemical Reactor Analysis and Design*, John Wiley & Sons, New York, NY (1979).

Ghani, M.U., Radulovic, P.T. and Smoot, L.D., Modeling of Coal Conversion Processes in Fixed Beds, presented at the Fall 1993 Meeting of the American Chemical Society, preprints of the Division of Fuel Chemistry, American Chemical Society, 38 (4), pp. 1358-1364 (1993).

Gray, D.D. and Stiles, J.M., On the Constitutive Relations for Frictional Flow of Granular Materials, Topical Report for the U.S. Department of Energy, Morgantown Energy Technology Center, Morgantown, WV, West Virginia University, Morgantown, WV, Contract No. DE-AC21-85MC21353, DOE/MC/21353-2584 (DE88001089) (1988).

Hindmarsh, A.C., ODEPACK, A Systematized Collection of ODE Solvers, R.S. Stepleman, Ed., Scientific Computing, Vol. 1, IMACS Transactions on Scientific Computation, North-Holland, Amsterdam, pp. 55-64 (1983) .

Hobbs, M.L., Modeling Countercurrent Fixed-Bed Coal Gasification, Ph.D. Dissertation, Brigham Young University, Provo, UT (1990).

Hobbs, M.L., Radulovic, P.T. and Smoot, L.D., Prediction of Effluent Compositions for Fixed-Bed Coal Gasifiers, Fuel, 71, 1177-1194 (1992a).

Hobbs, M.L., Radulovic, P.T. and Smoot, L.D., Modeling Fixed-Bed Coal Gasifiers, AIChE J., 38 (5), pp. 681-702 (1992b).

Ko, G.H., Sanchez, D.M., Peters, W.A. and Howard, J.B., Correlations for Effects of Coal Type and Pressure on Tar Yields From Rapid Devolatilization, Twenty-Second Symposium (International) on Symposium, The Combustion Institute, Pittsburgh, PA , pp. 115-124 (1988).

Krishnudu, T., Madhusudham, B., Reddy, S.N., Sastry, V.S.R., Rao, K.S. and Vaidyeswaran, R., Studies in a Moving Bed Pressure Gasifier,: Prediciton of Reaction Zones and Temperature Profile, Ind. Eng. Chem. Res., 28, pp. 438-444 (1989).

Kunii, D. and Smith, J.M., Heat Transfer Characteristics of Porous Rocks, AIChE J., 6, pp. 71-78 (1960).

Laurendeau, N.M., Heterogeneous Kinetics of Coal Char Gasification and Combustion, Prog. Energy Combust. Sci., 4, pp. 221-270 (1978).

Merrick, D., Mathematical Models of the Thermal Decomposition of Coal. 2. Specific Heats and Heats of Reaction, Fuel, 62, pp. 540-546. (1983)

Park, K.Y. and Edgar, T.F., Modeling of Early Cavity Growth for Underground Coal Gasification, Ind. Eng. Chem. Res., 26, pp. 237-246 (1987).

Perry, R.H. and Chilton, C.H., Eds., *Chemical Engineers' Handbook*, Fifth Edition, McGraw-Hill, New York, NY (1973).

Sen Gupta, A. and Thodos, G., Direct Analogy Between Mass and Heat Transfer to Beds of Spheres, AIChE J., 9, pp. 751-754 (1963).

Serio, M.A., Hamblen, D.G., Markham, J.R. and Solomon P.R., Kinetics of Volatile Product Evolution in Coal Pyrolysis: Experiment and Theory, Energy & Fuels, 1, pp. 138-152 (1987).

Smoot, L.D. and Pratt, D.T., *Pulverized Coal Combustion and Gasification*, Plenum Publishing, New York, NY (1979).

Solomon, P.R., Hamblen, D.G., Carangelo, R.M., Serio, M.A. and Deshpande, G.V., General Model of Coal Devolatilization, Energy & Fuels, 2, pp. 405-422 (1988).

Solomon, P.R., Hamblen, D.G., Yu, Z. and Serio, M.A., Network Models of Coal Thermal Decomposition, Fuel, 69, pp. 754-763 (1990).

Stull, D.R. and Prophet, H., *JANAF Thermochemical Tables*, Second Edition, The U.S. Department of Commerce, National Bureau of Standards, Washington, DC, NSRDS-NBS37 (1971).

Suuberg, E.M., Peters, W.A. and Howard, J.B., Product Compositions and Formation Kinetics in Rapid Pyrolysis of Pulverized Coal-Implications for Combustion, Seventeenth Symposium (International) on Combustion, The Combustion Institute, Pittsburgh, PA, pp. 117-130 (1978).

Thimsen, D., Maurer, R.E., Poole, A.R., Pui, D.Y.H., Liu, B.Y.H. and Kittelson, D.B., Fixed-Bed Gasification Research Using U.S. Coals, Volumes 1-19, Reports for U.S. Department of Energy, Morgantown Energy Technology Center, Morgantown, WV, Black, Sivails and Bryson, Inc., Houston, TX, Interagency Agreement No. DE-AI21-7ET10205, DOE/ET/10205-1689 (DE85002000) (1984).

Thorsness, C.B. and Kang, S.-W., Further Development of a General-Purpose, Packed-Bed Model for Analysis of Underground Coal Gasification Processes, Lawrence Livermore National Laboratory, University of California, Livermore, CA, Preprint UCRL-92489 (1985).

Von Fredersdorff, C.G. and Elliott, M.A., Coal Gasification, H.H. Lowry, Walker, P.L., Jr., Rusinko, F., Jr. and Austin, L.G., Gas Reactions of Carbon, D.D. Eley, P.W. Selwood and P.B. Weisz, Eds., Advances in Catalysis and Related Subjects, Vol. XI, Academic Press, New York and London, pp. 134-221(1959).

Wang, S.C. and Wen, C.Y., Experimental Evaluation of Nonisothermal Solid-Gas Reaction Model, AIChE J., 18, pp. 1231-1238 (1972).

Wen, C.Y., Chen, H. and Onozaki, M., User's Manual for Computer Simulation and Design of the Moving Bed Coal Gasifier, Final Report for the U.S. Department of Energy, Morgantown Energy Technology Center, Morgantown, WV, West Virginia University, Morgantown, WV, Contract No. DE-AT21-79MC16474, DOE/MC/16474-1390 (DE 83009533) (1982).

Wen, C.Y. and Chaung, T.Z., Entrainment Coal Gasification Modeling, Ind. Eng. Chem. Process Des. Dev., 18, pp. 684-695 (1979).

Yoon, H., Wei, J. and Denn, M.M., A Model for Moving-Bed Coal Gasification Reactors, AIChE Journal, 24, pp. 885-903 (1978).

SUBTASK 3.C. - GENERALIZED FUELS FEEDSTOCK SUBMODEL

Senior Investigators - B. Scott Brewster and L. Douglas Smoot
Brigham Young University
Provo, UT 84602
(801) 378-6240 and 4326

Objective

The objective of this subtask is to generalize PCGC-2 to include sorbent injection, as outlined in the Phase II Research Plan.

Accomplishments

The particle feeding submodel of 87-PCGC-2 was generalized to allow coal and sorbent injection in multiple inlets. Previously, particle feeding was allowed only in the primary stream, and only coal or inert particles could be fed. The submodel was tested by simulating the BYU gasifier with and without sidewall injection of sorbent. The cases that were simulated are Test No. I9, Sample No. 3 (without sorbent injection) and Test No. I10, Sample No. 4 (with sorbent injection) from Table II.H-2 in the 3rd Annual Report (Solomon et al., 1989). The results were presented under Subtask 2.g. The degree of sulfur capture was over-predicted, presumably because of inadequate representation of the 3-D mixing effects due to sidewall injection. Details are given in the paper by Boardman et al. (1992) which is contained in the appendix. Thus, while generalized feeding of solids (e.g. sorbent) in sidewall inlets has been accomplished in the code, the applicability of the code to practical configurations is somewhat limited. Better predictions with the 2-D code are expected when the feed geometry in the physical apparatus is truly axisymmetric. For sidewall injection, work is underway under independent funding to incorporate the sorbent injection and sulfur capture submodel into a 3-D code.

References for Subtask 3.c.

Boardman, R. D., Brewster, B. S., Huque, Z. and Smoot, L. D., Modeling Sorbent Injection and Sulfur Capture in Pulverized Coal Combustion, presented at the 1992 International Joint Power Generation Conference, Air Toxic Reduction and Combustion Modeling, FACT-Vol. 15, Atlanta, GA, October 18-22, 1-9 (1992).

SECTION IV. TASK 4. APPLICATION OF INTEGRATED CODES

Objectives

The objectives of this task were to evaluate the integrated comprehensive codes for pulverized coal and fixed-bed reactors and to apply the codes to selected cases of interest to METC.

Task Outline

This task was accomplished in two subtasks, one for the entrained-bed lasting 69 months and one for the fixed-bed lasting 60 months. Each of these subtasks consisted of three components: 1) Simulation of demonstration cases on BYU computers; 2) Implementation on a workstation at BYU and AFR; and 3) Simulation of demonstration cases on a workstation.

IV.A. SUBTASK 4.A. - APPLICATION OF GENERALIZED, PULVERIZED-COAL COMPREHENSIVE CODE

Senior Investigators - B. Scott Brewster and L. Douglas Smoot
Brigham Young University
Provo, UT 84602
(801) 378-6240 and 4326

Research Assistant - Ziaul Huque

Objectives

The objectives of this subtask are to 1) demonstrate application of the code by simulating reactors of interest to METC and 2) implement the code at METC and conduct training.

Accomplishments

Two commercial processes were selected for application of the improved entrained-bed code (93-PCGC-2). One is the Coal Tech Corp. advanced, air-cooled cyclone combustor, and the other is the Solar Turbines, Inc. combustor. The Coal Tech cyclone combustor was chosen because it is approximately two-dimensional and is one of the processes that has been developed under the DOE Clean Coal Technology Program (Zauderer and Fleming, 1991). It is currently being developed under an SBIR Phase III project funded by the DOE/Pittsburgh Energy Technology Center ("Development and Testing of an Industrial-Scale Coal-Fired Combustion System," Contract no. DE-AC22-91PC91162). A paper on the simulation of the Coal Tech cyclone combustor was presented at the Ninth Annual International Pittsburgh Coal Conference (Brewster, 1992).

Several design issues were investigated with the model. The results showed that the 2-D entrained-bed model is a useful tool for investigating some design issues, such as the effects of L/D ratio, swirl velocity, combustion efficiency, slag retention, and exit nozzle diameter. Based on these results, it was shown that consideration should be given to moving the slag tap upstream and decreasing the combustor length. Detailed investigation of the coal injector geometry requires a 3-D model. A detailed description of the combustor geometry, operation, and simulation results is given in the paper by Brewster (1992). A complete evaluation cannot be given without knowing the 3-D effects of particle injection and mixing.

The Solar Turbines combustor utilizes a coal slurry feed. Its simulation was performed under an independent study and is reported separately in Brewster et al. (1993).

93-PCGC-2 was installed at METC and a short course was conducted on June 29-30, 1993.

Summary and Conclusions

93-PCGC-2 was successfully applied to two practical-scale reactors of commercial interest. One was a cyclone combustor and the other was a coal-slurry-fed gas turbine combustor. The code was installed at METC and training was conducted.

References for Subtask 4.a.

Brewster, B. S., Smoot, L. D., Solomon, P. R., Serio, M. A., Hamblen, D. G., Final Report to Solar Turbines, Inc., submitted to Advanced Fuel Research, Inc. (1993).

Brewster, B. S., Application of a Coal-General, 2-D Combustion Model, Ninth Annual International Pittsburgh Coal Conference, Pittsburgh, PA, October 12-16 (1992).

Zauderer, B. and Fleming, E. S., The Demonstration of an Advanced Cyclone Coal Combustor, with Internal Sulfur, Nitrogen, and Ash Control for the Conversion of a 23 MMBtu/hour Oil Fired Boiler to Pulverized Coal, U.S. DOE-Clean Coal Program, Final Technical Report, DOE Cooperative Agreement No. DE-FC22-87PC79799 (1991).

IV.B. SUBTASK 4.B. - APPLICATION OF FIXED-BED CODE

Senior Investigator - Predrag T. Radulovic and L. Douglas Smoot
Brigham Young University
Provo, UT 84602
(801) 378-3097 and (801) 378-4326

Research Assistants - M. Usman Ghani and Michael L. Hobbs

Objective

The objectives of this subtask are: (1) to apply the advanced fixed-bed code developed in Subtask 3.b to simulate fixed-bed gasifiers of interest to METC, (2) to document the code, and (3) to implement the code at METC and to conduct the training.

Accomplishments

The fixed-bed coal combustion, gasification, and devolatilization codes, MBED-1 and FBED-1, developed in Subtask 3.b., can be used as design tools to assist in the design of new gasification units or as analysis tools to analyze the performance of existing units. Four dry-ash, fixed-bed gasifiers were approved for simulation by METC:

(1) a high-pressure, oxygen-blown Lurgi gasifier;
(2) a medium-presure, air-blown METC gasifier;
(3) an atmospheric-pressure, air-blown Wellman-Galusha gasifier; and
(4) a high-pressure, air-blown, PyGas™ staged gasifier.

Comprehensive design and test data are available for the first three gasifiers. The most comprehensive test data, including temperature and pressure profiles, are available for the atmospheric-pressure Wellman-Galusha gasifier in Minneapolis, Minnesota, Very comprehensive test data, but without temperature and pressure profiles, are also available for the medium-pressure METC gasifier in Morgantown, West Virginia and the high-pressure Lurgi gasifier in Westfield, Scotland. The Wellman-Galusha test data were used to validate the fixed-bed codes and the corresponding simulations were presented in Subtask 3.b.

The main accomplishments of this subtask are: (1) application of the MBED-1 code and (2) application, documentation, and implementation of the FBED-1 code. The MBED-1 code was applied to simulate the high-pressure, oxygen-blown Lurgi gasifier and the medium-pressure, air-blown METC gasifier. The FBED-1 code was applied to simulate the medium-pressure, air-blown METC gasifier and the high pressure, air-blown PyGas™ gasifier.

Application of MBED-1 Code

High-Pressure, Oxygen-Blown Lurgi Gasifier - Four cases were simulated: the gasifier fired with Illinois #6 bituminous coal, Illinois #5 bituminous coal, Pittsburgh #8 bituminous coal, and Rosebud subbituminous coal. The Rosebud case also included the predicted temperature profiles from Yoon (1978) and Cho (1980). No measured profiles were available. The input data for these four cases are presented in Table IV.B-1.

Predicted axial solid and gas temperatures for gasification of Illinois #5, Illinois #6, Pittsburgh #8, and Rosebud coals in the high-pressure, oxygen-blown Lurgi gasifier are shown in Fig. IV.B-1. Predicted axial temperature, pressure drop, gas concentration, oxidation and gasification carbon consumption rates, burnout, and particle diameter are shown in Fig. IV.B-2 for the Rosebud Lurgi case. The most obvious

TABLE IV.B-1

OPERATING PARAMETERS AND TAR DATA FOR LURGI GASIFIER SIMULATIONS

Coal	Illinois #6	Illinois #5 *	Pittsburgh #8	Rosebud
Type	Bituminous	Bituminous	Bituminous	Subbituminous
Proximate analysis, weight %				
Ash	9.1	8.1	7.7	9.7
Fixed carbon	46.0	44.7	50.3	36.4
Moisture	10.2	11.9	4.6	24.7
Volatile	34.7	35.2	37.4	29.2
Ultimate analysis, weight %				
Carbon	79.5	80.2	84.6	77.1
Hydrogen	5.4	5.4	5.8	4.9
Nitrogen	1.5	1.5	1.6	1.4
Sulfur	3.5	3.9	2.9	1.7
Oxygen	10.1	8.9	5.3	15.0
Operating Parameters				
Chamber diameter, m	3.66	3.66	3.66	3.66
Chamber length, m	3.05	3.05	3.05	3.05
Chamber pressure, kPa	2410	2450	2510	2560
Inlet coal temperature, K	298	298	370	370
Feed gas temperature, K	644	644	644	644
Wall temperature, K	438	438	496	498
Coal mass flow, kg/s	1.67	1.80	1.02	2.23
Oxygen mass flow, kg/s	0.81	0.88	0.63	0.58
Steam mass flow, kg/s	4.20	4.04	3.29	2.80
Jacket steam mass flow, kg/s	0.89	0.73	0.66	0.31
Wall heat loss (jacket steam), MW --	1.00	0.82	1.24	0.58
Wall heat loss (1-D model), MW ---	0.72	0.31	0.27	0.47
Predicted T_{exit}, $T_{equilibrium}$, K	967, 1110	1010, 1180	1090, 1160	760, 1030
Measured T_{fb}, K †	864	908	928	664
Adjusted x° for tar predictions	0.106	0.132	0.0654	0.128
Predicted Tar Data §				
Product tar, kg/s	0.070	0.107	0.054	0.123
Recycle tar, kg/s	0.058	0.068	0.000	0.046
Total Tar, kg/s	0.128	0.175	0.054	0.169
Measured Tar Data †				
Product tar, kg/s	0.070	0.107	0.054	0.123
Recycle tar, kg/s	0.058	0.068	0.000	0.046
Total Tar, kg/s	0.128	0.175	0.054	0.169

* Illinois #5 is reported to be from the same basin as Kentucky #9, and is taken to be equivalent.

-- Calculated from jacket steam flow rate. The jacket steam flow rates are uncertain, and the MBED-1 predictions are assumed to be more accurate.

--- Calculated from the MBED-1 model.

§ Predictions are from the two-zone, partial equilibrium model using adjusted x^o, which requires predicted tar data to be in exact correspondence with measured tar data.

† Measurements are from Elgin and Perks (1974).

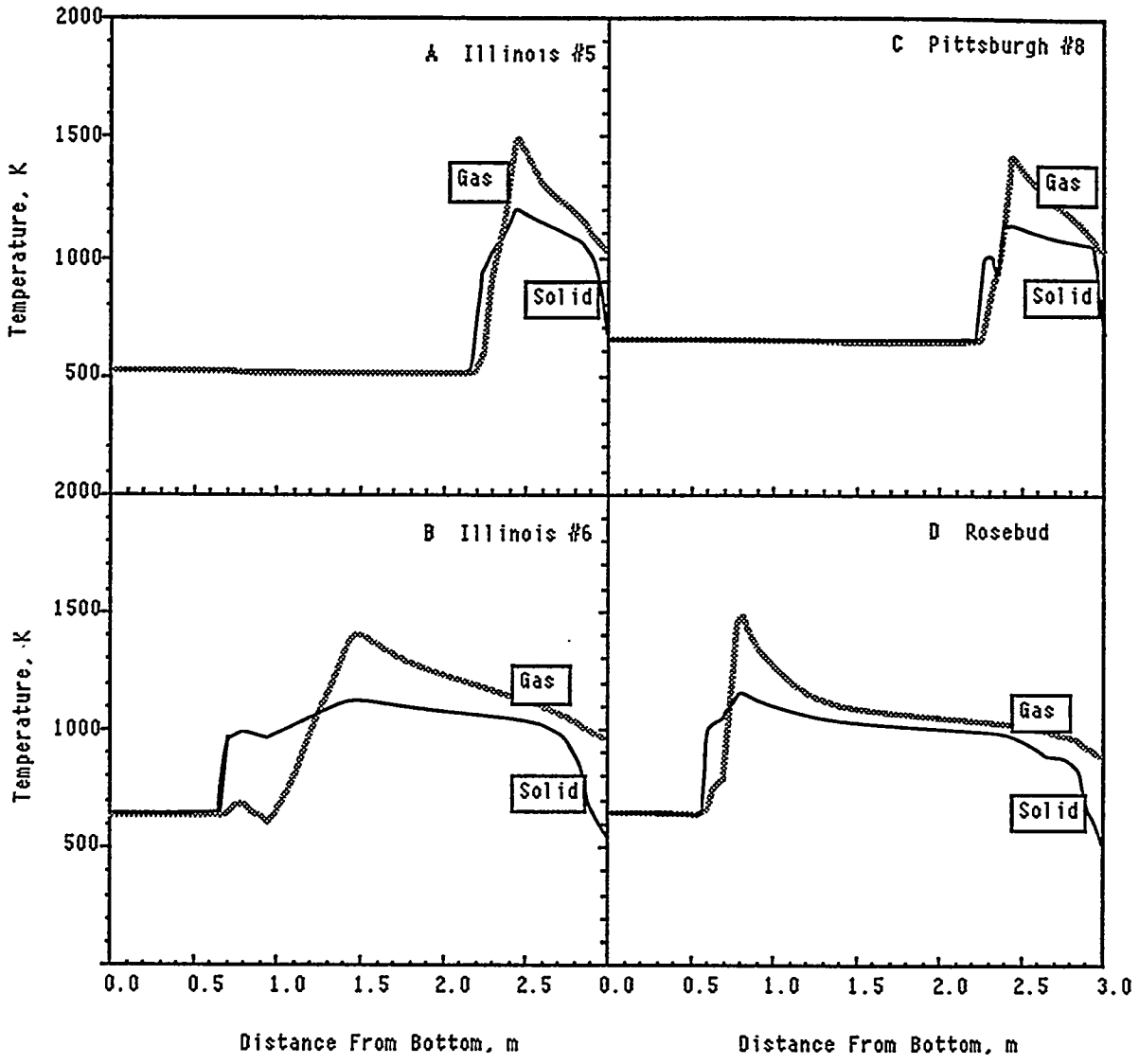

Figure IV.B-1. Predicted axial temperatures for gasification of A) Illinois #5, B) Illinois #6, C) Pittsburgh #8, and C) Rosebud coals in a high pressure, oxygen-blown Lurgi Gasifier. Input parameters given in Table IV.B-1.

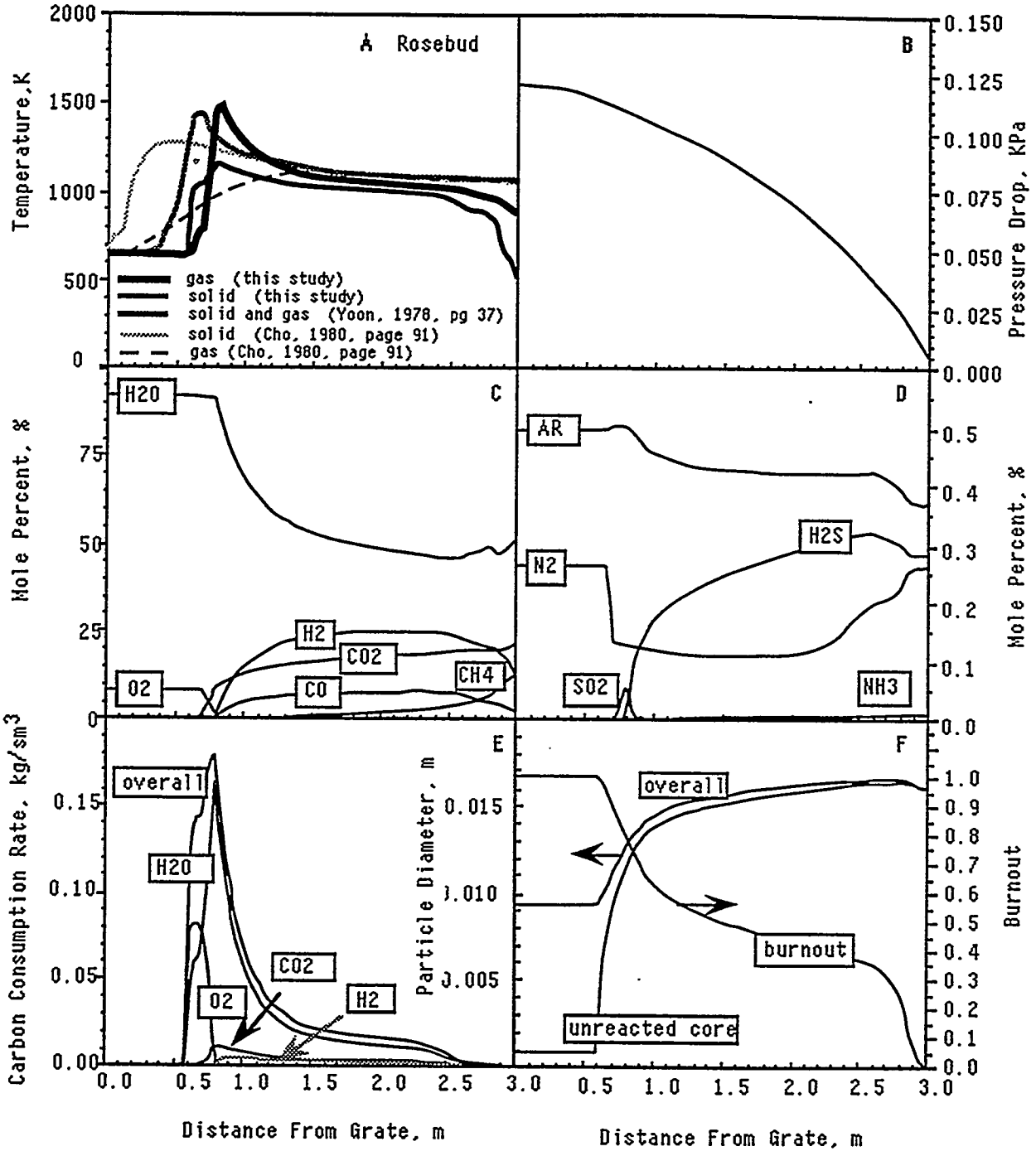

Figure IV.B-2. Predicted axial A) temperature, B) pressure drop, C) major species concentration, D) minor species concentration, E) oxidation/gasification carbon consumption rate, F) burnout, overall and unreacted particle diameter in a high pressure, oxygen-blown Lurgi gasifier with Rosebud subbituminous coal. Input parameters given in Table IV.B-1. Part A shows results from the homogeneous model of Yoon (1978) and the heterogeneous model of Cho (1980).

difference between results from the atmospheric air-blown gasifiers and results from the high- pressure, oxygen-blown Lurgi cases was the absence of a carbon dioxide peak.

The shape of the carbon dioxide profile was due to the low temperature of the solid in the gasification section of the gasifier. The low temperature resulted from large quantities of steam in the feed gas stream. The temperature was low enough that the only significant heterogeneous reaction in this section of the gasifier was the steam gasification reaction. Gasification with carbon dioxide was essentially quenched due to low temperatures. With only hydrogen and carbon monoxide being produced in the gasification section, the hydrogen and carbon monoxide profiles should have corresponded. However, gas phase reactions, such as the water-gas shift reaction, produced a slight increase in carbon dioxide concentration.

Temperature predictions from two other one-dimensional models are also shown in Fig. IV.B-2A. These cases were reported to be the Illinois #6 Westfield case (Yoon, 1978 and Cho, 1980). However, the input conditions were different from that reported by Elgin and Perks (1974) and seemed to be closer to the Rosebud case. The source of Yoon's input data is uncertain. Also, Cho (1980) used the values provided by Yoon (1978). Yoon assumed equal solid and gas temperature, instantaneous devolatilization with a fixed composition, and gas phase chemistry dominated by the water-gas shift reaction. Cho essentially extended the model of Yoon to include separate solid and gas temperatures. The Yoon prediction was similar to the prediction made by the MBED-1 model developed in this project. The shape of the solid temperature profile predicted by Cho is similar to the solid profile predicted here. However, Cho's gas temperature profile does not correspond to either the prediction of Yoon or the prediction made in this project. Cho's gas temperatures were less than the solid temperature in the oxidation zone. The gas temperatures will be less when important gas phase reactions are neglected. For example, steam gasification will produce H_2 and CO in the oxidation zone. Also, CO will be produced from oxidation. In the presence of oxygen, the homogeneous reactions of H_2 and CO with O_2 will react to produce H_2O, CO_2 and heat. These exothermic gas phase reactions will cause a dramatic increase in gas temperature as shown in the predictions presented in this project.

Although all four high pressure Lurgi simulations were converged, results from the Illinois #5 simulation and the Pittsburgh #8 simulation seem to be unrealistic in some respects. For example, both cases predict very large ash zones, on the order of 2 meters. All reactions were predicted to occur near the top of the gasifier. These results were obtained by using the same fixed values for the solid-to-gas heat transfer coefficient and the effective diffusivity as were used by the low pressure Wellman-Galusha cases. If different solid-to-gas heat transfer coefficients had been used for these cases, the length of the ash zone could have been shortened. However, it is not useful to adjust parameters when there are no data for comparison. Also, no pressure profiles were available to check the validity of the bed void distribution assumption.

Medium-Pressure, Air-Blown METC Gasifier - One METC gasifier case was simulated: the gasifier was fired with Arkwright bituminous coal. For this case, the predicted temperature and concentration profiles were compared to the predictions of Desai and Wen (1978).

A comparison of solid and gas temperature profiles and selected gas species profiles for gasification of Arkwright bituminous coal in the air-blown, METC gasifier operated at 6.4 atmospheres (absolute) is shown in Fig. IV.B-3. The input conditions for the METC case were found in Desai and Wen (1978). The solid and gas temperature profiles of Desai and Wen are indistinguishable. Desai and Wen stated that the prediction was the average of the gas and solid temperatures. However, the sample run in the Appendix of Desai and Wen (1978) indicated that the solid and gas temperatures were indeed equal. Desai and Wen did not account for the difference between the nonreacting and reacting solid-to-gas heat transfer. In other words, the correction factor was assumed to equal unity which would give equal solid and gas temperatures as indicated by the sensitivity analysis on the correction factor presented in Subtask 3.b. Desai and Wen's predicted concentration profiles show the instantaneous devolatilization

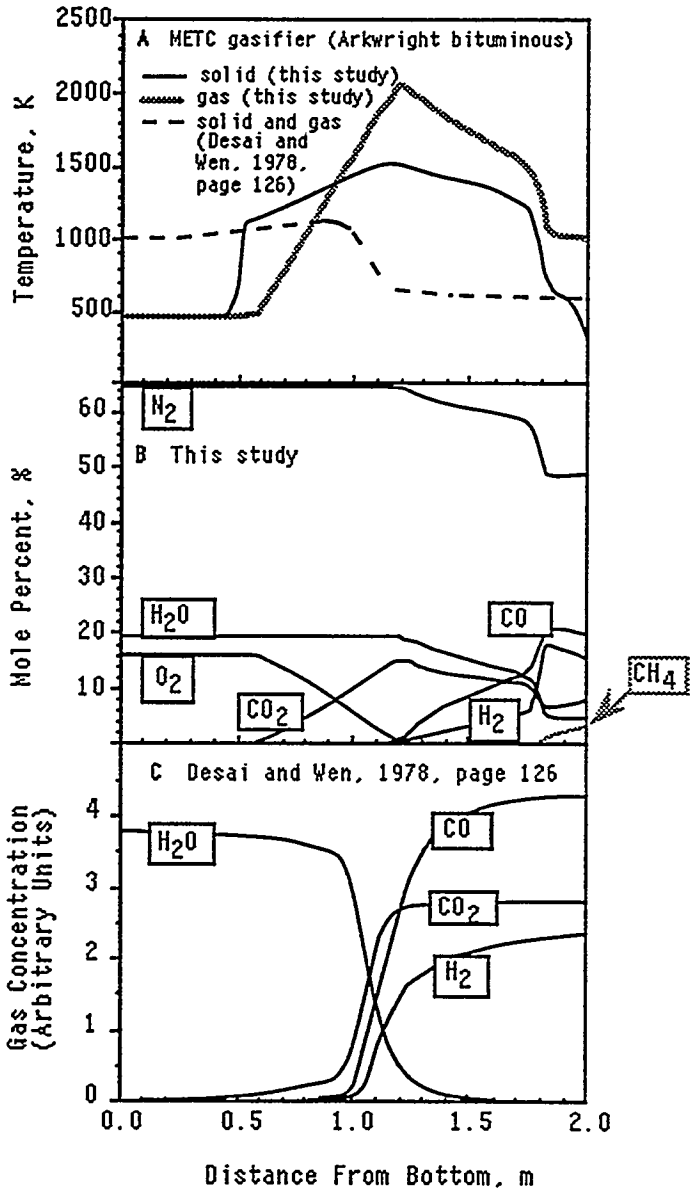

Figure IV.B-3. Comparison of A) solid and gas temperature profiles, and B) selected gas species profiles from this study and C) Desai and Wen (1978) for gasification of Arkwright bituminous coal in the air-blown METC gasifier operated at 6.4 atmospheres (absolute). Input conditions and model predictions from Desai and Wen (1978). Coal, air, and steam mass flow rates are 0.138, 0.518, and 0.0631 kg/s, respectively.

assumption. Also the lack of a peak in the CO_2 profile indicated simplified assumptions regarding the gas phase chemistry. The low gas temperatures also indicated simplified gas phase chemistry. However, since experimental data were not available for comparison, absolute verification of the one-dimension model discussed in this section was not possible.

Application, Documentation, and Implementation of FBED-1 Code

Application

Medium-Pressure, Air-Blown METC Gasifier - The simulation results for the medium-pressure METC gasifier fired with the Arkwright bituminous coal are shown in Fig. IV.B-4. Due to the higher operating pressure, the devolatilization zone is somewhat extended as shown in Fig. IV.B-4E. The oxidation zone is also longer. For this coal, substantial amounts of H_2S and HCN are predicted in the product gas. The pressure drop as predicted in Fig. IV.B-4B is lower as compared with atmospheric units such as the Wellman-Galusha gasifier. The product gas temperature and composition are also compared with the experimental data from Desai and Wen (1978) and shown in Fig. IV.B-5. A comparison of the predicted profiles for the temperature and pressure could not be made due to the lack of experimental profiles. The feed gas temperature and composition are satisfied exactly. The comparison between the predicted and reported composition of the product gas if fair. It is noted that due to the uncertainty in the experimental values, both the average values and the ranges were reported. The observed ranges for some selected species are shown in Table IV.B-2. A comparison of the predictions, on dry-basis, and the experimental ranges shows that the predicted composition of the product gas is in reasonable agreement with the reported ranges.

The predicted values for the wall heat loss and the product tar flow rate do not compare well with the experimental values. The experimental heat loss has actually been computed from an energy balance and is not reliable.

High-Pressure, Air-Blown, PyGas™ Staged Gasifier - The proprietary CRS Sirrine Engineers, Inc. PyGas™ staged gasifier is the gasifier to be developed under the Gasification Product Improvement Facility (GPIF) program. DOE/METC selected the PyGas™ gasifier for the application of the advanced fixed-bed code, FBED-1. The existing fixed bed technology is not well suited for caking coals due to agglomeration problems which lead to low conversion efficiencies. The PyGas™ staged gasification process was specifically designed to facilitate the handling of caking coals. A schematic of the PyGas™ staged gasifier is shown in Figure IV.B-6. The process is carried out in four stages: (1) The coal is rapidly pyrolyzed in a transport or bubbling fluidized bed portion of the gasifier. The heating rates in the pyrolyzer are such that the tars are liberated in gaseous form rather than in liquid form. This eliminates agglomeration of the coal particles initiated by coating of the particle surface by liquid tars. The temperature at the exit of the pyrolyzer is around 1150 K; (2) The gas and the char are separated in the freeboard zone due to gravity. Additional air is added to the freeboard zone to cause gas phase cracking of the tars and the higher hydrocarbons generated in the pyrolyzer. The amount of additional air is adjusted to attain temperatures high enough (around 1500 K) to initiate the gasification of the char; (3) The char is then gasified in a cocurrent fixed bed portion of the gasifier. Only part of the char is converted by the endothermic gasification reactions during this stage. This cools down the gas stream to around 1100 K and the gasification reactions are diminished; (4) The char is burnt completely in a countercurrent fixed bed. Additional quantities of air and steam are added at the bottom of the countercurrent fixed bed. The final product gas is the combined stream from the exits of the cocurrent and countercurrent stages of the gasification process and its temperature is around 1100 K. The gasifier is operated at 4240 kPa.(41.8 atm), coal throughput is 5440 kg/h (12000 lb/hr), and air and steam are preheated to 755 K (900 F). The overall diameter of the gasifier is 2.44 m (8 ft) and the diameter of the pyrolyzer section is 0.61 m (2 ft). The approximate lengths of the upper and the lower fixed bed zones are 4.6 m (15 ft) and 1.5 m (5 ft) respectively. The flow rates of air and steam to the pyrolyzer are about 0.9 kg air/kg of coal and 0.4 kg steam/kg of coal respectively. The design data above were provided by DOE/METC.

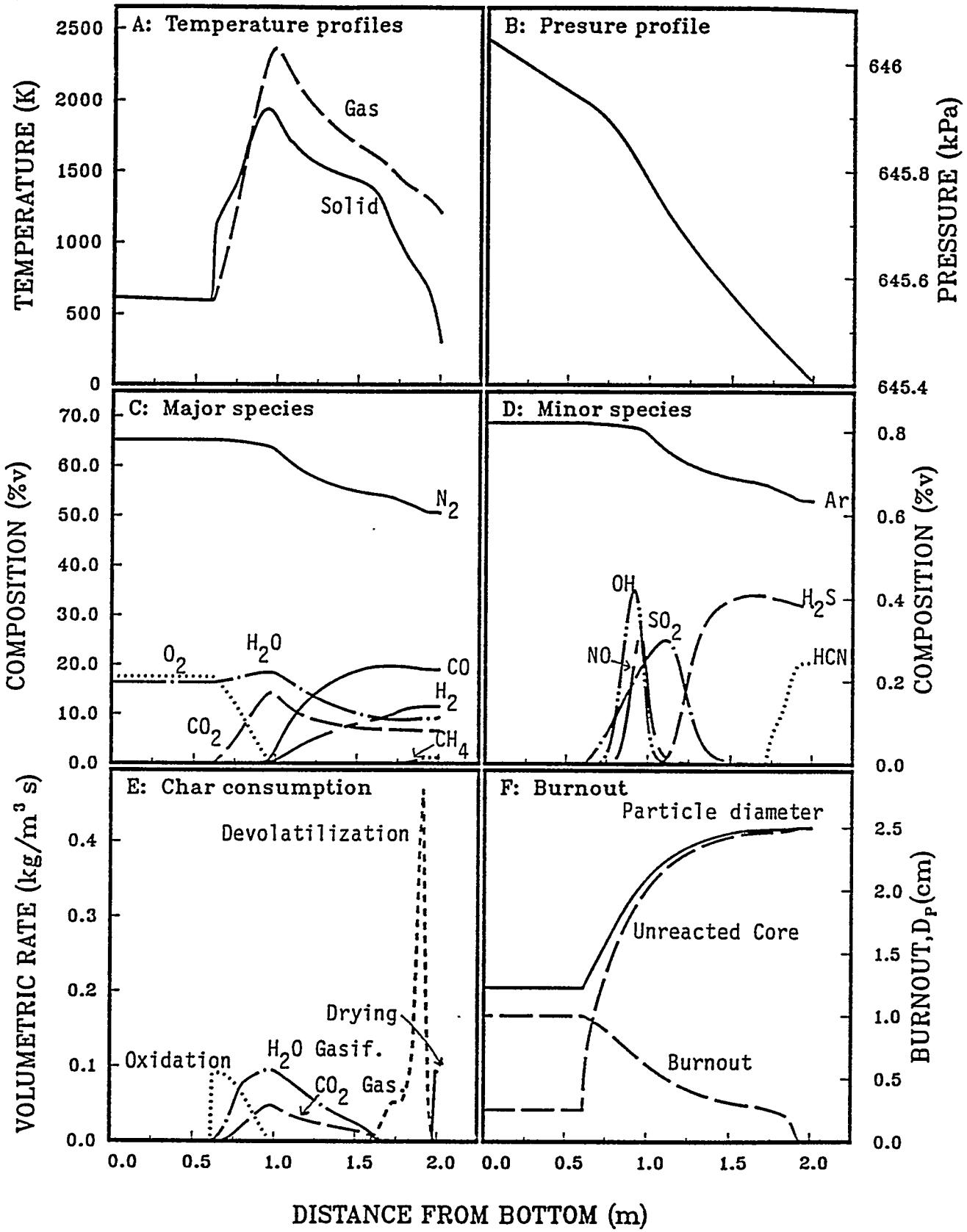

Figure IV.B-4. Predicted axial A) temperature, B) pressure, C) major species composition, D) minor species composition, E) volumetric char consumption rate, F) burnout and overall particle and unreacted particle diameter in a medium-pressure METC gasifier fired with the Arkwright bituminous coal.

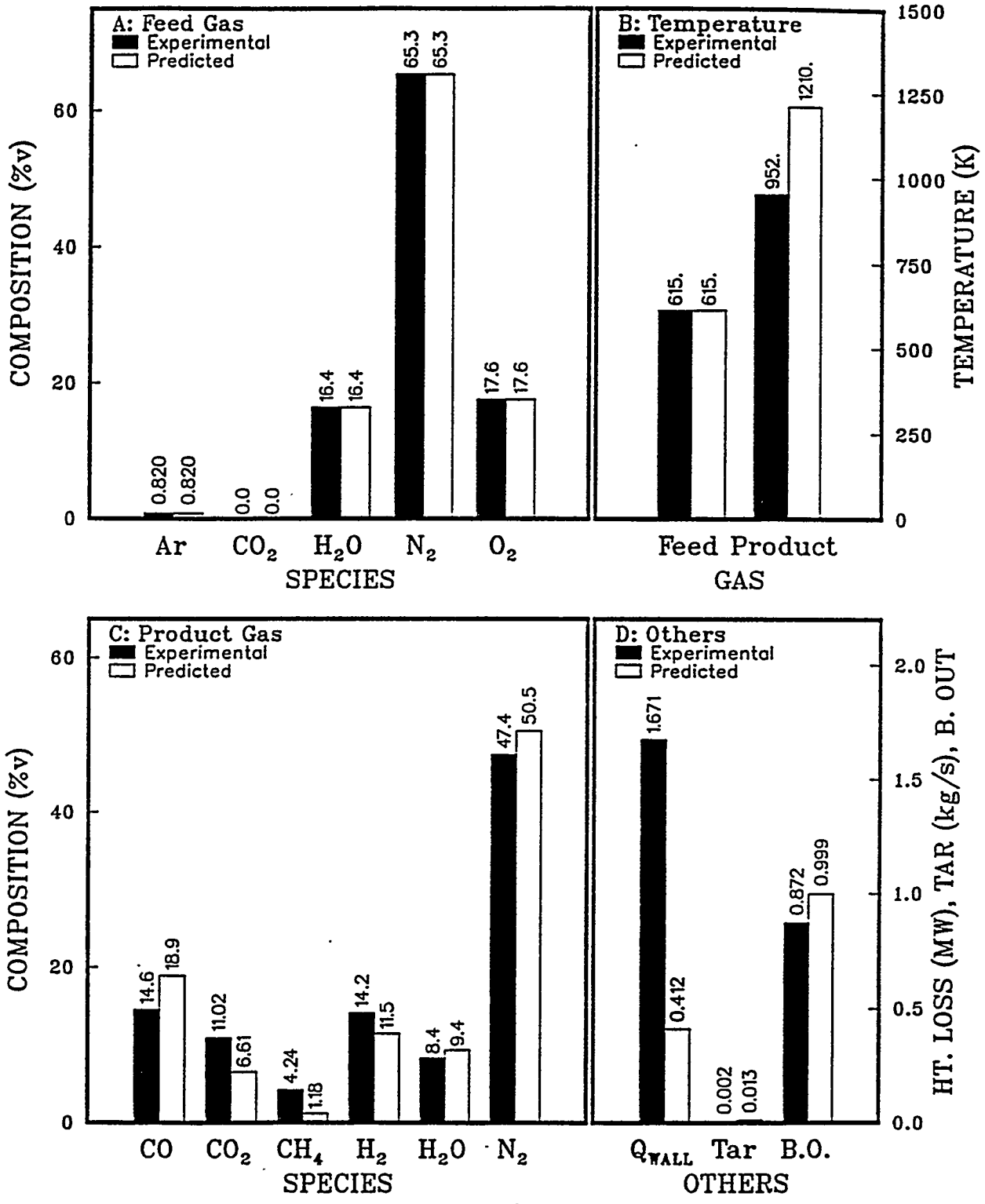

Figure IV.B-5. Comparison of the predicted and experimental results for a medium-pressure METC gasifier fired with the Arkwright bituminous coal. Experimental data are from Desai and Wen (1978).

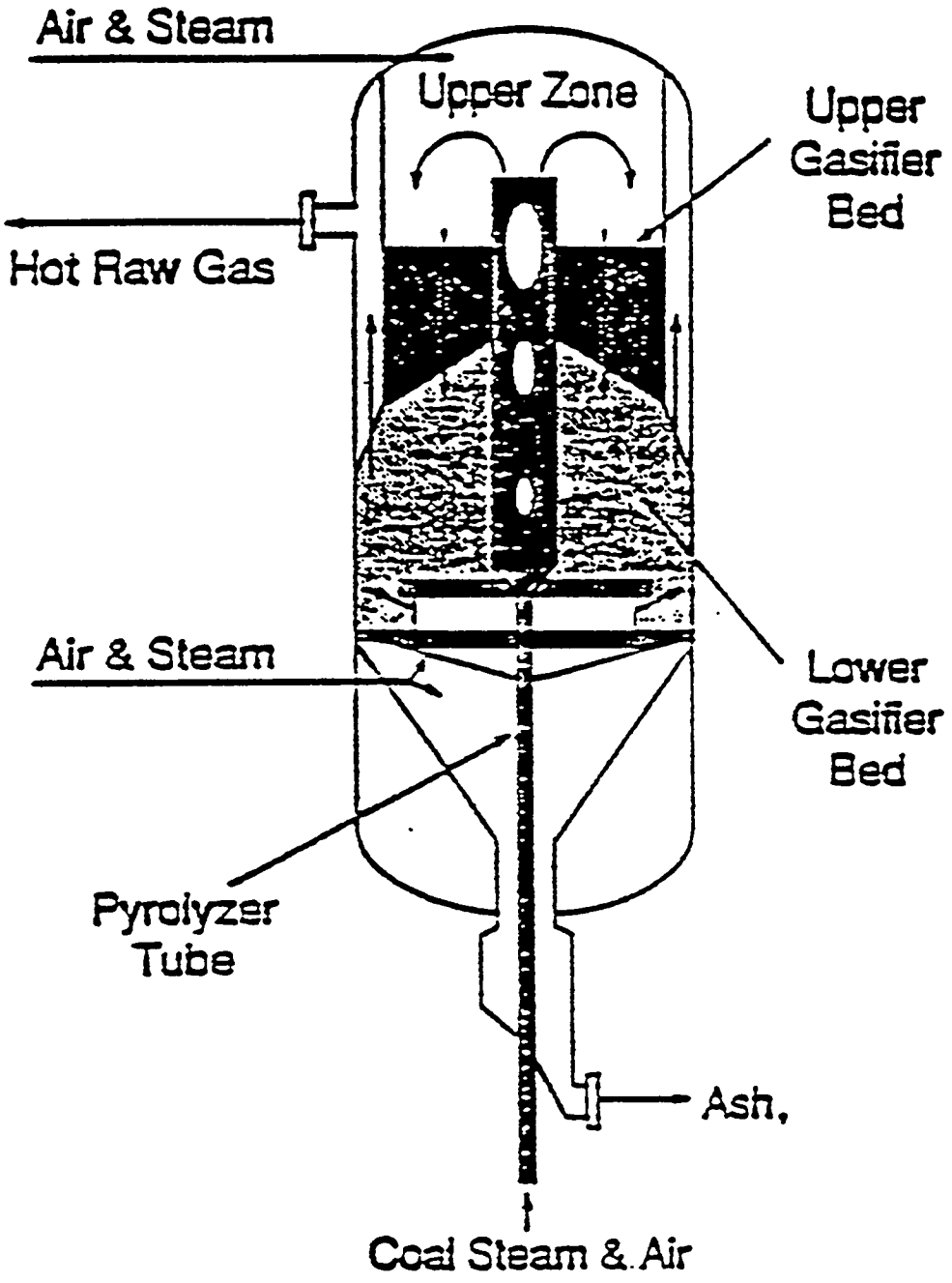

Figure IV.B-6. Schematic of the high-pressure, air-blown PyGas™ staged gasifier (Johnson and Schmidt, 1993).

TABLE IV.B-2

DRY PRODUCT GAS COMPOSITION IN A METC GASIFIER

Species	Experimental Range (%v)	Predicted Composition (%v)
CO	16.0 - 23.0	20.86
CO_2	7.0 - 12.0	7.30
CH_4	2.0 - 3.5	1.30
H_2	13.0 - 17.0	12.69
N_2	48.0 - 55.0	55.74

The assumptions made for the simulation of the PyGas™ staged gasifier are: (1) The solid residence time in the pyrolyzer is assumed to be long enough to allow complete devolatilization of coal. The feed coal is assumed to enter the pyrolyzer at room temperature and both the oxidant and the steam streams are taken to be at 755 K; (2) The amount of additional air fed to the freeboard zone is adjusted to allow complete cracking of the tars and to raise the temperature of the gas phase to about 1530 K. The solid residence times in the freeboard zone are assumed to be too small to allow any significant heat transfer between the solid and the gas phases and any heterogeneous reactions; (3) The amount of char consumed in the cocurrent, fixed-bed stage of the process is just sufficient to lower the temperature of the exit gas to about 1100 K; (4) The char is assumed to be completely burned in the countercurrent fixed bed portion of the gasifier. The flow rates of air and steam are adjusted to achieve complete conversion of char and to obtain the gas temperature close to 1100 K. The length and equivalent diameter of the countercurrent, fixed-bed are taken to be 1.524 m and 2.361 m respectively.

The pyrolyzer was simulated by using the zero-dimensional submodel of the fixed bed code. It is pointed out that devolatilization is based on the FG-DVC submodel; thus, the elemental composition of the product tar and char are predicted. The gas composition was computed assuming partial equilibrium by keeping tar out of chemical equilibrium. In the freeboard zone, the composition was computed by taking into account the supplementary air feed and allowing the tar to react to equilibrium. The temperature and the composition of the gas phase at the exit of the cocurrent, fixed-bed portion was also computed by assuming complete chemical and thermal equilibrium. The simulation of the final countercurrent fixed-bed portion was performed using the one-dimensional fixed-bed code, FBED-1. The zero-dimensional submodel, FBED-0, was used to provide the initial guesses for the effluent gas composition and temperature. The input composition and flow rate of char to the lower fixed bed was adjusted to reflect the conversion during the previous stages of the gasifier.

The predicted results for the PyGas™ staged gasifier simulation are presented in Tables IV.B-3 and IV.B-4. Table IV.B-3 shows the ultimate composition and proximate analysis of char entering and leaving the pyrolyzer. Table IV.B-4 shows the gas phase composition and temperature at various stages of the gasification process. About 40% of coal mass is devolatilized in the pyrolyzer. The product gas is rich in H_2 but the amount of CO is rather small. About 8.5% of coal mass is evolved as tar. The pyrolyzer gas is at 1275 K. The addition of air in the freeboard zone and the reactions of the tar and the higher hydrocarbons generated in the pyrolyzer section increase the gas temperature to 1530 K. The amounts of CO and CO_2 are also increased. In the upper fixed bed, 62.5% of the remaining char is consumed by the endothermic gasification reactions. This lowers the gas temperature to 1086 K. Large quantities of CO and CH_4 are observed. This is as expected since CH_4 is favored at high pressure. Finally, the char is completely burnt in the lower fixed bed. The gas temperature of the product stream is 1090 K. The amounts of CO are large which is consistent with the smaller amount of oxygen available for the oxidation reaction. It is also observed that the char undergoes a secondary devolatilization process. The quantities of tar generated, however, are negligible. The predicted results show a very short reactive zone and an extended ash zone.

TABLE IV.B-3
FEED COAL AND PRODUCT CHAR COMPOSITION

	Feed Coal	Product Char
Proximate Analysis (%w)		
Fixed Carbon	0.5486	0.5729
Volatile Matter	0.2982	———
Moisture	0.0181	———
Ash	0.1441	0.4271
Ultimate Analysis (DAF, %w)		
C	0.8239	0.9678
H	0.0535	0.0155
O	0.0595	0.0
N	0.0150	0.0012
S	0.0117	0.0155

TABLE IV.B-4
FLOW RATES AND COMPOSITIONS FOR PYGAS™ GASIFICATION PROCESS

	Pyrolyzer	Freeboard	Upper Gasifier	Lower Gasifier	Product Gas
Coal, kg/s	1.5117	0.7790	0.7790	0.2921	
T_{coal}, K	298	———	———	550	
Air, kg/s	1.2093	1.1000	———	0.99	
Tar, K	755	755	———	755	
Steam, kg/s	0.5140	———	———	0.20	
T_{Steam}, K	755	———	———	755	
Product Gas, kg/s	2.0619	3.3382	3.8250	1.4917	5.3167
Composition, %v					
Ar	0.41	0.54	0.49	0.53	0.50
CO	4.10	9.87	21.88	35.50	25.75
CO_2	5.85	6.70	8.70	1.72	6.72
CH_4	0.01	0.0	9.28	1.33	7.02
H_2	16.81	13.98	14.34	16.90	15.07
H_2O	39.52	25.62	5.48	1.45	4.33
N_2	33.28	43.22	39.56	42.31	40.34
O_2	0.0	0.0	0.0	0.0	0.0
T,K	1275	1533	1086	1090	1087
Tar, kg/s	0.1763	0.0	0.0	0.0	0.01

The profiles for the reactive zone are shown in detail in Figure IV.B-7. This suggests that much shorter lengths of the lower fixed bed may be used in a staged gasification process. It is, however, pointed out that the combustion and gasification kinetic parameters used in our simulation were rank-independent and were obtained for atmospheric conditions. Recently, Monson (1992) conducted experiments at pressures up to 15 atmospheres to study the effect of pressure on kinetic parameters. His results suggest that the oxidation and gasification kinetic rates may be an order of magnitude lower at higher pressure when the pressure dependence is expressed by a power law. The effect of pressure on kinetic parameters was, however, found to be non-linear. Therefore, extrapolation of Monson's (1992) results to the operating pressure of PyGas™ gasifier, 41.8 atm, was not attempted. Incorporation of pressure- dependent, kinetic parameters may yield longer reactive zone.

Table IV.B-5 provides the overall and elemental mass balances. The overall and elemental mass balances close reasonably well.

Documentation and Implementation

The final version of the fixed-bed code, FBED-1 includes the functional group-depolymerization, vaporization, and crosslinking submodel, FG-DVC. A user's manual for FBED-1 was prepared and presented as Volume III of this final report. The manual consists of two parts. The first part includes the model formulation and the solution procedure whereas the second part includes the user's and the implementation guides as well as the sample problem. The code was ported to a Silicon Graphics workstation and the sample case was successfully executed. The sample case was for the Wellman-Galusha gasifier fired with Jetson bituminous coal. The code, the user's manual, and the installation instructions were sent to METC. A short course on the use of the FBED-1 code was conducted at METC.

Summary and Conclusions

The fixed-bed coal combustion, gasification, and devolatilization codes, MBED-1 and FBED-1, developed in Subtask 3.b, were successfully demonstrated by simulating the four dry-ash, fixed-bed gasifiers of interest to METC: the high-pressure, oxygen-blown Lurgi gasifier, the medium-pressure, air-blown METC gasifier, the atmospheric-pressure, air-blown Wellman-Galusha gasifier, and the high-pressure, air-blow, PyGas™ staged gasifier. The most comprehensive test data, including the temperature and the pressure profiles, were available for the atmospheric-pressure Wellman-Galusha gasifier. The Wellman-Galusha test data were used to validate the fixed-bed codes and the corresponding simulations were presented in Subtask 3.b. The simulations of the high-pressure Lurgi gasifier, the medium-pressure METC gasifier, and the high-pressure, air-blow, PyGas™ staged gasifier were presented as part of this subtask.

The user's manual was prepared for the FBED-1 code. The code was ported to a Silicon Graphics workstation and the sample case was successfully executed. The code, the user's manual, and the installation instructions were sent to METC. A short course on the use of the FBED-1 code was conducted at METC.

TABLE IV.B-5

OVERALL AND ELEMENTAL MASS BALANCE*

	INPUT								OUTPUT			
		Pyrolyzer		Freeboard		Fixed-bed						
	Coal	Steam	Air	Steam	Air	Steam	Air	Total	Char	Tar	Gas	Total
C	1.0435	—	—	—	—	—	—	1.0435	0.0001	0.0103	1.0527	1.0631
H	0.0708	0.0575	—	—	—	0.0224	—	0.1507	0.0	0.0002	0.1509	0.1511
O	0.1458	0.4565	0.2804	—	0.2551	0.1776	0.2296	1.5450	0.0	0.0	1.5449	1.5449
N	0.0190	—	0.9126	—	0.8300	—	0.7470	2.5086	0.0	0.0	2.5087	2.5087
S	0.0148	—	—	—	—	—	—	0.0148	0.0	0.0002	0.0149	0.0151
Ar	—	—	0.0163	—	0.0149	—	0.0134	0.0446	—	—	0.0446	0.0446
Ash	0.2178	—	—	—	—	—	—	0.2178	0.2178	—	—	0.2178
Total	1.5117	0.5140	1.2093	—	1.1000	0.2000	0.9900	5.5250	0.2179	0.0107	5.3167	5.5453

*All values are in kg/s.

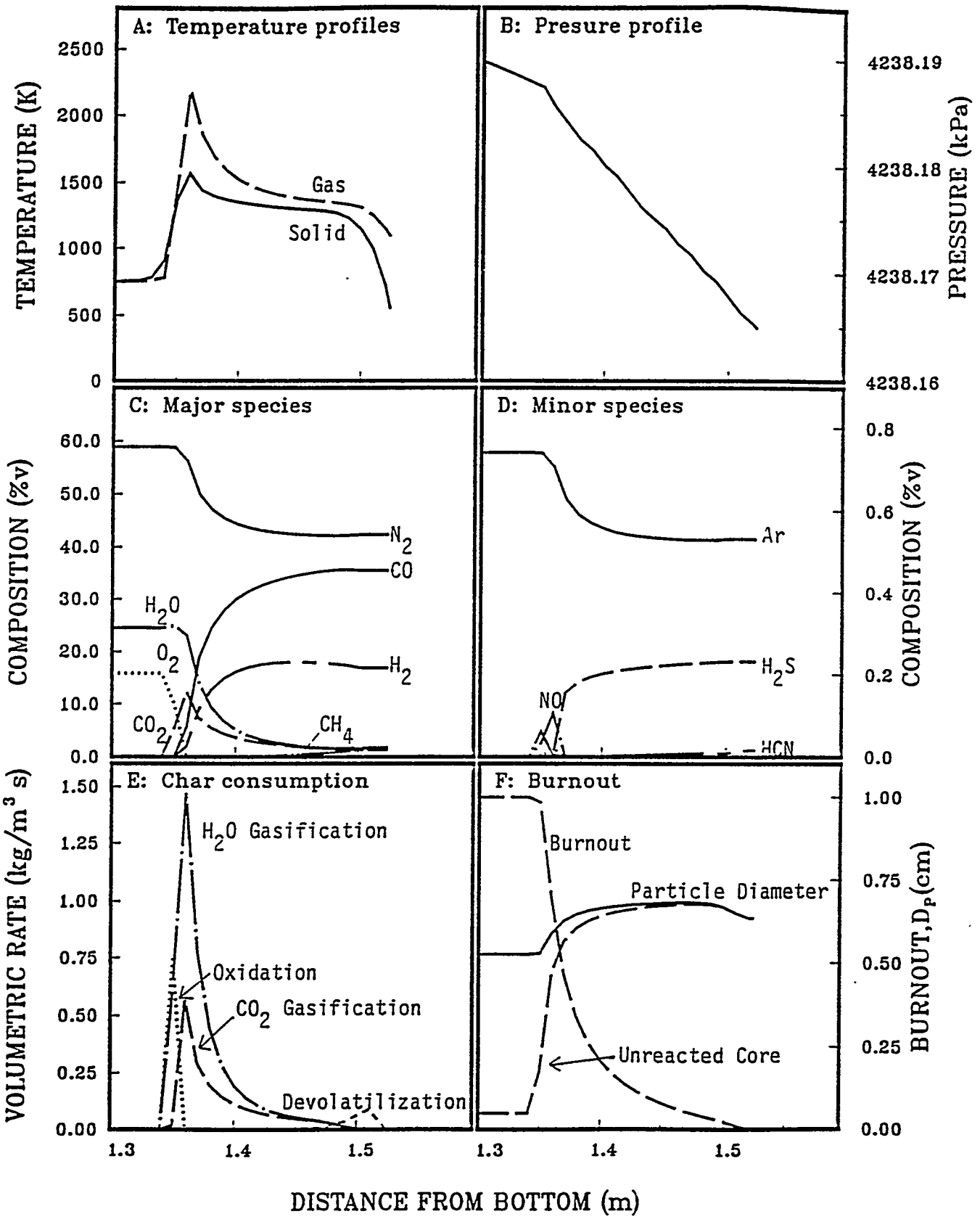

Figure IV.B-7. Predicted axial profiles for reactive zone of the lower fixed bed of the PyGas™ staged gasifier.

References for Subtask 4.b.

Cho, Y.S., Modeling and Simulation of Lurgi-Type Gasifier, M.S. Thesis, Washington University, St. Louis, MO (1980).

Desai, P.R. and Yen, C.Y., Computer Modeling of the MERC Fixed Bed Gasifier, Report for the U.S. Department of Energy, Morgantown Energy Research Center, Morgantown, WV, West Virginia University, Morgantown, WV, Contract No. EY-760S-21-8039, MERC/CR-7813 (1978).

Elgin, D.C. and Perks, H.R., Results of Trials of American Coals in Lurgi Pressure-Gasification Plant at Westfield, Scotland, proceedings of the Sixth Synthetic Pipeline Gas Symposium, Chicago, 247 (1974).

Johnson, R. and Schmidt, D., Gas Product Improvement Facility (GPIF), information flyer, Morgantown Energy Technology Center, U.S. Department of Energy, Morgantown, WV (1993).

Monson, C.R., Char Oxidation of Elevated Pressures, Ph.D. Dissertation, Department of Mechanical Engineering, Brigham Young University, Provo, UT (1992).

Yoon, H., Wei, J. and Denn, M.M., A Model for Moving-Bed Coal Gasification Reactors, AIChE Journal, 24, 885 (1978).

APPENDIX A

Papers and/or Publications Resulting from DOE Contract No. DE-AC21-86MC23075 (1986-1993)

AFR Papers and Publications

1. Bassilakis, R., Serio, M.A., and Solomon, P.R., Sulfur and Nitrogen Evolution in The Argonne Coals, ACS Div. of Fuel Chem. Preprints, **37**, (4), 1712, (1992).

2. Bassilakis, R., Zhao, Y., Solomon, P.R. and Serio, M.A., Sulfur and Nitrogen Evolution in the Argonne Coals: Experiment and Modeling, Energy & Fuels, **7**, 710, (1993).

3. Carangelo, R.M., Serio, M.A., Solomon, P.R., Charpenay, S., Yu, Z.Z., and Bassilakis, R., Coal Pyrolysis: Measurements and Modeling of Product Evolution Kinetics and Char Properties, ACS Div. of Fuel Chem. Preprints, **36** (2), 796, (1991).

4. Charpenay, S., Serio, M.A., and Solomon, P.R., The Prediction of Coal Char Reactivity under Combustion Conditions, 24th Symposium (Int) on Combustion, The Combustion Institute, Pittsburgh, PA, 1189-1197 (1992).

5. Charpenay, S., Serio, M.A., Teng, H., and Solomon, P.R., The Influence of Char Structure on Low Temperature Combustion Reactivity, ACS Div. of Fuel Chem Preprints, **37** (4), 1937, (1992).

6. Charpenay, S., Serio, M.A., and Solomon, P.R., A General Model for Prediction of Char Oxidation Reactivity, proceedings of the Int. Conf. on Coal Science, Alberta, Canada, **II** (189), (1993).

7. dela Rosa, L., Pruski, M., Lang, D., Gerstein, B., and Solomon, P.R., Characterization of the Argonne Premium Coals by Using ^{1}H and ^{13}C NMR and FT-IR Spectroscopies, Energy and Fuels, **6**, 460, (1992).

8. Hamblen, D.G., Yu, Z.Z., Charpenay, S., Serio, M.A., and Solomon, P.R., Comparison of Percolation Theory and Monte Carlo Method Applied to Network Statistics for Coal Pyrolysis, proceedings of the Int. Conf. on Coal Science, Alberta, Canada, **II** (401), (1993).

9. Khan, M.R., Serio, M.A., Malhotra, R., and Solomon, P.R., A Comparison of Liquids Produced from Coal by Rapid and Slow Heating Pyrolysis Experiments, ACS Div. of Fuel Chem. Preprints, **34**, (4), 1054, (1989).

10. Markham, J.R., Zhang. Y.P., Carangelo, R.M., and Solomon, P.R., FT-IR Emission/Transmission Tomography of a Coal Flame, 23rd Symposium (Int) on Combustion, The Combustion Institute, pp 1869-1875, (1990).

11. Serio, M.A., Solomon, P.R., and Carangelo, R.M., Pyrolysis of the Argonne Premium Coals under Slow Heating Conditions, ACS Div of Fuel Chem. Preprints **33**, (2), 295, (1988).

12. Serio, M.A., Solomon, P.R., Yu, Z.Z., Desphande, G.V., and Hamblen, D.G., Pyrolysis Modeling of Argonne Premium Coals, ACS Div. of Fuel Chem. Preprints, **33**, (3), 91, (1988).

13. Serio, M.A., Solomon, P.R., Bassilakis, R., and Suuberg, E.M., The Effects of Minerals and Pyrolysis Conditions on Char Gasification Rates, ACS Div. of Fuel Chem. Preprints, **34**, (1), 9, (1989).

14. Serio, M.A., Solomon, P.R., Bassilakis, R., and Suuberg, E.M., The Effects of Minerals on Coal Reactivity, Int. Conference on Coal Science Proceedings, IEA, Tokyo, Japan, p. 341, (October 23-

27, 1989).

15. Serio, M.A., Solomon, P.R., Yu, Z.Z., and Deshpande, G.V., An Improved Model of Coal Devolatilization, Int. Conference on Coal Science Proceedings, IEA, Tokyo, Japan, p. 209, (October 23-27, 1989).

16. Serio, M.A., Solomon, P.R., Yu, Z.Z., Bassilakis, R., The Effect of Rank on Coal Pyrolysis Kinetics, ACS Div. of Fuel Chem. Preprints, **34**, (4), 1324, (1989).

17. Serio, M.A., Solomon, P.R., Charpenay, S., Yu, Z.Z., and Bassilakis, R., Kinetics of Volatile Product Evolution from the Argonne Premium Coals, ACS Div of Fuel Chem. Preprints, **35**, (3), 808, (1990).

18. Serio, M.A., Solomon, P.R., Yang, Y.P., and Suuberg, E.M., The Use of TG-FTIR Analysis to Determine Char Combustion Properties, presented at the AIChE Annual Meeting, Chicago, IL, (Nov. 11-16, 1990).

19. Serio, M.A., Solomon, P.R,. Yu, Z.Z., and Charpenay, S., Modeling of Mild Gasification Processes, proceedings of the 8th Annual Int. Pittsburgh Coal Conference, pp 183-188, (Oct. 14-18, 1991).

20. Serio, M.A., Zhao, Y., Wójtowicz, M.A., Charpenay, S., and Solomon, P.R., Modeling of Coal Quality Effects Based on a Comprehensive Devolatilization Model, presented at the EPRI - Sponsored Fourth Int. of Conf. on the Effects of Coal Quality on Power plants, Charleston, S.C., Aug. 17-19, 1994.

21. Solomon, P.R., Chien, P.L., Carangelo, R.M., Best, P.E., and Markham, J.R., Application of FT-IR E/T Spectroscopy to Study Coal Combustion Phenomena, paper presented at the Int. Coal Combustion Symposium, Beijing, China, (1987).

22. Solomon, P.R. and Carangelo, R.M., FT-IR Analysis of Coal 2. Aliphatic and Aromatic Hydrogen Concentration, Fuel, **67**, 949, (1988).

23. Solomon, P.R., Chien, P.L., Carangelo, R.M., Best, P.E., and Markham, J.R., Application of FT-IR Emission/Transmission (E/T) Spectroscopy to Study Coal Combustion Phenomena, The 22nd Symposium (Int) on Combustion, The Combustion Institute, Pittsburgh, PA, p. 211, (1988).

24. Solomon, P.R., Hamblen, D.G., Carangelo, R.M., Serio, M.A., and Deshpande, G.V., A General Model of Coal Devolatilization, Energy and Fuel, **2**, 405, (1988).

25. Solomon, P.R., Hamblen, D.G., Carangelo, R.M., Serio, M.A. and Deshpande, G.V., Models of Tar Formation During Coal Devolatilization, Combustion and Flame, **71**, 137, (1988).

26. Solomon, P.R., Best, P.E., Markham, J.R., and Klapheke, J., The Study of Coal Flames using FT-IR Emission/Transmission Tomography, Int. Conference on Coal Science Proceedings, IEA, Tokyo, Japan, p. 329, (October 23-27, 1989).

27. Solomon, P.R., Serio, M.A., and Carangelo, R.M., Coal Analysis by TG-FTIR, Int. Conference on Coal Science Proceedings, IEA, Tokyo, Japan, p. 67, (October 23-27, 1989).

28. Solomon, P.R., Serio, M.A., and Markham, J.R., Kinetics of Coal Pyrolysis, Int. Conference on Coal Science Proceedings, IEA, Tokyo, Japan, p. 575, (October 23-27, 1989).

29. Solomon, P.R., Can Coal Science be Predictive, paper presented at the Fourth Annual Australian Coal Science Conf., Brisbane, Australia, (Dec. 3-5, 1990).

30. Solomon, P.R., Chien, P.L., Carangelo, R.M., Serio, M.A., and Markham, J.R., New Ignition Phenomenon in Coal Combustion, Combustion & Flame, **79**, 214, (1990).

31. Solomon, P.R., Fletcher, T.H., and Pugmire, R.J., Progress in Coal Pyrolysis, Proceedings of the Pittsburgh Coal Conference, pp. 3-12, (Sept. 10-14, 1990).

32. Solomon, P.R., Hamblen, D.G., Yu, Z.Z., and Serio, M.A., Network Models of Coal Thermal Decomposition, Fuel, **69**, 754, (1990).

33. Solomon, P.R., Markham, J.R., Zhang, Y.P., and Carangelo, R.M., FT-IR Emission/Transmission Tomography of Coal Flames, ACS Div. of Fuel Chem. Preprints, **35**, (3), 746, (1990).

34. Solomon, P.R., Markham, J.R., Zhang, Y.P., Carangelo, R.M., Brewster, B.S., and L.D. Smoot, The Study of a Coal Flame by FT-IR Emission/Transmission Tomography and Comprehensive Modeling, Sci - Mix Poster Session, American Chemical Society, Meeting, Washington, DC (1990).

35. Solomon, P.R., Serio, M.A., Carangelo, R.M., Bassilakis, R., Gravel, D., Baillargeon, M., Baudais, F., and Vail, G., Analysis of the Argonne Premium Coal Samples by TG-FTIR", Energy & Fuels, **4**, (3), 319, (1990).

36. Solomon, P.R., Serio, M.A., Hamblen, D.G., Yu, Z.Z., and Charpenay, S., Advances in the FG -DVC Model of Coal Devolatilization, ACS Div. of Fuel Chem. Preprints, **35**, (2), 479, (1990).

37. Solomon, P.R., Serio, M.A., Deshpande, G.V., and Kroo, E., Crosslinking Reactions During Coal Conversion, Energy & Fuels, **4**, (1), 42, (1990).

38. Solomon, P.R. and Best, P.E., Fourier Transform Infrared Emission/Transmission Spectroscopy in Flames, in *Combustion Measurements*, (N. Chigier, Ed.), Hemisphere Publishing Corp., pp. 385-344, (1991).

39. Solomon, P.R., Charpenay, S., Yu, Z.Z., Serio, M.A., Kroo, E., Solum, M.S., and Pugmire, R.J., Network Changes During Coal Pyrolysis: Experiment and Theory, presented at the 1991 Int. Conf. on Coal Science, New Castle, England, (Sept. 1991).

40. Solomon, P.R., Hamblen, D.G., Serio, M.A., Yu, Z.Z., Charpenay, S., Can Coal Science be Predictive, Storch Award Symposium Lecture, ACS Div. of Fuel Chemistry Preprints, **36** (1) 267, (1991).

41. Solomon, P.R., Serio, M.A., Carangelo, R.M., Bassilakis, R., Yu, Z.Z., Charpenay, S., and Whelan, J., Analysis of Coal by TG-FTIR and Pyrolysis Modeling, presented at the Pyrolysis '90 Meeting in Holland, June 1990, also published in Journal of Analytical and Applied Pyrolysis, **19**, 1, (1991).

42. Solomon, P.R., On-Line Fourier Transform Infrared Spectroscopy in Coal Research, in *Advances in Coal Spectroscopy*, (H.L.C. Meuzelaar, Ed.), Plenum Publishing Corp., pp 341 - 371, (1992).

43. Solomon, P.R., Best, P.E., Yu, Z.Z., and Charpenay, S., An Empirical Model for Coal Fluidity Based on a Macromolecular Network Pyrolysis Model, Energy & Fuel, **6**, 143, (1992).

44. Solomon, P.R., Serio, M.A., and Suuberg, E.M., Coal Pyrolysis: Experiments, Kinetic Rates, and Mechanisms, Progress in Energy and Combustion Science, **18**, pp 133-220, (1992).

45. Solomon, P.R., Fletcher, T.H., and Pugmire, R.J., Progress in Coal Pyrolysis, Fuel, **72**, (5), 587, (1993).

46. Solomon, P.R., Hamblen, D.G., Serio, M.A., Yu, Z.Z., and Charpenay, S., A Characterization Method and Model for Predicting Coal Conversion Behavior, Fuel, **72** (4), 469, (1993).

47. Solomon, P.R., and Fletcher, T.H., Impact of Coal Pyrolysis on Combustion, 25th Symposium (Int.) on Combustion, The Combustion Institute, pp. 463-474, (1994).

48. Solomon, P.R., and Serio, M., Progress in Coal Pyrolysis Research, ACS Div. of Fuel Chem., Preprints, 39, (1), 69, (1994).

49. Wójtowicz, M.A., Zhao, Y., Serio, M., Bassilakis, R., Solomon, P.R., and Nelson, P.F. Modeling of Nitrogen Evolution from Coal During Flash Pyrolysis, paper submitted to the 25th Symposium (Int.) on Combustion, (1993).

50. Zhao, Y., Serio, M.A., and Solomon, P.R., A Piori Simulation of Coal Pyrolysis Experiments Based on Coal Elemental Compositions, ACS Div. of Fuel Chem., Preprints, 39 (2) 569, (1994).

51. Zhao, Y., Serio, M.A., Bassilakis, R., and Solomon, P.R., A Method of Predicting Coal Devolatilization Behavior Based on the Elemental Composition, 25th Symposium (Int.) on Combustion/The Combustion Institute, pp 553-560 (1994).

BYU Publications Funded in Whole or in Part by DOE Contract No. DE-AC21-86MC23075 (1986-1993)

Journal Publications

1. Blackham, A. U., Smoot, L. D. and Yousefi, P., Oxidation Rates of cm-sized Char Particles, Fuel, in press, (1993).

2. Boardman, R. D., Eatough, C. N., Germane, G. J. and Smoot, L. D., Comparison of Measurements and Predictions of Flame Structure and Thermal NO_x in a Swirling, Natural Gas Diffusion Flame, Comb.Sci. Tech., XX, 1-18 (1993).

3. Boardman, R. D. and Smoot, L. D., Prediction of Nitric Oxide in Advanced Combustion Systems, AIChE J., 34, 1573 (1988).

4. Brewster, B. S., Baxter, L. L. and Smoot, L. D., Treatment of Coal Devolatilization in Comprehensive Combustion Modeling, Energy & Fuels, 2, 362-370 (1988).

5. Brewster, B. S., Smoot, L. D., Solomon, P. R. and Markham, J. R., Structure of a Near-Laminar Coal Jet Flame, Energy & Fuels, in press, (Nov/Dec 1993).

6. Germane, G. J., Thrust Area 6: Model Evaluation Data and Process Strategies, Energy & Fuels, in press, (1993).

7. Hobbs, M. L., Radulovic, P. T. and Smoot, L. D., Combustion and Gasification of Coals in Fixed Beds, Prog. Energy Combust. Sci., in press, (1993).

8. Hobbs, M. L., Radulovic, P. T. and Smoot, L. D., Modeling Fixed-Bed Coal Gasifiers, AIChE J., 38, 681-702 (1992).

9. Hobbs, M. L., Radulovic, P. T. and Smoot, L. D., Prediction of Effluent Compositions for Fixed-Bed Coal Gasifiers, Fuel, 71, 1177-1194 (1992).

10. Monson, C. R., Germane, G. J., Blackham, A. U. and Smoot, L. D., Char Oxidation at Elevated Pressures, Comb. Flame, in press, (1993).

11. Monson, C. R. and Germane, G. J., A High Pressure Drop-Tube Facility for Coal Combustion Studies, Energy & Fuels, in press, (1993).

12. Sanderson, D. K. and Germane, G. J., Composition of Combustion Gases and Particles in a Pulverized Coal-Fired Reactor, Energy & Fuels, in press, (1993).

13. Smoot, L. D., Boardman, R. D., Brewster, B. S., Hill, S. C. and Foli, A. K., Development and Application of an Acid Rain Precursor Model for Practical Furnaces, Energy & Fuels, in press, (1993).

Book Chapters

1. Boardman, R. and Smoot, L. D., Pollutant Formation and Control, Chapter 6 in Smoot, L. D., ed., *Fundamentals of Coal Combustion for Clean and Efficient Use*, Elsevier, New York, 433-510 (1993).

2. Brewster, B. S., Hill, S. C., Radulovic, P. R. and Smoot, L. D., Comprehensive Modeling, Chapter 8 in Smoot, L. D., ed., *Fundamentals of Coal Combustion for Clean and Efficient Use*, Elsevier, New York, 567-706 (1993).

3. Eatough, C. N., Boardman, R. D., Germane, G. J. and Smoot, L. D., Comparison of Combustion Measurements and Model Predictions of Thermal NO_x, Temperatures, Velocities and Major Species in a Swirling Natural Gas Diffusion Flame, *Combustion Technologies for a Clean Environment*, Gordon and Breach, (1993).

4. Germane, G. J., Eatough, C. N. and Cannon, J. N., Process Data and Strategies, Chapter 2 in Smoot, L. D., ed., *Fundamentals of Coal Combustion for Clean and Efficient Use*, Elsevier, New York, 79-130 (1993).

5. Radulovic, P. T. and Smoot, L. D., Coal Processes and Technologies, Chapter 1 in Smoot, L. D., ed., *Fundamentals of Coal Combustion for Clean and Efficient Use*, Elsevier, New York, 1-77 (1993).

Theses and Dissertations

1. Bateman, K. J., Millimeter Sized Coal Particle Combustion at Elevated Pressure, M.S. thesis, Brigham Young University, Provo, UT (1993).

2. Boardman, R. D., Development and Evaluation of a Combined Thermal and Fuel Nitric Oxide Predictive Model, Ph.D. dissertation, Brigham Young University, Provo, UT (1990).

3. Braithwaite, D. J., Cross Flow Jet Mixing Measurements in a Simulated Entrained-Flow Coal Gasifier, M.S. thesis, Brigham Young University, Provo, UT (1988).

4. Daines, R., Collection and Characterization of Pyrolized Coal Char and Tar at High Pressure, M.S. thesis, Brigham Young University, Provo, UT (1990).

5. Hobbs, M. L., Modeling Countercurrent Fixed-Bed Coal Gasification, Ph.D. dissertation, Brigham Young University, Provo, Utah (1990).

6. Huber, A. M., Effect of Sorbent on Sulfur Pollutant Species in an Entrained-Flow Coal Gasifier, M.S. thesis, Brigham Young University, Provo, Utah (1989).

7. Monson, C. R., Char Oxidation at Elevated Pressure, Ph.D. dissertation, Brigham Young University, Provo, UT (1992).

Conference Presentations

1. Boardman, R. D., Brewster, B. S., Huque, Z. and Smoot, L. D., Modeling Sorbent Injection and Sulfur Capture in Pulverized Coal Combustion, presented at the 1992 International Joint Power Generation Conference, Air Toxic Reduction and Combustion Modeling, FACT-Vol. 15, Atlanta, GA, October 18-22, 1-9 (1992).

2. Boardman, R. D., Smoot, L. D. and Brewster, B. S., Measurement and Prediction of Thermal and Fuel NO, 1989 Fall Meeting of the Western States Section/The Combustion Institute, Livermore, CA, October 23-25 (1989).

3. Boardman, R. D. and Smoot, L. D., Prediction of Fuel and Thermal NO in Advanced Combustion Systems, 1989 Joint EPA/EPRI Symposium on Stationary Combustion NO_x Control, San Francisco, CA (1989).

4. Brewster, B. S., Application of a Coal-General, 2-D Combustion Model, Ninth Annual International Pittsburgh Coal Conference, Pittsburgh, PA, October 12-16 (1992).

5. Brewster, B. S., Baxter, L. L. and Smoot, L. D., The Role of Coal Devolatilization in Comprehensive Combustion Models, Preprints of papers presented at the 194th National Meeting, American Chemical Society, Vol. 32, No. 3, New Orleans, LA, August 31-September 4, 106 (1987).

6. Brewster, B. S. and Smoot, L. D., Structure of a Near-Laminar Coal Jet Diffusion Flame, Twenty Third International Symposium on Combustion, Abstracts of Symposium Papers and Abstracts of Poster Session Presentations, The Combustion Institute, Pittsburgh, PA, Poster No. P148, Orléans, France, 281, July 22-27 (1990).

7. Brewster, B. S., Smoot, L. D., Solomon, P. R. and Markham, J. R., Structure of a Near-Laminar Coal Jet Flame, presented at Fall Meeting of the Western States Section/The Combustion Institute, San Diego, CA, October 14-16, (1990).

8. Brewster, B. S. and Smoot, L. D., Predicted Effects of Coal Volatiles Compositions in Turbulent Flames, presented at 1988 Spring Meeting of the Western States Section/The Combustion Institute, Salt Lake City, UT, March 21, (1988).

9. Cope, R. F., Monson, C. R., Hecker, W. C. and Germane, G. J., Improved Temperature, Velocity and Diameter Measurements for Char Particles in Drop-Tube Reactors, Western States Section/The Combustion Institute, Los Angeles, CA, October (1991).

10. Eatough, C. N., Boardman, R. D., Germane, G. J. and Smoot, L. D., Comparison of Combustion Measurements and Model Predictions of Thermal NO_x, Temperatures, Velocities and Major Species in a Swirling Natural Gas Diffusion Flame, First International Conference on Combustion Technologies for a Clean Environment, Vilamoura, Portugal, September 3-6, (1991).

11. Ghani, M. U., Radulovic, P. T. and Smoot, L. D., Modeling of Coal Conversion Processes in Fixed Beds, Preprints of papers presented at the 206th ACS National Meeting, American Chemical Society, 38, Chicago, IL, August 22-26, 1358-1365 (1993).

12. Hobbs, M. L., Radulovic, P. T. and Smoot, L. D., Fixed-Bed Coal Gasification Modeling, Twenty -Third International Symposium on Combustion, Abstracts of Symposium Papers and Abstracts of Poster Session Presentations, The Combustion Institute, Pittsburgh, PA, Poster No. P147, Orléans, France, July 22-27, 280 (1990).

13. Monson, C. R., Germane, G. J., Blackham, A. U. and Smoot, L. D., Experimental Char Oxidation at Atmospheric and Elevated Pressures, Fall Meeting of the Western States Section/The Combustion Institute, Berkeley, CA, October 12 (1992).

14. Pyper, D., Blackham, A. U., Warren, D., Hansen, L., Christensen, J., Haslam, J. et al., CARS Temperature Measurements in the BYU Controlled Profile Reactor in Natural Gas and Natural Gas-Assisted Coal Flames, Fall Meeting of the Western States Section/The Combustion Institute, Berkeley, CA, October 12 (1992).

15. Yi, S., Smoot, L. D., Brewster, B. S. and Radulovic, P., Numerical Model of a Moving-Bed Coal Reactor, Spring Meeting of the Western States Section/The Combustion Institute, Salt Lake City, UT, March 21 (1988).

In Preparation or Submitted

16. Barthelson, S. H., Smoot, L. D., Brewster, B. S., Fletcher, T. H. and Thornock, D. E., Model Comparisons with Drop-Tube Combustion Data for Various Devolatilization Submodels, Fuel, in preparation (1993).

17. Bateman, K. J., Germane, G. J. and Smoot, L. D., A Facility for High Pressure Measurement of Oxidation Rates of mm-Sized Char, Fuel, in preparation (1993).

18. Bateman, K. J., Germane, G. J. and Smoot, L. D., Effect of Pressure on Oxidation Rates of mm Sized Char, 25th Symposium (International) on Combustion, The Combustion Institute, Pittsburgh, PA, in preparation (1993).

19. Cope, R. F., Monson, C. R., Hecker, W. C. and Germane, G. J., Improved Temperature, Velocity and Diameter Measurements for Char Particles in Drop-Tube Reactors, Comb. Sci. Tech., in revision (1993).